

From Hermitian to non-Hermitian topological phases of matter

Von der Fakultät Mathematik und Physik der Universität
Stuttgart zur Erlangung der Würde eines Doktors der Naturwissenschaften
(Dr. rer. nat.) genehmigte Abhandlung

vorgelegt von

Wenbin Rui

aus Jiangsu, CHINA

Hauptberichter: Prof. Dr. Walter Metzner

Mitberichter: Dr. Andreas Schnyder

Prof. Dr. Maria Daghofer

Prof. Dr. Jörg Wrachtrup

Tag der mündlichen Prüfung: 12. Juli 2019

**Max-Planck-Institut für Festkörperforschung
Stuttgart 2019**

To my parents

Acknowledgements

First of all, I would like to express my sincere gratitude to my supervisor Andreas Schnyder for constantly supporting my research and encouraging me to explore many interesting problems. This work would have not have been possible without his guidance. The knowledge and skill I developed during my research will certainly serve as a sound foundation for my future career. I am very thankful to Prof. Walter Metzner for giving me the opportunity to join his theoretical department within the inspiring environment at the Max Planck Institute, and for providing the freedom to attend many academic conferences with financial support, which will definitely benefit my career.

I am deeply indebted to Prof. Yuxin Zhao for close collaborations on many exciting projects. A large portion of what I have learned during my PhD study has come from our collaborations, which also have contributed to the main part of this work. I have no doubt that that Yuxin's rigorous attitude and elegant taste towards physics have an influential impact on me. Yuxin as a professional physicist serves as a great role model for me by demonstrating not only how to conduct research, but also how to find a balance between work and life.

I am very thankful to Moritz Hirschmann for collaborations on many interesting projects, in which I have benefited a lot from his expertise in numerical calculations. I have been constantly impressed by his great patience with complicated and sophisticated problems. Moritz also helped me a lot in painstakingly proofreading many of my manuscripts, including this thesis. I would like to thank Eslam Khalaf for his help with analytical problems and for sharing his thesis template, which greatly accelerated the preparation of this thesis. I am very thankful to Satoshi Ikegaya for many fun discussions on various topics and for his encouragement during hard times. I would also like to thank Andreas Leonhardt and Darshan Joshi for commenting on my research results and sharing their opinions. Andreas and Moritz also helped me with the German version of this thesis abstract.

I have very much enjoyed the casual discussions with the group members during our lunch time and coffee break. I wish to thank Jachym Sykora, Lukas Schwarz, Johannes Mitscherling, Oleksii Maistrenko, Pietro Bonetti, Demetrio Vilardi, Nikolai Bittner, Raquel Queiroz, Tobias Holder, Berkay Kilic, Henri Menke, Xueyang Song, Mohamed Shaaban, and Jonathan Zhang. Together with our senior scientists, Dirk Manske, Peter Horsch, Roland Zeyer, and Andrzej Oles, they have created a relaxed environment that is ideal for theoretical research.

I would also like to thank Jeanette Schüller-Knapp, Hans-Georg Libuda, and Birgit King. Their invaluable help in administrative affairs has made me focus more on my own research.

Further thanks go to Xiaodong Cao, who began his PhD study almost at the same time with me. We have helped each other and witnessed each other's growth during these four years. I am very thankful to Yi Lu and his girlfriend Ru Yang for giving me a lot support during my time in Stuttgart. I am also very grateful to Prof. Zhicheng Zhong, who gave much help on my future career and encouraged me a lot with his own experience.

I would like to express my deep gratitude to Jie Pan, for his constant help and lasting encouragement on both my life and work, and particularly for his comments on this thesis.

Finally, I am greatly indebted to my family, for providing the best they can to support my education and career. They always encourage me to make the choices that I truly want and support them without

any condition. Their lasting love is the certain thing I have to face uncertainties in this world. I dedicate this thesis to them.

Zusammenfassung

Der Schwerpunkt dieser Arbeit liegt in der Erweiterung der Theorie topologischer Phasen von hermiteschen zu nicht hermiteschen Systemen. Dazu gehört nicht nur die Erweiterung konventioneller Konzepte wie topologische Invarianten und topologische Randzustände über die Theorie der hermiteschen Phasen hinaus, sondern auch die Erforschung und Charakterisierung völlig neuer topologischer Phasen, die ausschließlich in nicht hermiteschen Systemen vorkommen.

Inspiziert durch die enge Beziehung zwischen \mathcal{PT} -Symmetrie und nicht hermitescher Physik werden in Kapitel 2 zuerst topologische Halbmetalle mit Dirac-Linien besprochen. Diese zeichnen sich durch eindimensionale Bandkreuzungen aus, die durch \mathcal{PT} -Symmetrie, also der Kombination aus Inversion \mathcal{P} und Zeitumkehr \mathcal{T} geschützt sind und weisen eine Dispersion ähnlich einem Dirac-Punkt auf. Die Stabilität dieser Dirac-Linien wird durch eine quantisierte $\pm\pi$ Berry-Phase gewährleistet. Diese nichttrivialen topologischen Invarianten im Inneren eines Festkörpers führen zu exotischen Zuständen an dessen Oberfläche. Die Physik eines Dirac-Halbmetalls wird bei niedrigen Energien durch eine einparametrische Familie von $(2+1)$ -dimensionalen Quantenfeldtheorien beschrieben, die eine Paritätsanomalie aufweisen. Es wird gezeigt, dass diese Anomalie zu einem anomalen transversalen Strom führt. Aufgrund dieses intrinsischen Hall-Effekts fließen Ladungsträger an gegenüberliegenden Seiten eines Dirac-Ringes in entgegengesetzte Richtungen, wenn ein elektrisches Feld angelegt wird. Um diese topologischen Ströme messbar zu machen, wird eine hantelförmige Systemgeometrie untersucht, in der mittels der Oberflächenzustände die Teilchen entsprechend ihrem Kristallimpuls gefiltert werden. Am Ende dieses Kapitels werden \mathcal{PT} -symmetrische hermitesche und nicht hermitesche Halbmetalle mit Bandkreuzungs-Linien verglichen, insbesondere deren Unterschiede bezüglich topologischen Invarianten und Randzuständen.

Kapitel 3 konzentriert sich auf die Untersuchung nicht hermitescher topologischer Systeme mit einer Bandlücke, bei denen nicht hermitesche Terme keine Bandkreuzungen erzeugen, wenn sie einem ursprünglich hermiteschen topologischen System hinzugefügt werden. Da die meisten hermiteschen topologischen Systeme mit Bandlücke durch massive Dirac-Modelle beschrieben werden können, werden diese systematisch in d Dimensionen unter Berücksichtigung dreier verschiedener Klassen von nicht hermiteschen Termen untersucht: (i) nicht hermitesche Terme, die mit dem Dirac-Hamilton-Operator antikommutieren, (ii) nicht hermitesche kinetische Terme und (iii) nicht hermitesche Massenterme. Es wird gezeigt, dass diese Terme den Hamilton-Operator entweder intrinsisch oder oberflächlich nicht hermitisch machen, je nachdem ob die Nicht-Hermitizität durch eine nicht-unitäre Ähnlichkeitstransformation beseitigt werden kann. Es zeigt sich eine Dualität für die ersten beiden Klassen von nicht hermiteschen Störungen: Bei offenen Randbedingungen führen nicht hermitesche Terme vom Typ (i) zu intrinsischer Nicht-Hermitizität, während Terme vom Typ (ii) zu einer oberflächlichen Nicht-Hermitizität führen. Umgekehrt induziert Typ (i) in Systemen mit periodischen Randbedingungen eine oberflächliche Nicht-Hermitizität, während Typ (ii) eine intrinsische Nicht-Hermitizität hervorrufen. Störungen vom Typ (iii) hingegen machen den Hamilton-Operator immer intrinsisch nicht hermitisch, unabhängig von der Wahl der Randbedingung. Da Randbedingungen in unserer Theorie eine zentrale Rolle spielen, wird deren Einfluss auf die Bandstruktur mit der Transfermatrix-Methode diskutiert. Wichtig dabei ist, dass für Terme vom Typ (i) oder Typ (ii) $(d - 2)$ -dimensionale exzeptionelle Sphären in den Bandstrukturen der Oberfläche beziehungsweise im Inneren des Systems entstehen, die nur in

nicht hermiteschen Systemen auftreten. Zum Abschluss dieses Kapitels werden die Eigenschaften von exzeptionellen Punkten und ihre physikalischen Auswirkungen untersucht.

Im letzten Teil dieser Arbeit werden schließlich topologische Weyl- und Dirac-Halbmatalle mit nicht hermiteschen Potentialen untersucht. Zuerst werden hermitesche Weyl-Halbmatalle diskutiert, insbesondere die topologischen Invarianten, Oberflächenzustände in Form von Fermi-Bögen und der chirale magnetische Effekt vorgestellt werden. Danach werden nicht hermitesche Weyl-Halbmatalle unter Berücksichtigung aller möglichen nicht hermiteschen Potentiale besprochen. Es werden wieder zwei Arten von nicht hermiteschen Potentialen unterschieden: nicht hermitesche kinetische und nicht hermitesche Massenpotentiale. Die topologischen Invarianten und die Korrespondenz zwischen der Oberfläche und dem Inneren eines Systems für diese nicht hermiteschen Potentiale werden ausführlich erläutert. Im Falle der nicht hermiteschen Dirac-Halbmatalle liegt der Fokus auf (\mathcal{PT}) -symmetrischen, nicht hermiteschen Störungen. Diese Störungen können einen Dirac-Punkt in folgende Objekte verwandeln: (i) Zwei getrennte Weyl-Punkte, deren Energien sich im Imaginärteil unterscheiden. (ii) Ein Paar von relativ zueinander komplex konjugierten exzeptionellen Weyl-Ringen, deren Bandkreuzungen durch eine topologische Ladung geschützt sind und die eine neue topologische Phase darstellen. (iii) Eine exzeptionelle Dirac-Sphäre, die durch zwei topologische Ladungen charakterisiert ist. Eine leitet sich direkt von der \mathbb{Z}_2 Dirac-Monopolladung ab, während sich die andere aus der Nicht-Hermitizität ergibt. Für alle drei Fälle werden die topologischen Invarianten und topologischen Oberflächenzustände ausführlich diskutiert.

Abstract

The focus of this thesis lies on extending the theory of topological phases of matter from the Hermitian to the non-Hermitian regime. This includes not only the extension of conventional concepts such as topological invariants and topological boundary states in the theory of Hermitian topological phases, but also the exploration and characterization of entirely new topological phases unique to non-Hermitian systems.

Inspired by the close relation between \mathcal{PT} symmetry and non-Hermitian physics, in chapter 2, we first discuss the topological nodal-line semimetals, which are characterized by one-dimensional Dirac nodal rings protected by the combined symmetry of inversion \mathcal{P} and time-reversal \mathcal{T} . The stability of these Dirac rings is guaranteed by a quantized $\pm\pi$ Berry phase. This non-trivial topological invariant in the bulk will lead to exotic drumhead surface states at the boundary. The low-energy physics of the nodal-line semimetal is described by a one-parameter family of (2+1)-dimensional quantum field theories exhibiting the parity anomaly. We find that this parity anomaly leads to anomalous transverse current. Due to this Hall-like current, carriers at opposite sides of the Dirac nodal ring flow to opposite surfaces when an electric field is applied. To detect the topological currents, we propose a dumbbell device, which uses surface states to filter charges based on their momenta. At the end of this chapter, we compare the \mathcal{PT} -symmetric Hermitian and non-Hermitian nodal-line semimetals, especially their difference in topological invariant and topological boundary states.

We focus on studying non-Hermitian topological gapped systems where non-Hermitian terms do not induce band gap closings when added to the original Hermitian topological system in chapter 3. As most Hermitian topological gapped systems can be described by massive Dirac models, we present a systematic investigation of d -dimensional massive Dirac models with three different types of non-Hermitian terms: (i) non-Hermitian terms that anti-commute with the Dirac Hamiltonian, (ii) non-Hermitian kinetic terms, and (iii) non-Hermitian mass terms. We show that these terms render the Hamiltonian either intrinsically or superficially non-Hermitian, depending on whether the non-Hermiticity can be removed by non-unitary similarity transformations. A two-fold duality is revealed for the first two types of non-Hermitian perturbations: With open boundary conditions non-Hermitian terms of type (i) give rise to intrinsic non-Hermiticity, while terms of type (ii) lead to superficial non-Hermiticity. Vice versa, with periodic boundary conditions type (i) perturbations induce superficial non-Hermiticity, while type (ii) perturbations generate intrinsic non-Hermiticity. Type (iii) perturbations, in contrast, render the Hamiltonian always intrinsically non-Hermitian, independent of the boundary condition. As the boundary conditions play an important role in our theory, we discuss their impact on the band structure with the transfer matrix method. Importantly, we find that for type (i) and type (ii) terms, $(d - 2)$ -dimensional exceptional spheres, unique to non-Hermitian systems, emerge in the surface and bulk band structures, respectively. We close this chapter by studying the properties of exceptional points and their physical consequences.

Finally, in the last part of this thesis, we investigate topological Weyl and Dirac semimetals with non-Hermitian potentials. The Hermitian Weyl semimetals are discussed first, where we introduce the topological invariants, the Fermi arc surface states, and the chiral magnetic effect. Then we discuss non-Hermitian Weyl semimetals by considering all possible non-Hermitian potentials. We find that

there are two kinds of non-Hermitian potentials, the non-Hermitian kinetic and non-Hermitian mass potentials. The topological invariants and the bulk boundary correspondence for these non-Hermitian potentials are discussed in detail. For the non-Hermitian Dirac semimetals, we focus on the parity-time (\mathcal{PT})-symmetric non-Hermitian perturbations. We find that these perturbations can turn a Dirac point into: (i) two separate Weyl points; (ii) a pair of mutually complex conjugate Weyl exceptional rings; (iii) a Dirac exceptional sphere. In case (i), we find the Dirac point splits into a pair of Weyl points, which are separated by their imaginary energies. In case (ii), the complex band crossing of the pair of Weyl exceptional rings is protected by the topological charge from the non-Hermiticity, forming a new topological phase. In case (iii), a new kind of topological state, called Dirac exceptional sphere state, is discovered, which is protected by two topological charges. One originates from the \mathbb{Z}_2 Dirac monopole charge, and the other is associated with the non-Hermiticity. For all three cases, the topological invariants and topological surface states are discussed in detail.

Contents

Zusammenfassung	vii
Abstract	ix
1 Introduction	1
1.1 Band topology	2
1.1.1 Berry phase and Berry curvature	3
1.1.2 Quantum Hall effect	4
1.2 Topological materials	6
1.2.1 Time-reversal symmetry breaking topological insulators	7
1.2.2 Time-reversal symmetric topological insulators	11
1.2.3 Wilson loop	14
1.3 Symmetry and topology	17
1.3.1 Dirac Hamiltonian and classification scheme	20
1.4 Non-Hermitian topological phases	24
1.4.1 Classification of non-Hermitian topological phases	26
1.5 Organization of this thesis	27
2 \mathcal{PT}-symmetric topological nodal-line semimetals	29
2.1 Symmetry and topology	30
2.2 Dirac nodal-line semimetals	32
2.3 Drumhead surface states	35
2.3.1 Surface spectrum from the continuum model	35
2.3.2 LDOS from the lattice model	37
2.4 Parity anomaly	38
2.4.1 Parity anomaly of (2+1)-dimensional massless Dirac fields	38
2.4.2 Parity anomaly of (3 + 1)-dimensional DNLSMs	40
2.5 Topological current	41
2.5.1 Semiclassical response theory	42
2.5.2 Berry curvature in DNLSMs	44
2.5.3 Transverse Hall current	46
2.6 Proposal for generating the topological current	48
2.6.1 Landauer formula	49
2.6.2 Dumbbell filter device	51
2.6.3 Robustness of the topological current	52
2.7 \mathcal{PT} -symmetric non-Hermitian topological nodal-line semimetals	58
2.8 Conclusions	59

3	Non-Hermitian topological gapped systems	61
3.1	General theory	62
3.1.1	Non-Hermitian terms of type (i)	64
3.1.2	Non-Hermitian terms of type (ii)	66
3.1.3	Non-Hermitian terms of type (iii)	68
3.2	Representative non-Hermitian topological gapped systems	69
3.2.1	2D quantum spin hall insulator	70
3.2.2	4D topological insulator characterized by the second Chern number	76
3.3	Effects of boundary conditions in non-Hermitian lattice systems	78
3.4	Exceptional points	83
3.4.1	Physics around exceptional points	85
3.4.2	\mathbb{Z}/N classification of non-Hermitian Hamiltonian with exceptional point	87
3.4.3	Green's function at exceptional points	89
3.5	Conclusions	90
4	Non-Hermitian topological Weyl and Dirac semimetals	93
4.1	Introduction	93
4.2	Weyl semimetals	94
4.2.1	Fermi arc surface states and topological invariants	95
4.2.2	Landau bands and magnetoconductivity	97
4.2.3	Chiral Anomaly	99
4.3	Non-Hermitian Weyl semimetals	105
4.3.1	Non-Hermitian potential $i\lambda\sigma_2$	108
4.3.2	Non-Hermitian potential $i\lambda\sigma_3$	117
4.4	\mathcal{PT} -symmetric non-Hermitian Dirac semimetals	118
4.4.1	Classification of \mathcal{PT} -symmetric non-Hermitian Dirac semimetals	122
4.4.2	Case (II): Double Weyl exceptional rings	124
4.4.3	Case III: Dirac exceptional sphere	131
4.5	Conclusions	135
5	Conclusion and outlook	137
	Bibliography	146

List of publications

- [1] **Surface magnetism in a chiral d -wave superconductor with hexagonal symmetry**
J. Goryo, Y. Imai, W. B. Rui, M. Sigrist, and A. P. Schnyder
Phys. Rev. B **96**, 140502 (R) (2017).

- [2] **Topological transport in Dirac nodal-line semimetals**
W. B. Rui, Y. X. Zhao, and A. P. Schnyder
Phys. Rev. B **97**, 161113 (R) (2018).

- [3] **Topology and exceptional points of massive Dirac models with generic non-Hermitian perturbations**
W. B. Rui, Y. X. Zhao, and A. P. Schnyder
Phys. Rev. B **99**, 241110 (R) (2019), Editors' Suggestion.

- [4] **\mathcal{PT} -symmetric non-Hermitian Dirac semimetals**
W. B. Rui, M. Hirschmann, and A. P. Schnyder
arXiv: 1907.10417 (2019).

List of Figures

1.1	(a) Hexagonal structure of graphene. A and B denote different sites. Blue arrows denote the lattice vectors for the nearest neighbors and the red arrows denote those for next-nearest neighbors. (b) Phase diagram against parameters M/t_2 and ϕ of the Haldane model. The shaded region denotes the topological non-trivial phases.	8
1.2	(a) The Chern number γ_- against parameter M for the Chern insulator Hamiltonian described in Eq. (1.42). (b) The corresponding vector field of $\mathbf{d}(\mathbf{k}) = (\sin k_x, \sin k_y, 2 + M - \cos k_x - \cos k_y)$ on the two-dimensional Brillouin zone.	10
1.3	(a) The Wilson loop spectrum against k_x for $M = -1$ (upper panel) and $M = +1$ (lower panel) for the Chern insulator described in Eq. (1.42). (b) The Wilson loop spectrum against k_x for $M = 1.5$ (upper panel) and $M = +2.5$ (lower panel) for the BHZ model described in Eq. (1.51).	16
2.1	The topological charge is defined in terms of a line integral along the green loop. The blue plane indicates the two-dimensional subsystems that are parameterized by the angle ϕ	32
2.2	Drumhead surface states. (a) Relationship of the Dirac ring to the surface states of a topological nodal-line semimetal. The yellow and blue regions show the bulk and surface BZ, respectively. Drumhead surface states occur within the red region, which is bounded by the projected Dirac ring. Within this region the topological charge ν , Eq. (2.12), takes on the value $\nu = 1$, while outside this region it is zero. (b) Local density of states on the surface. The total number unit cells in z direction is $N_z = 50$. The number of states near the Fermi surface that summed is $N_{\text{eigen}} = 50$ and the first $N_{\text{edge}} = 5$ unit cells from the boundary are taken into account. Γ is taken as 1.	34
2.3	Energy dispersion $E_{\pm}(\mathbf{k})$ close to the Dirac ring as a function of the radial coordinate k_{ρ} . The chemical potential μ is in the conduction band, slightly above the gap energy m	45
2.4	Topological currents in a Dirac nodal-line semimetal. The red arrows indicate the Berry curvature $\mathbf{\Omega}(\mathbf{k})$, Eq. (2.84), in the presence of a small PT breaking mass term $m\sigma_1$. The green arrows represent the transverse topological current $\mathbf{j}_{t,\phi}$, Eq. (2.91), that is induced by an external electric field applied along (a) the y direction and (b) the z direction.	47
2.5	Schematic diagram of dumbbell filter device. (a) The device consists of two bulk regions (“i” and “ii”) separated by a constriction (“iii”) with (001) surface states. (b) Schematic dispersion relation for fixed $k_x = 0$ in the bulk regions and in the constriction. An electron with $k_y > 0$ (red filled circles) can be transmitted, while an electron with $k_y < 0$ (open blue circles) is reflected.	51
2.6	Dispersion relation, conductance, and polarization for the dumbbell filter device of Fig. 2.5. (a) Dispersion relation of the DNLSM \mathcal{H}_L , Eq. (2.29), in bar geometry with dimensions $N_x = 20$ and $N_z = 10$ and mass $m = 0.05$. (b) Conductance G for the dumbbell filter as a function of chemical potential μ in the constriction. The inset shows the polarization P	52

- 2.7 The parameters of the tight-binding model are $t_{\parallel} = 0.638$ eV, $t_{\perp} = -0.303$ eV, $t'_{\perp} = 0.262$ eV, $\mu_z = 1.609$ eV obtained from fitting the DFT bands of CaAgP [1, 2]. (a) Wave function profile for bulk and surface bands for $N_z = 10$ and $N_x = 20$, with a small gap of 0.05 eV. (b) Energy window (dE) against thickness or (N_z) in a Log-Log graph. The lattice constant of CaAgP in z direction is 0.42 nm. The blue dots are obtained from numerical simulations and the red solid line is the fitting curve. 53
- 2.8 Berry curvature and properties of the dumbbell filter device for a DNLSM with finite dispersion $c(\mathbf{k})$. (a) Berry curvature as computed from the tight-binding model Eq. (2.29) together with Eq. (2.104). (b) Band structure of the dumbbell filter device with dimensions $N_x = 20$ and $N_z = 10$. (c) and (d) conductance G and polarization P of the dumbbell filter device against chemical potential μ , respectively. The parameter values are the same as in Fig. 2.6 except for $c_1 = 0.2$ and $c_2 = 0.1$ 54
- 2.9 Berry curvature and properties of the dumbbell filter device for the DNLSM (2.105) with spin-orbit coupling. (a) Berry curvature as computed from the tight-binding model (2.105). (b) Band structure of the dumbbell filter device with dimensions $N_x = 20$ and $N_z = 10$. (c) and (d) Conductance G and polarization P of the filter device against chemical potential μ . The parameter values are the same as in Fig. 2.6 except for $b_1 = 0.08$ 55
- 2.10 Band structure and Berry curvature of the dumbbell filter device as a function of increasing spin-orbit coupling. (a)-(d) Band structure of the dumbbell constriction with dimensions $N_x = 20$ and $N_z = 10$ with spin-orbit coupling strengths $b_1 = 0.02, 0.14, 0.20$ and 0.50 respectively. (e)-(h) Berry curvature of the DNLSM for the same parameters as in panels (a)-(d). 57
- 2.11 Conductance G of the dumbbell filter device with disorder. The dimensions of the constriction in the filter device are $N_x = 20$, $N_y = 20$, and $N_z = 10$. The disorder is described by the disorder potentials (2.107), where $v(\mathbf{r}_n)$ is drawn from a Gaussian distribution with width V_0 . The parameters of the DNLSM are the sam as in Fig. 2.6. 57
- 2.12 \mathcal{PT} -symmetric non-Hermitian topological nodal-line semimetal. (a) Topological exceptional torus. (b) The real part of the Berry phase, which is not defined in the white region. (c) Wavefunction amplitude $|\psi(k_x, k_y, N_z)|^2$ for the surface states for $N_z = 100$ layers in z direction. The region of the localized wavefunction forms two disks at top and bottom layer. 58
- 3.1 2D topological insulator with non-Hermitian anti-commuting terms. (a) and (b) show the windings of the Wilson loop against k_x for Hermitian topological insulator with $\lambda = 0.0$ and non-Hermitian topological insulator with $\lambda = 0.3$. Here M is set to be 1.0 for both Hermitian and non-Hermitian 2D topological insulator. Blue and green indicates the real and imaginary parts of the Wilson loop, respectively. 71
- 3.2 Spectra for 2D topological insulator with non-Hermitian anti-commuting terms. (a), (b) and (c) are the bulk spectra for $\lambda^2 < \min d_{\text{TI}}(\mathbf{k})^2$, $\min d_{\text{TI}}(\mathbf{k})^2 < \lambda^2 < \max d_{\text{TI}}(\mathbf{k})^2$ and $d_{\text{TI}}(\mathbf{k})^2 < \lambda^2$. (d), (e) and (f) are the corresponding spectra for the open boundary Hamiltonian. Here M is set to be 1.0, and λ is set to be 0.3, 2.0 and 3.2 for (a), (b) and (c), respectively. Blue and green indicates the real and imaginary parts of the energy spectrum respectively. Red denotes the position of exceptional points. 72

3.3	Spectra for 2D topological insulator with non-Hermitian kinetic terms.(a) and (b) are the spectra for PBCs and OBCs, respectively. The parameters are set as $\lambda = 0.5$ and $M = 1.5$, so that the open boundary spectrum is purely real and there are exceptional points emerging in the bulk. The blue and green denote real and imaginary parts of the spectrum. The exceptional points are highlighted in red. (c) The wavefunction profile of the right eigenvector for boundary (solid) and bulk (dashed) states.	74
3.4	(a),(c) Real and (b),(d) imaginary parts of the energy spectra of the two-dimensional topological insulator $H_{\text{TI},0}$ perturbed by the non-Hermitian mass term $i\lambda\Gamma_3$ with periodic and open boundary conditions, respectively. The parameters are chosen as $M = 1.5$ and $\lambda = 0.3$. Solid and dotted lines represent bulk and surface states, respectively.	76
3.5	(a) real and (b) imaginary parts of the spectrum of the SSH model with non-Hermitian kinetic term $i\lambda\sigma_2$. (c) real and (d) imaginary parts of the spectrum of the SSH model with non-Hermitian anti-commuting term $i\lambda\sigma_3$. Solid blue represents the spectrum with OBCs, while dashed gray represent spectrum with PBCs. The red dots denote the exceptional points.	81
4.1	(a) Energy spectrum of the Hermitian lattice model of the Weyl semimetal in Eq. (4.3) with $k_y = 0$. The parameter is chosen as $M = 2$ so that the two Weyl points are located at $(0, 0, -\pi/2)$. (b) The vector field of $\mathbf{d} = (\sin k_x, \sin k_y, M - \cos k_x - \cos k_y - \cos k_z)$ for the Weyl semimetal, with the monopole region highlighted in red.	96
4.2	(a) The energy spectrum against wavevector k_z of the Landau levels for the low-energy effective model of Eq. (4.4) in a magnetic field B applied along the z direction. (b) The schematic picture describing the change of electron number at the two Weyl nodes under the parallel electric and magnetic fields.	98
4.3	Non-Hermitian Weyl semimetal. (a) The red ring denotes the Weyl exceptional ring, which can be enclosed by the one-dimensional sphere S^1 (blue) and two-dimensional sphere S^2 (green). (b) Real part of the energy spectra for the Weyl Hamiltonian with the non-Hermitian term $i\lambda\sigma_2$. The green curves are for the case of open boundary conditions and the gray curves for that of periodic boundary conditions. The surface states is highlighted in blue and black. The topological invariant C_{k_z} is given in red and shows that we find topological surface states when $C_{k_z} = +1$ and no surface states when $C_{k_z} = 0$. The parameters are chosen as $\lambda = 0.3$ and $m = 2.5$	106
4.4	(a) The energy spectrum against wavevector k_z of the Landau levels for the low-energy effective model of Eq. (4.166) in a magnetic field B applied along the z direction. (b) The schematic picture showing the change of electrons at two Dirac points under the parallel electric and magnetic fields. L and R denotes the Weyl nodes with opposite chirality inside the Dirac point.	121
4.5	Double Weyl exceptional rings.	126
4.6	(a) The inner red sphere denotes the Dirac exceptional sphere. \mathbf{k}_1 and \mathbf{k}_2 together form S^0 that is used to calculate the topological charge $\nu(S^0)$. The outer blue sphere S^2 is chosen to enclose the Dirac exceptional sphere, and is used to calculate the \mathbb{Z}_2 topological charge. (b) The location of the two Dirac exceptional spheres. (c) The real part of the surface spectrum from the tight-binding model. (d) The imaginary part of the surface spectrum. The green curve is the surface spectrum calculated analytically.	130

1

Chapter 1

Introduction

The electronic band theory of solids developed in the 20th century is one of the great triumphs of solid state physics. It provides a theoretical understanding for a vast number of physical properties of solids and gives the foundation for designing solid-state devices. It was not realized, however, that a large piece of the theory was still missing until the discovery of the quantum Hall effect [3]. The quantized Hall conductance measured in two-dimensional electronic materials under magnetic field was found to be a topological invariant determined by the electronic quantum state [4]. Since then, the importance of the geometry of the electronic quantum state has been gradually recognized, along with a growing interest in materials with non-trivial topological structure [5–8]. A significant breakthrough, including the theoretical prediction of a two-dimensional topological insulator materials and the experimental observation of quantum spin Hall effect, took place in 2006 [6, 9]. The rapid development of the topological band theory has led to many discoveries of intriguing topological materials and unprecedented physical properties [10–16].

Besides its own rapid development, the field of topological phases also brings new insights into other fields. A hallmark is the discovery of Weyl fermions in topological semimetals, a previously elusive particle in high-energy physics [17]. Moreover, the less strict symmetry requirements in solids lead to the discovery of new types of fermions that have no counterpart in high-energy physics [18, 19]. The theory of topological phases has also been applied beyond electronic systems, and is undergoing an increasing diversification by taking into account unique properties of systems such as phononic, photonic and cold atom systems. Remarkably, a recent development even goes beyond Hermitian physics, which poses questions about both topological phases and non-Hermitian physics [20, 21].

This chapter serves as an introduction to the basic notions and concepts in the field of topological phases of matter. The theoretical background of the topological phases in periodic systems is explained first, and through this, the geometric origin of the quantum Hall effect in two-dimensional materials is explained. Then we will introduce the key examples of topological materials in the development of this field, where the formulation of different topological invariants is discussed. Later on, the classification of topological phases of matter is achieved in terms of generic symmetries and spatial dimensions. As the main focus of this thesis is the non-Hermitian topological phases, we will make a brief introduction to the non-Hermitian topological systems at the end.

1.1 Band topology

In a perfect crystal with N unit cells ($N = N_1 N_2 N_3$), assuming the Born-von Karman periodic boundary conditions, any function defined on the periodic lattice must fulfill $f(\mathbf{r} + N_i \mathbf{a}_i) = f(\mathbf{r})$, where \mathbf{a}_i are basis vectors. The fundamental symmetry of a crystal is the translation symmetry, i.e., the crystal is invariant under the translation of an arbitrary lattice constant $\mathbf{R}_l = l_1 \mathbf{a}_1 + l_2 \mathbf{a}_2 + l_3 \mathbf{a}_3$ with $l_i \in \mathbb{Z}$. Denoting the translation operator by $\{E|\mathbf{R}_l\}$, the total N operators form a translation group of order N . Since all the group elements satisfy the relation of $\{E|\mathbf{R}_l\}^{-1} \{E|\mathbf{R}_m\} \{E|\mathbf{R}_l\} = \{E|\mathbf{R}_m\}$, each element of the translation group forms a conjugacy class. According to group theory, the number of conjugacy classes is equal to the number of irreducible representations. Thus, there are N irreducible representations of the translation group. The dimension of the N irreducible representations can be determined by the formula from group theory as $\sum_{\alpha=1}^N n_{\alpha}^2 = N$, which means the N irreducible representations of the translation group are all one dimensional. Suppose that $\psi(\mathbf{r})$ is the basis function for the one dimensional representation. We have,

$$\{E|\mathbf{a}_i\}^{-1} \psi(\mathbf{r}) = \psi(\{E|\mathbf{a}_i\} \mathbf{r}) = \psi(\mathbf{r} + \mathbf{a}_i) = D(\{E|\mathbf{a}_i\}) \psi(\mathbf{r}), \quad (1.1)$$

with D the representation of the basis function of ψ . Under the Born-von Karman periodic boundary conditions, it can be inferred that

$$\psi(\mathbf{r}) = \{E|N_i \mathbf{a}_i\}^{-1} \psi(\mathbf{r}) = \underbrace{\{E|\mathbf{a}_i\}^{-1} \{E|\mathbf{a}_i\}^{-1} \cdots \{E|\mathbf{a}_i\}^{-1}}_{N_i} \psi(\mathbf{r}) = D^{N_i}(\{E|\mathbf{a}_i\}) \psi(\mathbf{r}), \quad (1.2)$$

which yields $D^{N_i}(\{E|\mathbf{a}_i\}) = 1$ and thus $D(\{E|\mathbf{a}_i\}) = e^{2\pi i \frac{n_i}{N_i}}$, with $n_i = 0, \pm 1, \pm 2, \dots$. Accordingly,

$$\{E|\mathbf{R}_l\}^{-1} \psi(\mathbf{r}) = \psi(\mathbf{r} + \mathbf{R}_l) = \psi(\mathbf{r} + l_1 \mathbf{a}_1 + l_2 \mathbf{a}_2 + l_3 \mathbf{a}_3) = e^{2\pi i \sum_{i=1}^3 \frac{l_i n_i}{N_i}} \psi(\mathbf{r}). \quad (1.3)$$

Eq. (1.3) defines a vector in reciprocal space as $\mathbf{k} = \sum_{i=1}^3 \frac{n_i}{N_i} \mathbf{b}_i$ with $\mathbf{a}_i \cdot \mathbf{b}_j = 2\pi \delta_{i,j}$. Here \mathbf{b}_i are the reciprocal lattice vectors. The reciprocal vector \mathbf{k} defined by D can serve as the label for the irreducible representation of the translation group. Here the \mathbf{k} -th irreducible representation can be written as $e^{i\mathbf{k} \cdot \mathbf{R}_l}$.

Bloch theorem As $\{E|\mathbf{R}_l\}^{-1}$ denotes the translation operator, $e^{i\mathbf{k} \cdot \mathbf{R}_l}$ can be understood as its \mathbf{k} -th eigenvalue, whose eigenvector can be labeled as $\psi_{\mathbf{k}}(\mathbf{r})$. For an arbitrary lattice vector \mathbf{R}_l , according to Eq. (1.3), the following relation holds,

$$\{E|\mathbf{R}_l\}^{-1} \psi_{\mathbf{k}}(\mathbf{r}) = \psi_{\mathbf{k}}(\mathbf{r} + \mathbf{R}_l) = e^{i\mathbf{k} \cdot \mathbf{R}_l} \psi_{\mathbf{k}}(\mathbf{r}), \quad (1.4)$$

which is the celebrated Bloch theorem. We can take $u_{\mathbf{k}}(\mathbf{r}) = e^{-i\mathbf{k} \cdot \mathbf{r}} \psi_{\mathbf{k}}(\mathbf{r})$, and from Eq. (1.4), we will arrive at an important relation of $u_{\mathbf{k}}(\mathbf{r} + \mathbf{R}_l) = u_{\mathbf{k}}(\mathbf{r})$, which means $u_{\mathbf{k}}(\mathbf{r})$ is periodic in lattice constant \mathbf{R}_l . The state of electrons on the lattice can thus be expressed as the Bloch wavefunction,

$$\psi_{\mathbf{k}}(\mathbf{r}) = e^{i\mathbf{k} \cdot \mathbf{r}} u_{\mathbf{k}}(\mathbf{r}). \quad (1.5)$$

It should be noted that the reciprocal vector \mathbf{k} is not uniquely determined. According to Eq. (1.4), when the difference between two reciprocal vectors of \mathbf{k} and \mathbf{k}' is equal to a reciprocal lattice vector $\mathbf{k}' - \mathbf{k} = \mathbf{k}_h$, they can both be used to denote the irreducible representation of $\{E|\mathbf{R}_l\}^{-1}$, because $e^{i(\mathbf{k}+\mathbf{k}_h)\cdot\mathbf{R}_l} = e^{i\mathbf{k}\cdot\mathbf{R}_l}$. Thus, the Bloch wavefunction $\psi_{\mathbf{k}}(\mathbf{r})$ is periodic in \mathbf{k} ,

$$\psi_{\mathbf{k}}(\mathbf{r}) = \psi_{\mathbf{k}+\mathbf{k}_h}(\mathbf{r}). \quad (1.6)$$

In order to avoid repetition, it is necessary to restrict the reciprocal vector \mathbf{k} in a region where the difference between each two reciprocal vectors is less than the smallest of the reciprocal lattice vectors. This region is called the first Brillouin zone (BZ).

For non-interacting lattice systems, the translational symmetry tells us that the state on the lattice can be described by the Bloch wavefunction for a single electron. The Schrödinger equation reads

$$H\psi_{\mathbf{k}}(\mathbf{r}) = E(\mathbf{k})\psi_{\mathbf{k}}(\mathbf{r}). \quad (1.7)$$

By multiplying $e^{-i\mathbf{k}\cdot\mathbf{r}}$ on both sides, we arrive at

$$H(\mathbf{k})u_{\mathbf{k}}(\mathbf{r}) = E(\mathbf{k})u_{\mathbf{k}}(\mathbf{r}), \quad (1.8)$$

with $H(\mathbf{k}) = e^{-i\mathbf{k}\cdot\mathbf{r}}He^{i\mathbf{k}\cdot\mathbf{r}}$. Thus, the band structure of periodic systems consists a mapping from the crystal momentum \mathbf{k} defined on the manifold of BZ to the Hilbert space defined by the Bloch Hamiltonian $H(\mathbf{k})$.

1.1.1 Berry phase and Berry curvature

We introduce the very basic concept of Berry phase in periodic systems in this subsection. From Eq. (1.8), the Hamiltonian depends on the parameter \mathbf{k} defined in the Brillouin zone. Suppose that electrons can move around the Brillouin zone adiabatically. The state at time t can be denoted as $|u_n(\mathbf{k}(t))\rangle$. Due to the arbitrariness in the phase, there could be an extra phase factor $|\psi_n(t)\rangle = e^{-i\theta(t)}|u_n(\mathbf{k}(t))\rangle$ with n the band index. With the Schrödinger equation of $H(\mathbf{k}(t))|\psi_n(t)\rangle = i\hbar\partial_t|\psi_n(t)\rangle$, the dynamics of the state can be obtained as [22]

$$E_n(\mathbf{k}(t))|u_n(\mathbf{k}(t))\rangle = \hbar\partial_t\theta(t)|u_n(\mathbf{k}(t))\rangle + i\hbar\partial_t|u_n(\mathbf{k}(t))\rangle, \quad (1.9)$$

where $E_n(\mathbf{k}(t))$ is the eigenvalue for the band n . Applying the left eigenvector $\langle u_n(\mathbf{k}(t))|$ with the normalization condition of $\langle u_m(\mathbf{k}(t))|u_n(\mathbf{k}(t))\rangle = \delta_{m,n}$, and after the integration, the total phase is obtained as

$$\theta(t) = \frac{1}{\hbar} \int_0^t E_n(\mathbf{k}(t'))dt' - i \int_0^t \langle u_n(\mathbf{k}(t'))|\partial_{t'}|u_n(\mathbf{k}(t'))\rangle dt'. \quad (1.10)$$

The first and the second parts at the RHS are dynamical phase and geometrical phase, respectively. On a cyclic path of Γ in the Brillouin zone, the geometrical part can be written as

$$\gamma_n = i \int_0^t \langle u_n(\mathbf{k}(t'))|\partial_{t'}|u_n(\mathbf{k}(t'))\rangle dt' = i \oint_{\Gamma} d\mathbf{k} \langle u_n(\mathbf{k})|\nabla_{\mathbf{k}}|u_n(\mathbf{k})\rangle. \quad (1.11)$$

Accordingly, the form of the Berry connection can be derived as

$$\gamma_n = \oint_{\Gamma} d\mathbf{k} \cdot \mathbf{A}_n = \iint_{\Gamma} d\mathbf{S} \cdot \nabla_{\mathbf{k}} \times \mathbf{A}_n, \quad (1.12)$$

where we have used the Stokes' theorem. In the above expression, \mathbf{A}_n and $\nabla_{\mathbf{k}} \times \mathbf{A}_n$ are Berry connection and Berry curvature, respectively, which are expressed as

$$\mathbf{A}_n = i\langle u_n(\mathbf{k}) | \nabla_{\mathbf{k}} | u_n(\mathbf{k}) \rangle, \quad \boldsymbol{\Omega}_n = \nabla_{\mathbf{k}} \times \mathbf{A}_n(\mathbf{k}). \quad (1.13)$$

The components of the Berry curvature $\boldsymbol{\Omega}_n$ read,

$$\Omega_{n,\gamma} = i\varepsilon_{\alpha\beta\gamma} \partial_{\alpha} \left(\langle u_n(\mathbf{k}) | \partial_{\beta} | u_n(\mathbf{k}) \rangle \right) = i\varepsilon_{\alpha\beta\gamma} \langle \partial_{\alpha} u_n(\mathbf{k}) | \partial_{\beta} u_n(\mathbf{k}) \rangle, \quad (1.14)$$

where we have used the fact that the symmetric term is zero under the Levi-Civita tensor. With the orthonormal condition $\langle u_n(\mathbf{k}) | u_m(\mathbf{k}) \rangle = \delta_{mn}$, we have the relation $\langle \partial_{\alpha} u_n(\mathbf{k}) | u_m(\mathbf{k}) \rangle = -\langle u_n(\mathbf{k}) | \partial_{\alpha} u_m(\mathbf{k}) \rangle$. Thus, the component of the Berry curvature is

$$\Omega_{n,\gamma} = i\langle \partial_{\alpha} u_n(\mathbf{k}) | \partial_{\beta} u_n(\mathbf{k}) \rangle - i\langle \partial_{\beta} u_n(\mathbf{k}) | \partial_{\alpha} u_n(\mathbf{k}) \rangle = i \sum_{m \neq n} \langle \partial_{\alpha} u_n(\mathbf{k}) | u_m(\mathbf{k}) \rangle \langle u_m(\mathbf{k}) | \partial_{\beta} | u_n(\mathbf{k}) \rangle - (\alpha \leftrightarrow \beta) \quad (1.15)$$

By the following relation for $m \neq n$,

$$\begin{aligned} \langle u_n(\mathbf{k}) | \partial_{\alpha} H(\mathbf{k}) | u_m(\mathbf{k}) \rangle &= \partial_{\alpha} (\langle u_n(\mathbf{k}) | H(\mathbf{k}) | u_m(\mathbf{k}) \rangle) - \langle \partial_{\alpha} u_n(\mathbf{k}) | H(\mathbf{k}) | u_m(\mathbf{k}) \rangle \\ &= (E_n - E_m) \langle u_n(\mathbf{k}) | \partial_{\alpha} | u_m(\mathbf{k}) \rangle, \end{aligned} \quad (1.16)$$

the Berry curvature can be re-expressed as

$$\Omega_{n,\gamma} = i \sum_{m \neq n} \frac{\langle u_n(\mathbf{k}) | (\partial_{\alpha} H) | u_m(\mathbf{k}) \rangle \langle u_m(\mathbf{k}) | (\partial_{\beta} H) | u_n(\mathbf{k}) \rangle}{(E_n - E_m)^2} - (\alpha \leftrightarrow \beta). \quad (1.17)$$

The vector form of Berry curvature then is

$$\boldsymbol{\Omega}_n = i \sum_{m \neq n} \frac{\langle u_n(\mathbf{k}) | (\nabla_{\mathbf{k}} H(\mathbf{k})) | u_m(\mathbf{k}) \rangle \times \langle u_m(\mathbf{k}) | (\nabla_{\mathbf{k}} H(\mathbf{k})) | u_n(\mathbf{k}) \rangle}{(E_n - E_m)^2}. \quad (1.18)$$

In the following subsection, we will show that the Berry curvature plays a role for physically observable quantities.

1.1.2 Quantum Hall effect

Historically, the first observed quantity that results from the geometric aspect of the electronic quantum state is the integer quantum Hall effect, measured in two-dimensional materials, in the presence of an external magnetic field [3]. To calculate the conductance we may use the Kubo formula. We add a background electric field $\mathbf{E} = -\partial_t \mathbf{A}$ to the system, with $A_t = 0$. The Hamiltonian is changed as [23],

$$H_0 \rightarrow H_0 - \mathbf{J} \cdot \mathbf{A}, \quad (1.19)$$

where \mathbf{J} is the operator of the electric current. Treating $\Delta H = -\mathbf{J} \cdot \mathbf{A}$ as a perturbation, we can adopt the linear response theory. Then the expectation value of the current at time t can be obtained as

$$\langle \mathbf{J}(t) \rangle = \langle 0 | \left(\mathbf{J}(t) + \frac{i}{\hbar} \int_{-\infty}^t dt' [\Delta H(t'), \mathbf{J}(t)] \right) | 0 \rangle, \quad (1.20)$$

with $|0\rangle$ the ground state. The first term in this expression is assumed to be zero as it represents the current without the field. We consider an AC electric field with the expression $\mathbf{E}(t) = \mathbf{E}e^{-i\omega t}$. Taking the limit of $\omega \rightarrow 0$, it will approach to a DC electric field. The corresponding vector potential is obtained as $\mathbf{A} = \frac{\mathbf{E}}{i\omega}e^{-i\omega t}$. Thus the expectation value of the current can be obtained as

$$\langle J_i(t) \rangle = \frac{1}{\hbar\omega} \int_0^\infty dt'' e^{i\omega t''} \langle 0 | [J_j(0), J_i(t'')] | 0 \rangle E_j e^{-i\omega t}. \quad (1.21)$$

Here we have done the replacement of $t'' = t - t'$ in Eq. (1.20). The Hall conductivity comes from the part $i \neq j$, and it can be expressed explicitly as

$$\sigma_{xy} = \frac{1}{\hbar\omega} \int_0^\infty dt e^{i\omega t} \langle 0 | [J_y(0), J_x(t)] | 0 \rangle. \quad (1.22)$$

The current operator at time t is $\mathbf{J}(t) = e^{iH_0 t/\hbar} \mathbf{J}(0) e^{-iH_0 t/\hbar}$. Plugging it into the above equation, and inserting the identity $\sum_n |n\rangle \langle n| = 1$, the frequency dependent Hall conductivity can be obtained as

$$\sigma_{xy}(\omega) = -\frac{i}{\omega} \sum_{n \neq 0} \left(\frac{\langle 0 | J_y | n \rangle \langle n | J_x | 0 \rangle}{\hbar\omega + E_n - E_0} - \frac{\langle 0 | J_x | n \rangle \langle n | J_y | 0 \rangle}{\hbar\omega + E_0 - E_n} \right). \quad (1.23)$$

Taking the limit of $\omega \rightarrow 0$, the above conductivity becomes the DC conductivity. Taking the Taylor expansion on $1/(\hbar\omega + E_0 - E_n)$ with respect to $\hbar\omega$, the conductivity to the first order reads

$$\sigma_{xy} = i\hbar \sum_{n \neq 0} \left(\frac{\langle 0 | J_y | n \rangle \langle n | J_x | 0 \rangle}{(E_n - E_0)^2} - \frac{\langle 0 | J_x | n \rangle \langle n | J_y | 0 \rangle}{(E_n - E_0)^2} \right). \quad (1.24)$$

Next we focus on the current operator $\mathbf{J} = e\dot{\mathbf{r}}$ with $\dot{\mathbf{r}}$ describing the velocity of the electron. In the interaction picture, the dynamics of the position operator is given by $\dot{\mathbf{r}} = 1/(i\hbar)[\mathbf{r}, H_0]$. Notice that in the periodic system, $H_0 = H(\mathbf{k}) = e^{-i\mathbf{k}\cdot\mathbf{r}} H e^{i\mathbf{k}\cdot\mathbf{r}}$ as given in Eq. (1.8), thus the relation $\nabla_{\mathbf{k}} H_0 = -i\mathbf{r}H_0 + iH_0\mathbf{r} = -i[\mathbf{r}, H_0]$ can be established. Accordingly, the velocity is given by

$$\dot{\mathbf{r}} = \frac{1}{i\hbar} [\mathbf{r}, H_0] = \frac{1}{\hbar} \nabla_{\mathbf{k}} H_0. \quad (1.25)$$

Thus the current operator can be expressed as

$$\mathbf{J} = e\dot{\mathbf{r}} = \frac{e}{\hbar} \nabla_{\mathbf{k}} H_0. \quad (1.26)$$

Plugging the above relation into Eq. (1.24), the Hall conductance is given by

$$\sigma_{xy} = i \frac{e^2}{\hbar} \sum_{n \neq 0} \left(\frac{\langle 0 | \partial_{k_y} H(\mathbf{k}) | n \rangle \langle n | \partial_{k_x} H(\mathbf{k}) | 0 \rangle}{(E_n - E_0)^2} - \frac{\langle 0 | \partial_{k_x} H(\mathbf{k}) | n \rangle \langle n | \partial_{k_y} H(\mathbf{k}) | 0 \rangle}{(E_n - E_0)^2} \right). \quad (1.27)$$

Comparing with the Berry curvature in Eq. (1.17), we can arrive at the relation between Hall conductivity and Berry phase,

$$\sigma_{xy} = \frac{e^2}{\hbar} \int d\mathbf{k}^2 \Omega_{xy}(\mathbf{k}). \quad (1.28)$$

We can see that the geometrical phase (Chern number) actually corresponds to a physical observable. As the Chern number of the 2D BZ is always quantized, the Hall conductivity σ_{xy} is quantized with a universal constant. The above formula for the Hall conductivity was first obtained by Thouless, Kohmoto, Nightingale and Nijs and is thus also called the TKNN invariant [4].

1.2 Topological materials

In the previous section, from the derivation of the Hall conductivity, we can see that the topological property of a material is intrinsic, in that it only depends on the geometry of the electron's quantum state in the material and does not depend on external factors such as electric and magnetic fields. It is natural to ask whether there are materials with non-trivial topological property without applying external fields.

Early attempts were made by trying to find materials that realize an anomalous quantum Hall effect, i.e., a quantum Hall effect without magnetic field. A key factor is that the time-reversal symmetry needs to be broken in these materials, otherwise the Chern number would vanish as we show in the following. Denote the time-reversal symmetry operator as \mathcal{T} . If a periodic system is invariant under the time-reversal symmetry, then the states satisfy $\mathcal{T}|u_n(\mathbf{k})\rangle = e^{i\chi}|u_n(-\mathbf{k})\rangle$, with n the band index and χ the phase factor. We focus on the Berry curvature which is defined as $\Omega_{n,\gamma}(\mathbf{k}) = i\varepsilon_{\alpha\beta\gamma} \langle \partial_{k_\alpha} u_n(\mathbf{k}) | \partial_{k_\beta} u_n(\mathbf{k}) \rangle$, with repeated index as summation. At $-\mathbf{k}$, Berry curvature is

$$\begin{aligned} \Omega_{n,\gamma}(-\mathbf{k}) &= i\varepsilon_{\alpha\beta\gamma} \langle \partial_{-k_\alpha} u_n(-\mathbf{k}) | \partial_{-k_\beta} u_n(-\mathbf{k}) \rangle \\ &= i\varepsilon_{\alpha\beta\gamma} \partial_{k_\alpha} \left(\langle \mathcal{T} u_n(\mathbf{k}) | e^{i\chi} \right) \partial_{k_\beta} \left(e^{-i\chi} | \mathcal{T} u_n(\mathbf{k}) \rangle \right) \\ &= i\varepsilon_{\alpha\beta\gamma} \left(\partial_{k_\alpha} \chi \partial_{k_\beta} \chi + \partial_{k_\alpha} \langle \mathcal{T} u_n(\mathbf{k}) | \partial_{k_\beta} | \mathcal{T} u_n(\mathbf{k}) \rangle \right) \\ &= i\varepsilon_{\alpha\beta\gamma} \partial_{k_\beta} \langle u_n(\mathbf{k}) | \partial_{k_\alpha} | u_n(\mathbf{k}) \rangle \\ &= -\Omega_{n,\gamma}(\mathbf{k}). \end{aligned} \quad (1.29)$$

The anti-symmetric property of $\varepsilon_{\alpha\beta\gamma}$ is used in the calculation process. We can see that the Berry curvature is an odd function with time-reversal symmetry. Thus, when the time-reversal symmetry is preserved, the Chern number which is the integration over the entire Brillouin zone is zero.

The first example of the time-reversal symmetry breaking topological material exhibiting non-trivial Chern number was proposed by Haldane, by considering time-reversal symmetry breaking terms in spinless systems [5]. Later, a more general model called Chern insulator was established [8]. How-

ever, these materials are hard to realize due to the breaking of time-reversal symmetry. Historically, to overcome such difficulty, theorists turned towards considering time-reversal symmetric topological materials. Kane and Mele constructed a time-reversal invariant version of Haldane model, and thus it is called Kane-Mele model. At the mean time, Bernevig, Hughes, and Zhang proposed a time-reversal symmetric version of the Chern model, which is called the BHZ model [6]. Based on this, the quantum spin Hall effect was experimentally observed [9]. The various topological invariants that are used to characterize these different topological phases are discussed. At the end of this section, we introduce a more general topological invariant defined through the Wilson loop, which is widely used in characterizing topological materials from first principle calculations.

1.2.1 Time-reversal symmetry breaking topological insulators

We start with the tight-binding model for graphene, on which Haldane model is based. In Fig. 1.1 (a), the Hexagonal structure of the graphene is plotted. By considering only nearest-neighbor hoppings, the second quantized Hamiltonian reads,

$$H_D = t_1 \sum_{\langle i,j \rangle} c_i^\dagger c_j = \sum_{\mathbf{k}} \begin{pmatrix} c_{A,\mathbf{k}}^\dagger & c_{B,\mathbf{k}}^\dagger \end{pmatrix} \mathcal{H}_D(\mathbf{k}) \begin{pmatrix} c_{A,\mathbf{k}} \\ c_{B,\mathbf{k}} \end{pmatrix}, \quad (1.30)$$

where t_1 is the hopping strength between the nearest neighbors denoted by $\langle i, j \rangle$, $c_{A,\mathbf{k}}^\dagger$ ($c_{A,\mathbf{k}}$) the creation and annihilation operator for spinless electrons at the sublattice A as shown by solid and open dots in Fig. 1.1 (a). The first quantized Hamiltonian in momentum space reads,

$$\mathcal{H}_D(\mathbf{k}) = t_1 \sum_{i=1}^3 [\cos(\mathbf{k} \cdot \mathbf{a}_i) \sigma_1 + \sin(\mathbf{k} \cdot \mathbf{a}_i) \sigma_2], \quad (1.31)$$

where \mathbf{a}_i are the vectors between the nearest neighbors with the expression $\mathbf{a}_1 = (\frac{\sqrt{3}}{2}a, -\frac{1}{2}a)$, $\mathbf{a}_2 = (0, a)$, and $\mathbf{a}_3 = (-\frac{\sqrt{3}}{2}a, -\frac{1}{2}a)$, as shown by the blue arrows in Fig. 1.1 (a). For simplicity we set the lattice constant $a = 1$. The energy eigenvalues are $E_D = \pm t_1 \left(1 + 4 \cos \frac{3}{2} k_y \cos \frac{\sqrt{3}}{2} k_x + 4 \cos^2 \frac{\sqrt{3}}{2} k_x \right)^{1/2}$. The band crossing points are located at $\mathbf{K}_\pm = \left(\pm \frac{2\pi}{3\sqrt{3}}, \frac{2\pi}{3} \right)$, around which the energy disperses linearly in all directions, forming Dirac cones.

Haldane model In Haldane's original paper, he proposed a toy model based on the tight-binding model in Eq. (1.30). Besides the nearest neighbor hoppings, he considered the next-nearest neighbor hoppings, namely electrons hopping from sublattice A to A and B to B, as indicated by the red vectors in Fig. 1.1 (a). Instead of a real hopping constant, the next-nearest neighbor hopping carries an extra phase of $e^{-iv_{ij}\phi}$ with $v_{ij} = +1$ for hopping terms $c_{A,\mathbf{R}}^\dagger c_{A,\mathbf{R}+\mathbf{b}_i}$ and $v_{ij} = -1$ for $c_{B,\mathbf{R}}^\dagger c_{B,\mathbf{R}+\mathbf{b}_i}$. With $\varepsilon_i = +1$ for the A site and -1 for the B site, the Haldane model reads [5]

$$H_H = t_1 \sum_{\langle i,j \rangle} c_i^\dagger c_j + t_2 \sum_{\langle\langle i,j \rangle\rangle} e^{-iv_{ij}\phi} c_i^\dagger c_j + M \sum_i \varepsilon_i c_i^\dagger c_i = \sum_{\mathbf{k}} \begin{pmatrix} c_{A,\mathbf{k}}^\dagger & c_{B,\mathbf{k}}^\dagger \end{pmatrix} \mathcal{H}_H(\mathbf{k}) \begin{pmatrix} c_{A,\mathbf{k}} \\ c_{B,\mathbf{k}} \end{pmatrix}, \quad (1.32)$$

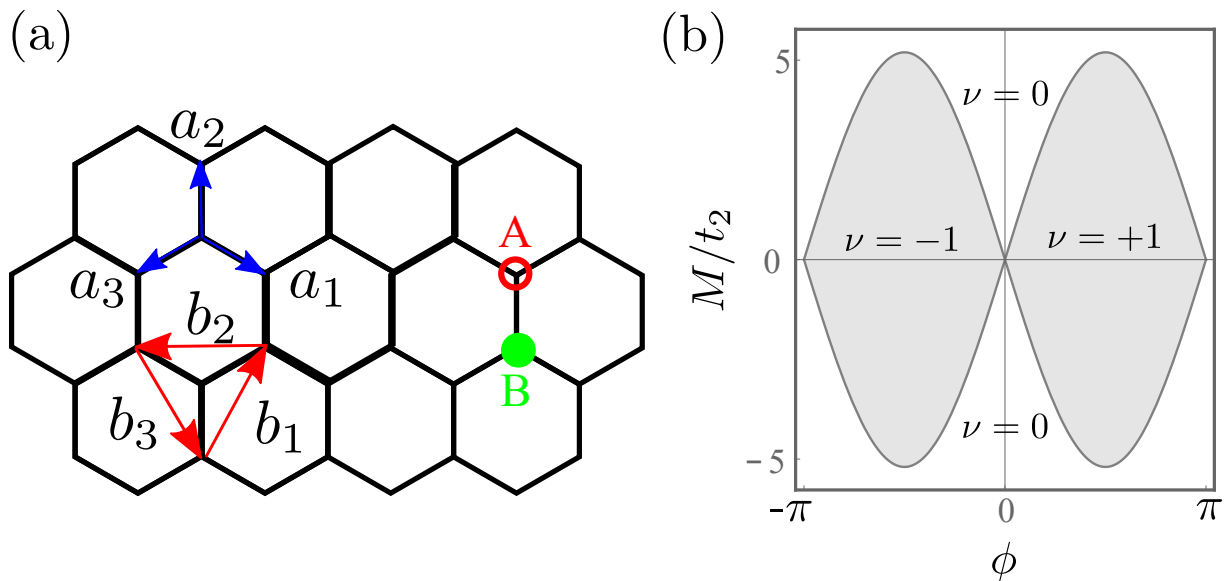


Figure 1.1: (a) Hexagonal structure of graphene. A and B denote different sites. Blue arrows denote the lattice vectors for the nearest neighbors and the red arrows denote those for next-nearest neighbors. (b) Phase diagram against parameters M/t_2 and ϕ of the Haldane model. The shaded region denotes the topological non-trivial phases.

where $\langle\langle i, j \rangle\rangle$ denotes the next-nearest neighbor hoppings. The first quantized Hamiltonian $\mathcal{H}_H(\mathbf{k})$ in momentum space reads

$$\mathcal{H}_H(\mathbf{k}) = 2t_2 \cos \phi \sum_i \cos(\mathbf{k} \cdot \mathbf{b}_i) \mathbb{1} + t_1 \sum_i [\cos(\mathbf{k} \cdot \mathbf{a}_i) \sigma_1 + \sin(\mathbf{k} \cdot \mathbf{a}_i) \sigma_2] + [M - 2t_2 \sin \phi \sum_i \sin(\mathbf{k} \cdot \mathbf{b}_i)] \sigma_3. \quad (1.33)$$

Here $\mathbf{b}_1 = (\sqrt{3}/2, 3/2)$, $\mathbf{b}_2 = (-\sqrt{3}, 0)$ and $\mathbf{b}_3 = (\sqrt{3}/2, -3/2)$ are the lattice vectors between the next-nearest neighbors as shown by the red arrows in Fig. 1.1 (a). We can denote $\varepsilon_{\mathbf{k}} = 2t_2 \cos \phi \sum_i \cos(\mathbf{k} \cdot \mathbf{b}_i)$, $d_1(\mathbf{k}) = t_1 \sum_i \cos(\mathbf{k} \cdot \mathbf{a}_i)$, $d_2(\mathbf{k}) = t_2 \sum_i \sin(\mathbf{k} \cdot \mathbf{a}_i)$, and $d_3(\mathbf{k}) = M - 2t_2 \sin \phi \sum_i \sin(\mathbf{k} \cdot \mathbf{b}_i)$. Thus the energy eigenvalues are obtained as $E_H(\mathbf{k}) = \varepsilon_{\mathbf{k}} \pm \sqrt{d_1(\mathbf{k})^2 + d_2(\mathbf{k})^2 + d_3(\mathbf{k})^2}$.

The Chern number can be calculated from the Berry curvature in Eq. (1.17). The corresponding phase diagram of the Haldane model is plotted in Fig. 1.1 (b). We find that the topological phase transition is related to the gap closing in the bulk. From the energy eigenvalues, the energy gap equals to $\Delta E = 2\sqrt{d_1(\mathbf{k})^2 + d_2(\mathbf{k})^2 + d_3(\mathbf{k})^2}$. The gap closing starts at the original Dirac points located at $\mathbf{K}_{\pm} = \left(\pm \frac{2\pi}{3\sqrt{3}}, \frac{2\pi}{3} \right)$. The boundary of the gap closing region can be obtained as

$$M \pm 3\sqrt{3}t_2 \sin \phi = 0, \quad (1.34)$$

which is identical to the boundaries in the phase diagram in Fig. 1.1 (b).

The major difference between the graphene model in Eq. (1.31) and the Haldane model in Eq. (1.33) lies in the extra $d_3(\mathbf{k})\sigma_3$ term, which comes from the next-nearest neighbor hoppings. We now analyze this difference through symmetry argument. Under the time-reversal operation $\mathcal{T} = \hat{\mathcal{K}}$ with $\hat{\mathcal{K}}$ the complex conjugation, the graphene model satisfies the symmetry constraint of

$$\mathcal{T}\mathcal{H}_D(\mathbf{k})\mathcal{T}^{-1} = \mathcal{H}_D(-\mathbf{k}), \quad (1.35)$$

which will be explained later in Eq. (1.87). Thus the Chern number should be zero according to Eq. (1.29). However, the inclusion of the next-nearest neighbor hoppings in the Haldane model brings the extra term $d_3(\mathbf{k})\sigma_3$, which breaks the time-reversal symmetry. This makes a non-zero Chern number possible in the Haldane model in Eq. (1.33).

Chern Insulator From above discussion of the Haldane model, we know that a two band model is sufficient to describe the topological phase transition characterized by the Chern number, and it is clear that the topological phase transition is closely related to the band closing in the bulk. A natural question is whether we can construct a more general model to describe topological materials characterized by the Chern number. The answer is yes, and we call this kind of materials "Chern insulators" [8]. Though, the theoretical prediction was made at an early stage, the experimental discovery of anomalous quantum Hall effect in topological materials with non-trivial Chern number was made in 2013 [24].

We start from a two-band model in two-dimensional space, which can be expressed in terms of Pauli matrices as,

$$H(\mathbf{k}) = \sum_{i=1}^3 d_i(\mathbf{k})\sigma_i = \begin{pmatrix} d_3(\mathbf{k}) & d_1(\mathbf{k}) - id_2(\mathbf{k}) \\ d_1(\mathbf{k}) + id_2(\mathbf{k}) & -d_3(\mathbf{k}) \end{pmatrix}, \quad (1.36)$$

with $\mathbf{k} = (k_x, k_y)$. The Berry curvature can be obtained from the eigenvectors,

$$|u_+(\mathbf{k})\rangle = \frac{1}{\sqrt{2d(\mathbf{k})(d(\mathbf{k}) - d_3(\mathbf{k}))}} \begin{pmatrix} d_1(\mathbf{k}) - id_2(\mathbf{k}) \\ d(\mathbf{k}) - d_3(\mathbf{k}) \end{pmatrix}, \quad (1.37)$$

$$|u_-(\mathbf{k})\rangle = \frac{1}{\sqrt{2d(\mathbf{k})(d(\mathbf{k}) + d_3(\mathbf{k}))}} \begin{pmatrix} -d_1(\mathbf{k}) + id_2(\mathbf{k}) \\ d(\mathbf{k}) + d_3(\mathbf{k}) \end{pmatrix}, \quad (1.38)$$

with the energy eigenvalues of $E_{\pm}(\mathbf{k}) = \pm d(\mathbf{k}) = \pm\sqrt{d_1(\mathbf{k})^2 + d_2(\mathbf{k})^2 + d_3(\mathbf{k})^2}$.

From the expression in Eq. (1.17), the Berry curvature for the occupied band can be obtained as

$$\Omega_-(\mathbf{k}) = i \frac{\langle u_-(\mathbf{k}) | \partial_{k_x} H | u_+(\mathbf{k}) \rangle \langle u_+(\mathbf{k}) | \partial_{k_y} H | u_-(\mathbf{k}) \rangle}{(E_-(\mathbf{k}) - E_+(\mathbf{k}))^2} - (k_x \leftrightarrow k_y). \quad (1.39)$$

After plugging the expression of the eigenvectors and eigenvalues, the expression for the Berry curvature can be obtained as

$$\Omega_-(\mathbf{k}) = \frac{1}{2d^3} \mathbf{d}(\mathbf{k}) \cdot \partial_{k_x} \mathbf{d}(\mathbf{k}) \times \partial_{k_y} \mathbf{d}(\mathbf{k}), \quad (1.40)$$

with the vector $\mathbf{d}(\mathbf{k}) = (d_1(\mathbf{k}), d_2(\mathbf{k}), d_3(\mathbf{k}))$. The Berry phase (Chern number) is obtained by integration over the two-dimensional Brillouin zone,

$$\gamma_- = \frac{1}{2} \iint_{\text{BZ}} dk_x dk_y \frac{1}{d^3} \mathbf{d}(\mathbf{k}) \cdot \partial_{k_x} \mathbf{d}(\mathbf{k}) \times \partial_{k_y} \mathbf{d}(\mathbf{k}). \quad (1.41)$$

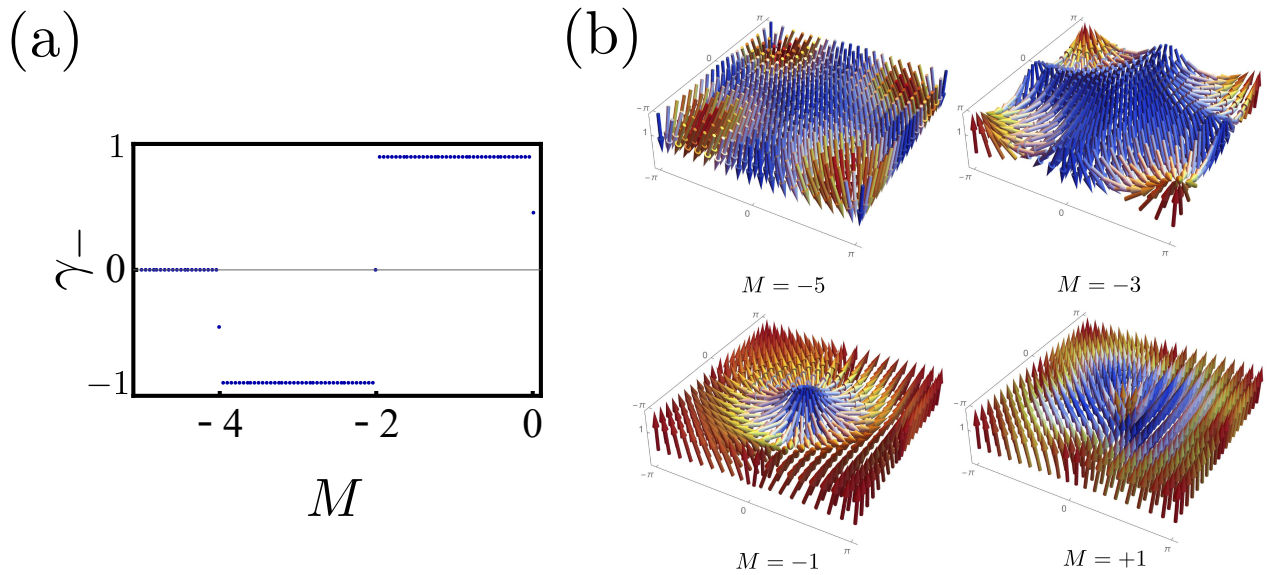


Figure 1.2: (a) The Chern number γ_- against parameter M for the Chern insulator Hamiltonian described in Eq. (1.42). (b) The corresponding vector field of $\mathbf{d}(\mathbf{k}) = (\sin k_x, \sin k_y, 2 + M - \cos k_x - \cos k_y)$ on the two-dimensional Brillouin zone.

Notice that the integrand is just the Jacobian of the mapping from the Brillouin zone to a unit sphere. As a result, the integration equals to the area on the sphere that $\mathbf{d}(\mathbf{k})$ covers, which equals to the half of the multiple of the solid angle of the sphere, $2\pi n$ with n the integer.

The simplest lattice model Hamiltonian for the Chern insulator can be constructed as

$$\mathcal{H}_{\text{Chern}}(\mathbf{k}) = \sin k_x \sigma_x + \sin k_y \sigma_y + \left(2 + M - \cos k_x - \cos k_y\right) \sigma_z. \quad (1.42)$$

By denoting $\mathbf{d}(\mathbf{k}) = (\sin k_x, \sin k_y, 2 + M - \cos k_x - \cos k_y)$, we can calculate the Chern number by the formula in Eq. (1.41). In Fig. 1.2(a), the Chern number (γ_-) is plotted against the parameter M . As we can see, the topological phase transition happens at $M = -4$, $M = -2$ and $M = 0$. If we investigate the energy spectrum of $E_{\text{Chern}}(\mathbf{k}) = \pm \sqrt{\sin^2 k_x + \sin^2 k_y + (2 + M - \cos k_x - \cos k_y)^2}$, we will find that the phase transition points of M correspond to the gap closing points as listed below, i.e.,

- at $M = 0$, gap closes at $(k_x, k_y) = (0, 0)$;
- at $M = -2$, gap closes at $(k_x, k_y) = (\pi, 0), (0, \pi)$;
- at $M = -4$, gap closes at $(k_x, k_y) = (\pi, \pi)$;

In Fig. 1.2(b), we plot out the vector field of $\mathbf{d}(\mathbf{k})$ in the first Brillouin zone for different topological phases. For $M = -3$ and $M = -1$ with non-zero Chern number, in contrast to $M = -5$ and $M = +1$, the vector $\mathbf{d}(\mathbf{k})$ winds non-trivially on the two-dimensional Brillouin zone.

1.2.2 Time-reversal symmetric topological insulators

One main feature of Haldane model is that time-reversal symmetry is broken, which results from introducing the symmetry breaking next-nearest neighbor hopping. However, the realization of such materials was experimentally challenging at that time. In 2005, Kane and Mele proposed an upgraded version of Haldane model [7], which is called the Kane-Mele model. Their idea is to restore the time-reversal symmetry by introducing the spin-orbit coupling. The corresponding model Hamiltonian reads

$$\begin{aligned} H_{\text{K-M}} &= t_1 \sum_{\langle i,j,\alpha \rangle} c_{i,\alpha}^\dagger c_{j,\alpha} + \lambda_{\text{SO}} \sum_{\langle\langle i,j \rangle\rangle, \alpha, \beta} e^{-iv_{ij}\phi} c_{i,\alpha}^\dagger s_{\alpha\beta}^z c_{j,\beta} + M \sum_{i,\alpha} \varepsilon_{i\alpha} c_{i,\alpha}^\dagger c_{i\alpha} \\ &= \sum_{\mathbf{k}} (c_{A,\uparrow,\mathbf{k}}^\dagger, c_{B,\uparrow,\mathbf{k}}^\dagger, c_{A,\downarrow,\mathbf{k}}^\dagger, c_{B,\downarrow,\mathbf{k}}^\dagger) \mathcal{H}_{\text{K-M}}(\mathbf{k}) (c_{A,\uparrow,\mathbf{k}}, c_{B,\uparrow,\mathbf{k}}, c_{A,\downarrow,\mathbf{k}}, c_{B,\downarrow,\mathbf{k}})^T, \end{aligned} \quad (1.43)$$

where α, β label spin degrees of freedom and λ_{SO} denotes the spin-orbit coupling constant. By taking $\phi = \pi/2$, the first quantized Hamiltonian in momentum space reads,

$$\mathcal{H}_{\text{K-M}}(\mathbf{k}) = t_1 \sum_i [\cos(\mathbf{k} \cdot \mathbf{a}_i) \sigma_1 \otimes \tau_0 + \sin(\mathbf{k} \cdot \mathbf{a}_i) \sigma_2 \otimes \tau_0] + [M \sigma_3 \otimes \tau_0 - 2t_2 \sum_i \sin(\mathbf{k} \cdot \mathbf{b}_i) \sigma_3 \otimes \tau_3], \quad (1.44)$$

with σ and τ for the sublattice and spin degree of freedom, respectively. The time-reversal operator for the spinful electrons now becomes,

$$\mathcal{T} = \sigma_0 \otimes i\tau_2 \hat{\mathcal{K}}, \quad (1.45)$$

with $\hat{\mathcal{K}}$ the complex conjugation operator. It can be verified that the system is invariant under the time-reversal operator,

$$\mathcal{T} \mathcal{H}_{\text{K-M}}(\mathbf{k}) \mathcal{T}^{-1} = \mathcal{H}_{\text{K-M}}(-\mathbf{k}). \quad (1.46)$$

It should be noted for the Hamiltonian in Eq. (1.44), the eigenvalues of spin operator τ_z are still good quantum numbers. Thus, the Chern number can be computed in the projections of $|\uparrow\rangle$ and $|\downarrow\rangle$. Therefore, though with time-reversal symmetry, the total Chern number is zero, we can still define a spin Chern number to characterize the topological phases,

$$\nu = \frac{C_\uparrow - C_\downarrow}{2} \pmod{2} \in \mathbb{Z}_2. \quad (1.47)$$

However, it is possible to have other types of spin-orbit couplings, for example, the Rashba type in the form of $\frac{\lambda}{\hbar}(\tau_x s_y - \tau_y s_x)$, in which the τ_z is no longer good quantum number. Thus, a new kind of topological invariant should be considered for time-reversal symmetric topological materials.

Bernevig-Hughes-Zhang (BHZ) model The BHZ model represents another type of time-reversal symmetric topological material, based on which the quantum spin Hall effect was experimentally observed [6, 9]. The time-reversal symmetric operator is anti-unitary, which means $\mathcal{T} e^{i\mathbf{k}\cdot\mathbf{r}} = e^{-i\mathbf{k}\cdot\mathbf{r}} \mathcal{T}$. Recall that a general Hamiltonian in the Brillouin zone can be represented as $H(\mathbf{k}) = e^{-i\mathbf{k}\cdot\mathbf{r}} H e^{i\mathbf{k}\cdot\mathbf{r}}$, as shown in Eq. (1.8). Thus, under time reversal symmetry operator, we have the relation $\mathcal{T} H(\mathbf{k}) \mathcal{T}^{-1} = H(-\mathbf{k})$. For a spin-1/2 electron, time-reversal operator should flip the direction of spin, thus the time-reversal symmetry operator is usually $\mathcal{T} = i\tau_2 \hat{\mathcal{K}}$, with $\hat{\mathcal{K}}$ the complex conjugation operator.

We can construct a time-reversal symmetric Hamiltonian from a spinless Hamiltonian as $h(\mathbf{k})$

$$H(\mathbf{k}) = \begin{pmatrix} h(\mathbf{k}) & \\ & h^*(-\mathbf{k}) \end{pmatrix}, \quad (1.48)$$

which is invariant under the time-reversal symmetry operator $\mathcal{T} = i\tau_2\hat{\mathcal{K}}$,

$$(i\tau_2\hat{\mathcal{K}})H(\mathbf{k})(i\tau_2\hat{\mathcal{K}})^{-1} = H(-\mathbf{k}). \quad (1.49)$$

Under a closer investigation, the Kane-Mele model in Eq. (1.44) is also in the form of Eq. (1.48). Thus it is natural to consider a generalization of Chern insulator to making it time-reversal symmetric. Therefore, we take $h(\mathbf{k})$ to be the Chern insulator with the Hamiltonian of $h(\mathbf{k}) = \sum_{i=1}^3 d_i(\mathbf{k})\sigma_i$ as that in Eq. (1.42), where

$$d_1 = A \sin k_x, \quad d_2 = A \sin k_y, \quad d_3 = M - B(\cos k_x + \cos k_y). \quad (1.50)$$

Now we arrive at the time-reversal symmetric version of the Chern insulator model, which we call BHZ model that was first discovered by Bernevig, Hughes and Zhang in 2006 [6]. The Hamiltonian can be represented by four-dimensional gamma matrices

$$H_{\text{BHZ}}(\mathbf{k}) = \sum_i d_i \gamma_i, \quad (1.51)$$

with $d_1 = A \sin k_x, d_2 = A \sin k_y, d_3 = M - B(\cos k_x + \cos k_y)$, and $\gamma_1 = \sigma_1 \otimes \tau_3, \gamma_2 = \sigma_2 \otimes \tau_0$ and $\gamma_3 = \sigma_3 \otimes \tau_0$. The corresponding two-dimensional topological insulator material was experimentally observed in the HgTe/CdTe quantum well, where the topological phase transition is induced by the band gap closing by tuning the thickness of the quantum wells [9]. In the following section, we discuss the topological invariants that characterize the time-reversal symmetric topological insulators.

\mathbb{Z}_2 topological invariant We now consider the topological invariants for time-reversal symmetric topological materials. If a system preserves time-reversal symmetry, then we have $[\mathcal{T}, H] = 0$. Suppose that $|n\rangle$ and $\mathcal{T}|n\rangle$ denote the same state, then $|n\rangle = \mathcal{T}|n\rangle = \mathcal{T}^2|n\rangle$. However, this is not true for the case $\mathcal{T}^2 = -1$. Note that if $H|n\rangle = E|n\rangle$, then $H\mathcal{T}|n\rangle = \mathcal{T}H|n\rangle = E_n\mathcal{T}|n\rangle$ which means $|n\rangle$ and $\mathcal{T}|n\rangle$ form degenerate pairs for $\mathcal{T}^2 = -1$. In momentum space, with the symmetry constraints $\mathcal{T}H(\mathbf{k})\mathcal{T}^{-1} = H(-\mathbf{k})$, the pair of the states at $+\mathbf{k}$ and $-\mathbf{k}$ are linked by time-reversal symmetry and have the same energy, thus they are called "Kramers pairs". Notably, Kramers pairs are degenerate at the point in the Brillouin zone where $+\mathbf{k}$ and $-\mathbf{k}$ are equivalent. The corresponding points are called time-reversal invariant momenta (TRIMs).

In a two-dimensional system with time-reversal symmetry, we focus on the two bands that form a Kramers pair. We can treat the system as one-dimensional by regarding k_x as momentum k and k_y as an index for the time evolution t . This one-dimensional system is periodic in time t , $H(t+T) = H(t)$. We can denote the Bloch wavefunction for the Kramers pair as $|u_1(k)\rangle$ and $|u_2(k)\rangle$. At $t = 0$ and $t = T/2$, we have the relation $\mathcal{T}|u_2(k)\rangle = e^{-i\chi(k)}|u_1(-k)\rangle$ and $\mathcal{T}|u_1(k)\rangle = -e^{-i\chi(-k)}|u_2(-k)\rangle$. We can construct the matrix $\omega_{\alpha\beta}(k) = \langle u_\alpha(-k)|\mathcal{T}|u_\beta(k)\rangle$, which is expressed as [25],

$$\omega(k) = \begin{pmatrix} & e^{-i\chi(k)} \\ -e^{-i\chi(-k)} & \end{pmatrix}. \quad (1.52)$$

According to the modern theory of ferroelectricity, the integral of the Berry connection over the occupied states through the BZ yields the charge polarization,

$$P_\rho = P^I + P^{II}, \quad (1.53)$$

with the partial polarization coming from each band as $P^I = \int_{-\pi}^{\pi} \frac{dk}{2\pi} a_{11}(k)$ and $P^{II} = \int_{-\pi}^{\pi} \frac{dk}{2\pi} a_{22}(k)$, with the Berry connection $a_{ii} = i\langle u_i(k) | \partial_k | u_i(k) \rangle$. A time-reversal polarization can be defined as [25]

$$P_\theta = P^I - P^{II} = 2P^I - P_\rho, \quad (1.54)$$

as the difference between two spin components. We focus on the partial polarization of P^I ,

$$P^I = \int_0^\pi \frac{dk}{2\pi} (a_{11}(k) + a_{11}(-k)). \quad (1.55)$$

From Eq. (1.52), it can be shown that $a_{11}(-k) = a_{22}(k) - \partial_k \chi(k)$, and then P^I becomes

$$P^I = \int_0^\pi \frac{dk}{2\pi} (a_{11}(k) + a_{22}(k) - \partial_k \chi(k)) = \int_0^\pi \frac{dk}{2\pi} A(k) - \frac{1}{2\pi} (\chi(\pi) - \chi(0)), \quad (1.56)$$

with $A(k) = a_{11}(k) + a_{22}(k) = \text{tr} a(k)$. Thus the time-reversal polarization is

$$P_\theta = 2P^I - P_\rho = \int_0^\pi \frac{dk}{2\pi} (A(k) - A(-k)) - \frac{1}{\pi} (\chi(\pi) - \chi(0)). \quad (1.57)$$

To calculate P_θ , we need to first deal with the term $A(k)$, which is the trace of the Berry connection $a(k)$, with the matrix component $a_{\alpha\beta}(k) = i\langle u_\alpha(k) | \partial_k | u_\beta(k) \rangle$. Since $|u_\alpha(-k)\rangle = \sum_\beta \omega_{\alpha\beta}(k)^* \mathcal{T} |u_\beta(k)\rangle$, it can be obtained that $\text{tr} a(-k) = \text{tr} a(k) - i \text{tr} [\omega^\dagger(k) \partial_k \omega(k)]$. Thus, the time-reversal polarization becomes

$$P_\theta = \int_0^\pi \frac{dk}{2\pi} i \text{tr} [\omega^\dagger(k) \partial_k \omega(k)] - \frac{1}{\pi} (\chi(\pi) - \chi(0)). \quad (1.58)$$

This expression can be simplified further by noticing that the first term is the winding of the $U(1)$ phase of ω and $\chi(k) = i \log \omega_{12}(k)$. Thus, we arrive at the expression [12, 25],

$$P_\theta = i \int_0^\pi \frac{dk}{2\pi} \partial_k \log \det \omega(k) - \frac{i}{\pi} \log \frac{\omega_{12}(\pi)}{\omega_{12}(0)} = \frac{1}{i\pi} \log \left(\frac{\sqrt{\omega_{12}(0)^2} \omega_{12}(\pi)}{\omega_{12}(0) \sqrt{\omega_{12}(\pi)^2}} \right). \quad (1.59)$$

It is emphasized that the quasi one-dimensional system can only be in two distinct polarization states characterized by $P_\theta = 0$ or 1 module 2, as the argument of the log function in the above expression can only be +1 or -1. The topological property of the entire system can be characterized by considering the change from $t = 0$ to $T/2$, $\Delta = P_\theta(T/2) - P_\theta(0)$, where

$$(-1)^\Delta = \prod_{i=1}^4 \frac{\omega_{12}(\Lambda_i)}{\sqrt{\omega_{12}(\Lambda_i)^2}} = \prod_{i=1}^4 \frac{\text{Pf} \omega(\Lambda_i)}{\sqrt{\det \omega(\Lambda_i)}}, \quad (1.60)$$

with $\Lambda_1 = (k, t) = (0, 0)$, $\Lambda_2 = (\pi, 0)$, $\Lambda_3 = (0, T/2)$, and $\Lambda_4 = (\pi, T/2)$. If P_θ changes between $t = 0$ and $t = T/2$, then $\Delta = 1$ and the system is topological, and if there is no change in P_θ , then $\Delta = 0$ and the system is topologically trivial. As Δ is specified in taking integer values mod 2, it gives a \mathbb{Z}_2

topological invariant characterizing the system.

The topological invariant defined in Eq. (1.60) for two-dimensional systems can be easily generalized to three-dimensional materials. Notice that the topological invariants are obtained by calculating $\text{Pf } \omega(\Lambda_i) / \sqrt{\det \omega(\Lambda_i)}$ at each TRIM in the Brillouin zone. For a three dimensional material, for simplicity, we take a cubic system with lattice constant $a = 1$. A similar topological invariant can be calculated by the eight TRIMs denoted as $\Lambda_{0,0,0}$, $\Lambda_{0,0,\pi}$, $\Lambda_{0,\pi,0}$, $\Lambda_{\pi,0,0}$, $\Lambda_{\pi,0,\pi}$, $\Lambda_{\pi,\pi,0}$, $\Lambda_{\pi,\pi,0}$, and $\Lambda_{\pi,\pi,\pi}$ in the three-dimensional Brillouin zone.

1.2.3 Wilson loop

In this subsection, we introduce a general and computationally efficient method to characterize the topological materials. In condensed matter physics, there are usually multiple occupied bands, thus the Berry connection defined in Eq. (1.11) needs to be generalized to the multi band case. The adiabatic transport of a ground state at the initial momentum $k^{(i)}$ to a final momentum k can be viewed as a unitary rotation in the subspace for occupied bands. The Wilson-line matrix $\mathcal{W}_{k \leftarrow k^{(i)}}$ maps the subspace of the occupied bands at $k^{(i)}$ to the subspace of occupied bands at k , which satisfies the parallel transport equation [26, 27],

$$\partial_{k_\mu} \mathcal{W}_{k \leftarrow k^{(i)}} = -A_\mu(k) \mathcal{W}_{k \leftarrow k^{(i)}}, \quad (1.61)$$

with the generalized Berry connection $A_\mu(k)$ defined as $A_\mu^{mn}(k) = \langle u^m(k) | \partial_{k_\mu} | u^n(k) \rangle$ for the occupied bands. From the above parallel transport equation, it can be solved that

$$\mathcal{W}_{k \leftarrow k^{(i)}}(\mathcal{L}) = \overline{\exp} \left[- \int_{\mathcal{L}} A_\mu(k) dk_\mu \right], \quad (1.62)$$

with the overline — as the path ordering and \mathcal{L} as the path that connects the momenta $k^{(i)}$ and k .

Tight-binding Hamiltonian In the tight-binding approximation, the Hilbert space can be spanned by a finite number of atomic orbitals at each unit cell. In general, the eigenstate for the α -th atomic orbital at site \mathbf{R}_l can be labeled as $\phi_\alpha(\mathbf{r} - \mathbf{R}_l)$. We assume that at different sites, the orbital eigenstates are approximately orthogonal, $\int d\mathbf{r} \phi_\alpha(\mathbf{r} - \mathbf{R}_l)^* \phi_\alpha(\mathbf{r} - \mathbf{R}_{l'}) = \delta_{ll'}$. We can then construct the Bloch wavefunction as the linear combination of atomic orbitals (LCAO),

$$\psi_\alpha(\mathbf{r}) = \sum_{\mathbf{R}_l} b_\alpha(\mathbf{R}_l) \phi_\alpha(\mathbf{r} - \mathbf{R}_l). \quad (1.63)$$

From the Bloch theorem, $\psi_\alpha(\mathbf{r} + \mathbf{R}_n) = e^{i\mathbf{k} \cdot \mathbf{R}_n} \psi_\alpha(\mathbf{r})$, the relation $\sum_{\mathbf{R}_l} b_\alpha(\mathbf{R}_l) \phi_\alpha(\mathbf{r} - (\mathbf{R}_l - \mathbf{R}_n)) = \sum_{\mathbf{R}_l} e^{i\mathbf{k} \cdot \mathbf{R}_n} b_\alpha(\mathbf{R}_l) \phi_\alpha(\mathbf{r} - \mathbf{R}_l)$ yields $b_\alpha(\mathbf{R}_l + \mathbf{R}_n) = e^{i\mathbf{k} \cdot \mathbf{R}_n} b_\alpha(\mathbf{R}_l)$. Using this relation in Eq. (1.63), we have $\psi_\alpha(\mathbf{r}) = b_\alpha(0) \sum_{\mathbf{R}_l} e^{i\mathbf{k} \cdot \mathbf{R}_l} \phi_\alpha(\mathbf{r} - \mathbf{R}_l)$. By the normalization condition of $\psi_\alpha(\mathbf{r})$, it can be obtained that $\int d\mathbf{r} \psi_\alpha(\mathbf{r})^* \psi_\alpha(\mathbf{r}) = N b_\alpha(0)^* b_\alpha(0) = 1$, which indicates $|b_\alpha(0)| = \frac{1}{\sqrt{N}}$. Thus the Bloch function in Eq. (1.63) is obtained as

$$\psi_{\alpha,\mathbf{k}}(\mathbf{r}) = \frac{1}{\sqrt{N}} \sum_{\mathbf{R}_l} e^{i\mathbf{k} \cdot \mathbf{R}_l} \phi_\alpha(\mathbf{r} - \mathbf{R}_l). \quad (1.64)$$

In the second quantization language, a state in the tight-binding approximation can be expressed as $\Psi(\mathbf{r}) = \sum_{\alpha l} \phi_{\alpha}(\mathbf{r} - \mathbf{R}_l) \hat{C}_{\alpha l}$. In this representation, the Hamiltonian is

$$\int d\mathbf{r} \Psi(\mathbf{r})^{\dagger} \hat{H}(\mathbf{r}) \Psi(\mathbf{r}) = \sum_{\alpha, \beta} \sum_{\mathbf{R}_l, \mathbf{R}'_l} \hat{C}_{\alpha l}^{\dagger} \hat{C}_{\beta l'} \int d\mathbf{r} \phi_{\alpha}(\mathbf{r} - \mathbf{R}_l)^* \hat{H}(\mathbf{r}) \phi_{\beta}(\mathbf{r} - \mathbf{R}'_l). \quad (1.65)$$

For the part $\int d\mathbf{r} \phi_{\alpha}(\mathbf{r} - \mathbf{R}_l)^* \hat{H}(\mathbf{r}) \phi_{\beta}(\mathbf{r} - \mathbf{R}'_l)$, since $\hat{H}(\mathbf{r})$ is periodic in \mathbf{R}_l , this integral only depends on $\mathbf{R}_l - \mathbf{R}'_l$, we denote it as $\mathcal{H}_{\alpha\beta}(\mathbf{R}_l - \mathbf{R}'_l)$. The Hamiltonian becomes, $H = \int d\mathbf{r} \Psi(\mathbf{r})^{\dagger} \hat{H}(\mathbf{r}) \Psi(\mathbf{r}) = \sum_{\alpha, \beta} \sum_{\mathbf{R}_l, \mathbf{R}'_l} \hat{C}_{\alpha l}^{\dagger} \mathcal{H}_{\alpha\beta}(\mathbf{R}_l - \mathbf{R}'_l) \hat{C}_{\beta l'}$, which is regarded as the tight-binding Hamiltonian in real space. With the standard Fourier transform of $\hat{C}_{\alpha l} = \frac{1}{\sqrt{N}} \sum_{\mathbf{k} \in \text{BZ}} e^{i\mathbf{k} \cdot \mathbf{R}_l} \hat{C}_{\alpha \mathbf{k}}$ and $\hat{C}_{\alpha l}^{\dagger} = \frac{1}{\sqrt{N}} \sum_{\mathbf{k} \in \text{BZ}} e^{-i\mathbf{k} \cdot \mathbf{R}_l} \hat{C}_{\alpha \mathbf{k}}^{\dagger}$, the Hamiltonian can be expressed as

$$\begin{aligned} H &= \frac{1}{N} \sum_{\alpha, \beta} \sum_{\mathbf{R}_l, \mathbf{R}'_l} \sum_{\mathbf{k}, \mathbf{k}'} e^{-i\mathbf{k} \cdot \mathbf{R}_l} e^{i\mathbf{k}' \cdot \mathbf{R}'_l} \hat{C}_{\alpha \mathbf{k}}^{\dagger} \mathcal{H}_{\alpha\beta}(\mathbf{R}_l - \mathbf{R}'_l) \hat{C}_{\beta \mathbf{k}'} \\ &= \sum_{\mathbf{k}} \sum_{\alpha, \beta} \hat{C}_{\alpha \mathbf{k}}^{\dagger} \mathcal{H}_{\alpha\beta}(\mathbf{k}) \hat{C}_{\beta \mathbf{k}}, \end{aligned} \quad (1.66)$$

where $\mathcal{H}_{\alpha\beta}(\mathbf{k}) = \sum_{\mathbf{R}_l - \mathbf{R}'_l} e^{-i\mathbf{k}'(\mathbf{R}_l - \mathbf{R}'_l)} \mathcal{H}_{\alpha\beta}(\mathbf{R}_l - \mathbf{R}'_l)$ is periodic in reciprocal space $\mathcal{H}_{\alpha\beta}(\mathbf{k} + \mathbf{k}_h) = \mathcal{H}_{\alpha\beta}(\mathbf{k})$, with \mathbf{k}_h the lattice vectors in reciprocal space.

Tight-binding Wilson loop In the tight-binding model expressed in Eq. (1.66), we can first obtain the eigenstates that satisfy $\sum_{\beta} \mathcal{H}_{\alpha\beta}(\mathbf{k}) u_{n, \beta}(\mathbf{k}) = \varepsilon_n(\mathbf{k}) u_{n, \alpha}(\mathbf{k})$, with $n = 1, 2, \dots, N$ denoting the energy bands, and α, β the labels for atomic orbitals. The Wilson loop can be obtained from the definition in Eq. (1.62) as

$$\mathcal{W}(\mathcal{L}) = \overline{\exp} \left[- \int_{\mathcal{L}} d\mathbf{k} \cdot \mathbf{A}(\mathbf{k}) \right], \quad (1.67)$$

with the Berry connection of $\mathbf{A}_{mn} = \langle u_m(\mathbf{k}) | \nabla_{\mathbf{k}} | u_n(\mathbf{k}) \rangle$ for the occupied bands and \mathcal{L} a loop in the Brillouin zone.

For numerical evaluations, the expression for $\mathcal{W}(\mathcal{L})$ is obtained by discretizing the loop \mathcal{L} as $\{\mathbf{k}^{(0)} + \mathbf{G}, \mathbf{k}^{(N)}, \mathbf{k}^{(N-1)}, \dots, \mathbf{k}^{(2)}, \mathbf{k}^{(1)}, \mathbf{k}^{(0)}\}$ with $N \gg 1$ and the interval is $\Delta \mathbf{k} = \mathbf{k}^{(i+1)} - \mathbf{k}^{(i)}$. From the relation of

$$\begin{aligned} F_{i+1, i}^{mn} &= \langle u_m(\mathbf{k}^{(i+1)}) | u_n(\mathbf{k}^{(i)}) \rangle = \delta_{mn} - \langle u_m(\mathbf{k}^{(i+1)}) | (|u_n(\mathbf{k}^{(i+1)})\rangle - |u_n(\mathbf{k}^{(i)})\rangle) \rangle = \delta_{mn} - \mathbf{A}_{i+1, i}^{mn} \Delta \mathbf{k} \\ &\approx e^{-\mathbf{A}_{i+1, i}^{mn} \Delta \mathbf{k}}, \end{aligned} \quad (1.68)$$

the following relation can be established,

$$\mathcal{W}(\mathcal{L}) = \overline{\exp} \left[- \int_{\mathcal{L}} d\mathbf{k} \cdot \mathbf{A}(\mathbf{k}) \right] = \prod_{i=0}^N e^{-\mathbf{A}_{i+1, i} \Delta \mathbf{k}} = \prod_{i=0}^N F_{i+1, i}, \quad (1.69)$$

with $F_{i+1, i}^{mn} = \langle u_m(\mathbf{k}^{(i+1)}) | u_n(\mathbf{k}^{(i)}) \rangle$ for the occupied bands. Compared with the expression in Eq. (1.67), the expression in Eq. (1.69) can be evaluated numerically in a more efficient manner.

We consider the path \mathcal{L} is chosen parallel to the x direction and winds around the Brillouin zone once.

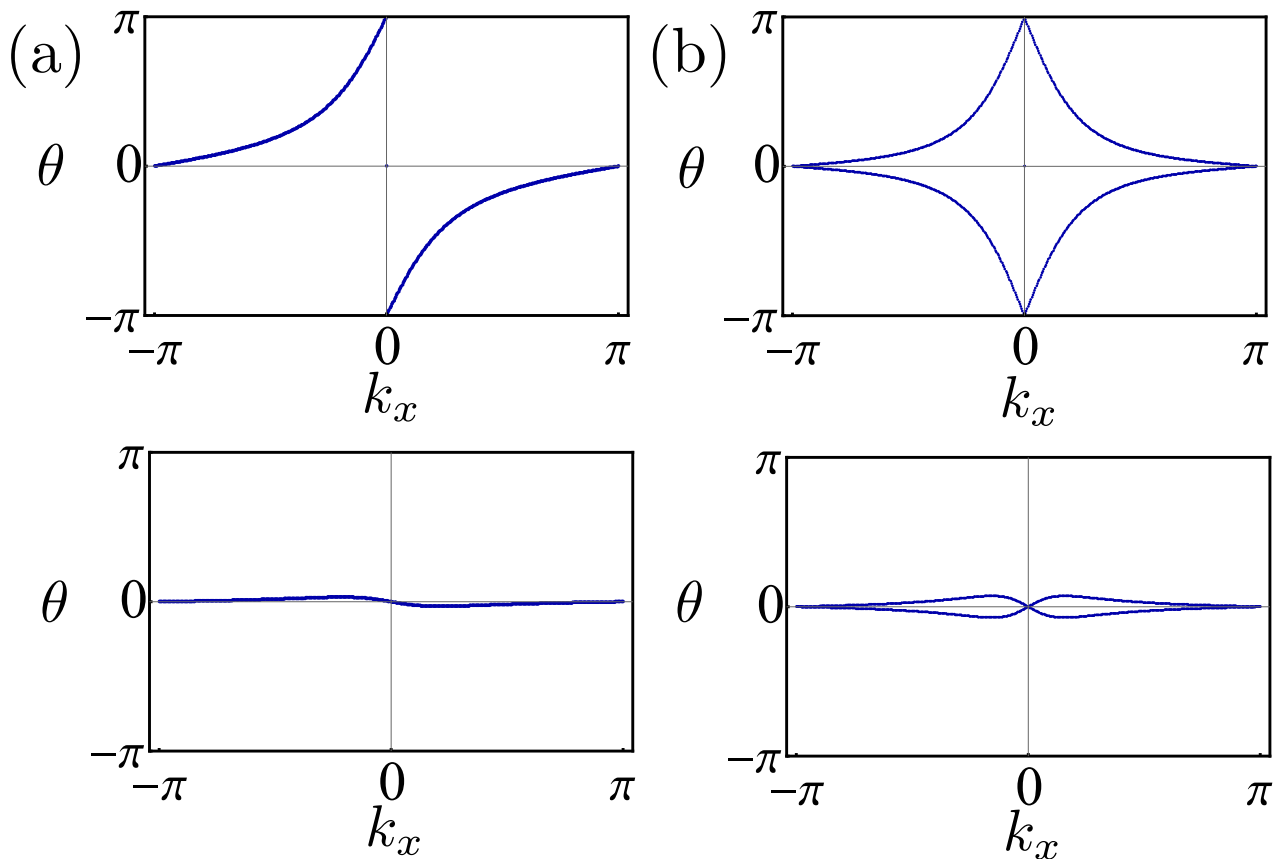


Figure 1.3: (a) The Wilson loop spectrum against k_x for $M = -1$ (upper panel) and $M = +1$ (lower panel) for the Chern insulator described in Eq. (1.42). (b) The Wilson loop spectrum against k_x for $M = 1.5$ (upper panel) and $M = +2.5$ (lower panel) for the BHZ model described in Eq. (1.51).

The momenta in the remaining $(d-1)$ directions are denoted as $\tilde{\mathbf{k}}$, and thus the Wilson loop labeled by these momenta can be denoted as $\mathcal{W}(\tilde{\mathbf{k}})$. We represent the eigenvalues of $\mathcal{W}(\tilde{\mathbf{k}})$ as $\exp(i\theta_\alpha(\mathbf{k}))$, with $\alpha = 1, \dots, n_{\text{occ}}$. The band structure of the set of the phases $\theta_\alpha(\mathbf{k})$ in the $(d-1)$ -dimensional Brillouin zone forms the Wilson loop spectrum, which will be used to characterize the topological phases.

It is natural to ask what is the physical meaning of the phases $\theta_\alpha(\mathbf{k})$. To answer this question, we first construct the projection operator as [26]

$$\mathcal{P}^{\text{occ}}(\tilde{\mathbf{k}}) = \sum_{i=1}^{n_{\text{occ}}} \int_{-\pi}^{\pi} \frac{dk_x}{2\pi} |u_i(\mathbf{k})\rangle \langle u_i(\mathbf{k})|, \quad (1.70)$$

where n_{occ} denotes the highest occupied band. With \hat{x} the position operator in the x direction, the

eigenvalue denoted by $\frac{\bar{\theta}(\tilde{\mathbf{k}})}{2\pi}$ of the projected position operator can be obtained by

$$\left(\mathcal{P}^{\text{occ}}(\tilde{\mathbf{k}}) \hat{x} \mathcal{P}^{\text{occ}}(\tilde{\mathbf{k}}) - \frac{\bar{\theta}(\tilde{\mathbf{k}})}{2\pi} \right) |\Psi(\tilde{\mathbf{k}})\rangle = 0, \quad (1.71)$$

where the eigenfunction $|\Psi(\tilde{\mathbf{k}})\rangle$ can be expanded in terms of the occupied Bloch function as $|\Psi(\tilde{\mathbf{k}})\rangle = \sum_{i=1}^{n_{\text{occ}}} \int \frac{dk_x}{2\pi} f_{n,\tilde{\mathbf{k}}}(k_x) |u_i(\mathbf{k})\rangle$. Acting with $\langle u_n(\mathbf{k})|$ on Eq. (1.71), we arrive at the following equation

$$i \partial_{k_x} f_{n,\tilde{\mathbf{k}}}(k_x) + i \sum_{m=1}^{n_{\text{occ}}} \langle u_n(\mathbf{k}) | \partial_{k_x} | u_m(\mathbf{k}) \rangle f_{m,\tilde{\mathbf{k}}}(k_x) = \frac{\bar{\theta}(\tilde{\mathbf{k}})}{2\pi} f_{n,\tilde{\mathbf{k}}}(k_x). \quad (1.72)$$

After the integration, the coefficient $f_{n,\tilde{\mathbf{k}}}(k_x)$ can be obtained as

$$f_{n,\tilde{\mathbf{k}}}(k_x) = e^{-i(k_x - k_x^0) \frac{\bar{\theta}(\tilde{\mathbf{k}})}{2\pi}} \sum_{m=1}^{n_{\text{occ}}} \overline{\text{exp}} \left(- \int_{k_x^0}^{k_x} dk_x A_x(\mathbf{k}) \right)_{nm} f_{n,\tilde{\mathbf{k}}}(k_x^0), \quad (1.73)$$

with $A_x(\mathbf{k})_{nm} = \langle u_n(\mathbf{k}) | \partial_{k_x} | u_m(\mathbf{k}) \rangle$. As the path winds the Brillouin zone in the x direction once, $k_x = k_x^0 + 2\pi$, from the periodic boundary condition on f , we arrive at the following equation,

$$\sum_{n=1}^{n_{\text{occ}}} \mathcal{W}_{k_x+2\pi \leftarrow k_x}^{mn}(\tilde{\mathbf{k}}) f_{n,\tilde{\mathbf{k}}}(k_x) = e^{i\bar{\theta}(\tilde{\mathbf{k}})} f_{m,\tilde{\mathbf{k}}}(k_x). \quad (1.74)$$

It is now clear that the eigenvalue $\theta_\alpha(\mathbf{k})$ of the Wilson loop operator $\mathcal{W}(\tilde{\mathbf{k}})$ corresponds to the eigenvalue of the projected position operator $\bar{\theta}(\tilde{\mathbf{k}})$, which is commonly denoted as the position of Wannier centers.

As the eigenvalues of the Wilson loop $e^{i\theta_\alpha(\mathbf{k})}$ along a non-contractible loop in the Brillouin zone define a map $S^1 \rightarrow U(1)$, the winding number of these eigenvalues can be used as the topological invariants to characterize the topological property of the system.

Examples Here we explain how the spectrum of the Wilson loops is used to characterize the topological phases, by two concrete examples of the Chern insulator defined in Eq. (1.42) and the BHZ model defined in Eq. (1.51).

For the Chern insulator, there is only one occupied band. As shown in Fig. 1.3 (a), the eigenvalue of the Wilson loop winds non-trivially against k_x for the non-trivial phase with $M = -1$, and in contrast, for the trivial phase with $M = +1$, the eigenvalue of the Wilson loop winds trivially. For the BHZ model, the Wilson loop spectrum is shown in Fig. 1.3 (b). The two eigenvalues corresponding to different spin components wind non-trivially for the topological non-trivial phase with $M = 1.5$, as shown in the upper panel.

1.3 Symmetry and topology

From our previous discussions, we can see that topological phases cannot be deformed continuously into trivial phases without closing the bulk energy gap, or without breaking the generic symmetry of

the systems. In this sense, the topological phases are symmetry protected and it is possible to classify them in terms of generic symmetries. In this section, we follow Ref. [10] and [13] to establish the classification of topological phases with respect to symmetry classes and spatial dimensions.

First it is necessary to distinguish the most generic symmetries. For symmetries that can be represented by unitary operators that commute with the Hamiltonian, the Hamiltonian can generally be block decomposed. It is therefore more fundamental to work with the most generic symmetries, that act on the symmetry irreducible Hamiltonians. It turns out that these are anti-unitary symmetries, which include time-reversal and particle-hole symmetries.

Consider a general non-interacting system of fermions described by the Hamiltonian H . The "second quantized" \hat{H} can be written as

$$\hat{H} = \sum_{I,J} \hat{\psi}_I^\dagger H_{IJ} \hat{\psi}_J, \quad (1.75)$$

where $\{\hat{\psi}_I, \hat{\psi}_I^\dagger\}$ with $I = 1, \dots, N$ a set of fermion annihilation and creation operators which satisfy the anticommutation relation $\{\hat{\psi}_I, \hat{\psi}_J\} = \delta_{I,J}$. Here I and J denote the combined labels of the lattice sites and internal quantum numbers such as spin and orbital quantum numbers.

Under the time-reversal symmetry, the fermion creation and annihilation operators transform as

$$\hat{\mathcal{T}} \hat{\psi}_I \hat{\mathcal{T}}^{-1} = \sum_J (U_T)_I^J \hat{\psi}_J, \quad \hat{\mathcal{T}} i \hat{\mathcal{T}}^{-1} = -i. \quad (1.76)$$

with $\hat{\mathcal{T}}$ an anti-unitary operator and U_T a unitary matrix. A system is time-reversal invariant if $\hat{\mathcal{T}}$ preserves the anticommutation relation and the Hamiltonian satisfies $\hat{\mathcal{T}} \hat{H} \hat{\mathcal{T}}^{-1} = \hat{H}$, which leads to the relation $U_T^\dagger H^* U_T = +H$. Applying the time-reversal symmetry operator twice, one can obtain $(U_T^* U_T)^\dagger H (U_T^* U_T) = H$. As the first quantized Hamiltonian runs over an irreducible representation space, it is found that $U_T^* U_T = e^{i\alpha} \mathbb{1}$ according to Schur's lemma [13]. Since U_T is unitary $U_T^\dagger U_T = \mathbb{1}$, we can infer that $U_T^* = e^{i\alpha} U_T^\dagger$ and $U_T^T = e^{i\alpha} U_T$. From the relation $1 = U_T^* U_T^T = e^{2i\alpha}$, it can be obtained that $e^{i\alpha} = \pm 1$. Thus, the time-reversal invariance leads to the relation

$$\hat{\mathcal{T}} : \quad U_T^\dagger H^* U_T = +H, \quad U_T^* U_T = \pm \mathbb{1}. \quad (1.77)$$

The particle-hole transformation mixes the fermion creation and annihilation operators as,

$$\hat{\mathcal{C}} \hat{\psi}_I \hat{\mathcal{C}}^{-1} = \sum_J (U_C)_I^J \hat{\psi}_J^\dagger, \quad (1.78)$$

with U_C a unitary matrix so that the fermionic anticommutation relation is preserved. The invariance under the particle-hole symmetry requires that $\hat{\mathcal{C}} \hat{H} \hat{\mathcal{C}}^{-1} = \hat{H}$, which leads to the relation $U_C^\dagger H^* U_C = -H$. Similar to the time-reversal symmetry, by applying particle-hole operator twice, we arrive at the relation $(U_C^* U_C)^\dagger H (U_C^* U_C) = H$. Together with the unitary property of U_C , the particle-hole invariance leads to the relation

$$\hat{\mathcal{C}} : \quad U_C^\dagger H^* U_C = -H, \quad U_C^* U_C = \pm \mathbb{1}. \quad (1.79)$$

Finally, the combination of time-reversal and particle-hole symmetry leads to a third symmetry called chiral symmetry. The operator for the chiral symmetry is denoted as $\hat{\mathcal{S}}$, which acts on the fermion

creation operator as

$$\hat{S}\hat{\psi}_I\hat{S}^{-1} = \sum_J (U_C U_T)_I^J \hat{\psi}_J. \quad (1.80)$$

If the system preserves the chiral symmetry, $\hat{S}\hat{H}\hat{S}^{-1} = \hat{H}$, then the following relation can be obtained,

$$\hat{S}: \quad U_S^\dagger H U_S = -H, \quad U_S^2 = +\mathbb{1}. \quad (1.81)$$

Here $U_S^2 = +\mathbb{1}$ is obtained with a similar procedure in the time-reversal and particle-hole symmetry by applying the symmetry operator twice.

The relation of Eq. (1.77), Eq. (1.79), and Eq. (1.81) can be summarized as

$$\begin{aligned} T^{-1}HT &= H, \quad T = U_T \mathcal{K}, \quad U_T U_T^* = \pm\mathbb{1}, \\ C^{-1}HC &= -H, \quad C = U_C \mathcal{K}, \quad U_C U_C^* = \pm\mathbb{1}, \\ S^{-1}HS &= -H, \quad S = U_S, \quad U_S^2 = +\mathbb{1}, \end{aligned} \quad (1.82)$$

with \mathcal{K} the complex conjugation operator. These symmetry constraints on the Hamiltonian define the ten Altland-Zirnbauer classes, as we will show [13].

Usually, we are interested in momentum space Hamiltonians. We start from a d -dimensional real-space Hamiltonian in the quadratic form $\hat{H} = \sum_{r,r'} \sum_{i,j} \hat{\psi}_i^\dagger(r) H_{ij}(r,r') \hat{\psi}_j(r')$, with i, j the internal quantum numbers and r the spatial position. After the Fourier transformation by

$$\hat{\psi}_i(r) = \sqrt{N}^{-1} \sum_{k \in \text{BZ}^d} e^{ik \cdot r} \hat{\psi}_i(k), \quad (1.83)$$

the Hamiltonian in momentum space reads,

$$\hat{H} = \sum_{k \in \text{BZ}^d} \sum_{i,j} \hat{\psi}_i^\dagger(k) H_{ij}(k) \hat{\psi}_j(k), \quad (1.84)$$

with $H_{ij}(k) = \sum_r e^{-ik \cdot r} H_{ij}(r)$ and $\hat{\psi}_i(k) = \sqrt{N}^{-1} \sum_r e^{-ik \cdot r} \hat{\psi}_i(r)$.

We now investigate the transformation of the momentum space Hamiltonian $H(k)$ under different symmetries. In Eq. (1.84), under time-reversal symmetry operator,

$$\begin{aligned} \hat{T}\hat{\psi}_i(k)\hat{T}^{-1} &= \sqrt{N}^{-1} \sum_r e^{ik \cdot r} \hat{T}\hat{\psi}_i(r)\hat{T}^{-1} = \sum_j (U_T)_i^j \hat{\psi}_j(-k), \\ \hat{T}H_{ij}(k)\hat{T}^{-1} &= H_{ij}(k)^* \end{aligned} \quad (1.85)$$

And in Eq. (1.84), under particle-hole symmetry operator,

$$\begin{aligned} \hat{C}\hat{\psi}_i(k)\hat{C}^{-1} &= \frac{1}{\sqrt{N}} \sum_r e^{-ik \cdot r} \hat{C}\hat{\psi}_i(r)\hat{C}^{-1} = \sum_j (U_C^*)_i^j \frac{1}{\sqrt{N}} \sum_r e^{-ik \cdot r} \hat{\psi}_j^\dagger(r) = \sum_j (U_C^*)_i^j \hat{\psi}_j^\dagger(-k), \\ \hat{C}H_{ij}(k)\hat{C}^{-1} &= H_{ij}(k). \end{aligned} \quad (1.86)$$

By replacing the k with $-k$ in the summation in Eq. (1.84), the time-reversal invariance leads to the relation $U_T^\dagger H(-k)^* U_T = +H(k)$, and the particle-hole invariance leads to the relation $U_C^\dagger H(-k)^* U_C =$

$-H(k)$. Or equivalently, they can be expressed as

$$\begin{aligned} T^{-1}H(k)T &= H(-k), & T &= U_T\mathcal{K}, \\ C^{-1}H(k)C &= -H(-k), & C &= U_C\mathcal{K}, \\ S^{-1}H(k)S &= -H(k), & S &= U_S. \end{aligned} \tag{1.87}$$

The combination of time-reversal and particle-hole symmetry leads to the relation for the chiral symmetry.

Now it is clear that there are only ten possible kinds of Hamiltonians for a system to respond to time-reversal (T), particle hole (C), and chiral (S) symmetry. For the time-reversal symmetry, we can denote different symmetry classes of Hamiltonians as $T = 0, -1, +1$, for (i) Hamiltonians that do not preserve time-reversal symmetry, (ii) Hamiltonians that preserve time-reversal symmetry and the symmetry operator squares to be -1 , and (iii) Hamiltonians that preserve time-reversal symmetry and the symmetry operator squares to be $+1$. Similarly for particle-hole symmetry, we can denote different symmetry classes of Hamiltonians as $C = 0, -1, +1$. Hence with respect to time-reversal and particle-hole symmetry, there are $3 \times 3 = 9$ possible kinds of Hamiltonians. For 8 out of the 9 cases, the chiral symmetry is fully determined. However, for the case when T and C are both absent $T = C = 0$, the chiral symmetry can still be preserved, i.e., $S = 0$ and $S = 1$ is possible. Thus there are $3 \times 3 - 1 + 2 = 10$ possible kinds of the Hamiltonians, which are called the Altland-Zirnbauer (AZ) classes. These classes are listed in Table 1.1 [10, 13].

1.3.1 Dirac Hamiltonian and classification scheme

There are several ways to do the classification of topological insulators and superconductors. It is noteworthy that almost all entries in the classification table 1.1 can be represented by Dirac Hamiltonians. In this section, we will use Dirac Hamiltonians together with Clifford algebras to achieve the classification of topological phases [28].

We start with the massive Dirac Hamiltonian, which can be used to describe almost all topologically gapped systems. In d -dimensional momentum space, the general form of the massive Dirac Hamiltonian in the continuum limit reads

$$\mathcal{H}(\mathbf{k}) = \sum_{i=1}^d k_i \gamma_i + m \gamma_{d+1}, \tag{1.88}$$

with gamma matrices satisfying the Clifford algebra $\{\gamma_i, \gamma_j\} = 2\delta_{i,j}$. Here the terms $k_i \gamma_i$ are called Dirac kinetic terms and the term $m \gamma_{d+1}$ is called the Dirac mass term. As we have discussed, the band closings in the bulk are closely related to topological phase transitions. For the massive Dirac Hamiltonian in Eq. (1.88), the band closing happens at $m = 0$, which means $m < 0$ and $m > 0$ may represent topologically distinct phases. In this sense, the classification of topological phases is equivalent to the classification of Dirac mass terms.

The basic strategy is to form a matrix representation of the Clifford algebra from the Dirac Hamiltonian in Eq. (1.88), together with the symmetry constraints in Eq. (1.87). As the classification of topological phases is equivalent to the classification of the mass terms, we first treat the mass term γ_{d+1} as the generator of a Clifford algebra, denoted as $e_0 = \gamma_{d+1}$. We then construct the matrix representation of the Clifford algebra without e_0 , denoted as $\{e_i\}$. Finally, we search for all possible extensions of this Clifford algebra after including the additional generator e_0 , which forms a "classifying space" V . Thus, topologically distinct phases are equivalent to different extensions of the Clifford

class	T	C	S	extension	V_d	$d=0$	1	2	3	4	5	6	7
A	0	0	0	$Cl_d \rightarrow Cl_{d+1}$	C_{0+d}	\mathbb{Z}	0	\mathbb{Z}	0	\mathbb{Z}	0	\mathbb{Z}	0
AIII	0	0	1	$Cl_{d+1} \rightarrow Cl_{d+2}$	C_{1+d}	0	\mathbb{Z}	0	\mathbb{Z}	0	\mathbb{Z}	0	\mathbb{Z}
AI	+	0	0	$Cl_{0,d+2} \rightarrow Cl_{1,d+2}$	R_{0-d}	\mathbb{Z}	0	0	0	$2\mathbb{Z}$	0	\mathbb{Z}_2	\mathbb{Z}_2
BDI	+	+	1	$Cl_{d+1,2} \rightarrow Cl_{d+1,3}$	R_{1-d}	\mathbb{Z}_2	\mathbb{Z}	0	0	0	$2\mathbb{Z}$	0	\mathbb{Z}_2
D	0	+	0	$Cl_{d,2} \rightarrow Cl_{d,3}$	R_{2-d}	\mathbb{Z}_2	\mathbb{Z}_2	\mathbb{Z}	0	0	0	$2\mathbb{Z}$	0
DIII	-	+	1	$Cl_{d,3} \rightarrow Cl_{d,4}$	R_{3-d}	0	\mathbb{Z}_2	\mathbb{Z}_2	\mathbb{Z}	0	0	0	$2\mathbb{Z}$
AII	-	0	0	$Cl_{2,d} \rightarrow Cl_{3,d}$	R_{4-d}	$2\mathbb{Z}$	0	\mathbb{Z}_2	\mathbb{Z}_2	\mathbb{Z}	0	0	0
CII	-	-	1	$Cl_{d+3,0} \rightarrow Cl_{d+3,1}$	R_{5-d}	0	$2\mathbb{Z}$	0	\mathbb{Z}_2	\mathbb{Z}_2	\mathbb{Z}	0	0
C	0	-	0	$Cl_{d+2,0} \rightarrow Cl_{d+2,1}$	R_{6-d}	0	0	$2\mathbb{Z}$	0	\mathbb{Z}_2	\mathbb{Z}_2	\mathbb{Z}	0
CI	+	-	1	$Cl_{d+2,1} \rightarrow Cl_{d+2,2}$	R_{7-d}	0	0	0	$2\mathbb{Z}$	0	\mathbb{Z}_2	\mathbb{Z}_2	\mathbb{Z}

Table 1.1: Classification of topological insulators and superconductors with respect to their symmetry classes (Atland-Zirnbauer classes) and spatial dimension d . The ten symmetry classes of single-particle Hamiltonians are characterized by the presence/absence of time-reversal (T), particle-hole (C), and chiral (S) symmetry of different types denoted by ± 1 . The symmetry classes can be grouped into complex and real classes, depending on whether the reality conditions arising from the anti-unitary symmetries are imposed on the Hamiltonian. V_d denotes the classifying space from the extension problem of the Clifford algebra. The symbols “ \mathbb{Z} ”, “ \mathbb{Z}_2 ”, and “ $2\mathbb{Z}$ ” represent the integer classification, the binary classification, and the even classification of topological phases. “0” means the entry is topologically trivial.

algebra, and the topological classification of each AZ class is found to be the zeroth homotopy group of the classifying space $\pi_0(V)$.

It is therefore necessary to review some basic knowledge of complex and real Clifford algebra. A complex Clifford algebra Cl_n has n generators satisfying

$$\{e_i, e_j\} = 2\delta_{ij}. \quad (1.89)$$

A 2^n -dimensional complex vector space can be formed by linear combinations of their products $e^{p_1} e^{p_2} \dots e^{p_n}$ ($p_i = 0, 1$) with complex coefficients. A real Clifford algebra $Cl_{p,q}$ has $p + q$ generators satisfying

$$\{e_i, e_j\} = 0 \quad (i \neq j), \text{ and } e_i^2 = \begin{cases} -1 & (i = 1, 2, \dots, p), \\ +1 & (i = p + 1, \dots, p + q). \end{cases} \quad (1.90)$$

A 2^{p+q} -dimensional real vector space can be formed by linear combinations of their products. The complex classes (A, AIII), without anti-unitary symmetries, correspond to complex Clifford algebras, while the real classes (AI, BDI, D, DIII, AII, CII, C, CI), with anti-unitary symmetries, correspond to real Clifford algebras. According to K -theory, for complex Clifford algebras, the classifying space for the extension $Cl_p \rightarrow Cl_{p+1}$ is known to be C_p ; and the classifying space for the extension $Cl_{p,q} \rightarrow Cl_{p,q+1}$ is known to be R_{q-p} , while for $Cl_{p,q} \rightarrow Cl_{p+1,q}$, it is R_{p+2-q} [28, 29].

Complex classes In class A without any symmetry constraint, from the Dirac Hamiltonian in Eq. (1.89), the generators are found to be $e_0 = \gamma_{d+1}, e_1 = \gamma_1, \dots, e_i = \gamma_i, \dots, e_d = \gamma_d$. We need

to consider the extension problem for complex Clifford algebras,

$$C_d : Cl_d \rightarrow Cl_{d+1} \quad (\text{class A}), \quad (1.91)$$

with C_d the classifying space in d dimension. In the zero-dimensional case with $d = 0$, we find $\pi_0(C_0) = \mathbb{Z}$ which means in class A zero-dimensional systems have integer classification.

In class AIII with chiral symmetry, the Dirac Hamiltonian satisfies,

$$\{\mathcal{H}(\mathbf{k}), \Gamma\} = 0, \quad (1.92)$$

where the chiral symmetry operator Γ is unitary. We can always take $\Gamma^2 = +\mathbb{1}$ by normalization with an extra factor, and it can be treated as an additional generator of the Clifford algebra. The corresponding generators are found to be $e_0 = \gamma_{d+1}, e_1 = \Gamma, e_2 = \gamma_1, \dots, e_{i+1} = \gamma_i, \dots, e_d = \gamma_{d-1}, e_{d+1} = \gamma_d$. Thus we need to consider the extension problem for complex Clifford algebras of

$$C_{1+d} : Cl_{1+d} \rightarrow Cl_{2+d} \quad (\text{class AIII}). \quad (1.93)$$

We can see that the classifying space for AIII class is always one dimension large than for A class. In the zero-dimensional case with $d = 0$, we find $\pi_0(C_1) = 0$, which means that zero-dimensional systems in class AIII are topologically trivial.

Real classes

1. *Time-reversal symmetry only (class AI and AII)* Under the time-reversal symmetry, the Dirac Hamiltonian in Eq. (1.88) satisfies $T^{-1}H(k)T = H(-k)$, which requires the following relation between gamma matrices and the time-reversal operator,

$$T\gamma_i = -\gamma_i T \quad (i = 1, \dots, d), \quad T\gamma_{d+1} = \gamma_{d+1} T. \quad (1.94)$$

We can treat the symmetry operators as generators or Clifford algebras. The generators for the corresponding real Clifford algebra are

$$e_0 = J\gamma_0, \quad e_1 = T, \quad e_2 = TJ, \quad e_3 = \gamma_1, \quad e_4 = \gamma_2, \quad \dots, \quad e_{d+2} = \gamma_d, \quad (1.95)$$

where J is the imaginary unit with $J^2 = -1$.

For class AI with $T^2 = +1$, without e_0 , the generators in the above equation form the Clifford algebra of $Cl_{0,2+d}$. With $e_0^2 = -1$, the extension of the real Clifford algebra leads to the classifying space

$$R_{0-d} : Cl_{0,d+2} \rightarrow Cl_{1,d+2} \quad (\text{class AI}). \quad (1.96)$$

For class AII with $T^2 = -1$, without e_0 , the generators form the Clifford algebra of $Cl_{2,d}$. With $e_0^2 = -1$, the extension of the real Clifford algebra leads to the classifying space

$$R_{4-d} : Cl_{2,d} \rightarrow Cl_{3,d} \quad (\text{class AII}). \quad (1.97)$$

2. *Particle-hole symmetry only (class C and D)* Under the particle-hole symmetry, the Dirac Hamiltonian in Eq. (1.88) satisfies $C^{-1}H(k)C = -H(-k)$, which requires the following relation between

gamma matrices and the particle-hole operator,

$$C\gamma_i = \gamma_i C \quad (i = 1, \dots, d), \quad C\gamma_{d+1} = -\gamma_{d+1}C, \quad (1.98)$$

Thus we can construct generators for a real Clifford algebra as

$$e_0 = \gamma_0, \quad e_1 = C, \quad e_2 = CJ, \quad e_3 = J\gamma_1, \quad e_4 = J\gamma_2, \quad \dots, \quad e_{d+2} = J\gamma_d. \quad (1.99)$$

For class D with $C^2 = +1$, without e_0 , the above generators form the Clifford algebra of $Cl_{d,2}$. With $e_0^2 = +1$, the extension of the real Clifford algebra leads to the classifying space

$$R_{2-d} : Cl_{d,2} \rightarrow Cl_{d,3} \quad (\text{class D}). \quad (1.100)$$

For class C with $C^2 = -1$, without e_0 , the above generators form the Clifford algebra of $Cl_{d+2,0}$. With $e_0^2 = -1$, the extension of the real Clifford algebra leads to the classifying space

$$R_{6-d} : Cl_{d+2,0} \rightarrow Cl_{d+2,1} \quad (\text{class C}), \quad (1.101)$$

3. *Time-reversal and particle-hole symmetry (BDI, DIII, CII, CI)* The Dirac Hamiltonian satisfies both time-reversal and particle-hole symmetry, thus the gamma matrices satisfy both Eq. (1.94) and Eq. (1.98). Accordingly, we can construct generators for a real Clifford algebra as

$$e_0 = \gamma_0, \quad e_1 = C, \quad e_2 = CJ, \quad e_3 = TCJ, \quad e_4 = J\gamma_1, \quad e_5 = J\gamma_3, \quad \dots, \quad e_{d+3} = J\gamma_d, \quad (1.102)$$

with a total of $d + 4$ generators.

For class BDI with $T^2 = +1$ and $C^2 = +1$, without e_0 , the generators in Eq. (1.102) form the real Clifford algebra $Cl_{d+1,2}$, where $e_1^2 = e_2^2 = +1$ and the square of the rest $d + 1$ terms equals -1 . Thus the classifying space is given by

$$R_{1-d} : Cl_{d+1,2} \rightarrow Cl_{d+1,3} \quad (\text{class BDI}). \quad (1.103)$$

For class DIII with $T^2 = -1$ and $C^2 = +1$, without e_0 , the generators form the real Clifford algebra $Cl_{d,3}$, where $e_1^2 = e_2^2 = e_3^2 = +1$ and the square of the rest d terms equals -1 . Thus the classifying space is given by

$$R_{3-d} : Cl_{d,3} \rightarrow Cl_{d,4} \quad (\text{class DIII}). \quad (1.104)$$

For class CII with $T^2 = -1$ and $C^2 = -1$, without e_0 , the generators form the real Clifford algebra $Cl_{d+3,0}$, where the square of the $d + 3$ terms equals -1 . Thus the classifying space is given by

$$R_{5-d} : Cl_{d+3,0} \rightarrow Cl_{d+3,1} \quad (\text{class CII}). \quad (1.105)$$

For class CI with $T^2 = +1$ and $C^2 = -1$, without e_0 , the generators form the real Clifford algebra $Cl_{d+2,1}$, where $e_3^2 = +1$ and the square of the rest $d + 2$ terms equals -1 . Thus the classifying space is given by

$$R_{7-d} : Cl_{d+2,1} \rightarrow Cl_{d+2,2} \quad (\text{class CI}). \quad (1.106)$$

Thus the classification of topological phases is reduced to determining the zeroth homotopy group of the classifying spaces C_q and R_q discussed above, which is given in Table. 1.1 [28, 29].

Example Here we give an example of class A in two-dimensional space, which can be used to describe the integer quantum Hall effect. The $2N \times 2N$ dimensional Dirac Hamiltonian in two-dimensional momentum space reads [28],

$$\mathcal{H}(\mathbf{k}) = k_x \sigma_x \otimes \mathbb{1}_N + k_y \sigma_y \otimes \mathbb{1}_N + \gamma_3, \quad (1.107)$$

with σ_i Pauli matrices and $\mathbb{1}_N$ the identity matrix of dimension N . As the mass term γ_3 anti-commutes with the kinetic terms, it must take the form of $\gamma_3 = \sigma_z \otimes A$, with A a normalized $N \times N$ Hermitian matrix.

The Hermitian matrix A can be diagonalized by a unitary matrix, $A = U \text{diag}(\mathbb{1}_n, -\mathbb{1}_m) U^\dagger$, with $n+m = N$. With fixed m and n , the set of A corresponds to a complex Grassmannian $U(n+m)/U(n) \times U(m)$. Thus, the classifying space after the extension with the mass term γ_3 corresponds to the union of complex Grassmannian with different values of n, m ,

$$\gamma_3 \leftrightarrow \oplus_{n,m} U(n+m)/U(n) \times U(m). \quad (1.108)$$

Since $\pi_0[\oplus_{n,m} U(n+m)/U(n) \times U(m)] = \mathbb{Z}$, the topologically distinct phases are characterized by integers.

1.4 Non-Hermitian topological phases

A recent development in this field is to investigate non-Hermitian topological phases [20, 21, 30]. In non-Hermitian systems without the constraints of Hermiticity $H \neq H^\dagger$, the left eigenvectors are no longer the adjoint of the right eigenvectors. For a non-Hermitian Hamiltonian with discrete spectrum, the orthonormality can be achieved through the set of biorthonormal eigenbasis $\{|u_n\rangle, |u_n\rangle\rangle\}$ which satisfies

$$H|u_n\rangle = E_n|u_n\rangle, \quad \langle\langle u_n|H = \langle\langle u_n|E_n, \quad (1.109)$$

$$\langle\langle u_m|u_n\rangle = \langle u_m|u_n\rangle = \delta_{mn}, \quad (1.110)$$

$$\sum_n |u_n\rangle\langle\langle u_n| = \sum_n |u_n\rangle\rangle\langle u_n| = \mathbb{1}. \quad (1.111)$$

Here, the adjoints of a left eigenvector $|u_n\rangle\rangle$ and a right eigenvector $|u_n\rangle$ also satisfy $\langle u_n|H^\dagger = \langle u_n|E_n^*$ and $H^\dagger|u_n\rangle\rangle = E_n^*|u_n\rangle\rangle$. As the choice of eigenbasis satisfying Eqs. (1.109) to (1.111) is in drastic contrast to Hermitian systems, it is natural to ask whether the topological invariants can be defined similarly in non-Hermitian systems, and if they can, whether they can be used to characterize the non-Hermitian topological phases.

class	$d=0$	1	2	3	4	5	6	7
A, DIII, CI	0	\mathbb{Z}	0	\mathbb{Z}	0	\mathbb{Z}	0	\mathbb{Z}
AIII	0	$\mathbb{Z} \oplus \mathbb{Z}$	0	$\mathbb{Z} \oplus \mathbb{Z}$	0	$\mathbb{Z} \oplus \mathbb{Z}$	0	$\mathbb{Z} \oplus \mathbb{Z}$
AI, D	\mathbb{Z}_2	\mathbb{Z}	0	0	0	$2\mathbb{Z}$	0	\mathbb{Z}_2
BDI	$\mathbb{Z}_2 \oplus \mathbb{Z}_2$	$\mathbb{Z} \oplus \mathbb{Z}$	0	0	0	$2\mathbb{Z} \oplus 2\mathbb{Z}$	0	$\mathbb{Z}_2 \oplus \mathbb{Z}_2$
AII, C	0	$2\mathbb{Z}$	0	\mathbb{Z}_2	\mathbb{Z}_2	\mathbb{Z}	0	0
CII	0	$2\mathbb{Z} \oplus 2\mathbb{Z}$	0	$\mathbb{Z}_2 \oplus \mathbb{Z}_2$	$\mathbb{Z}_2 \oplus \mathbb{Z}_2$	$\mathbb{Z} \oplus \mathbb{Z}$	0	0

Table 1.2: Classification of non-Hermitian topological phases [21]. A prominent feature is that Classes A, DIII and CI, classes AI and D, and classes AII and C are unified in the Atland-Zirnbauer ten-fold classes.

Berry phase We take the Berry phase in non-Hermitian systems as an example. The dynamics of the right eigenvector can be obtained similar to that of Eq. (1.9), which reads

$$E_n(\mathbf{k}(t))|u_n(\mathbf{k}(t))\rangle = \hbar\partial_t\theta(t)|u_n(\mathbf{k}(t))\rangle + i\hbar\partial_t|u_n(\mathbf{k}(t))\rangle, \quad (1.112)$$

with $E_n(\mathbf{k}(t))$ the eigenvalue for the band n . Applying the left eigenvector $\langle\langle u_n(\mathbf{k}(t))|$ with the normalization condition of $\langle\langle u_n(\mathbf{k}(t))|u_n(\mathbf{k}(t))\rangle\rangle = 1$, after the integration, the phase is obtained as

$$\theta(t) = \frac{1}{\hbar} \int_0^t E_n(\mathbf{k}(t')) dt' - i \int_0^t \langle\langle u_n(\mathbf{k}(t'))|\partial_{t'}|u_n(\mathbf{k}(t'))\rangle\rangle dt'. \quad (1.113)$$

We emphasize that the second term at the RHS can still be treated as the geometrical phase. On a cyclic path of Γ in the Brillouin zone, it can be written as

$$\gamma_n = i \int_0^t \langle\langle u_n(\mathbf{k}(t'))|\partial_{t'}|u_n(\mathbf{k}(t'))\rangle\rangle dt' = i \oint_{\Gamma} d\mathbf{k} \langle\langle u_n(\mathbf{k})|\nabla_{\mathbf{k}}|u_n(\mathbf{k})\rangle\rangle. \quad (1.114)$$

The form of the Berry connection can be derived accordingly

$$\gamma_n = \oint_{\Gamma} d\mathbf{k} \mathbf{A}_n = \iint_{\Gamma} d\mathbf{S} \nabla_{\mathbf{k}} \times \mathbf{A}_n, \quad (1.115)$$

with the Berry connection and Berry curvature of

$$\mathbf{A}_n = i \langle\langle u_n(\mathbf{k})|\nabla_{\mathbf{k}}|u_n(\mathbf{k})\rangle\rangle, \quad \mathbf{\Omega}_n = \nabla_{\mathbf{k}} \times \mathbf{A}_n(\mathbf{k}) = i \nabla_{\mathbf{k}} \times \langle\langle u_n(\mathbf{k})|\nabla_{\mathbf{k}}|u_n(\mathbf{k})\rangle\rangle. \quad (1.116)$$

From Eqs. (1.115) and (1.116), the Berry phase and Berry curvature can still be defined in terms of the biorthonormal eigenbasis.

It is important to notice that in Eq. (1.113), the first part which is called the dynamic phase is also different from the Hermitian case, because the energy eigenvalues are complex $E_n(\mathbf{k}) \in \mathbb{C}$. On a cyclic path of Γ in the Brillouin zone, the winding number for the n -th band can be defined as [20]

$$\omega_n = \oint_{\Gamma} \frac{d\mathbf{k}}{2\pi} \nabla_{\mathbf{k}} \arg E_n(\mathbf{k}), \quad (1.117)$$

where \arg takes the argument of the complex energy.

1.4.1 Classification of non-Hermitian topological phases

In this section, we extend the classification table of topological phases to non-Hermitian regime. An arbitrary invertible Hamiltonian H has a unique polar decomposition $H = UP$ with U being unitary and $P = \sqrt{H^\dagger H}$ being Hermitian and positive definite. It can be proved that H and U are homotopically equivalent, $H \simeq U$ [21]. Accordingly, the classification of Hamiltonians is equivalent to the classification of corresponding unitary matrices.

It should be noted that in the previous section, the classification of topological phases of gapped systems is achieved through Dirac Hamiltonians. A more fundamental treatment should start with a general gapped Hermitian Hamiltonian, which can be continuously deformed to a ‘‘spectrum flattened’’ Hamiltonian which satisfies $H^2 = \mathbb{1}$. The energy eigenvalues above and below the energy gap are deformed to $+1$ and -1 , respectively, and the wavefunctions are preserved during the spectrum flattening, so that any topological property is preserved. After this treatment, H can be considered as a generator of a Clifford algebra Cl_H . Notice that the symmetry operators already form a Clifford algebra Cl_S . Thus the classifying space is formed by the extension of the Clifford algebra $Cl_S \rightarrow Cl_H$. In this way, the classification of topological phases can be achieved from these classifying spaces.

For a non-Hermitian Hamiltonian H , after the unitarization by the polar decomposition $H = UP$, in general $U^2 \neq \pm\mathbb{1}$, which means U cannot be treated as a generator of a Clifford algebra. However, a corresponding Hermitian Hamiltonian can be constructed as [21]

$$H_U = \sigma_+ \otimes U + \sigma_- \otimes U^\dagger = \begin{pmatrix} & U \\ U^\dagger & \end{pmatrix}. \quad (1.118)$$

The constructed Hamiltonian satisfies $H_U^2 = \mathbb{1}$ as U is unitary. It should be emphasized that after such a construction, the Hamiltonian automatically acquires a chiral symmetry with the symmetry operator $\Sigma = \sigma_z \otimes \mathbb{1}$,

$$\{H_U, \Sigma\} = 0, \quad (1.119)$$

with $\Sigma^2 = \mathbb{1}$. In this way, the topological property of U can be obtained from H_U . Thus, the classification of non-Hermitian Hamiltonians H is equivalent to the classification of H_U with an additional chiral symmetry Σ .

Complex classes For class A, with the additional chiral symmetry Σ , the classification simply shifts to class AIII, since there are no other symmetry constraints.

For class AIII, because the additional chiral symmetry commutes with the original chiral symmetry $\sigma_0 \otimes \Gamma$, $[\Sigma, \sigma_0 \otimes \Gamma] = 0$, the topological number simply duplicates, that is, $\mathbb{Z} \rightarrow \mathbb{Z} \otimes \mathbb{Z}$ and $0 \rightarrow 0$ for entries in class AIII.

Real classes *AZ classes with a single anti-unitary symmetry* This includes class AI ($T^2 = +1$), class D ($C^2 = +1$), class AII ($T^2 = -1$), and class C ($C^2 = -1$). Denote the anti-unitary operator as $A = U_A \mathcal{K}$. Thus, from the relation $AU = \eta_A U A$ and $AU^\dagger = \eta_A U^\dagger A$ with $\eta_A = \pm 1$ from the single anti-unitary symmetry, we can construct an anti-unitary operator $A_U = \sigma_0 \otimes A$ and obtain

$$A_U H_U = \eta_A H_U A_U, \quad (1.120)$$

which means H_U follows a similar anti-unitary symmetry as that of U . Since A_U commutes with Σ , it can be inferred that there is another anti-unitary operator, the square of which is the same as A^2 .

Thus, class AI and class D with $T^2 = C^2 = +1$ are unified to class BDI, while class AII and class C with $T^2 = C^2 = -1$ are unified to class CII.

AZ classes of both time-reversal and particle-hole symmetry They can be separated into two groups. In the first group of classes CI ($T^2 = +1$, $C^2 = -1$) and class DIII ($T^2 = -1$, $C^2 = +1$), an operator can be constructed as $i\Sigma(\sigma_0 \otimes \Gamma) = i\sigma_z \otimes \Gamma$, with the original chiral symmetry Σ . Here we note that this operator squares to be $(i\sigma_z \otimes \Gamma)^2 = -\mathbb{1}$, and it commutes with all the generators in the original Clifford algebra. Thus this operator can simply be treated as an imaginary unit, which turns the corresponding real Clifford algebra to complex Clifford algebra. As a result, classes CI and DIII are unified to be AIII. In the second group of classes BDI ($T^2 = +1$, $C^2 = +1$) and CII ($T^2 = -1$, $C^2 = -1$), a similar operator of $\Sigma(\sigma_0 \otimes \Gamma) = \sigma_z \otimes \Gamma$ can be constructed, which squares to be $+\mathbb{1}$ and commutes with the generators in the original Clifford algebra. Since $\sigma_z \otimes \Gamma$ has two different subspaces corresponding to eigenvalues ± 1 , the topological invariants just get doubled.

1.5 Organization of this thesis

After introducing the basic concepts of Hermitian topological systems in this chapter, the remainder of this thesis is mainly devoted to investigating non-Hermitian topological phases. As \mathcal{PT} symmetry is found to be an alternative to the fundamental axiom of Hermiticity in quantum mechanics [31–34], we will first study the \mathcal{PT} -symmetric topological nodal-line semimetals in chapter 2. The topological properties, including topological invariants, topological surface states, and topological current, will be studied through both analytical and numerical calculations. It is found that \mathcal{PT} symmetric nodal-line semimetals exhibit a parity anomaly in $(3 + 1)$ -dimensional spacetime that is not possible in high-energy physics. The proposal of generating and detecting a topological current that originates from the parity anomaly is suggested. At the end of this chapter, we relax the constraints of Hermiticity but keep the \mathcal{PT} symmetry to realize a \mathcal{PT} -symmetric non-Hermitian Dirac nodal-line semimetal. The corresponding topological invariants and surface states are calculated and compared with their Hermitian counterparts.

In chapter 3 we focus on general non-Hermitian topological gapped systems. As can be seen in the section "symmetry and topology", most Hermitian topological gapped systems can be represented by massive Dirac Hamiltonians described in Eq. (1.88) and based on it, the classification table of topological phases can also be established. Similarly, the non-Hermitian topological gapped systems can be represented by non-Hermitian Dirac Hamiltonians, after introducing non-Hermitian terms. We present a systematic investigation of d -dimensional massive Dirac Hamiltonians with three different types of non-Hermitian terms: (i) non-Hermitian terms that anti-commute with the Dirac Hamiltonian, (ii) non-Hermitian kinetic terms, and (iii) non-Hermitian mass terms. With respect to different boundary conditions, we adopt a method using non-unitary similarity transformation, unique to non-Hermitian systems, to reveal the intimate connection between different types of non-Hermitian Dirac Hamiltonians. The bulk-boundary correspondence is discussed in detail for each kind of Dirac Hamiltonians. At the end of this chapter, we introduce the notion of exceptional points, along with a comprehensive discussion of their physical properties.

Finally, in chapter 4, we extend our discussion to non-Hermitian topological gapless systems, with a focus on non-Hermitian topological Weyl and Dirac semimetals. We first introduce the topological properties of Hermitian Weyl semimetals, which includes the chirality of Weyl points, the Fermi arc

surface states, the chiral anomaly and the associated chiral magnetic effect. Then we turn to non-Hermitian Weyl semimetals by considering all possible non-Hermitian terms. It is found that there are only non-Hermitian kinetic and mass terms in non-Hermitian Weyl Hamiltonians. The corresponding topological features of these two kinds of non-Hermitian Weyl semimetals are studied in detail. As \mathcal{PT} symmetry is of fundamental interest, we will focus on the \mathcal{PT} -symmetric non-Hermitian perturbations in Dirac semimetals. Besides turning a Dirac point into Weyl points, these non-Hermitian perturbations induce topological phase transitions from a Dirac point to a pair of mutually complex conjugated Weyl exceptional rings and a Dirac exceptional sphere with periodic boundary conditions. However, as the usual bulk-boundary correspondence fails in the non-Hermitian topological systems, special attention is paid to the topological surface states in the \mathcal{PT} -symmetric non-Hermitian Dirac semimetals with open boundary conditions.

2

Chapter 2

\mathcal{PT} -symmetric topological nodal-line semimetals

The last decade witnessed a growing interest in topological semimetals [13, 35–43]. Different from normal metals, the band crossings between valence and conduction bands in topological semimetals are protected by symmetry. A distinct feature between topological and normal metals is the dimension of the Fermi surface. The Fermi surface of topological semimetals can have reduced dimensions, for instance the Weyl semimetals possess 0D Fermi surfaces in 3D and the Fermi surface of Dirac semimetals is 0D in either 2D or 3D space, while the normal metals usually have Fermi surfaces with one dimension less than the spatial dimension [44–48]. Other than 0D Fermi surfaces, topological semimetals can also possess 1D Fermi surface (nodal line) in either 2D or 3D spatial dimensions [1, 49–59]. In topological semimetals, the bulk topological invariants of the topological semimetals lead to exotic boundary states due to the bulk-boundary correspondence, such as the Fermi arc surface states in Weyl/Dirac semimetals.

Furthermore, topological semimetals possess anomalous transport properties, such as the axial current in Weyl semimetals [60] and the valley Hall effect in graphene [61, 62]. These topological currents have their origin in quantum anomalies of the relativistic field theories describing the low-energy physics of semimetals [63–65]. Quantum anomalies arise whenever a symmetry of the classical theory is broken by the regularization of the quantum theory. For example, in Weyl semimetals the famous (3+1)-dimensional chiral anomaly [66–72] manifests itself as the non-conservation of the chiral charge. Another example of an anomaly leading to topological currents is the (2+1)-dimensional parity anomaly [5, 73–75], which is realized in graphene [76–78] and graphene-like systems [79–81]. The fermionic excitations near the Dirac cones of graphene are described by a (2+1)-dimensional quantum field theory exhibiting the parity anomaly. Any gauge symmetric regularization of this quantum field theory must necessarily break spacetime inversion symmetry, which manifests itself by a parity-breaking Chern-Simons term in the electromagnetic response theory of a single graphene Dirac cone. This Chern-Simons term gives rise to the valley Hall effect, where fermions from different Dirac cones flow to opposite transverse edges, upon applying an electric field [76, 76–79].

In this chapter, we focus on a specific class of topological semimetals with one dimensional Fermi surface in 3D space, the \mathcal{PT} -symmetric Dirac nodal-line semimetals (DNLSM). The band crossings in such materials form a 1D nodal lines, and are topologically stable as they are protected by the \mathcal{PT}

symmetry. The topological charges of these finite-dimensional Fermi surfaces are defined in a similar way as for Weyl and Dirac points, namely, by the topology of the Berry bundle on a sphere that encloses the Fermi surface from its transverse dimension [40–43]. We explicitly discuss the topological invariants associated with the Fermi surface. By studying the surface spectrum, we find there are drumhead surface states in DNLSMs. We explain the formation of such novel surface states by revealing their intimate relation with bulk topological invariants.

Since topologically nontrivial Berry bundles are closely connected to quantum anomalies, one may wonder whether the quantum field theories describing nodal-line semimetals exhibit any anomalies and, if so, whether they lead to unusual transport phenomena. Thus we further investigate this question for the (3+1)-dimensional Dirac nodal-line semimetals (DNLSMs) protected by the combined symmetry of time-reversal \mathcal{T} and inversion \mathcal{P} with $(\mathcal{PT})^2 = 1$ [49–51]. We find that the low-energy fermionic excitations of these DNLSMs are described by a one-parameter family of (2+1)-dimensional quantum field theories with a parity anomaly. We show that in the presence of small inversion breaking, this parity anomaly leads to a Hall-like topological current, which can be controlled by using electric fields. To detect this anomalous current, we propose a dumbbell-shaped device, which utilizes the drumhead surface states of DNLSMs to filter electrons based on their momenta.

In the last section, since \mathcal{PT} symmetry is closely related to the non-Hermitian physics, we will discuss the topological nodal-line semimetals in the presence of \mathcal{PT} -symmetric non-Hermitian potentials. We find that the \mathcal{PT} -symmetric non-Hermitian potential turns the 1D nodal line to a 2D torus. Though the topological invariant of such systems can still be computed similar to Hermitian systems, it does not have a good correspondence between the topological boundary states, which suggests a theory for non-Hermitian topological phases of matter should be developed.

2.1 Symmetry and topology

We have discussed in the first chapter that there is an intimate relation between symmetry and topology. In this chapter, we focus on a topological system with two most fundamental symmetries, the inversion (parity) symmetry \mathcal{P} and the time-reversal symmetry \mathcal{T} . In real space, the inversion flips all directions of space and the time-reversal flips the direction of time

$$\mathcal{P} : (t, \mathbf{x}) \rightarrow (t, -\mathbf{x}), \quad \mathcal{T} : (t, \mathbf{x}) \rightarrow (-t, \mathbf{x}), \quad (2.1)$$

where t denotes the time and \mathbf{x} the space of the spacetime vector. It should be noted that in even spatial dimensions, the parity operation is equivalent to rotation.

In condensed matter physics, with translational symmetry and periodic boundary conditions, it suffices to discuss the systems in the first Brillouin zone (BZ). As we consider systems without interaction, we denote the system by a single particle Hamiltonian $\mathcal{H}(\mathbf{k})$, with \mathbf{k} running over the first BZ. Under \mathcal{P} and \mathcal{T} symmetry, the Hamiltonian satisfies

$$\hat{\mathcal{P}}\mathcal{H}(\mathbf{k})\hat{\mathcal{P}}^{-1} = \mathcal{H}(-\mathbf{k}) \text{ and } \hat{\mathcal{T}}\mathcal{H}(\mathbf{k})\hat{\mathcal{T}}^{-1} = \mathcal{H}(-\mathbf{k}), \quad (2.2)$$

where $\hat{\mathcal{T}}$ is an anti-unitary operator, $\hat{\mathcal{T}}i\hat{\mathcal{T}}^{-1} = -i$, and $\hat{\mathcal{P}}$ is a unitary operator, $\hat{\mathcal{P}}i\hat{\mathcal{P}}^{-1} = i$. For our discussion, we take $\hat{\mathcal{P}}^2 = +1$ and $\hat{\mathcal{T}}^2 = +1$ for spinless systems without spin-orbit coupling (SOC).

Furthermore, we consider the combined symmetry of space inversion and time-reversal, denoted by

\mathcal{PT} . Under this combined symmetry, the Hamiltonian satisfies

$$\hat{\mathcal{P}}\hat{\mathcal{T}}\mathcal{H}(\mathbf{k})(\hat{\mathcal{P}}\hat{\mathcal{T}})^{-1} = \mathcal{H}(\mathbf{k}), \quad (2.3)$$

which acts on each \mathbf{k} point. In a system without SOC, the combined symmetry operator is an anti-unitary operator, $\hat{\mathcal{P}}\hat{\mathcal{T}}i(\hat{\mathcal{P}}\hat{\mathcal{T}})^{-1} = -i$, which satisfies $(\hat{\mathcal{P}}\hat{\mathcal{T}})^2 = +1$. Hence the $\hat{\mathcal{P}}\hat{\mathcal{T}}$ operator can be represented by the complex conjugation operator $\hat{\mathcal{P}}\hat{\mathcal{T}} = UK$, with U unitary and \mathcal{K} complex conjugation operator. Note that under the condition $(\hat{\mathcal{P}}\hat{\mathcal{T}})^2 = +1$, we have the relation $UU^* = 1$. Actually, the \mathcal{PT} symmetry is a reality condition for the Hamiltonian. Up to a basis choice, $\hat{\mathcal{P}}\hat{\mathcal{T}} = \mathcal{K}$, and it can be derived that from Eq. (2.3), the Hamiltonian $\mathcal{H}(\mathbf{k})$ is a real matrix at each \mathbf{k} in BZ. Such a constraint imposed by symmetry will lead to quantization of topological invariants in specific dimensions, as we show below.

For each \mathbf{k} , we can find a set of eigenstates of the Hamiltonian $|\alpha, \mathbf{k}\rangle$ with the band index α , that satisfy,

$$\hat{\mathcal{P}}\hat{\mathcal{T}}|\alpha, \mathbf{k}\rangle = e^{i\theta(\mathbf{k})}|\alpha, \mathbf{k}\rangle, \quad (2.4)$$

with $\theta(\mathbf{k})$ an arbitrary phase. Such relation holds for each band as there is no Kramers degeneracy for $(\hat{\mathcal{P}}\hat{\mathcal{T}})^2 = +1$. Now we turn to the constraint imposed on the topology by the \mathcal{PT} symmetry. The relation of Eq. (2.4) can be rewritten as $|\alpha, \mathbf{k}\rangle = e^{-i\theta(\mathbf{k})}\hat{\mathcal{P}}\hat{\mathcal{T}}|\alpha, \mathbf{k}\rangle$. The Berry phase for the α th band, along a closed loop in BZ is

$$\begin{aligned} \gamma_\alpha &= i \oint d\mathbf{k} \langle \alpha, \mathbf{k} | \partial_{\mathbf{k}} | \alpha, \mathbf{k} \rangle = i \oint d\mathbf{k} \langle \alpha, \mathbf{k} | (\hat{\mathcal{P}}\hat{\mathcal{T}})^{-1} e^{i\theta(\mathbf{k})} \partial_{\mathbf{k}} e^{-i\theta(\mathbf{k})} (\hat{\mathcal{P}}\hat{\mathcal{T}}) | \alpha, \mathbf{k} \rangle \\ &= i \oint d\mathbf{k} \langle \alpha, \mathbf{k} | (UK)^{-1} \partial_{\mathbf{k}} (UK) | \alpha, \mathbf{k} \rangle + i \oint d\mathbf{k} e^{i\theta(\mathbf{k})} \partial_{\mathbf{k}} e^{-i\theta(\mathbf{k})} \\ &= - \left(i \oint d\mathbf{k} \langle \alpha, \mathbf{k} | \partial_{\mathbf{k}} | \alpha, \mathbf{k} \rangle \right)^* + i \oint d\mathbf{k} e^{i\theta(\mathbf{k})} \partial_{\mathbf{k}} e^{-i\theta(\mathbf{k})}. \end{aligned} \quad (2.5)$$

In the last step, we have adopted the relation

$$\langle k | \partial_k | k \rangle = -(\partial_k \langle k |) | k \rangle = -\langle k | \partial_k | k \rangle^*. \quad (2.6)$$

Further $i \oint d\mathbf{k} e^{i\theta(\mathbf{k})} \partial_{\mathbf{k}} e^{-i\theta(\mathbf{k})}$ is the winding number of $\theta(k)$ along the closed loop, which equals to $2\pi n$ with n integer. As the Berry phase is real in Hermitian systems, we have,

$$\gamma = -\gamma + 2\pi n \longrightarrow \gamma = n\pi, \quad (2.7)$$

which is quantized as $n\pi$. Since in the Brillouin zone, the eigenstates can be altered by a global phase of $2\pi m$, $|k\rangle \rightarrow e^{i2\pi m}|k\rangle$, the Berry phase can differ by $2\pi m$ with m an integer. Thus, we can define the topological invariant as

$$\nu = n\pi \bmod 2\pi \in \mathbb{Z}_2. \quad (2.8)$$

Historically this was first pointed out by Zak [82].

The above derivation can be generalized to the multi-band case with the Berry phase given as

$$\gamma = \oint d\mathbf{k} \operatorname{tr} \hat{A}(\mathbf{k}), \quad (2.9)$$

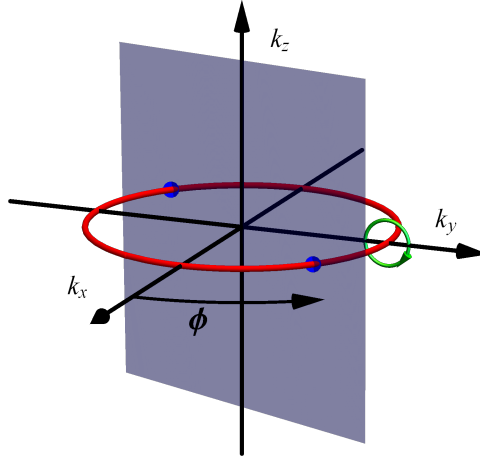


Figure 2.1: The topological charge is defined in terms of a line integral along the green loop. The blue plane indicates the two-dimensional subsystems that are parameterized by the angle ϕ .

with $\hat{A}_{\alpha\beta} = \langle \alpha, \mathbf{k} | i\partial_{\mathbf{k}} | \beta, \mathbf{k} \rangle$ denoting the Berry connection of the occupied eigenstates $|\alpha, \mathbf{k}\rangle$.

2.2 Dirac nodal-line semimetals

We consider the \mathcal{PT} -symmetric Dirac nodal-line semimetals with \mathbb{Z}_2 topological charge. The Fermi surface of Dirac nodal-line semimetals (DNLSM) consists of one-dimensional Dirac rings. We define the co-dimension as the dimension of the submanifold that encloses the Fermi surface in its transverse dimension. As the nodal ring can be enclosed by a 1D loop in the three-dimensional Brillouin zone, the co-dimension is $d_c = 1$. Without loss of generality, we assume that the DNLSM exhibits only a single Dirac ring, which is located within the $k_z = 0$ plane. Its low-energy Hamiltonian reads

$$\mathcal{H}_{\text{nl}}(\mathbf{k}) = \frac{1}{\Lambda} [k_0^2 - (k_x^2 + k_y^2) - b^2 k_z^2] \sigma_3 + v_z k_z \sigma_2 + m \sigma_1, \quad (2.10)$$

where for later use we have introduced a small \mathcal{PT} breaking mass $m\sigma_1$. In a DNLSM material this mass term could be generated, for example, by inversion breaking uniaxial strain or pressure. In the absence of $m\sigma_1$ the Hamiltonian $\mathcal{H}(\mathbf{k})$ is \mathcal{PT} -symmetric

$$\hat{\mathcal{P}}\hat{\mathcal{T}}\mathcal{H}_{\text{nl}}(\mathbf{k})(\hat{\mathcal{P}}\hat{\mathcal{T}})^{-1} = \mathcal{H}_{\text{nl}}(\mathbf{k}), \quad (2.11)$$

with the \mathcal{PT} operator $\hat{\mathcal{P}}\hat{\mathcal{T}} = \sigma_3\hat{\mathcal{K}}$. The energy spectrum of the low-energy Hamiltonian in Eq. (2.10) is $E_{\text{nl}} = \pm \sqrt{\frac{1}{\Lambda^2} [k_0^2 - (k_x^2 + k_y^2) - b^2 k_z^2]^2 + v_z^2 k_z^2}$. The nodal line centers at $(k_x, k_y) = 0$ with radius k_0 on the $k_z = 0$ plane. The Dirac nodal line is plotted out in red in Fig. 2.1.

As discussed in the section of symmetry and topology, the \mathcal{PT} symmetry leads to the quantization of \mathbb{Z}_2 type topological invariants, which can be obtained by calculating the Berry phase along a closed loop. For the DNLSM, we choose a loop S^1 that interlinks with the Dirac ring [green loop in Fig. 2.1].

Then according to Eq. (2.9), the topological invariant is given by

$$\nu[S^1] = \frac{1}{\pi} \int_{S^1} d\phi \operatorname{tr} \hat{A}(\varphi) \pmod{2}, \quad (2.12)$$

where the integration is along the loop S^1 , parameterized by $\varphi \in [-\pi, \pi)$, and $\hat{A}_{\alpha\beta,j} = \langle \alpha, \mathbf{k} | i\partial_{k_j} | \beta, \mathbf{k} \rangle$ denotes the Berry connection of the occupied Bloch eigenstates $|\alpha, \mathbf{k}\rangle$. \mathcal{PT} symmetry ensures that ν can only take on the quantized values of 0 and 1. Loops S^1 that interlink with a Dirac ring have a nontrivial Berry bundle, which results in a nonzero topological charge $\nu = 1$. This can be seen by a simple calculation. As the topological invariant does not depend on the shape of the loop S^1 , we can parameterize S^1 by $(k_x, k_y, k_z) = (0, k_0 - \frac{\Lambda}{2k_0} r \cos \theta, \frac{1}{v_z} r \sin \theta)$, with $r \ll k_0$. To the first order of r , the Hamiltonian on loop S^1 becomes,

$$\mathcal{H}_{S^1}(\theta) = r \cos \theta \sigma_3 + r \sin \theta \sigma_2 + \mathcal{O}(r^2). \quad (2.13)$$

Under a unitary transformation by σ_2 , the Hamiltonian becomes $\mathcal{H}'_{S^1}(\theta) = r \cos \theta \sigma_1 + r \sin \theta \sigma_2$. The eigenstate for the occupied band is $\frac{1}{\sqrt{2}}(-e^{-i\theta}, 1)^T$, with T the matrix transposition. Thus the topological invariant equals,

$$\nu[S^1] = \frac{1}{\pi} \int_{-\pi}^{\pi} d\theta \frac{1}{2} \begin{pmatrix} -e^{i\theta} & 1 \end{pmatrix} i\partial_{\theta} \begin{pmatrix} -e^{-i\theta} \\ 1 \end{pmatrix} = 1 \pmod{2}, \quad (2.14)$$

which is non-trivial. The Berry phase can also be calculated from the Berry curvature over the surface around the nodal line. As we will see, the Berry curvature is of Dirac delta function type, which reflects the singularity of the Dirac nodal line. In two dimensions, Eq. (2.12) assures the stability of the Dirac points like in graphene. In fact, since graphene is \mathcal{PT} -symmetric and its Dirac points have co-dimension $d_c = 1$, it belongs to the same entry in the classification of topological semimetals as DNLSMs [47].

Guided by the similarity between Dirac nodal line in 3D and Dirac points in 2D space, we introduce cylindrical coordinates $\{k_{\rho}, \phi, k_z\}$ and decompose the (3+1)-dimensional DNLSM into a family of (2+1)-dimensional subsystems parameterized by the angle ϕ , as shown in Fig. 2.1. Each subsystem exhibits two Dirac points with opposite Berry phase¹, denoted by two blue dots in Fig. 2.1. The low-energy physics of a single Dirac point in a given subsystem is described by a (2+1)-dimensional quantum field theory with the action

$$S^{\phi} = \int d^3x \bar{\psi} \left[i\gamma^{\mu} (\partial_{\mu} + ieA_{\mu}) + m \right] \psi, \quad (2.15)$$

where ψ is a two-component Dirac spinor coupled to the electromagnetic gauge field A_{μ} . Here, $\bar{\psi} = \psi^{\dagger} \gamma^0$, $\{\gamma^{\mu}, \gamma^{\nu}\} = 2\eta^{\mu\nu}$, and $\eta^{\mu\nu} = \operatorname{diag}(1, -1, -1)$. The mass term $m\bar{\psi}\psi$ breaks spacetime inversion symmetry, since the spinors transform under \mathcal{PT} as $\psi \rightarrow \gamma^2 \gamma^0 \psi$ and $\psi^{\dagger} \rightarrow -\psi^{\dagger} \gamma^0 \gamma^2$. In the absence of the mass term $m\bar{\psi}\psi$, Eq. (2.15) is \mathcal{PT} -symmetric [with $(\mathcal{PT})^2 = 1$] and can be viewed as a classical action of (2 + 1)-dimensional Dirac fields.

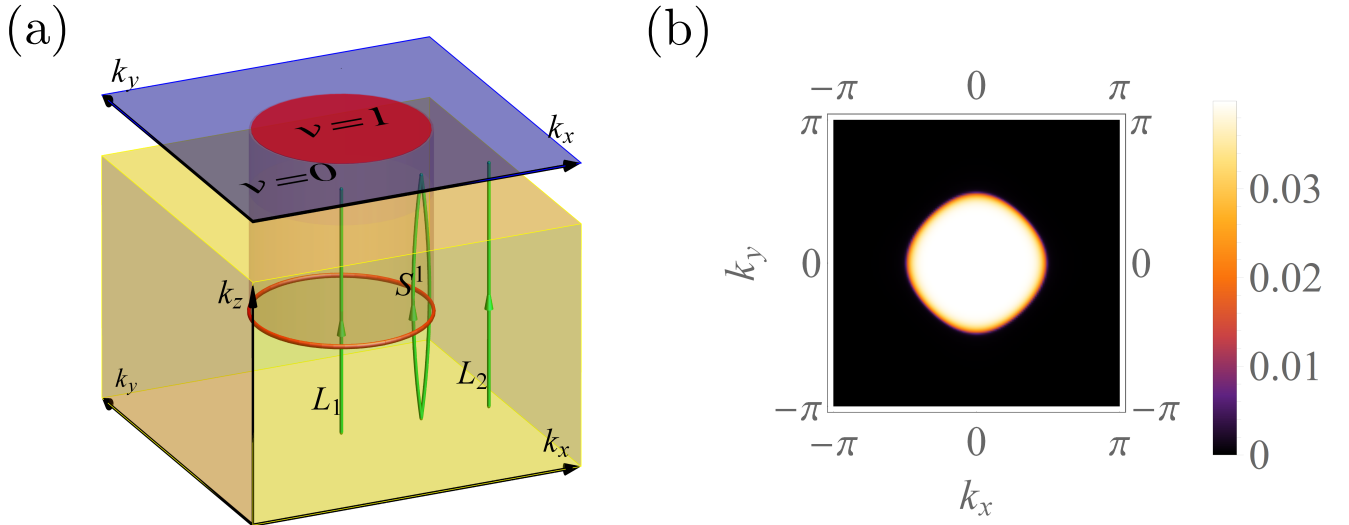


Figure 2.2: Drumhead surface states. (a) Relationship of the Dirac ring to the surface states of a topological nodal-line semimetal. The yellow and blue regions show the bulk and surface BZ, respectively. Drumhead surface states occur within the red region, which is bounded by the projected Dirac ring. Within this region the topological charge ν , Eq. (2.12), takes on the value $\nu = 1$, while outside this region it is zero. (b) Local density of states on the surface. The total number unit cells in z direction is $N_z = 50$. The number of states near the Fermi surface that summed is $N_{eigen} = 50$ and the first $N_{edge} = 5$ unit cells from the boundary are taken into account. Γ is taken as 1.

2.3 Drumhead surface states

The topologically nontrivial Berry bundle of DNLSMs leads to the appearance of drumhead surface states. This can be seen by deforming the green integration loop in Fig. 2.1 into two lines along the (001) direction, denoted by "L_i" in Fig. 2.2(a). It follows from the bulk-boundary correspondence [83] that in-gap surface states appear at the (001) face of DNLSMs whenever $\nu[L_i] \neq 0$. This corresponds to regions of the surface BZ that are bounded by the projected Dirac ring, since moving L_i along transverse directions without crossing the Dirac ring preserves $\nu[L_i]$. As the drumhead surface states are of topological origin, their existence does not depend on the surface termination or any other microscopic details of the crystal surface.

In this section, we first analytically calculate the surface spectrum from the low-energy effective model in Eq. (2.10). We will see that the surface states localize exactly inside the regions predicted by the bulk-boundary correspondence. Further, we will turn to a lattice model of DNLSMs and numerically calculate the local density of states (LDOS) on the surface, which can be probed directly by angle-resolved photoemission spectroscopy (ARPES) experiments.

2.3.1 Surface spectrum from the continuum model

To investigate the surface states, we take a semi-infinite system in the half plane of $z \leq 0$ with open boundary conditions. The translational symmetry is broken in z direction due to the boundary, while it is still preserved in other directions, which means k_x and k_y are still good quantum numbers. Hence, the real space Hamiltonian with open boundary conditions can be denoted as $\mathcal{H}_{\text{nl}}(k_x, k_y, -i\partial_z)$, with the replacement of $k_z \rightarrow -i\partial_z$. We adopt the ansatz for the boundary eigenstates as

$$|\psi_\lambda\rangle = e^{ik_x x + k_y y} e^{\lambda z} \begin{pmatrix} \psi_1 \\ \psi_2 \end{pmatrix}. \quad (2.16)$$

With this, the Schrödinger equation becomes $\mathcal{H}_{\text{nl}}(k_x, k_y, -i\partial_z)\psi_\lambda = E\psi_\lambda$, and the eigenenergies satisfy the secular equation of

$$\det |\mathcal{H}_{\text{nl}}(k_x, k_y, -i\lambda) - E| = 0, \quad (2.17)$$

where $\mathcal{H}_{\text{nl}}(k_x, k_y, -i\lambda) = \frac{1}{\Lambda}[k_0^2 - (k_x^2 + k_y^2) + b^2\lambda^2]\sigma_3 - iv_z\lambda\sigma_2$. For simplicity, from now on, we denote $\Delta_k = k_0^2 - (k_x^2 + k_y^2)$. From the above secular equation, we can obtain the expression for λ ,

$$\lambda_\alpha^2 = \frac{-(2\Delta_k - v_z^2\Lambda^2) + (-1)^\alpha \sqrt{(2\Delta_k - v_z^2\Lambda^2)^2 - 4(\Delta_k^2 - \Lambda^2 E^2)}}{2}, \quad (2.18)$$

with $\alpha = 1, 2$. Each value of λ can be represented by $\beta\lambda_\alpha$, with $\beta = \pm 1$. Solving the Schrödinger equation

$$\mathcal{H}_{\text{nl}}(k_x, k_y, -i\lambda) \begin{pmatrix} \psi_1 \\ \psi_2 \end{pmatrix} = E \begin{pmatrix} \psi_1 \\ \psi_2 \end{pmatrix}, \quad (2.19)$$

¹To see this, one may move the green integration loop in Fig. 2.1 along the Dirac ring from one Dirac point to the other. This demonstrates that the green loop encloses the two Dirac points with opposite orientations.

the spinor part can be obtained in terms of λ ,

$$\psi_{\alpha\beta} = \begin{pmatrix} v_z \lambda \\ \frac{1}{\Lambda}(\Delta_k + b^2 \lambda^2) - E \end{pmatrix}, \text{ or equivalently } \psi_{\alpha\beta} = \begin{pmatrix} \frac{1}{\Lambda}(\Delta_k + b^2 \lambda^2) + E \\ v_z \lambda \end{pmatrix}. \quad (2.20)$$

Thus the boundary states can be written as the superposition of,

$$|\psi\rangle = e^{ik_x x + k_y y} \sum_{\alpha=1,2,\beta=\pm} C_{\alpha\beta} \psi_{\alpha\beta} e^{\beta \lambda_\alpha z}. \quad (2.21)$$

The coefficient $C_{\alpha\beta}$ and the expression for λ are to be found as follows. With open boundary conditions in z direction, the wavefunction vanishes at $z = -\infty$ and $z = 0$. The former condition requires positive β with $\text{Re } \lambda_\alpha > 0$ (or negative β with $\text{Re } \lambda_\alpha < 0$), so that the wavefunction decays to zero towards negative infinity. The latter condition gives the secular equation

$$\det |\psi_{1+} \quad \psi_{2+}| = 0, \quad (2.22)$$

as two wavefunctions becomes linearly dependent. The two equivalent expressions for $\psi_{\alpha\beta}$ lead to the following two equivalent relations

$$v_z(\lambda_1 - \lambda_2) \left[E - \frac{1}{\Lambda}(\Delta_k - \lambda_1 \lambda_2) \right] = 0, \quad (2.23)$$

$$v_z(\lambda_1 - \lambda_2) \left[E + \frac{1}{\Lambda}(\Delta_k - \lambda_1 \lambda_2) \right] = 0. \quad (2.24)$$

As for non-trivial solutions with $\lambda_1 \neq \lambda_2$, the above two equivalent equations yield,

$$E = 0, \quad (2.25)$$

$$\Delta_k = \lambda_1 \lambda_2. \quad (2.26)$$

Notice the real part of $\lambda_{1,2}$ is required to be positive, $\text{Re } \lambda_\alpha > 0$. From Eq. (2.18), it can be inferred that λ_1 and λ_2 are real or form complex conjugate pairs. Thus, $\lambda_1 \lambda_2 > 0$, and correspondingly

$$\Delta_k = \lambda_1 \lambda_2 = k_0^2 - (k_x^2 + k_y^2) > 0. \quad (2.27)$$

This means that the boundary states are localized inside the ring of $k_x^2 + k_y^2 < k_0^2$. The surface spectrum is finally obtained as

$$E = 0, \quad \text{with } k_x^2 + k_y^2 < k_0^2. \quad (2.28)$$

This is not unexpected, as we have learned from the bulk-boundary correspondence that the drumhead boundary states localized inside the region bounded by the projection of the Dirac nodal ring, as shown in Fig. 2.2 (a).

2.3.2 LDOS from the lattice model

We consider a lattice version of DNLSMs, which is given by $\mathcal{H}_L = \sum_{\mathbf{k}} \Psi_{\mathbf{k}}^\dagger \mathcal{H}_L(\mathbf{k}) \Psi_{\mathbf{k}}$, with $\Psi_{\mathbf{k}} = (c_{p\mathbf{k}}, c_{d\mathbf{k}})^\top$ a two-component spinor describing electrons in p and d orbitals, and [50]

$$\mathcal{H}_L(\mathbf{k}) = [\mu_z - 2t_{\parallel}(\cos k_x + \cos k_y) - 2t_{\perp} \cos k_z] \sigma_3 - 2t'_{\perp} \sin k_z \sigma_2 + m \sigma_1. \quad (2.29)$$

Here, μ_z is an on-site energy, and t_{\parallel} , t_{\perp} , and t'_{\perp} represent intra- and inter-orbital hopping amplitudes on the cubic lattice. Assuming that $0 < (\mu_z - 2t_{\perp})/2t_{\parallel} < 2$ and $m = 0$, Eq. (2.29) describes a single Dirac ring located within the $k_z = 0$ plane. In the low-energy limit, this lattice Hamiltonian returns to the continuum model described in Eq. (2.10).

To investigate the drumhead surface states, we take open boundary conditions in z direction, while in x and y directions, the system is still periodic with translational symmetry. The hybrid Hamiltonian reads,

$$\begin{aligned} \mathcal{H}'_L = & - \sum_{k_x, k_y, z} t_{\perp} (c_{k_x, k_y, z, p}^\dagger c_{k_x, k_y, z+\hat{z}, p} - c_{k_x, k_y, z, d}^\dagger c_{k_x, k_y, z+\hat{z}, d}) + \text{H.c.} \\ & + \sum_{k_x, k_y, z} t'_{\perp} (c_{k_x, k_y, z, p}^\dagger c_{k_x, k_y, z+\hat{z}, d} - c_{k_x, k_y, z, d}^\dagger c_{k_x, k_y, z-\hat{z}, d}) + \text{H.c.} \\ & + \sum_{k_x, k_y, z} [\mu_z - 2t_{\parallel}(\cos k_x + \cos k_y)] (c_{k_x, k_y, z, p}^\dagger c_{k_x, k_y, z, p} - c_{k_x, k_y, z, d}^\dagger c_{k_x, k_y, z, d}), \end{aligned} \quad (2.30)$$

with p and d different orbitals and N_z unit cells in z direction ($1 \leq z \leq N_z$). The Hamiltonian can also be written as $\mathcal{H}'_L = \sum_{k_x, k_y} \Psi_{k_x, k_y}^\dagger \mathcal{H}'_L(k_x, k_y, z) \Psi_{k_x, k_y}$, where $\Psi_{k_x, k_y} = (C_{k_x, k_y, 1}, C_{k_x, k_y, 2}, \dots, C_{k_x, k_y, N_z})^\top$ with the spinor component at z^{th} site $C_{k_x, k_y, z} = (c_{pk_x, k_y, z}, c_{dk_x, k_y, z})^\top$, and

$$\mathcal{H}'_L(k_x, k_y, z) = \begin{pmatrix} H_0 & T^\dagger & & & \\ T & H_0 & T^\dagger & & \\ & \ddots & \ddots & \ddots & \\ & & T & H_0 & T^\dagger \\ & & & T & H_0 \end{pmatrix}_{N_z \times N_z}, \quad (2.31)$$

with $H_0 = [\mu_z - 2t_{\parallel}(\cos k_x + \cos k_y)] \sigma_3$ and $T = it'_{\perp} \sigma_2 - t_{\perp} \sigma_3$. From this Hamiltonian, we can calculate the local density of states at the surface. The local density of states can be obtained in terms of the Green's function,

$$\rho(k_x, k_y, z, \omega) = -\frac{1}{\pi} \lim_{\eta \rightarrow 0^+} \text{tr} G(k_x, k_y, z, \omega + i\eta), \quad (2.32)$$

with the expression of the Green's function,

$$G(k_x, k_y, z, \omega + i\eta) = \frac{1}{\omega - \mathcal{H}'_L(k_x, k_y, z) + i\eta}. \quad (2.33)$$

However, such a form of local density of states is not directly applicable for numerical evaluations.

Instead, we use the following expression of local density of states,

$$\rho(k_x, k_y, z, \omega) = -\frac{1}{\pi} \frac{1}{N} \text{Im} \sum_n \frac{\psi_n^\dagger(k_x, k_y, z) \psi_n(k_x, k_y, z)}{\omega - E_n(k_x, k_y, z) + i\Gamma/N}, \quad (2.34)$$

with N the normalization factor with respect to the number of lattice sites, which is equal to $2N_z$. Here $E_n(k_x, k_y, z)$ represents the n th eigenenergy and $\psi_n(k_x, k_y, z)$ the z th spinor component of the corresponding eigenstates. In numerical evaluations for real materials, several approximations are made as follows. (i) Since far away from the Fermi surface, the states only contribute to a tiny fraction to the local density of states, the summation over n is restricted to the N_{eigen} states that are closest to the Fermi surface; (ii) To take into account broadening effects due to disorder and finite temperature, we replace η in Eq. (2.32) with Γ/N . (iii) In the actual ARPES measurements, the electron can penetrate into several unit cells from the sample surface. Thus the local density of states of the first N_{edge} unit cells are summarized. The parameters and the corresponding local density of states at the boundary are given in Fig. 2.2 (b), from which the Drumhead surface states are clearly visible.

2.4 Parity anomaly

In Eq. (2.15), we have shown that at the $(2+1)$ -dimensional subsystem of the $(3+1)$ -dimensional DNLSM, the low-energy physics of a single Dirac point in a given subsystem can be described by an effective action of $(2+1)$ -dimensional massless Dirac fields. It is however impossible to quantize this classical action without breaking the spacetime inversion symmetry, i.e., \mathcal{PT} symmetry is broken by the regularization of the quantum theory. To see this, let us first review the parity anomaly in $(2+1)$ -dimensional massless Dirac fields in the subsection below.

2.4.1 Parity anomaly of $(2+1)$ -dimensional massless Dirac fields

The generating functional for the $(2+1)$ -dimensional Dirac fields is [36]

$$Z = \int D\psi \int D\bar{\psi} e^{iS(\psi, \bar{\psi})} = \int D\psi \int D\bar{\psi} e^{i\bar{\psi}(i\cancel{\partial} + \cancel{A} + m)\psi}, \quad (2.35)$$

with $\cancel{\partial} = \gamma^\mu \partial_\mu$ and $\cancel{A} = \gamma^\mu A_\mu$. The above action describes massless Dirac fields when $m = 0$. The integration variables ψ and $\bar{\psi}$ are Grassmann-valued Dirac spinors. Based on the property of Grassmann numbers (η), the rule for Grassmann integration can be defined:

$$\int d\eta = 0, \text{ and } \int d\eta \eta = 1. \quad (2.36)$$

Let η and $\bar{\eta}$ be two independent numbers and a an ordinary number. Based on above two rules, the Grassmannian analog of the Gaussian integral gives,

$$\int d\eta \int d\bar{\eta} e^{\bar{\eta} a \eta} = \int d\eta \int d\bar{\eta} (1 + \bar{\eta} a \eta) = \int d\eta a \eta = a = e^{+\log a}. \quad (2.37)$$

Generalizing this to N Grassmann numbers by letting $\eta = (\eta_1, \eta_2, \dots, \eta_N)$ and similarly for $\bar{\eta}$, the integration gives,

$$\int d\eta \int d\bar{\eta} e^{\bar{\eta} a \eta} = \det a. \quad (2.38)$$

Returning to the generating function Z , by integrating out the spinor field ψ and $\bar{\psi}$, we can obtain,

$$Z = \int D\psi \int D\bar{\psi} e^{\bar{\psi} i(\not{\partial} + \not{A} + m)\psi} = N \det i(\not{\partial} + \not{A} + m) = N e^{i \text{tr} \log (i\not{\partial} + \not{A} + m)}, \quad (2.39)$$

with N a factor after integration, where we have used the relation $\det A = e^{\text{tr} \log A}$ for a matrix A . Denote $Z = e^{iS_{\text{eff}}}$, the effective action is given by

$$S_{\text{eff}}[A, m] = \text{tr} \log (i\not{\partial} + \not{A} + m). \quad (2.40)$$

Due to ultra-violet divergences, for the massless case of $m = 0$, this effective action needs to be regularized. The regularization can be achieved by Pauli-Villars method,

$$S_{\text{eff}}^{\text{reg}}[A] = S_{\text{eff}}[A, 0] - \lim_{M \rightarrow \infty} S_{\text{eff}}[A, M]. \quad (2.41)$$

In the limit of $M \rightarrow \infty$, the Pauli-Villars term $M\psi\bar{\psi}$ will lead to a Chern-Simons term, as shown in the following.

We focus on the effective action $S_{\text{eff}}[A, M] = \text{tr} \log (i\not{\partial} + M) + \text{tr} \log (1 + \frac{\not{A}}{i\not{\partial} + M})$. It can be computed by the perturbation method as

$$S_{\text{eff}}[A, M] = \text{tr} \log (i\not{\partial} + M) + \text{tr} \frac{\not{A}}{i\not{\partial} + M} - \frac{1}{2} \text{tr} \frac{\not{A}}{i\not{\partial} + M} \frac{\not{A}}{i\not{\partial} + M} + \dots \quad (2.42)$$

The quadratic term contributes to the Chern-Simons term, which corresponds to a one loop correction of Feynman diagram. Denote this term as $S_{\text{eff}}^{[2]}[A, M]$, the full form is

$$\begin{aligned} S_{\text{eff}}^{[2]}[A, M] &= \int \frac{d^3 p}{(2\pi)^3} \int \frac{d^3 k}{(2\pi)^3} \text{tr} \left[\frac{1}{(\not{p} - \not{k}) + M} A_\rho \gamma^\rho \frac{1}{\not{k} + M} A_\mu \gamma^\mu \right] \\ &= \int \frac{d^3 p}{(2\pi)^3} A_\mu \Pi^{\mu\rho} A_\rho, \end{aligned} \quad (2.43)$$

with,

$$\Pi^{\mu\rho} = \int \frac{d^3 k}{(2\pi)^3} \text{tr} \left[\gamma^\mu \frac{(\not{p} - \not{k}) + M}{(p - k)^2 - M^2} \gamma^\rho \frac{\not{k} - M}{k^2 - M^2} \right]. \quad (2.44)$$

In 2 + 1 dimension space, γ are just Pauli matrices, and we have the trace relation,

$$\text{tr}(\gamma^\mu \gamma^\nu \gamma^\rho) = -2\varepsilon^{\mu\nu\rho}, \quad (2.45)$$

with $\varepsilon^{\mu\nu\rho}$ the Levi-Civita tensor. We can extract the term that contains the Levi-Civita tensor

$$\Pi_{\text{odd}}^{\mu\nu} = 2M\varepsilon^{\mu\nu\rho} p_\rho \int \frac{d^3 k}{(2\pi)^3} \frac{1}{(p - k)^2 - M^2} \frac{1}{k^2 - M^2}. \quad (2.46)$$

The wick rotation of $k_0 \rightarrow ik_0$ leads to $k^2 = k_0^2 - \vec{k}^2 \rightarrow -k_E^2 = -(k_0^2 + \vec{k}^2)$. Here \vec{k} denotes the spatial momenta. Consider p to be a small quantity, i.e., $p \rightarrow 0$, the integration can be evaluated as

$$\int \frac{d^3k}{(2\pi)^3} \frac{1}{(p-k)^2 - M^2} \frac{1}{k^2 - M^2} = \int_0^\infty \frac{4\pi k_E^2 dk_E}{(2\pi)^3} \frac{1}{(k_E^2 + M^2)^2} = \frac{1}{8\pi|M|}. \quad (2.47)$$

Keeping only the terms proportional to Levi-Civita tensor, the effective action from the quadratic term then becomes [74, 75] ,

$$S_{\text{CS}}[A, M] = \frac{1}{4\pi} \frac{M}{|M|} \int \frac{d^3x}{(2\pi)^3} \varepsilon^{\mu\nu\rho} A_\mu \partial_\nu A_\rho, \quad (2.48)$$

where we have replaced p_ρ with $-i\partial_\rho$ in real space. This is called the Chern-Simons term which emerges from the one loop correction. In the limit of $M \rightarrow \infty$, the higher order terms $\mathcal{O}(\frac{1}{M})$ will vanish. Thus, with the Pauli-Villars regularization, the regulated massless Fermion action is

$$S_{\text{eff}}^{\text{reg}}[A] = S_{\text{eff}}[A, 0] + \frac{1}{4\pi} \frac{M}{|M|} \int \frac{d^3x}{(2\pi)^3} \varepsilon^{\mu\nu\rho} A_\mu \partial_\nu A_\rho. \quad (2.49)$$

We now focus on the properties of the Chern-Simons term. As the Pauli-Villars Lagrangian is gauge invariant, the Chern-Simons term that arises from it must also be gauge invariant. This can be seen by direct verification. Under a gauge transformation $A_\mu \rightarrow A_\mu + \partial_\mu \omega$, Eq. (2.48) becomes

$$S_{\text{CS}}[A, M] \rightarrow S_{\text{CS}}[A, M] + \frac{1}{4\pi} \frac{M}{|M|} \int \frac{d^3x}{(2\pi)^3} \partial_\mu \left(\omega \varepsilon^{\mu\nu\rho} \partial_\nu A_\rho \right). \quad (2.50)$$

The gauge transformation leads to a total derivative in the Chern-Simons term, which vanishes in most situations after integration. Thus, the Chern-Simons term is gauge invariant.

However, the Chern-Simons term breaks both parity and time-reversal symmetry. We should emphasize here that parity operation in Eq. (2.1) is defined for odd spatial dimensions. For even spatial dimensions, to which (2+1)-dimensional spacetime belongs, the inversion (parity) is simply a rotation. Thus, the parity operation is defined as [23],

$$x_0 \rightarrow x^0, \quad x^1 \rightarrow -x^1, \quad x^2 \rightarrow x^2. \quad (2.51)$$

Correspondingly, the vector potential changes as $A_0 \rightarrow A_0$, $A_1 \rightarrow -A_1$ and $A_2 \rightarrow A_2$. Hence, under the parity operation, the integrand changes as

$$\varepsilon^{\mu\nu\rho} A_\mu \partial_\nu A_\rho \rightarrow -\varepsilon^{\mu\nu\rho} A_\mu \partial_\nu A_\rho. \quad (2.52)$$

As the measure $\int d^3x$ is invariant under parity, the Chern-Simons term effectively breaks the parity symmetry. A similar argument can be done for the time-reversal symmetry, as under the time-reversal operation, $(x_0, x_1, x_2) \rightarrow (-x_0, x_1, x_2)$ and $(A_0, A_1, A_2) \rightarrow (-A_0, A_1, A_2)$.

2.4.2 Parity anomaly of (3 + 1)-dimensional DNLSMs

We now return to the (3+1)-dimensional DNLSM system with the effective action of Eq. (2.15). With a similar regularization procedure for each (2+1)-dimensional subsystem labeled by ϕ , the Chern-Simons

term reads,

$$S_{\text{CS}}^{\phi} = \eta \frac{e^2}{4\pi} \int d^3x \epsilon^{\mu\nu\lambda} A_{\mu} \partial_{\nu} A_{\lambda}, \quad (2.53)$$

where $\eta = \pm 1$ is the sign of the Dirac point Berry phase. As discussed in Eq. (2.12), the Berry phase η is equal to the topological charge ν (up to a sign convention). It should be noted that since the Chern-Simons term is proportional to the anti-symmetric Levi-Civita symbol, strictly speaking, the parity anomaly occurs only in (2+1) dimensions. With the special configuration of the DNLSMs, it now can also appear in (3+1)-dimensional spacetime.

From the modern condensed matter viewpoint, the parity anomaly is attributed to the \mathbb{Z}_2 topological charge ν of the \mathcal{PT} -symmetric Dirac point. That is, because of the topological obstruction from the nontrivial topological charge, there exists no \mathcal{PT} -symmetric lattice ultraviolet regularization for a single (2+1)-dimensional Dirac point. I.e., any lattice regularization has to involve an *even* number of nontrivial Dirac points, since the sum over all topological charges in the BZ torus must be zero. This is consistent with the \mathbb{Z}_2 nature of the parity anomaly, since a doublet of (2+1)-dimensional Dirac points coupled to gauge fields can be quantized without breaking \mathcal{PT} symmetry.

Next we discuss the anomalous transport phenomena that are associated with the parity anomaly. Varying the Chern-Simons term (2.53) with respect to the electromagnetic gauge field A_{μ} yields the anomalous transverse current

$$j_{\text{t},\phi}^{\mu} = \eta \frac{e^2}{4\pi} \epsilon^{\mu\nu\lambda} \partial_{\nu} A_{\lambda} \quad (2.54)$$

for a single Dirac cone in a given (2+1)-dimensional subsystem. Thus, electromagnetic fields projected onto a two-dimensional subsystem induce a topological current, which flows perpendicular to the applied field. Since the energy bands of DNLSMs are, to a first approximation, nondispersive along the ϕ direction, one might expect that the electromagnetic response of DNLSMs in the presence of a small \mathcal{PT} breaking term is dominated by this topological current. However, for each two-dimensional subsystem there are two Dirac points that contribute to the transverse current with opposite signs $\eta = \pm 1$. Since these two contributions cancel out to zero, the topological current can only be measured by a device that filters electrons based on their momenta.

In practice, the modern semiclassical response theory is usually adopted for calculation of the anomalous transverse current in condensed matter systems. In the following section, we review the basic concept of the semiclassical response theory.

2.5 Topological current

In this section, we calculate the topological current from the semiclassical response theory. As we will see, the transverse topological current comes from the Berry curvature. We first review the basics of modern semiclassical response theory. Then we compute the Berry curvature from the low-energy effective model of Eq. (2.10), where we find that the Berry curvature is singular on the nodal line without the mass term. After obtaining the Berry curvature, we will calculate the topological current by taking into account the energy dispersion of the DNLSMs.

2.5.1 Semiclassical response theory

In the semiclassical response theory, the electrons are described by wave packets. The Bloch wave functions are $|\psi_{n\mathbf{k}}(r)\rangle = e^{-i\mathbf{k}\cdot\mathbf{r}}|u_{n\mathbf{k}}\rangle$ with n the band index, where $|u_{n\mathbf{k}}\rangle$ has the periodicity of the lattice. We assume that there are no transitions between different bands, which is justified if the bands are separated from each other by a finite gap. In three dimensional space, the wave packet is defined by [84]

$$|w\rangle = \int d^3\mathbf{k} a(\mathbf{k}, t) |\psi_{\mathbf{k}}(t)\rangle, \quad (2.55)$$

with $a(\mathbf{k}, t) = |a(\mathbf{k}, t)|e^{-i\gamma(\mathbf{k}, t)}$. The normalization condition requires $\int d^3\mathbf{k} |a(\mathbf{k}, t)|^2 = 1$, where we have used the relation $\langle \psi_{\mathbf{k}}(t) | \psi_{\mathbf{k}'}(t) \rangle = \delta(\mathbf{k} - \mathbf{k}')$. We comment here the explicit form of distribution function $a(\mathbf{k}, t)$ is never needed. Whenever we have to integrate some quantity, for instance $\int d^3\mathbf{k} |a(\mathbf{k}, t)|^2 A(\mathbf{k})$, we replace $A(\mathbf{k})$ by its value at the center of the wave packet \mathbf{k}_c . Thus the mean wave vector reads

$$\int d^3\mathbf{k} |a(\mathbf{k}, t)|^2 \mathbf{k} = \mathbf{k}_c. \quad (2.56)$$

These wave packets obey the semiclassical equations of motion, which describes the motion of electrons under collisions.

The mean position is

$$\mathbf{r}_c = \langle w | \hat{\mathbf{r}} | w \rangle = \int d^3\mathbf{k} \int d^3\mathbf{k}' a(\mathbf{k}, t)^* \langle \psi_{\mathbf{k}} | \hat{\mathbf{r}} a(\mathbf{k}', t) | \psi_{\mathbf{k}'} \rangle. \quad (2.57)$$

Plugging in the expression for $a(\mathbf{k}, t)$ and $|\psi_{\mathbf{k}}\rangle$, we have

$$\mathbf{r}_c = \int d^3\mathbf{k} |a(\mathbf{k}, t)|^2 [\partial_{\mathbf{k}}\gamma(\mathbf{k}, t) + \langle u_{\mathbf{k}} | i\partial_{\mathbf{k}} | u_{\mathbf{k}} \rangle]. \quad (2.58)$$

Integrating out the distribution function, the expectation value of \mathbf{r} is

$$\mathbf{r}_c = \partial_{\mathbf{k}_c}\gamma_c + \langle u_{\mathbf{k}_c} | i\partial_{\mathbf{k}_c} | u_{\mathbf{k}_c} \rangle. \quad (2.59)$$

with $\gamma_c = \gamma(\mathbf{k}_c, t)$. Our task now is to obtain the dynamics of \mathbf{r}_c , i.e., the velocity of the wave packet.

In principle, the dynamics of \mathbf{r}_c can be derived from calculating the Schrödinger equation for the wave packet. A more convenient approach is to start from the Lagrangian, and use a time-dependent variational principle to obtain the dynamics. The Lagrangian for the wave packet is given by,

$$\mathcal{L} = \langle w | i \frac{d}{dt} - \hat{H} | w \rangle. \quad (2.60)$$

With the Euler-Lagrange equation, the Schrödinger equation for the wave packet can be reproduced. \hbar here is set to 1. The Lagrangian is a function of t and $\mathbf{r}_c, \mathbf{k}_c$ with their derivatives,

$$\mathcal{L} = \mathcal{L}(\mathbf{r}_c, \dot{\mathbf{r}}_c, \mathbf{k}_c, \dot{\mathbf{k}}_c, t). \quad (2.61)$$

We first evaluate the time-derivative term $\langle w | i \frac{d}{dt} | w \rangle$. Here $\frac{d}{dt}$ is a total derivative that also depends on

\mathbf{r} (as $|u_{n\mathbf{k}}\rangle = e^{i\mathbf{k}\cdot\mathbf{r}}|\psi_{n\mathbf{k}}(r)\rangle$, the total derivative does not depend on \mathbf{k} directly), and explicitly it is

$$\frac{d}{dt} = \partial_t + \dot{\mathbf{r}} \cdot \partial_{\mathbf{r}}, \quad (2.62)$$

where \mathbf{r} becomes \mathbf{r}_c after integration with the distribution function. Notice that the partial time derivative term yields

$$\langle w|i\partial_t|w\rangle = \partial_t\gamma_c + \langle u_{\mathbf{k}_c}|i\partial_t|u_{\mathbf{k}_c}\rangle, \quad (2.63)$$

as the normalization of $\int d^3\mathbf{k}|a(\mathbf{k}, t)|^2 = 1$ leads to the vanish of the remaining term $\int d^3\mathbf{k}|a(\mathbf{k}, t)|\partial_t|a(\mathbf{k}, t)| = 0$. Since $\gamma_c = \gamma(\mathbf{k}_c, t)$, which means γ_c depends explicitly on \mathbf{k}_c and t , we can do the following replacement,

$$\partial_t\gamma_c = \frac{d\gamma_c}{dt} - \dot{\mathbf{k}}_c \cdot \partial_{\mathbf{k}_c}\gamma_c. \quad (2.64)$$

Plug the expression of $\partial_t\gamma_c$ in the relation Eq. (2.59),

$$\partial_t\gamma_c = \frac{d\gamma_c}{dt} - \dot{\mathbf{k}}_c \cdot \mathbf{r}_c + \dot{\mathbf{k}}_c \cdot \langle u_{\mathbf{k}_c}|i\partial_{\mathbf{k}_c}|u_{\mathbf{k}_c}\rangle. \quad (2.65)$$

Thus, we finally get

$$\langle w|i\frac{d}{dt}|w\rangle = \frac{d\gamma_c}{dt} - \dot{\mathbf{k}}_c \cdot \mathbf{r}_c + \dot{\mathbf{k}}_c \cdot \langle u_{\mathbf{k}_c}|i\partial_{\mathbf{k}_c}|u_{\mathbf{k}_c}\rangle + \dot{\mathbf{r}}_c \cdot \langle u_{\mathbf{k}_c}|i\partial_{\mathbf{r}_c}|u_{\mathbf{r}_c}\rangle + \langle u_{\mathbf{k}_c}|i\partial_t|u_{\mathbf{k}_c}\rangle. \quad (2.66)$$

The expectation value of the Hamiltonian $\langle w|\hat{H}|w\rangle$, which gives the wave packet energy, may be evaluated up to first order $\hat{H} = \hat{H}_c + \Delta\hat{H}$, with $\Delta\hat{H}$ change in first order. By ignoring the gradients in the Hamiltonian, the expectation value of the Hamiltonian is

$$\langle w|\hat{H}|w\rangle \approx \langle w|\hat{H}_c|w\rangle = \varepsilon_c. \quad (2.67)$$

Thus, the general expression for the Lagrangian is

$$\mathcal{L} = -\varepsilon_c + \frac{d\gamma_c}{dt} - \dot{\mathbf{k}}_c \cdot \mathbf{r}_c + \dot{\mathbf{k}}_c \cdot \langle u_{\mathbf{k}_c}|i\partial_{\mathbf{k}_c}|u_{\mathbf{k}_c}\rangle + \dot{\mathbf{r}}_c \cdot \langle u_{\mathbf{k}_c}|i\partial_{\mathbf{r}_c}|u_{\mathbf{r}_c}\rangle + \langle u_{\mathbf{k}_c}|i\partial_t|u_{\mathbf{k}_c}\rangle. \quad (2.68)$$

We can further do the simplification of

$$\frac{d\gamma_c}{dt} - \dot{\mathbf{k}}_c \cdot \mathbf{r}_c = \frac{d\gamma_c}{dt} - \frac{d}{dt}(\mathbf{k}_c \cdot \mathbf{r}_c) + \dot{\mathbf{r}}_c \cdot \mathbf{k}_c. \quad (2.69)$$

The total derivatives can be neglected as they only contribute a constant in time to the action $S = \int \mathcal{L}dt$ after integration. Notice in Eq. (2.68), the last three terms actually give the term $\langle u_{\mathbf{k}_c}|i\frac{d}{dt}|u_{\mathbf{k}_c}\rangle$. The final Lagrangian is of a simple form,

$$\mathcal{L} = -\varepsilon_c + \dot{\mathbf{r}}_c \cdot \mathbf{k}_c + \langle u_{\mathbf{k}_c}|i\frac{d}{dt}|u_{\mathbf{k}_c}\rangle. \quad (2.70)$$

It is natural to ask how the system responds to external perturbations. In the following, we turn to consider the response of the system to an external electromagnetic field, denoted by the gauge potential

$(\mathbf{A}(\mathbf{r}, t), \phi(\mathbf{r}, t))$. The local Hamiltonian is modified as

$$\hat{H}(\mathbf{k}) \rightarrow \hat{H}(\mathbf{k} + e\mathbf{A}(\mathbf{r}, t)) - e\phi(\mathbf{r}, t). \quad (2.71)$$

Notice here we again set $\hbar = 1$. Under the gauge potential, the eigenenergy is modified as

$$\varepsilon_c \rightarrow \varepsilon_c - e\phi(\mathbf{r}_c, t), \quad (2.72)$$

and the crystal momentum \mathbf{k} is also modified to $\mathbf{k} + e\mathbf{A}(\mathbf{r}, t)$, hence the eigenstates become $|u_{\mathbf{k}+e\mathbf{A}(\mathbf{r}, t)}\rangle$. It is noted that now the crystal momentum \mathbf{k} carries all the dynamics as it actually equals to $\mathbf{k} + e\mathbf{A}(\mathbf{r}, t)$. Thus, the last term in Eq (2.70) is simplified to $\dot{\mathbf{k}}_c \cdot \langle u_{\mathbf{k}_c} | \partial_{\mathbf{k}_c} | u_{\mathbf{k}_c} \rangle$. Finally, the Lagrangian takes the form

$$\mathcal{L} = -\varepsilon_c + e\phi(\mathbf{r}_c, t) + \dot{\mathbf{r}}_c \cdot \mathbf{k}_c - e\dot{\mathbf{r}}_c \cdot \mathbf{A}(\mathbf{r}_c, t) + \dot{\mathbf{k}}_c \cdot \langle u_{\mathbf{k}_c} | \partial_{\mathbf{k}_c} | u_{\mathbf{k}_c} \rangle. \quad (2.73)$$

For the evaluation of the dynamics $\dot{\mathbf{r}}_c$ and $\dot{\mathbf{k}}_c$ of the wave packets, we can adopt the Euler-Lagrange equations, $\frac{d}{dt} \frac{\partial \mathcal{L}}{\partial \dot{\mathbf{r}}_c} = \frac{\partial \mathcal{L}}{\partial \mathbf{r}_c}$, and $\frac{d}{dt} \frac{\partial \mathcal{L}}{\partial \dot{\mathbf{k}}_c} = \frac{\partial \mathcal{L}}{\partial \mathbf{k}_c}$. With the Lagrangian in Eq. (2.73), we can obtain the semiclassical equations of motion,

$$\dot{\mathbf{r}}_c = \frac{\partial \varepsilon_c}{\partial \mathbf{k}_c} - \dot{\mathbf{k}}_c \times \boldsymbol{\Omega}, \quad (2.74)$$

$$\dot{\mathbf{k}}_c = -e\mathbf{E} - e\dot{\mathbf{r}}_c \times \mathbf{B}, \quad (2.75)$$

with \mathbf{E} the electric field and \mathbf{B} the magnetic field. $\boldsymbol{\Omega}$ is actually the Berry curvature,

$$\boldsymbol{\Omega} = i\nabla_{\mathbf{k}_c} \times \langle u_{\mathbf{k}_c} | \partial_{\mathbf{k}_c} | u_{\mathbf{k}_c} \rangle. \quad (2.76)$$

In the absence of the magnetic field, the velocity of the packet is

$$\dot{\mathbf{r}}_c = \frac{\partial \varepsilon_c}{\partial \mathbf{k}_c} + e\mathbf{E} \times \boldsymbol{\Omega}. \quad (2.77)$$

Thus, from the semiclassical theory, the current is given by

$$\mathbf{j} = \int \frac{d^3\mathbf{k}}{(2\pi)^3} f(\mathbf{k}) \left(e \frac{\partial \varepsilon}{\partial \mathbf{k}} + \frac{e^2}{\hbar} \mathbf{E} \times \boldsymbol{\Omega} \right), \quad (2.78)$$

after we have recovered the constant \hbar and denote \mathbf{k}_c as \mathbf{k} as the integration goes over the entire Brillouin zone. Notice that in drastic difference with the first term at the RHS, the second term can result in current that is transverse to the electric field direction. We denote this anomalous transverse current as

$$\mathbf{j}_t = \frac{e^2}{\hbar} \int \frac{d^3\mathbf{k}}{(2\pi)^3} f(\mathbf{k}) \mathbf{E} \times \boldsymbol{\Omega}, \quad (2.79)$$

where $f(\mathbf{k})$ is the Fermi-Dirac distribution function and \mathbf{E} the electric field.

2.5.2 Berry curvature in DNLSMs

From the expression of the anomalous transverse current in Eq. (2.79), the Berry curvature is the key in obtaining the topological current. In DNLSMs, the Berry curvature is given in terms of the Berry

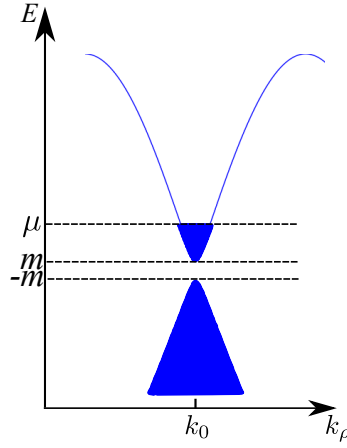


Figure 2.3: Energy dispersion $E_{\pm}(\mathbf{k})$ close to the Dirac ring as a function of the radial coordinate k_{ρ} . The chemical potential μ is in the conduction band, slightly above the gap energy m .

connection $\hat{\mathbf{A}}_{\alpha\beta}(\mathbf{k}) = \langle \alpha, \mathbf{k} | i\nabla_{\mathbf{k}} | \beta, \mathbf{k} \rangle$ by

$$\boldsymbol{\Omega}_{\alpha}(\mathbf{k}) = \nabla_{\mathbf{k}} \times \hat{\mathbf{A}}_{\alpha\alpha}(\mathbf{k}), \quad (2.80)$$

where $|\alpha, \mathbf{k}\rangle$ are the Bloch eigenstates of the continuum model of a DNLSM described in Eq. (2.10). The positive and negative energy eigenstates of $\mathcal{H}(\mathbf{k})$ are calculated as

$$|-, \mathbf{k}\rangle = \frac{1}{\sqrt{N_-}} \begin{pmatrix} \frac{1}{\Lambda} (k_0^2 - k_{\rho}^2 - b^2 k_z^2) - \lambda \\ m + i v_z k_z \end{pmatrix}, \quad (2.81a)$$

$$|+, \mathbf{k}\rangle = \frac{1}{\sqrt{N_+}} \begin{pmatrix} \frac{1}{\Lambda} (k_0^2 - k_{\rho}^2 - b^2 k_z^2) + \lambda \\ m + i v_z k_z \end{pmatrix}, \quad (2.81b)$$

with the eigenenergies

$$E_{\pm} = \pm\lambda = \pm\sqrt{\frac{1}{\Lambda^2} (k_0^2 - k_{\rho}^2 - b^2 k_z^2)^2 + v_z^2 k_z^2 + m^2}. \quad (2.81c)$$

Here we have used the short hand notation $k_{\rho}^2 = k_x^2 + k_y^2$ and $N_{\pm} = 2\lambda \left[\lambda \pm \frac{1}{\Lambda} (k_0^2 - k_{\rho}^2 - b^2 k_z^2) \right]$. The Berry connection of the conduction band $|+, \mathbf{k}\rangle$ is given by

$$\mathcal{A}_{++}^z(\mathbf{k}) = \frac{m v_z \left[\frac{1}{\Lambda} (k_0^2 - k_{\rho}^2 - b^2 k_z^2) - \lambda \right]}{2\lambda (v_z^2 k_z^2 + m^2)}, \quad (2.82a)$$

while $\mathcal{A}_{++}^x(\mathbf{k}) = \mathcal{A}_{++}^y(\mathbf{k}) = 0$. Similarly, for the valence band $|-, \mathbf{k}\rangle$ the Berry connection takes the form

$$\mathcal{A}_{--}^z(\mathbf{k}) = -\frac{mv_z \left[\frac{1}{\Lambda}(k_0^2 - k_\rho^2 - b^2 k_z^2) + \lambda \right]}{2\lambda(v_z^2 k_z^2 + m^2)}, \quad (2.82b)$$

while $\mathcal{A}_{--}^x(\mathbf{k}) = \mathcal{A}_{--}^y(\mathbf{k}) = 0$. Using the Berry connection (2.82), the topological charge of the Dirac ring of $\mathcal{H}(\mathbf{k})$ can also be computed.

From Eq. (2.82) we now compute the Berry curvature using Eq. (2.80)

$$\Omega_+^x(\mathbf{k}) = \frac{-mv_z k_y / \Lambda}{\left[\frac{1}{\Lambda^2}(k_0^2 - k_\rho^2 - b^2 k_z^2)^2 + v_z^2 k_z^2 + m^2 \right]^{\frac{3}{2}}}, \quad (2.83a)$$

$$\Omega_+^y(\mathbf{k}) = \frac{mv_z k_x / \Lambda}{\left[\frac{1}{\Lambda^2}(k_0^2 - k_\rho^2 - b^2 k_z^2)^2 + v_z^2 k_z^2 + m^2 \right]^{\frac{3}{2}}}, \quad (2.83b)$$

and $\Omega_+^z(\mathbf{k}) = 0$. Using cylindrical coordinates $\{k_\rho, \phi, k_z\}$ and Eq. (2.81c) the Berry curvature can be written in a more compact form

$$\mathbf{\Omega}(\mathbf{k}) = \frac{mv_z k_\rho / \Lambda}{\lambda^3} \hat{\mathbf{e}}_\phi, \quad (2.83c)$$

with the unit vector $\hat{\mathbf{e}}_\phi = (-\sin \phi, \cos \phi, 0)^T$. We observe from the above expressions that the Berry curvature is peaked at $(q_\rho, k_z) = (0, 0)$, where $q_\rho = k_\rho - k_0$ is the radial distance from the Dirac ring. If we neglect terms of order q_ρ^3 and k_z^2 , the Berry curvature simplifies to

$$\mathbf{\Omega}(\mathbf{k}) = \frac{mv_z k_\rho / \Lambda}{\left[\left(\frac{2k_0}{\Lambda} q_\rho \right)^2 + v_z^2 k_z^2 + m^2 \right]^{\frac{3}{2}}} \hat{\mathbf{e}}_\phi + \mathcal{O}[q_\rho^3, k_z^2]. \quad (2.84)$$

Notice that as $m \rightarrow 0$, the Berry curvature becomes singular on the Dirac nodal line, which is $\mathbf{\Omega}(\mathbf{k}) = \pi \delta(k_\rho - k_0) \delta(k_z) \hat{\mathbf{e}}_\phi$. We will use this expression to compute the transverse Hall current.

2.5.3 Transverse Hall current

The transverse Hall current is given by Eq. (2.79). To compute the transverse current \mathbf{j}_t we assume that the chemical potential $E_F = \mu$ lies within the conduction band, slightly above the gap energy m , i.e., $\mu > m$, see Fig. 2.3. Hence, at zero temperature $T = 0$ the integral in Eq. (2.79) is over states with energies E that lie within the interval $m < E < \mu$. In the vicinity of the Dirac ring the energy dispersion of the conduction band, Eq. (2.81c), can be approximated by

$$E_+(q_\rho, k_z) \simeq \sqrt{\left(\frac{2k_0}{\Lambda} q_\rho \right)^2 + v_z^2 k_z^2 + m^2}, \quad (2.85)$$

where we have neglected terms of order q_ρ^3 and k_z^2 .

Let us now compute the transverse current contributed by states with momentum angle ϕ by per-

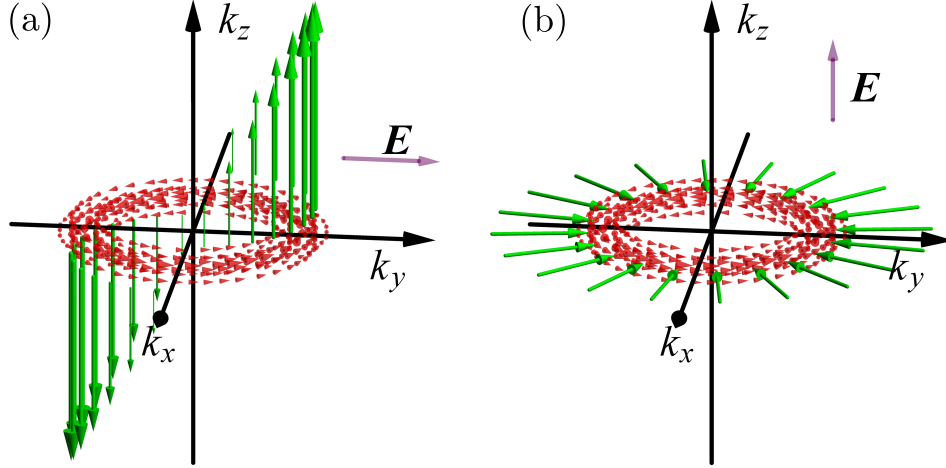


Figure 2.4: Topological currents in a Dirac nodal-line semimetal. The red arrows indicate the Berry curvature $\mathbf{\Omega}(\mathbf{k})$, Eq. (2.84), in the presence of a small PT breaking mass term $m\sigma_1$. The green arrows represent the transverse topological current $\mathbf{j}_{t,\phi}$, Eq. (2.91), that is induced by an external electric field applied along (a) the y direction and (b) the z direction.

forming the integral in Eq. (2.79) over the two cylindrical coordinates k_ρ and k_z

$$\mathbf{j}_{t,\phi} = s \frac{e^2}{\hbar} \int_{m < E_+ < \mu} \frac{dk_\rho dk_z k_\rho}{(2\pi)^3} \mathbf{E} \times \mathbf{\Omega}(\mathbf{k}) = \frac{e^2}{\hbar} I(\mu) \mathbf{E} \times \hat{\mathbf{e}}_\phi.$$

Using Eq. (2.84) the integral $I(\mu)$ can be expressed as

$$I(\mu) = \int_{m < E_+ < \mu} \frac{dq_\rho dk_z}{(2\pi)^3} \frac{mv_z k_\rho^2 / \Lambda}{\left[\left(\frac{2k_0}{\Lambda} q_\rho \right)^2 + v_z^2 k_z^2 + m^2 \right]^{\frac{3}{2}}}. \quad (2.86)$$

With the substitutions $\tilde{q} = (2k_0/\Lambda)q_\rho$ and $\tilde{k} = v_z k_z$ we obtain

$$I(\mu) = \int_{\tilde{q}^2 + \tilde{k}^2 < \mu^2 - m^2} \frac{d\tilde{q} d\tilde{k} \frac{m}{2k_0} \left(\frac{\Lambda}{2k_0} \tilde{q} + k_0 \right)^2}{(2\pi)^3 \left[\tilde{q}^2 + \tilde{k}^2 + m^2 \right]^{\frac{3}{2}}} \quad (2.87)$$

$$= \frac{k_0}{8\pi^2} \left[1 - \frac{m}{\mu} \left(1 - \frac{\Lambda^2 \mu^2}{8k_0^4} \right) \right] + \mathcal{O}[m^2], \quad (2.88)$$

where we have neglected terms of order m^2 . The second term in the round brackets of Eq. (2.88) can be rewritten in terms of the Fermi wave vector $\mathbf{k}_F = (q_{F,\rho}, k_{F,z})$, which is related to the chemical potential

by [cf. Eq. (2.85)]

$$\mu^2 = \frac{4k_0^2}{\Lambda^2} q_{F\rho}^2 + v_z^2 k_{Fz}^2 + m^2. \quad (2.89)$$

We have

$$\frac{\Lambda^2 \mu^2}{8k_0^4} = \frac{q_{F\rho}^2}{2k_0^2} + \Lambda^2 v_z^2 \frac{k_{Fz}^2}{k_0^4} + \frac{\Lambda^2 m^2}{8k_0^4}. \quad (2.90)$$

Since $q_{F\rho} \ll k_0$ and $k_{Fz} \ll k_0$, it follows that the first two terms in Eq. (2.90) are small and the third term is of order m^2 . Hence, we find the following approximate form for the ϕ -dependent transverse current

$$\mathbf{j}_{t,\phi} \simeq \frac{e^2}{\hbar} \frac{k_0}{8\pi^2} \left(1 - \frac{m}{\mu} \right) \mathbf{E} \times \hat{\mathbf{e}}_\phi + \mathcal{O}[m^2]. \quad (2.91)$$

Interestingly, when the chemical potential μ is bigger than the gap energy m , the transverse current $\mathbf{j}_{t,\phi}$ is dominated by the first term, which originates from the parity anomaly. Indeed, the first term of Eq. (2.91) is consistent with Eq. (2.54) as it differs only by the differential element $(k_0/2\pi)d\phi$ of the cylindrical coordinate system. Figure 2.4 displays the distribution of the transverse currents $\mathbf{j}_{t,\phi}$ (green arrows) along the Dirac ring for a constant electric field applied along the y and z directions. We observe that carriers on opposing sides of the Dirac ring flow into opposite directions transverse to the electric field. This leads to an accumulation of charge on opposite surfaces of the DNLSM.

2.6 Proposal for generating the topological current

From the above analysis it is now clear that the parity anomaly in DNLSMs gives rise to transverse topological currents. However, since the currents contributed by modes on opposing sides of the Dirac ring have opposite signs, the total transverse current vanishes (i.e., the anomaly cancels). A key observation is that electrons from the opposite sides of the Dirac nodal ring are with opposite momenta. It is possible to generate and measure a net topological current if electrons can be filtered based on their momenta. Thus we propose a dumbbell filter device, which is based on a ballistic constriction with (001) surface states [Fig. 2.5(a)] (i.e., a constriction in which the electronic states are confined along the z direction).

We adopt the the real space Hamiltonian corresponding to the lattice Eq. (2.29) for numerical eval-

uations, which reads

$$\begin{aligned}
H = & - \sum_{\mathbf{r}} t_{\parallel} (c_{\mathbf{r},p}^{\dagger} c_{\mathbf{r}+\hat{x},p} - c_{\mathbf{r},d}^{\dagger} c_{\mathbf{r}+\hat{x},d}) + \text{H.c.} \\
& - \sum_{\mathbf{r}} t_{\parallel} (c_{\mathbf{r},p}^{\dagger} c_{\mathbf{r}+\hat{y},p} - c_{\mathbf{r},d}^{\dagger} c_{\mathbf{r}+\hat{y},d}) + \text{H.c.} \\
& - \sum_{\mathbf{r}} t_{\perp} (c_{\mathbf{r},p}^{\dagger} c_{\mathbf{r}+\hat{z},p} - c_{\mathbf{r},d}^{\dagger} c_{\mathbf{r}+\hat{z},d}) + \text{H.c.} \\
& + \sum_{\mathbf{r}} t'_{\perp} (c_{\mathbf{r},p}^{\dagger} c_{\mathbf{r}+\hat{z},d} - c_{\mathbf{r},p}^{\dagger} c_{\mathbf{r}-\hat{z},d}) + \text{H.c.} \\
& + \sum_{\mathbf{r}} \mu_z (c_{\mathbf{r},p}^{\dagger} c_{\mathbf{r},p} - c_{\mathbf{r},d}^{\dagger} c_{\mathbf{r},d}) + \sum_{\mathbf{r}} m (c_{\mathbf{r},p}^{\dagger} c_{\mathbf{r},d} + c_{\mathbf{r},d}^{\dagger} c_{\mathbf{r},p}),
\end{aligned} \tag{2.92}$$

where t_{\parallel} is the nearest-neighbor intra-orbital hopping amplitude in the x and y directions, t_{\perp} is the nearest-neighbor intra-orbital hopping amplitude in the z direction, t'_{\perp} denotes the inter-orbital hopping amplitude, μ_z is an onsite energy, and m represent the gap energy. For the numerical computations we have used the following parameters $(t_{\parallel}, t_{\perp}, t'_{\perp}, \mu_z) = (0.5, 0.5, 0.5, 2.0)$ and for the gapped case, we have set the gap energy to $m = 0.05$.

2.6.1 Landauer formula

For calculating the topological current in our dumbbell device, we will adopt the Landauer Formula, which was first introduced by R. Landauer in 1957 to describe the ballistic transport of electrons [85]. Later, the multi-channel Landauer formula was developed for mesoscopic nanoscale systems [86]. In this section, we first give a brief derivation of the multi-channel Landauer formula and explain the mechanism of computing the conductance for our dumbbell filter device.

Suppose that the system is attached to two reservoirs $n = 1, 2$ via two leads. The chemical potential for the reservoirs is denoted as μ_n . The current that originates from lead n carried by the i th channel in the system for electrons with energy E is given by $I_{n,i} = \frac{2e}{L} \sum_k v(k) T_i(E) f(E - \mu_n)$, where $v(k) = \frac{1}{\hbar} dE/dk$ is the group velocity for the electron with momenta k and the Fermi-Dirac distribution function is $f(E - \mu_n)$. Here L is the length of the system. The transmission coefficient is $T_i(E) = \sum_j T_{ij}(E)$, with $T_{ij}(E)$ the transmission coefficient between channel i and j . The net current can be obtained from the difference between currents originated from two leads for all channels,

$$I = \sum_i (I_{1i} - I_{2i}) = \frac{2e}{L} \sum_{i,k} v(k) T_i(E) [f(E - \mu_1) - f(E - \mu_2)]. \tag{2.93}$$

The summation can be replaced by the integral over momentum k in a standard way $\sum_k \rightarrow \frac{L}{2\pi} \int dk$. As $v(k) = \frac{1}{\hbar} dE/dk$, the expression for the net current becomes,

$$I = \frac{2e}{h} \int \sum_i T_i(E) [f(E - \mu_1) - f(E - \mu_2)] dE. \tag{2.94}$$

Suppose the chemical potential difference $(\mu_1 - \mu_2)$ between two reservoirs is comparably small. We

can adopt the Taylor expansion and obtain,

$$I = (\mu_1 - \mu_2) \frac{2e}{h} \int \sum_i T_i(E) \left(-\frac{\partial f}{\partial E} \right) dE. \quad (2.95)$$

At zero temperature, the Fermi-Dirac distribution function is a step function, hence its derivative is a delta function of $-\delta(E - E_F)$. Thus we can obtain the conductance

$$G = \frac{eI}{\mu_1 - \mu_2} = \frac{2e^2}{h} \sum_i T_i(E_f), \quad (2.96)$$

at zero temperature. Here, the transmission coefficient is

$$T_i(E_f) = \sum_j T_{ij}(E_f). \quad (2.97)$$

For our dumbbell device described by the lattice Hamiltonian, the problem is to obtain the transmission coefficient $T_{ij}(E_f)$. As several leads attached to a system can be regarded effectively as a single lead with disjoint sections, without loss of generality, we consider a lattice system with a single lead [87],

$$H = \begin{pmatrix} \ddots & V_L & & & \\ V_L^\dagger & H_L & V_L & & \\ & V_L^\dagger & H_L & V_{LS} & \\ & & V_{LS}^\dagger & H_S & \end{pmatrix}, \quad (2.98)$$

where H_L is the Hamiltonian of one unit cell in the lead, V_L describes the hopping between unit cells in the lead, H_S is the Hamiltonian for the system, and V_{LS} the hopping between the lead and system.

We can define the wavefunction of the entire Hamiltonian as $(\cdots, \Psi_2^L, \Psi_1^L, \Psi_0^S)$, where $\Psi_i^L (i > 0)$ is the wavefunction for the i -th unit cell in the leads and Ψ_0^S the wavefunction of the system. There are different energy eigenvalues, which we denote as E_n and the corresponding component of the wavefunction are denoted as $\Psi_n(i)$. Note that the translational symmetry is preserved in the lead, thus the eigenstates of the translation operator in the lead take the form $\phi_n(j) = (\lambda_n)^j \chi_n$. The normalization condition requires that $|\lambda_n| \leq 1$, from which we can tell the modes with $|\lambda_n| < 1$ are evanescent, and those with $|\lambda_n| = 1$ are propagating modes. Furthermore, the propagating modes are distinguished as incoming ones (ϕ_n^{in}) and outgoing ones (ϕ_n^{out}). With these notations, the scattering states in the leads take the form,

$$\Psi_n(i) = \phi_n^{\text{in}}(i) + \sum_m S_{mn} \phi_m^{\text{out}}(i) + \sum_p \tilde{S}_{pn} \phi_p^{\text{ev}}(i) \quad (2.99)$$

and the scattering states inside the system are,

$$\Psi_n(0) = \phi_n^s. \quad (2.100)$$

By solving the Schrödinger equation $H\Psi_n = \varepsilon_n\Psi_n$ with the above form of wavefunction, and performing the wavefunction matching at the boundary between the lead and the system, we can obtain the scattering matrix S_{mn} . Thus the transmission coefficient can be obtained as $T_{mn} = |S_{mn}|^2$. The numerical calculation of the transmission coefficient is achieved by using the Kwant code [87].

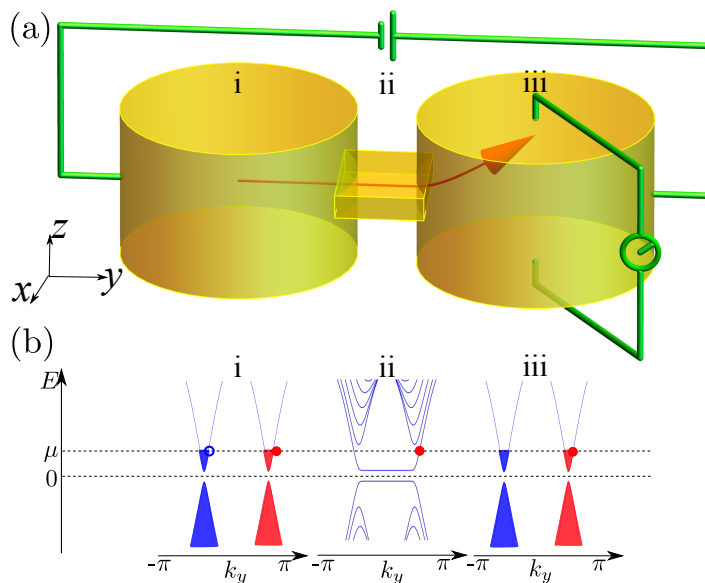


Figure 2.5: Schematic diagram of dumbbell filter device. (a) The device consists of two bulk regions (“i” and “iii”) separated by a constriction (“ii”) with (001) surface states. (b) Schematic dispersion relation for fixed $k_x = 0$ in the bulk regions and in the constriction. An electron with $k_y > 0$ (red filled circles) can be transmitted, while an electron with $k_y < 0$ (open blue circles) is reflected.

Note that in an ideal case, narrow constrictions can be treated as quantum point contacts (QPC). For channels in the constriction lying within the transport window, each has transmission probability equal to unity. Outside the window, the probability vanishes. Thus the transmission coefficient for the i th channel is a step function,

$$T_i(E_f) = \theta(E_f - E_n), \quad (2.101)$$

with E_n the eigenenergy for the mode n . Thus, the conductance is obtained as

$$G = \frac{2e^2}{h} N_m, \quad (2.102)$$

with N_m the number of modes in the window of transport.

2.6.2 Dumbbell filter device

The dumbbell filter device that we propose consists of two bulk regions connected by a ballistic constriction with drumhead surface states, as illustrated in Fig. 2.5(a). Such a device could be manufactured, for example, using focused ion beam micromachining [88]. The electronic states in the constriction are confined in the z direction, such that their low-energy spectrum is dominated by the drumhead surface states. We show the dispersion relation of the constriction with dimensions $N_x = 20$ and $N_z = 10$ in Fig. 2.6(a), which reveals that for this parameter choice all states with energies within the interval $-0.4 \lesssim E \lesssim 0.4$ are surface states. When a voltage is applied across the device, a current passes through the constriction, whose conductance can be determined using the multi-channel Landauer formula in Eq. (2.96). Assuming that the chemical potential μ lies slightly above (or below) the gap

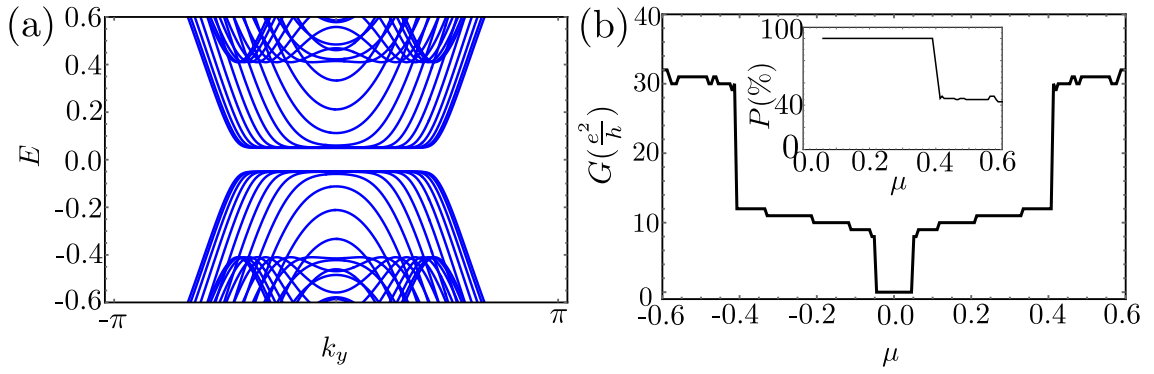


Figure 2.6: Dispersion relation, conductance, and polarization for the dumbbell filter device of Fig. 2.5. (a) Dispersion relation of the DNLSM \mathcal{H}_L , Eq. (2.29), in bar geometry with dimensions $N_x = 20$ and $N_z = 10$ and mass $m = 0.05$. (b) Conductance G for the dumbbell filter as a function of chemical potential μ in the constriction. The inset shows the polarization P .

energy, transport through the constriction is mediated mainly by the modes of the drumhead surface states. Indeed, as shown in Fig. 2.6, for $|\mu| \lesssim 0.4$ the current flows entirely within the surface states, leading to plateaus of quantized conductance with steps in multiples of $\frac{e^2}{h}$. For $|\mu| \gtrsim 0.4$, however, bulk modes start to contribute. Since the right propagating surface modes all have positive k_y , only electrons from the right half of the Dirac ring [red area in Fig. 2.5(b)] with $k_y > 0$ can pass through the constriction. Electrons from the left half of the Dirac ring [blue area in Fig. 2.5(b)], on the other hand, are reflected. Therefore, the dumbbell device acts as a filter for modes with $k_y > 0$. The effectiveness of the filter can be estimated by the polarization $P = G_{\text{surf}}/G_{\text{tot}}$, where G_{tot} and G_{surf} denote the total conductance and the conductance contributed by the surface modes, respectively. We find that P is close to 100% for $|\mu| \lesssim 0.4$, while it decreases once bulk modes start to mix in [inset of Fig. 2.6(b)].

Now, since the electric field is oriented along the y direction in the dumbbell device, electrons with $k_y > 0$ give rise to a transverse current that flows upwards along the z direction [see Fig. 2.4(a)]. Thus, a voltage difference develops between the upper and lower surfaces of the right weight plate of Fig. 2.5(a). This voltage difference can be measured experimentally and is a clear signature of the parity anomaly in DNLSMs.

2.6.3 Robustness of the topological current

In the last two subsections, we have explained explicitly how the parity anomaly leads to topological current in DNLSMs, and proposed a dumbbell filter device that generates and detects such topological current effectively. However, in actual materials, there are many factors that would possibly affect the generation of topological currents and the efficiency of our dumbbell device. In this section, we first adapt our model to the material CaAgP and investigate the effect of the thickness of the constriction, take into account the effects of a small dispersion of the band crossing, and consider the effects of the spin-orbit coupling and the disorder.

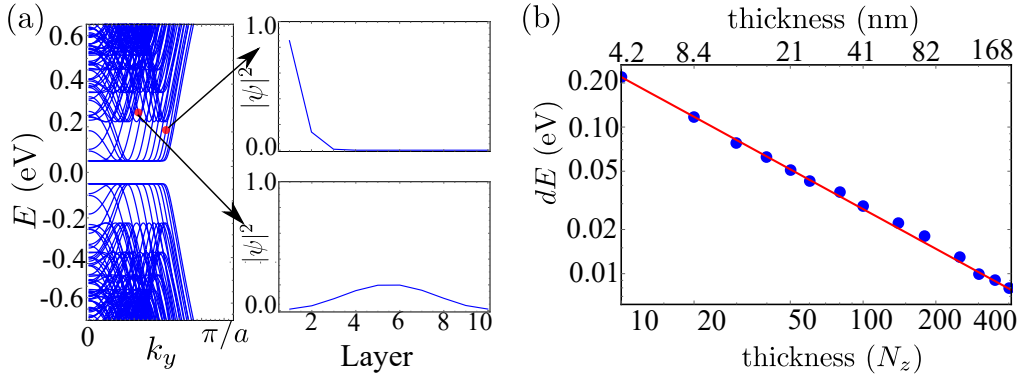


Figure 2.7: The parameters of the tight-binding model are $t_{\parallel} = 0.638$ eV, $t_{\perp} = -0.303$ eV, $t'_{\perp} = 0.262$ eV, $\mu_z = 1.609$ eV obtained from fitting the DFT bands of CaAgP [1, 2]. (a) Wave function profile for bulk and surface bands for $N_z = 10$ and $N_x = 20$, with a small gap of 0.05 eV. (b) Energy window (dE) against thickness or (N_z) in a Log-Log graph. The lattice constant of CaAgP in z direction is 0.42 nm. The blue dots are obtained from numerical simulations and the red solid line is the fitting curve.

Real material with thicker constriction

Our previous numerical calculation are obtained with the constriction dimensions of $N_x \times N_y \times N_z = 100 \times 20 \times 10$, where the constriction has a high performance of filtering. Similar results also hold for thicker constrictions, although the range of μ with 100% filtering polarization reduces with increasing thickness. The energy window of μ between the emergence of surface and bulk bands (dE) serves as a good indicator for the performance of the constriction, especially in experiments. Thus for experimental convenience, here we show the dE dependence on the thickness of N_z for the material CaAgP in Fig. 2.7(b). Empirically, we find this window can be fitted by the power law function

$$dE = 1.74N_z^{-0.90}(\text{eV}). \quad (2.103)$$

Clearly this energy window dE even extends to thicker constrictions. In order to detect the transverse topological currents, it is however not necessary to use a dumbbell filter with 100% polarization. Transverse Hall currents exist as long as the surface conductance is present, no matter how low the polarization is. In a DNLSM the transverse current is large (since it is produced by a large one-dimensional region in the BZ), which should be detectable even by a dumbbell device with reduced sensitivity.

We note that the fabrication of a thin constriction in a DNLSM is experimentally challenging, but entirely feasible. Indeed, it is possible to fabricate a 50 nm thin bridge using focused ion beam machining (see, e.g., Ref. [89]), or perhaps, also with electron-beam lithography. Hence, it should be possible to fabricate a dumbbell device that is able to detect the predicted transverse topological currents.

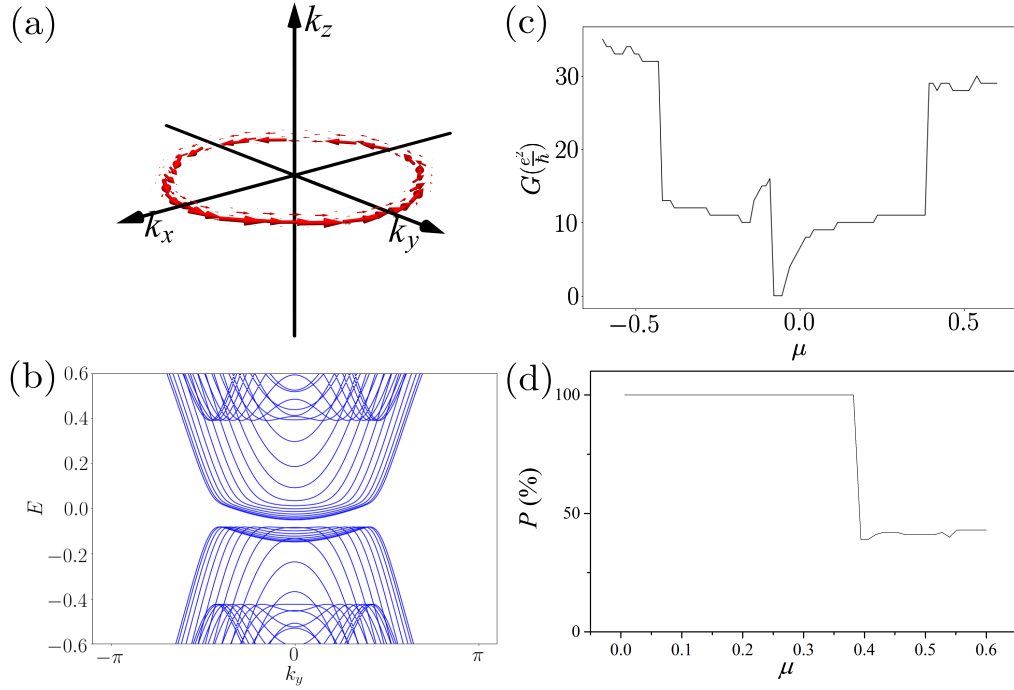


Figure 2.8: Berry curvature and properties of the dumbbell filter device for a DNLSM with finite dispersion $c(\mathbf{k})$. (a) Berry curvature as computed from the tight-binding model Eq. (2.29) together with Eq. (2.104). (b) Band structure of the dumbbell filter device with dimensions $N_x = 20$ and $N_z = 10$. (c) and (d) conductance G and polarization P of the dumbbell filter device against chemical potential μ , respectively. The parameter values are the same as in Fig. 2.6 except for $c_1 = 0.2$ and $c_2 = 0.1$.

Effects of a small dispersion of the band crossing

In real materials, it is possible that Dirac nodal line could have a dispersion. This can be described by the symmetry-allowed term

$$c(\mathbf{k})\sigma_0 = - \left[c_1(\cos k_x + \cos k_y - 1) + c_2(\cos k_z - 1) \right] \sigma_0, \quad (2.104)$$

that is added to the Hamiltonian \mathcal{H}_L , Eq. (2.29). In the presence of $c(\mathbf{k})$ the Fermi surface of the DNLSM becomes a thin anisotropic torus at zero Fermi energy. We note that in many DNLSM materials $c(\mathbf{k})$ is relatively small, such as, e.g., in Ca_3P_2 [50, 52] and CaAgAs [1, 2, 51]. Nevertheless, since the term (2.104) is symmetry allowed, one expects it to be present in general. We therefore study how $c(\mathbf{k})$ modifies the Berry curvature and the properties of the dumbbell filter device.

Using the tight-binding model Eq. (2.29) in the presence of the term (2.104), with $c_1 = 0.2$ and $c_2 = 0.1$, we have numerically computed the Berry curvature, see Fig. 2.8(a). We observe that the Berry curvature $\Omega(\mathbf{k})$ shows a similar structure as in the absence of $c(\mathbf{k})$ [compare Fig. 2.4 with Fig. 2.8(a)]. That is, $\Omega(\mathbf{k})$ is peaked at the Dirac ring and is oriented along the torus-like Fermi surface. It follows that the transverse Hall current \mathbf{j}_t , which is given by $\mathbf{j}_t = \frac{e^2}{h} \int \frac{d^3k}{(2\pi)^3} f(\mathbf{k}) \mathbf{E} \times \Omega(\mathbf{k})$, is qualitatively unchanged by $c(\mathbf{k})$.

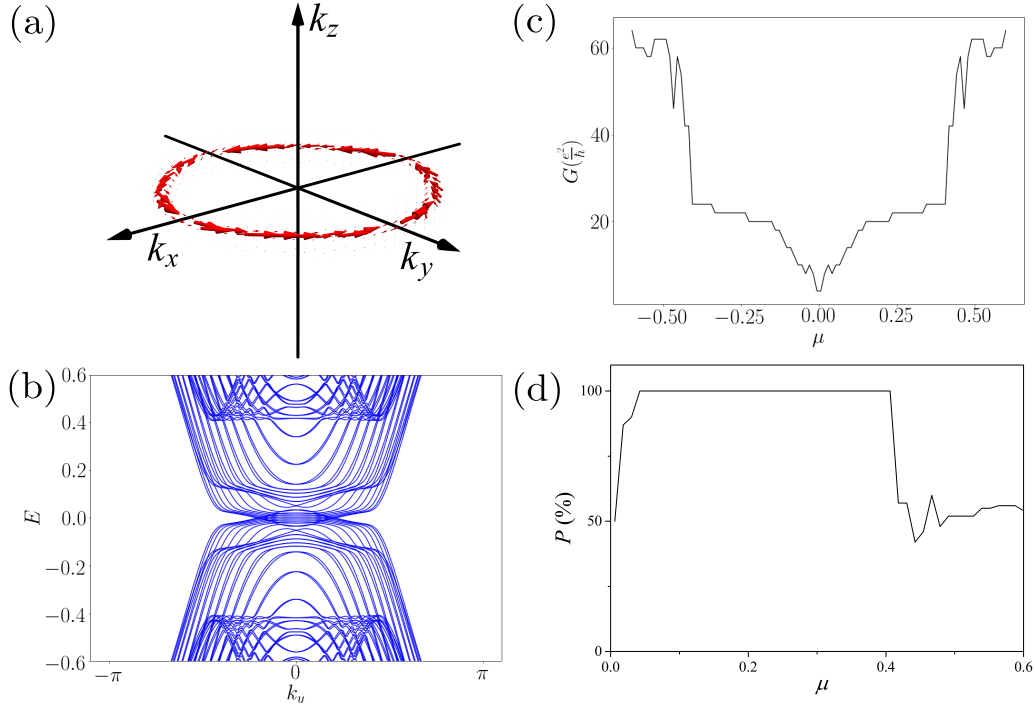


Figure 2.9: Berry curvature and properties of the dumbbell filter device for the DNLSM (2.105) with spin-orbit coupling. (a) Berry curvature as computed from the tight-binding model (2.105). (b) Band structure of the dumbbell filter device with dimensions $N_x = 20$ and $N_z = 10$. (c) and (d) Conductance G and polarization P of the filter device against chemical potential μ . The parameter values are the same as in Fig. 2.6 except for $b_1 = 0.08$.

Next, we study how the properties of the dumbbell filter device are modified by the term $c(\mathbf{k})$. Comparing Fig. 2.6(a) with Fig. 2.8(b), we find that the band structure of the filter device is modified only within a small energy range of $[-0.05, +0.05]$ around the Fermi energy. In accordance with this, the conductance G and the polarization P of the filter device is largely unchanged by $c(\mathbf{k})$, see Figs. 2.8(c) and 2.8(d).

Effects of spin-orbit coupling

There exist DNLSM materials with both weak and strong spin-orbit coupling. In the discussion of topological current, we have focused on the case of very weak spin-orbit coupling, which is relevant for, e.g., Ca_3P_2 . For materials with heavier elements, such as, CaAgAs , spin-orbit coupling cannot be neglected. In order to study the effects of spin-orbit coupling we need to explicitly include the spin degree of freedom in the tight-binding Hamiltonian \mathcal{H}_L , Eq. (2.29). Therefore we consider

$$\hat{\mathcal{H}}_L(\mathbf{k}) = \begin{pmatrix} \mathcal{H}_L(\mathbf{k}) & \Lambda(\mathbf{k}) \\ \Lambda^\dagger(\mathbf{k}) & \mathcal{H}_L^*(-\mathbf{k}) \end{pmatrix}, \quad (2.105)$$

where $\Lambda(\mathbf{k})$ represents a spin-orbit coupling term, which breaks spin-rotation symmetry. Time-reversal symmetry acts on Hamiltonian (2.105) as $T^{-1}\hat{\mathcal{H}}_L(-\mathbf{k})T = \hat{\mathcal{H}}_L(\mathbf{k})$, with the time-reversal operator $T = \sigma_0 \otimes is_y\mathcal{K}$, where s_y denotes the second Pauli matrix in spin space. Reflection and inversion symmetry act on $\hat{\mathcal{H}}_L(\mathbf{k})$ as $R^{-1}\hat{\mathcal{H}}_L(k_x, k_y, -k_z)R = \hat{\mathcal{H}}_L(k_x, k_y, k_z)$ and $P^{-1}\hat{\mathcal{H}}_L(-\mathbf{k})P = \hat{\mathcal{H}}_L(\mathbf{k})$, with the operators $R = \sigma_z \otimes s_z$ and $P = \sigma_z \otimes s_0$, respectively. The spin-orbit coupling term $\Lambda(\mathbf{k})$ is assumed to take the following symmetry-allowed form

$$\Lambda(\mathbf{k}) = b_1(\sin k_x + i \sin k_y)\sigma_1. \quad (2.106)$$

We observe that $\hat{\mathcal{H}}_L(\mathbf{k})$ with Eq. (2.106) satisfies time-reversal symmetry, reflection symmetry, and parity symmetry, but breaks SU(2) spin-rotation symmetry. In the presence of spin-orbit coupling the nodal line of the DNLSM becomes gapped and the drumhead surface states split. However, the Berry curvature $\Omega(\mathbf{k})$ remains finite and is of similar form as without spin-orbit coupling, see Fig. 2.9(a). Hence, we conclude that a transverse Hall current of the form $\mathbf{j}_t = \frac{e^2}{h} \int \frac{d^3k}{(2\pi)^3} f(\mathbf{k}) \mathbf{E} \times \Omega(\mathbf{k})$ also exists in DNLSMs with strong spin-orbit coupling.

Spin-orbit coupling splits the spin degeneracy of the drumhead surface states and therefore is expected to modify the properties of the filter device. In order to study this, we have numerically computed the band structure, the conductance, and the polarization of the dumbbell device for the DNLSM (2.105) with spin-orbit coupling strength $b_1 = 0.08$, see Figs. 2.9(b), 2.9(c), and 2.9(d). By comparing Fig. 2.6(a) with Fig. 2.9(b) we see that spin-orbit coupling splits the band structure of the dumbbell device. Within a small energy interval of $[-0.04, +0.04]$ around the Fermi energy there exist now both left propagating and right propagating surface modes with positive k_y . Hence, for $|\mu| \lesssim 0.04$ the dumbbell device is no longer a perfect filter for modes with $k_y > 0$. However, for $0.4 > \mu > 0.04$ the filtering property remains intact, see Fig. 2.9(d).

For experimental realizations it is important to know how large the spin-orbit coupling can be, such that the transverse topological current is still observable. To address this question, we have performed simulations of the dumbbell device as a function of increasing spin-orbit coupling strength b_1 . Figure 2.10 shows the band structure of the dumbbell constriction and the Berry curvature for a range of spin-orbit coupling values b_1 . We observe that with increasing spin-orbit coupling the Berry curvature becomes more and more smeared out. Once the spin-orbit coupling value b_1 is of the same order or larger than the intra-orbital hopping t_{\parallel} , the Berry curvature field is no longer concentrated along the nodal line, see Fig. 2.10(h). Hence, the transverse topological current disappears for $b_1 \gtrsim t_{\parallel}$. We conclude that in order for the dumbbell device to be well-functioning, the spin-orbit coupling strength should be roughly one order less than the hopping term.

It is interesting to note that the filtering effect of the dumbbell device is present even for large spin-orbit coupling. As we can see from Fig. 2.10(d), the band structure within the energy window $-0.5 < E < +0.5$ is dominated by surface states even for large spin-orbit coupling. These surface states filter electrons based on their momenta. We expect that the filtering property of the dumbbell device only disappears for a spin-orbit coupling value larger than the finite size gap in the bulk spectrum.

Robustness against disorder

Here, we study the effects of disorder on the dumbbell filter device. A simple renormalization group argument shows that short-range correlated disorder is a marginal perturbation to the DNLSM Hamiltonian. Therefore, it is expected that the DNLSM and the dumbbell filter devices are robust against weak short-range correlated disorder [44, 90]. To verify this expectation we numerically compute the

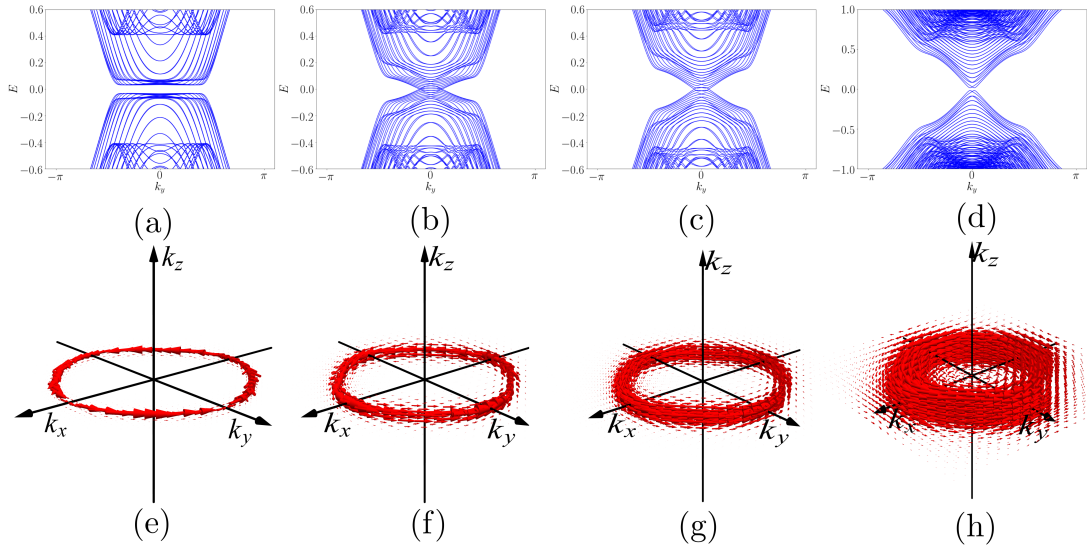


Figure 2.10: Band structure and Berry curvature of the dumbbell filter device as a function of increasing spin-orbit coupling. (a)-(d) Band structure of the dumbbell constriction with dimensions $N_x = 20$ and $N_z = 10$ with spin-orbit coupling strengths $b_1 = 0.02$, 0.14 , 0.20 and 0.50 respectively. (e)-(h) Berry curvature of the DNLSM for the same parameters as in panels (a)-(d).

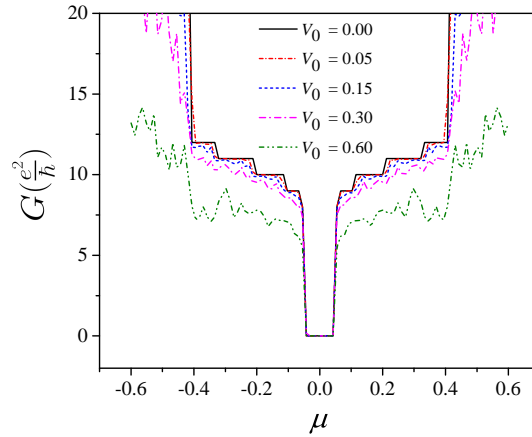


Figure 2.11: Conductance G of the dumbbell filter device with disorder. The dimensions of the constriction in the filter device are $N_x = 20$, $N_y = 20$, and $N_z = 10$. The disorder is described by the disorder potentials (2.107), where $v(\mathbf{r}_n)$ is drawn from a Gaussian distribution with width V_0 . The parameters of the DNLSM are the same as in Fig. 2.6.

conductance of the filter device in the presence of short-range impurity scatterers of the form

$$V(\mathbf{r}) = \sum_n v(\mathbf{r}_n) \delta(\mathbf{r} - \mathbf{r}_n), \quad (2.107)$$

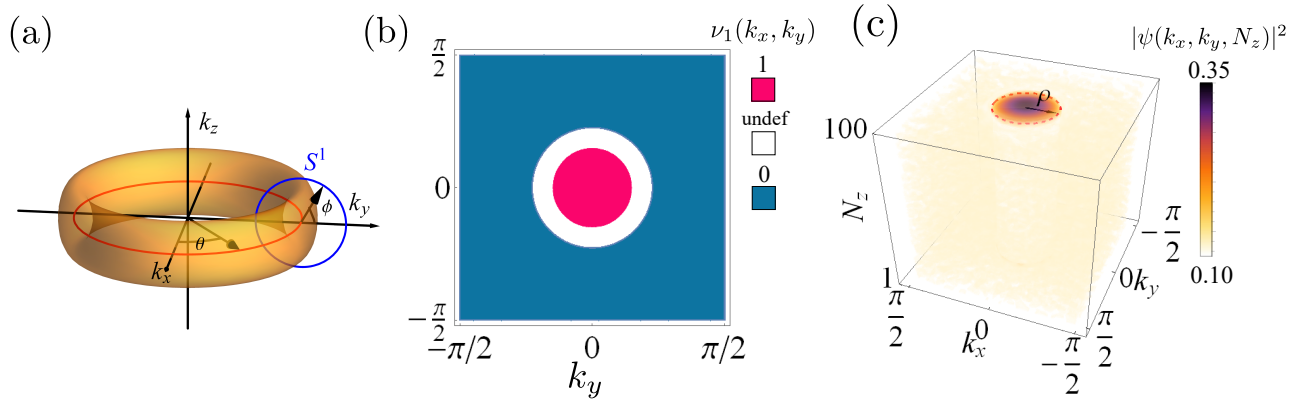


Figure 2.12: \mathcal{PT} -symmetric non-Hermitian topological nodal-line semimetal. (a) Topological exceptional torus. (b) The real part of the Berry phase, which is not defined in the white region. (c) Wavefunction amplitude $|\psi(k_x, k_y, N_z)|^2$ for the surface states for $N_z = 100$ layers in z direction. The region of the localized wavefunction forms two disks at top and bottom layer.

where $v(\mathbf{r}_n)$ denotes the scattering potential at the lattice site \mathbf{r}_n . For each lattice site the onsite potential $v(\mathbf{r}_n)$ is drawn from a Gaussian distribution with width V_0 . In Fig. 2.11 we present the conductance of the filter device as a function of disorder strength V_0 . We find that for $V_0 < 0.1$ the conductance steps in multiples of e^2/h are still clearly visible. This indicates that the filter device is robust against moderately strong disorder.

2.7 \mathcal{PT} -symmetric non-Hermitian topological nodal-line semimetals

At the end of last century, it was first pointed out by C. Bender that instead of Hermiticity, the reality of the spectrum of a Hamiltonian can be ensured by an unbroken \mathcal{PT} symmetry[91]. Indeed, as we have shown in section 2.1, the \mathcal{PT} symmetry with $(\mathcal{PT})^2 = +1$ is actually a reality requirement for the Hamiltonian. For our \mathcal{PT} -symmetric topological nodal-line semimetals, it is also possible to lift the restriction of Hermiticity. The non-Hermitian potential usually enters as perturbation experimentally, here we consider the non-Hermitian potentials expressed in terms of Pauli matrices $i\lambda\sigma_j$ with $j = 1, 2, 3$. The \mathcal{PT} symmetry operator in our case is $\hat{\mathcal{P}}\hat{\mathcal{T}} = \sigma_3\hat{\mathcal{K}}$, thus the only \mathcal{PT} -symmetric non-Hermitian potential is $i\lambda\sigma_1$. The \mathcal{PT} -symmetric non-Hermitian Hamiltonian in momentum space reads,

$$\mathcal{H}'_{\text{nl}}(\mathbf{k}) = [\mu_z - 2t_{\parallel}(\cos k_x + \cos k_y) - 2t_{\perp} \cos k_z]\sigma_3 - 2t'_{\perp} \sin k_z \sigma_2 + i\lambda\sigma_1. \quad (2.108)$$

The energy spectrum is $E'_{\text{nl}} = \pm\sqrt{E_{\text{nl}}(\mathbf{k})^2 - \lambda^2}$, which is purely real for \mathbf{k} in the region of $E_{\text{nl}}(\mathbf{k})^2 > \lambda^2$. As shown in Fig. 2.12 (a), the band crossing changes from a nodal line (red) to a torus (yellow).

Though the system is non-Hermitian, the topological invariant can still be calculated. Let's focus on Berry phase along a closed path S^1 that encircles the entire exceptional torus, denoted by blue circle in Fig. 2.12 (a). In the close neighborhood of the original nodal line, we can do the Taylor expansion

to the first order for Hamiltonian in Eq. (2.108), which yields $H_{\text{torus}}(\delta\mathbf{k}) = \delta k_{\parallel}\sigma_1 + \delta k_z\sigma_2 - i\lambda\sigma_3$ after a unitary transformation. Then the circle S^1 can be parameterized as $\delta\mathbf{k} = (r \cos \phi, r \sin \phi)$ with the radius $r \ll \rho$. In non-Hermitian systems, the eigenvalue equations read,

$$H|\alpha\rangle = E_{\alpha}|\alpha\rangle, \quad H^{\dagger}|\alpha\rangle = E_{\alpha}^*|\alpha\rangle, \quad (2.109)$$

where the left eigenvector $\langle\alpha|$ and the right eigenvector $|\alpha\rangle$ are not identical in general. Usually the biorthonormal condition of $\langle\alpha|\beta\rangle = \delta_{\alpha,\beta}$ is used. Then the Berry phase on S^1 of $H_{\text{torus}}(\delta\mathbf{k})$ for the conduction band is calculated

$$\gamma(S^1) = \oint d\phi \langle\langle +, \phi | i\partial_{\phi} | +, \phi \rangle\rangle = \frac{\sqrt{r^2 - \lambda^2} + i\lambda}{\sqrt{r^2 - \lambda^2}} \pi, \quad (2.110)$$

which is complex and not quantized if $\lambda \neq 0$. It seems that the quantization of Berry phase by \mathcal{PT} symmetry fails in the non-Hermitian regime, as the non-Hermitian potential $i\lambda\sigma_1$, similar to its Hermitian counterpart $\lambda\sigma_1$, breaks the quantization of π Berry phase.

However, from Eq. (2.110), we find that the real part of the Berry phase is still quantized for small perturbations. The loop S^1 can also be deformed to two lines at different k_y values going through $k_x \in [-\pi, \pi]$ that inside and outside the torus. The real part of Berry phase computed in this way is plotted in Fig. 2.12 (b). In Fig. 2.12 (c), we calculate the wavefunction amplitude $|\psi(k_x, k_y, N_z)|^2$ for the surface states from the lattice model $H'_L + i\lambda\sigma_1$ with H'_L from Eq. (2.30). Surprisingly, the drumhead surface states still exist and the region for the localization is basically the same as the Hermitian case, which can be seen at the surface in Fig. 2.12 (c), even though the topological invariant is not well defined in some regions in the first BZ. The question remains how to characterize non-Hermitian topological phases of matter and the non-Hermitian bulk-boundary correspondence.

2.8 Conclusions

We have studied \mathcal{PT} -symmetric Dirac nodal-line semimetals in detail. The non-trivial topological invariants in the bulk lead to exotic drumhead surface states, which have been studied from both low-energy effective model and the tight-binding lattice model. Furthermore, we focus on the parity anomaly in nodal-line semimetals, and find that it induces a topological current. To generate and test the topological current, we propose a dumbbell filtering device. We emphasize that the anomaly-induced currents are robust to small perturbations, since they are of topological origin. The same conclusions apply to the dumbbell device, as its properties originate from topologically protected surface states. Hence, the topological currents are observable even in systems with small spin-orbit coupling, finite dispersion of the nodal ring, as well as moderately strong disorder. Regarding experimental realizations of our proposal, the hexagonal pnictides CaAgAs and CaAgP [1, 2] are particularly promising candidate materials, because they are available in single crystal form and exhibit just a single Dirac ring at the Fermi energy [2, 92–94]. While the observation of the parity anomaly in DNLSMs would be of fundamental interest, the dumbbell device used for this purpose could also lead to new electronic devices, such as a topological current rectifier. We anticipate that similar devices could also be realized in Dirac or Weyl semimetals, whose Fermi arc surface states could be used as a valley filter.

Finally, we connect the \mathcal{PT} symmetry with non-Hermitian physics, and discuss the \mathcal{PT} -symmetric

non-Hermitian Dirac nodal-line semimetal. We find that the topological invariants can still be computed in the bulk, which are different to the Hermitian ones. However, the correspondence between the bulk topological invariants and the topological boundary states is not clear, as the bulk invariants are not well defined throughout the BZ. In the following chapters, we will focus on the non-Hermitian topological phases of matter.

3

Chapter 3

Non-Hermitian topological gapped systems

One fundamental assumption of quantum mechanics is that the Hamiltonian H which describes the dynamics of the quantum system is Hermitian, $H = H^\dagger$, with \dagger representing the combined operations of matrix transposition and complex conjugation. This assumption has its roots in the requirements of real eigenvalues of H and unitarity of the time-evolution operator e^{-iHT} . However, it was realized by Carl Bender that the requirement of Hermiticity can be replaced by a more physical one, the parity-time (\mathcal{PT}) symmetry, from which the requirements of reality and unitarity can be properly satisfied [31, 34]. Shortly after this discovery, it was observed experimentally that non-Hermitian \mathcal{PT} -symmetric systems exist, e.g., in optical systems with balanced loss and gain [95]. Later on, the field of non-Hermitian \mathcal{PT} -symmetric physics experiences a rapid development [96–101].

Apart from fundamental questions on the foundation of quantum mechanics, non-Hermitian Hamiltonians can serve as a good description of dissipative systems, open systems, or non-equilibrium systems that can exchange particle or energy with the environment. Typical examples are systems with open boundaries [102, 103], with particle loss or gain [104–107], and with dissipation and disorder [108–110]. In these systems, the expectation value of a physical operator might not be real, and its imaginary part has a physical meaning, such as finite life time of quasi-particles [111, 112]. Recently, it has been shown that non-Hermitian Hamiltonians provide useful descriptions of strongly correlated materials in the presence of disorder or dissipation [108–116]. This has given new insights into the Majorana physics of semiconductor-superconductor nanowires [116] and into the quantum oscillations of SmB_6 [109, 111].

There is a growing interest to study topological phases of matter in the context of non-Hermitian physics. The joint efforts of the fields of topological matter and non-Hermitian physics has led to fascinating discoveries, both at the fundamental and at the applied level [20, 21, 30, 117–131]. For instance, topological exceptional points have been found in one-dimensional non-Hermitian lattices [30, 123–125] and in non-Hermitian Chern insulators [20, 126–128]. Exceptional rings and bulk Fermi arcs have been discovered in non-Hermitian topological semimetals [129, 130, 132–135]. Despite these recent activities, a general framework for the study and the complete classification of non-Hermitian topological phases is still absent. Since most non-Hermitian experimental systems can be faithfully captured by Dirac Hamiltonians with small non-Hermitian perturbations [99, 117–119, 136–143], a systematic investigation of non-Hermitian Dirac models would be particularly valuable. This would be

not only of fundamental interest, but could also guide the design of new applications.

In this chapter, we present a systematic investigation of d -dimensional massive Dirac Hamiltonians perturbed by small non-Hermitian terms. We show that these can be either intrinsically or superficially non-Hermitian, depending on whether the non-Hermiticity can be removed by a similarity transformation with open or periodic boundary conditions. According to the Clifford algebra, general non-Hermitian terms can be categorized into three different types: (i) non-Hermitian terms that anti-commute with the whole Dirac Hamiltonian, (ii) kinetic non-Hermitian terms, and (iii) non-Hermitian mass terms. Remarkably, we find a two-fold duality for the first two types of non-Hermitian perturbations: Dirac models perturbed by type-(i) terms are superficially non-Hermitian with periodic boundary conditions (PBCs), but intrinsically non-Hermitian with open boundary conditions (OBCs). Vice versa, Dirac models with type-(ii) terms are intrinsically non-Hermitian with PBCs, but superficially non-Hermitian with OBCs. Interestingly, for type-(i) and type-(ii) terms the non-Hermiticity leads to $(d - 2)$ -dimensional exceptional spheres in the surface and bulk band structures, respectively. Type-(iii) terms, on the other hand, induce intrinsic non-Hermiticity both for OBCs and PBCs, but with a purely real surface-state spectrum and no exceptional spheres.

As boundary conditions play a key role in distinguishing different non-Hermitian terms in lattice systems, their role is investigated with the transfer matrix method [144]. It is revealed that different to Hermitian systems, the boundary conditions in non-Hermitian systems not only influence boundary states, but also bulk states, which results in drastic different band structures between non-Hermitian systems with OBCs and those with PBCs.

Finally, we study in detail the properties of exceptional points which are unique to non-Hermitian systems. At these exceptional points, two or more eigenstates become identical and self-orthogonal, leading to a defective Hamiltonian with nontrivial Jordan normal form [145]. We classify different exceptional points by \mathbb{Z}/N topological invariants, and apply this classification to concrete physical systems. The exceptional points will also affect the Green's function. We show that at exceptional points, Green's function will exhibit high-order poles.

3.1 General theory

We begin with connecting non-Hermitian lattice theory to the general theory of non-Hermitian physics. In non-Hermitian physics, a fundamental difference between Hermitian Hamiltonians and non-Hermitian ones is that a Hermitian Hamiltonian can only be transformed by unitary transformations in order to preserve the Hermiticity, but a non-Hermitian Hamiltonian can be transformed by similarity transformations, $H \rightarrow V^{-1}HV$, where V is an invertible matrix not necessarily unitary. It is significant to observe that there exists a large class of non-Hermitian Hamiltonians which can be converted into Hermitian ones by similarity transformations, i.e.,

$$V^{-1}HV = H', \quad H'^{\dagger} = H'. \quad (3.1)$$

For non-interacting lattice models, which are mainly concerned by us, if translational symmetry is preserved, we mainly deal with the Hamiltonian in momentum space, $\mathcal{H}_{\alpha\beta}(\mathbf{k})$ with α, β labeling sublattice and orbital degrees of freedom, and thereby we define that $\mathcal{H}(\mathbf{k})$ is intrinsically Hermitian in momentum space if there exists $\mathcal{V}(\mathbf{k})$ with $\mathcal{H}'(\mathbf{k}) = \mathcal{V}^{-1}(\mathbf{k})\mathcal{H}(\mathbf{k})\mathcal{V}(\mathbf{k})$ Hermitian. For instance, \mathcal{PT} -symmetric spinless tight-binding models without “spontaneously \mathcal{PT} symmetry breaking” are always

intrinsically Hermitian in momentum space with real spectra. Actually, $\mathcal{H}(\mathbf{k})$ is the Fourier transform of the Hamiltonian in real space $H_{(\mathbf{r}\alpha),(\mathbf{r}'\alpha')}$ with \mathbf{r} the positions of primitive cells if translational symmetry is preserved. More specifically, we first perform the Fourier transform for a finite lattice with periodic boundary conditions, and then send the lattice size to be infinite, with the Brillouin zone fully filled by \mathbf{k} . Thus, $\mathcal{H}(\mathbf{k})$ actually describes physics with periodic boundary conditions and translational symmetry, both of which are violated if boundaries are opened. Then, we have to consider $H_{(\mathbf{r}\alpha),(\mathbf{r}'\alpha')}$, and the associated similarity transformation $V_{(\mathbf{r}\alpha),(\mathbf{r}'\alpha')}$ in real space. In real space, it is natural to demand that the locality to be preserved by the similarity transformation, namely, that $|V_{(\mathbf{r}\alpha),(\mathbf{r}'\alpha')}|$ tends to zero sufficiently fast as $|\mathbf{r} - \mathbf{r}'| \rightarrow \infty$, for instance, as the simplest case, $V_{(\mathbf{r}\alpha),(\mathbf{r}'\alpha')} = V_{\mathbf{r}(\alpha,\alpha')}\delta_{\mathbf{r},\mathbf{r}'}$, diagonal in real space. It is worth noting that although $\mathcal{V}(\mathbf{k})$ is apparently local in momentum space, the locality in real space is essentially different from that in momentum space. Generically, $V_{(\mathbf{r}\alpha),(\mathbf{r}'\alpha')}$ has no translation symmetry, and $V_{\mathbf{r},\mathbf{r}'} = \sum_{\mathbf{k}} \mathcal{V}(\mathbf{k})e^{i\mathbf{k}\cdot(\mathbf{r}-\mathbf{r}')}$, the Fourier transform of $\mathcal{V}(\mathbf{k})$, is not local in general.

This chapter is mainly devoted to applying the above concepts to non-Hermitian Dirac models $H = H_0 + \lambda U$, where H_0 is the Hermitian massive Dirac model and U a non-Hermitian term. The non-Hermitian term will not induce band crossing, and thus can be treated as a perturbation. In d dimensional momentum space, the Hermitian lattice Dirac model reads,

$$\mathcal{H}_0(\mathbf{k}) = \sum_{i=1}^d \sin k_i \Gamma_i + (M - \sum_{i=1}^d \cos k_i) \Gamma_{d+1}, \quad (3.2)$$

where Γ_μ denotes the Hermitian gamma matrices that satisfy $\{\Gamma_\mu, \Gamma_\nu\} = 2\delta_{\mu\nu}$ and M a real parameter. The corresponding real space Hamiltonian in the \mathbf{j} direction with N_j layers is given by

$$H_0(\tilde{\mathbf{k}}) = \frac{1}{2i}(S - S^\dagger) \otimes \Gamma_j - \frac{1}{2}(S + S^\dagger) \otimes \Gamma_{d+1} + \mathbb{1}_{N_j} \otimes \left(\sum_{i \neq j} \sin k_i \Gamma_i + (M - \sum_{i \neq j} \cos k_i) \Gamma_{d+1} \right), \quad (3.3)$$

where $\tilde{\mathbf{k}}$ stands for the remaining momenta $k_{i \neq j}$, $\mathbb{1}_{N_j}$ is the identity matrix, and $S_{ij} = \delta_{i,j+1}$ is the right-translational operator in the \mathbf{j} -direction, which let $S|i\rangle = |i+1\rangle$ and $S^\dagger|i\rangle = |i-1\rangle$, where i labels the i th site in the j direction. As $\langle i|S|j\rangle = \delta_{i,j+1}$, with periodic boundary conditions (PBCs), the corresponding matrices are,

$$S = \begin{pmatrix} 0 & 0 & 0 & 0 & \cdots & 1 \\ 1 & 0 & 0 & 0 & \cdots & 0 \\ 0 & 1 & 0 & 0 & \cdots & 0 \\ 0 & 0 & 1 & 0 & \cdots & 0 \\ \vdots & \vdots & \vdots & \ddots & \ddots & \vdots \\ 0 & 0 & 0 & 0 & 1 & 0 \end{pmatrix}, \quad S_{i,j} = \begin{cases} \delta_{i,j+1} & \text{for } i = 1 \dots N-1 \\ \delta_{i,N} & \text{for } i = N \end{cases}. \quad (3.4)$$

For open boundary conditions (OBCs) we simply need to replace S and S^\dagger by \hat{S} and \hat{S}^\dagger

$$H_0(\tilde{\mathbf{k}}) = \frac{1}{2i}(\hat{S} - \hat{S}^\dagger) \otimes \Gamma_j - \frac{1}{2}(\hat{S} + \hat{S}^\dagger) \otimes \Gamma_{d+1} + \mathbb{1}_{N_j} \otimes \left(\sum_{i \neq j} \sin k_i \Gamma_i + (M - \sum_{i \neq j} \cos k_i) \Gamma_{d+1} \right), \quad (3.5)$$

where \hat{S} is given by S but with the upper right 1 removed, i.e.,

$$\widehat{S} = \begin{pmatrix} 0 & 0 & 0 & 0 & \cdots & 0 \\ 1 & 0 & 0 & 0 & \cdots & 0 \\ 0 & 1 & 0 & 0 & \cdots & 0 \\ 0 & 0 & 1 & 0 & \cdots & 0 \\ \vdots & \vdots & \vdots & \ddots & \ddots & \vdots \\ 0 & 0 & 0 & 0 & 1 & 0 \end{pmatrix}, \quad \widehat{S}^\dagger = \begin{pmatrix} 0 & 1 & 0 & 0 & \cdots & 0 \\ 0 & 0 & 1 & 0 & \cdots & 0 \\ 0 & 0 & 0 & 1 & \cdots & 0 \\ 0 & 0 & 0 & 0 & \ddots & 0 \\ \vdots & \vdots & \vdots & \vdots & \ddots & 1 \\ 0 & 0 & 0 & 0 & 0 & 0 \end{pmatrix}, \quad (3.6)$$

with dimension N_j . From the Eqs. (3.2) and (3.5), it is now clear that, according to the Clifford algebra, there exist only the three types of non-Hermitian terms discussed in the introduction. We will now study these individually.

3.1.1 Non-Hermitian terms of type (i)

We now start with the first case, namely terms that anti-commute with the Hermitian Dirac Hamiltonian and assume PBCs. Such non-Hermitian terms are possible for all chiral symmetry classes among the ten-fold Altland-Zirnbauer classes [13], with the non-Hermitian terms given by the corresponding chiral operators. The perturbed Hamiltonian in momentum space is given by

$$\mathcal{H}(\mathbf{k}) = \mathcal{H}_0(\mathbf{k}) + i\lambda\Gamma, \quad (3.7)$$

where $\mathcal{H}_0(\mathbf{k})$ is just Eq. (3.2), and Γ is a Hermitian matrix with $\Gamma^2 = 1$. $\mathcal{H}_0(\mathbf{k})$ anti-commutes with the chiral operator Γ ,

$$\{\Gamma, \mathcal{H}_0(\mathbf{k})\} = 0. \quad (3.8)$$

The spectrum is given by $E(\mathbf{k}) = \pm\sqrt{d^2(\mathbf{k}) - \lambda^2}$ with $d^2(\mathbf{k})\mathbb{1} = \mathcal{H}_0^2(\mathbf{k})$, which is completely real for all \mathbf{k} provided $|\lambda|$ is less than the energy gap of $\mathcal{H}_0(\mathbf{k})$. Thus for such non-Hermitian terms, the Hamiltonian is superficially non-Hermitian in momentum space.

The corresponding similarity transformation can be derived systematically by noticing that the flattened Hamiltonian $\tilde{\mathcal{H}}_0(\mathbf{k}) = \mathcal{H}_0(\mathbf{k})/d(\mathbf{k})$ and Γ form a Clifford algebra, and therefore $i[\tilde{\mathcal{H}}_0(\mathbf{k}), \Gamma]/4$ generates rotations of the plane spanned by $\tilde{\mathcal{H}}_0(\mathbf{k})$ and Γ . In the following, we shall construct this rotation operator. By using $(\tilde{\mathcal{H}}_0(\mathbf{k})\Gamma)^2 = -1$, we can obtain the following relation,

$$\mathcal{V}(\mathbf{k}) = e^{-i\frac{\eta(\mathbf{k})}{2}\tilde{\mathcal{H}}_0(\mathbf{k})\Gamma} = \cosh \frac{\eta(\mathbf{k})}{2} - i \sinh \frac{\eta(\mathbf{k})}{2} \tilde{\mathcal{H}}_0(\mathbf{k})\Gamma. \quad (3.9)$$

Applying this operator to the flattened Hamiltonian $\tilde{\mathcal{H}}_0(\mathbf{k})$, it is obtained that

$$\mathcal{V}(\mathbf{k})\tilde{\mathcal{H}}_0(\mathbf{k})\mathcal{V}(\mathbf{k})^{-1} = \cosh \eta(\mathbf{k})\tilde{\mathcal{H}}_0(\mathbf{k}) + i \sinh \eta(\mathbf{k})\Gamma, \quad (3.10)$$

which is equivalent to the relation of

$$\frac{1}{\cosh \eta(\mathbf{k})} \mathcal{V}(\mathbf{k})\tilde{\mathcal{H}}_0(\mathbf{k})\mathcal{V}(\mathbf{k})^{-1} = \tilde{\mathcal{H}}_0(\mathbf{k}) + i \tanh \eta(\mathbf{k})\Gamma. \quad (3.11)$$

Using Eq. (3.7), we can get

$$\frac{1}{d(\mathbf{k})} \mathcal{H}(\mathbf{k}) = \tilde{\mathcal{H}}_0(\mathbf{k}) + i \frac{\lambda}{d(\mathbf{k})} \Gamma. \quad (3.12)$$

By comparing Eq. (3.11) and Eq. (3.12), the following equivalent relation can be established,

$$\frac{1}{\cosh \eta(\mathbf{k})} \mathcal{V}(\mathbf{k}) \tilde{\mathcal{H}}_0(\mathbf{k}) \mathcal{V}(\mathbf{k})^{-1} = \frac{1}{d(\mathbf{k})} \mathcal{H}(\mathbf{k}), \quad (3.13)$$

provided that

$$\tanh \eta(\mathbf{k}) = \frac{\lambda}{d(\mathbf{k})}. \quad (3.14)$$

From $\tanh \eta(\mathbf{k})$, we can obtain the expression for $\eta(\mathbf{k})$, which is

$$e^{\eta(\mathbf{k})} = \sqrt{\frac{d(\mathbf{k}) + \lambda}{d(\mathbf{k}) - \lambda}}. \quad (3.15)$$

Correspondingly $\cosh \eta(\mathbf{k})^{-1} = \sqrt{1 - \lambda^2/d^2(\mathbf{k})}$. Then from Eq. (3.13), the similarity transformation can be obtained as

$$\mathcal{V}(\mathbf{k})^{-1} \mathcal{H}(\mathbf{k}) \mathcal{V}(\mathbf{k}) = \sqrt{1 - \lambda^2/d^2(\mathbf{k})} \tilde{\mathcal{H}}_0(\mathbf{k}), \quad (3.16)$$

with the similarity transformation operator expressed as

$$\mathcal{V}(\mathbf{k}) = \exp[-i\tilde{\mathcal{H}}_0(\mathbf{k})\Gamma\eta(\mathbf{k})/2]. \quad (3.17)$$

With OBCs, however, the topological phase of $\mathcal{H}_0(\mathbf{k})$ is intrinsically non-Hermitian. The intrinsic non-Hermiticity can be seen from a general solution to the chiral perturbation theory, $H = H_0 + i\lambda\Gamma$. For an eigenstate ψ_0 of H_0 with energy E_0 , $i\lambda\Gamma$ scatters it into $\Gamma\psi_0$, which is also an eigenstate of H_0 , but with opposite energy $-E_0$. Then, it is clear that any eigenstate of H is a superposition of ψ_0 and $\Gamma\psi_0$. Thus the eigenstates of H has the form,

$$\psi = a\psi_0 + b\Gamma\psi_0. \quad (3.18)$$

Solving the Schrödinger equation $H\psi = E\psi$ gives the energies as

$$E_{\pm} = \pm\sqrt{E_0^2 - \lambda^2}, \quad (3.19)$$

with the corresponding eigenstates,

$$\psi_{\pm} = \psi_0 + (iE_0/\lambda \pm \sqrt{1 - E_0^2/\lambda^2})\Gamma\psi_0. \quad (3.20)$$

If H_0 is in a topological phase, then the boundary low-energy excitations are described by massless Dirac fermions. Consequently, for arbitrarily tiny λ , there exists a region in the spectrum of H_0 where the energies are imaginary. Thus, because of the boundary massless Dirac fermions, the non-Hermitian Dirac model with open boundary conditions is intrinsically non-Hermitian.

As an aside, we remark that even arbitrarily large non-Hermitian terms $i\lambda\Gamma$ cannot remove the topological surface state. The reason for this is that $i\lambda\Gamma$ is a chiral operator, which acts only within a unit cell and does not couple different sites. In other words, the expectation value of the position operator X_i is independent of λ , i.e., $\frac{d}{d\lambda} \langle \psi_{\lambda}^{\alpha} | X_i | \psi_{\lambda}^{\beta} \rangle = 0$ with $\langle \psi_{\lambda}^{\alpha} |$ and $|\psi_{\lambda}^{\beta} \rangle$ the left and right eigenstates of H , respectively. Here α and β denote the internal degree of freedom. Hence, boundary states remain on the boundary even though their energies would be drastically changed.

Accordingly, the low-energy effective boundary theory can be generically given by

$$\mathcal{H}_b(\tilde{\mathbf{k}}) = \tilde{k}_i \gamma^i + i\lambda \gamma, \quad (3.21)$$

where $\tilde{k}_i \gamma^i$ is the boundary massless Dirac fermions of \mathcal{H}_0 , and γ is the projection of Γ into the low-energy boundary states, with $\{\gamma^i, \gamma\} = 0$. Hence, as the boundary spectrum $E_d(\tilde{k}) = \pm\sqrt{\tilde{k}^2 - \lambda^2}$, the non-Hermitian term leads to a $(d-2)$ -dimensional exceptional sphere in the boundary Brillouin zone consisting of exceptional points, and separating eigenstates with real energies from those with imaginary energies.

3.1.2 Non-Hermitian terms of type (ii)

We proceed by considering non-Hermitian kinetic terms that enter into the Dirac Hamiltonian in Eq. (3.2) with PBCs. The effects of non-Hermitian kinetic terms with PBCs can be clearly seen in the continuous version of Eq. (3.2), namely $\mathcal{H} = \mathcal{H}_0 + i\lambda\Gamma_j$ given by

$$\mathcal{H}(\mathbf{k}) = \sum_{i=1}^d k_i \Gamma_i + m\Gamma_{d+1} + i\lambda\Gamma_j, \quad (3.22)$$

with $1 \leq j \leq d$ and λ real. The energy spectrum is complex in general and is given by

$$E_{n-\mathbf{k}}(\mathbf{k}) = \pm \sqrt{\sum_{i \neq j} k_i^2 + (k_j + i\lambda)^2 + m^2}, \quad (3.23)$$

where exceptional points form a $(d-2)$ D sphere at $\sum_{i \neq j} k_i^2 = \lambda^2$ in the plane with $k_j = 0$. Hence, the Hamiltonian is intrinsically non-Hermitian in momentum space.

Next we want to study the effects of the non-Hermitian kinetic term with OBCs. Take OBCs in the j th direction, we simply replace k_j by $-i\partial_j$ to obtain $\mathcal{H}(\tilde{\mathbf{k}}, -i\partial_j)$. Then, it is obvious that

$$e^{-\lambda x_j} \mathcal{H}(\tilde{\mathbf{k}}, -i\partial_j) e^{\lambda x_j} = \mathcal{H}_0(\tilde{\mathbf{k}}, -i\partial_j), \quad (3.24)$$

namely, that the similarity transformation $e^{\lambda x_j}$ converts the Hamiltonian to be Hermitian. Accordingly, \mathcal{H} has real spectrum as that of \mathcal{H}_0 , with their eigenstates related by

$$\psi(x_j, \tilde{\mathbf{k}}) = e^{\lambda x_j} \psi_0(x_j, \tilde{\mathbf{k}}). \quad (3.25)$$

Thus, we see the continuous Dirac model with non-Hermitian kinetic terms is intrinsically non-Hermitian for PBCs, but intrinsically Hermitian for OBCs.

The conclusion holds on for Dirac lattice models with non-Hermitian kinetic perturbations. The model Hamiltonian in this case reads,

$$\mathcal{H}'(\mathbf{k}) = \mathcal{H}_0(\mathbf{k}) + i\lambda\Gamma_j = \sum_{i=1}^d \sin k_i \Gamma_i + (M - \sum_{i=1}^d \cos k_i) \Gamma_{d+1} + i\lambda\Gamma_j. \quad (3.26)$$

The corresponding real-space Dirac model of Eq. (3.5) perturbed by the non-Hermitian kinetic term,

$H = H_0 + \mathbb{1} \otimes i\lambda\Gamma_j$ reads

$$H(\tilde{\mathbf{k}}) = \frac{1}{2i}(\hat{S} - \hat{S}^\dagger) \otimes \Gamma_j - \frac{1}{2}(\hat{S} + \hat{S}^\dagger) \otimes \Gamma_{d+1} + \mathbb{1}_{N_j} \otimes \left(\sum_{i \neq j} \sin k_i \Gamma_i + (M - \sum_{i \neq j} \cos k_i) \Gamma_{d+1} + i\lambda\Gamma_j \right), \quad (3.27)$$

which is superficially non-Hermitian in real space. Note that for the part $(M - \sum_{i \neq j} \cos k_i) \Gamma_{d+1} + i\lambda\Gamma_j$ in the above Hamiltonian, the non-Hermitian term $i\lambda\Gamma_j$ can be regarded as a non-Hermitian anti-commuting perturbation. Hence, we can first convert this part to be Hermitian by the following similarity transformation,

$$\rho_i^{-1} \left[(M - \sum_{i \neq j} \cos k_i) \Gamma_{d+1} + i\lambda\Gamma_j \right] \rho_i = \sqrt{M_k^2 - \lambda^2} \Gamma_{d+1}, \quad (3.28)$$

with $M_k = M - \sum_{i \neq j} \cos k_i$. Here $\rho_i = (1 + \alpha)\mathbb{1} + i(1 - \alpha)\Gamma_j\Gamma_{d+1}$, with $\alpha = \sqrt{(M_k - \lambda)/(M_k + \lambda)}$, and its inverse is $\rho_i^{-1} = \frac{1}{4\alpha} \left[(1 + \alpha)\mathbb{1} - i(1 - \alpha)\Gamma_j\Gamma_{d+1} \right]$. Next we turn to the remaining terms in Eq. (3.27) with non-trivial spatial parts,

$$\frac{1}{2i}(\hat{S} - \hat{S}^\dagger) \otimes \Gamma_j - \frac{1}{2}(\hat{S} + \hat{S}^\dagger) \otimes \Gamma_{d+1} = \hat{S} \otimes \left(\frac{1}{2i}\Gamma_j - \frac{1}{2}\Gamma_{d+1} \right) - \hat{S}^\dagger \otimes \left(\frac{1}{2i}\Gamma_j + \frac{1}{2}\Gamma_{d+1} \right). \quad (3.29)$$

The operator ρ_i acts on the internal degree parts of terms in above equation as

$$\hat{S} \otimes \rho_i^{-1} \left(\frac{1}{2i}\Gamma_j - \frac{1}{2}\Gamma_{d+1} \right) \rho_i = \alpha \hat{S} \otimes \left(\frac{1}{2i}\Gamma_j - \frac{1}{2}\Gamma_{d+1} \right), \quad (3.30)$$

$$\hat{S}^\dagger \otimes \rho_i^{-1} \left(\frac{1}{2i}\Gamma_j + \frac{1}{2}\Gamma_{d+1} \right) \rho_i = \frac{1}{\alpha} \hat{S}^\dagger \otimes \left(\frac{1}{2i}\Gamma_j + \frac{1}{2}\Gamma_{d+1} \right). \quad (3.31)$$

We construct the spatial part similarity transformation $\rho_S = \text{diag}(1, \alpha, \alpha^2, \dots, \alpha^{N_j-1})$, which enables the transformation

$$\rho_S^{-1} (\alpha \hat{S}) \rho_S = \hat{S}, \quad (3.32)$$

$$\rho_S^{-1} \left(\frac{1}{\alpha} \hat{S}^\dagger \right) \rho_S = \hat{S}^\dagger. \quad (3.33)$$

Finally, the full similarity transformation operator can be constructed as

$$V = \rho_S \otimes \rho_i = \text{diag}(1, \alpha, \alpha^2, \dots, \alpha^{N_j-1}) \otimes [(1 + \alpha)\mathbb{1} + i(1 - \alpha)\Gamma_j\Gamma_{d+1}], \quad (3.34)$$

with $\alpha = \sqrt{(M_k - \lambda)/(M_k + \lambda)}$ and $M_k = M - \sum_{i \neq j} \cos k_i$. This similarity transformation converts the non-Hermitian Hamiltonian into

$$V^{-1} H(\tilde{\mathbf{k}}) V = \frac{1}{2i}(\hat{S} - \hat{S}^\dagger) \otimes \Gamma_j - \frac{1}{2}(\hat{S} + \hat{S}^\dagger) \otimes \Gamma_{d+1} + \mathbb{1}_{N_j} \otimes \left(\sum_{i \neq j} \sin k_i \Gamma_i + \sqrt{M_k^2 - \lambda^2} \Gamma_{d+1} \right). \quad (3.35)$$

The Hamiltonian of Eq. (3.27) is Hermitian if $M_k^2 \geq \lambda$ for all $\tilde{\mathbf{k}}$. The cases of $d = 1, 2$ with Γ_i being the Pauli matrices corresponds to the Su-Schrieffer-Heeger model and Chern insulator, respectively, and have been studied in Refs. [30, 126].

3.1.3 Non-Hermitian terms of type (iii)

Adding a non-Hermitian mass term $i\lambda\Gamma_{d+1}$ to Eq. (3.2) or (3.5) is equivalent to assuming M to be complex. In this case the spectrum is always complex no matter with PBCs or OBCs, and therefore the non-Hermitian Dirac model is really intrinsically non-Hermitian regardless of boundary conditions. Also in contrast to the previous two cases, the non-Hermitian mass terms lead to no exceptional point in both systems with PBCs and OBCs. Especially the boundary states have exactly the same real energies as those of the Hermitian Dirac models, and therefore are conservative. In other words, such non-Hermitian perturbations are irrelevant to them and only lead to renormalization of certain parameters.

We first consider the case of PBCs, the lattice Dirac model with non-Hermitian mass perturbation is given by

$$\mathcal{H}(\mathbf{k}) = \sum_{i=1}^d \sin k_i \Gamma_i + (M - \sum_{i=1}^d \cos k_i) \Gamma_{d+1} + i\lambda \Gamma_{d+1}. \quad (3.36)$$

The energy spectrum is $E(\mathbf{k}) = \pm \sqrt{\sum_{i=1}^d \sin^2 k_i + (M + i\lambda - \sum_{i=1}^d \cos k_i)^2}$, which is complex for general \mathbf{k} values.

We now turn discuss the in-gap boundary states of the perturbed Hamiltonian with OBCs, $H(\tilde{\mathbf{k}}) = H_0(\tilde{\mathbf{k}}) + \mathbb{1}_{N_j} \otimes i\lambda\Gamma_{d+1}$ with the boundary in the \mathbf{j} direction with N_j layers, where $H_0(\tilde{\mathbf{k}})$ is given by Eq. (3.5).

$$H(\tilde{\mathbf{k}}) = \frac{1}{2i}(\hat{S} - \hat{S}^\dagger) \otimes \Gamma_j - \frac{1}{2}(\hat{S} + \hat{S}^\dagger) \otimes \Gamma_{d+1} + \mathbb{1}_{N_j} \otimes \left(\sum_{i \neq j} \sin k_i \Gamma_i + (M - \sum_{i \neq j} \cos k_i) \Gamma_{d+1} \right) + \mathbb{1}_{N_j} \otimes i\lambda \Gamma_j. \quad (3.37)$$

Except for the \mathbf{j} direction, the translational symmetry in other directions is preserved. Thus we adopt the ansatz

$$|\psi_{\tilde{\mathbf{k}}}\rangle = \sum_{i=1}^{N_j} \beta^i |i\rangle \otimes |\xi_{\tilde{\mathbf{k}}}\rangle, \quad (3.38)$$

with $|\beta| < 1$ for the boundary states localized at the $i = 1$ layer. In solving the Schrödinger equation of

$$H(\tilde{\mathbf{k}})|\psi_{\tilde{\mathbf{k}}}\rangle = \hat{E}_{k_x} |\psi_{\tilde{\mathbf{k}}}\rangle, \quad (3.39)$$

we find it gives two constraints,

$$\left[\sum_{i \neq j} \sin k_i \Gamma_i + \frac{1}{2i}(\beta - \beta^{-1})\Gamma_j + (M - \sum_{i \neq j} \cos k_i - \frac{1}{2}(\beta + \beta^{-1}))\Gamma_{d+1} + i\lambda\Gamma_{d+1} \right] |\xi_{k_x}\rangle = \hat{E}_{k_x} |\xi_{k_x}\rangle \quad (3.40)$$

and

$$\left[\sum_{i \neq j} \sin k_i \Gamma_i + \frac{1}{2i}\beta\Gamma_j + (M - \sum_{i \neq j} \cos k_i - \frac{1}{2}\beta)\Gamma_{d+1} + i\lambda\Gamma_{d+1} \right] |\xi_{k_x}\rangle = \hat{E}_{k_x} |\xi_{k_x}\rangle. \quad (3.41)$$

The difference between the above two equations yields a simpler relation,

$$i\Gamma_{d+1}\Gamma_j |\xi_{k_x}\rangle = |\xi_{k_x}\rangle. \quad (3.42)$$

This means the boundary states are the positive eigenvalue of $i\Gamma_{d+1}\Gamma_j$, from which we can construct

the projector for the boundary states

$$P = \frac{1}{2} \left(1 + i\Gamma_{d+1}\Gamma_j \right). \quad (3.43)$$

With the relation of Eq. (3.42), Eq. (3.41) becomes,

$$\left[\sum_{i \neq j} \sin k_i \Gamma_i + (M - \sum_{i \neq j} \cos k_i + i\lambda - \beta) \Gamma_{d+1} \right] |\xi_{k_x}\rangle = \hat{E}_{k_x} |\xi_{k_x}\rangle, \quad (3.44)$$

and under the projection P , Eq. (3.41) also becomes,

$$\sum_{i \neq j} \sin k_i \Gamma_i |\xi_{k_x}\rangle = \hat{E}_{k_x} |\xi_{k_x}\rangle. \quad (3.45)$$

The difference between above two equations gives,

$$\beta = M - \sum_{i \neq j} \cos k_i + i\lambda. \quad (3.46)$$

We now calculate the effective boundary Hamiltonian. Remarkably, since the non-Hermitian mass term $i\lambda\Gamma_{d+1}$ anti-commutes with $i\Gamma_{d+1}\Gamma_j$ of the projector P , it will vanish after the projection. Thus, the resultant effective boundary Hamiltonian is

$$\mathcal{H}_b(\tilde{\mathbf{k}}) = \sum_{i \neq j} \sin k_i \gamma^i, \quad (3.47)$$

with $\gamma^i = P\Gamma_i P$, for $\tilde{\mathbf{k}}$ satisfying $|\beta| = |M - \sum_{i \neq j} \cos k_i + i\lambda| < 1$. Notably, the resultant boundary effective Hamiltonian $\mathcal{H}_b(\tilde{\mathbf{k}}) = \sum_{i \neq j} \sin k_i \gamma^i$ with $\gamma^i = P\Gamma_i P$ is exactly the same as that of the Hermitian Dirac model, although the range of $\tilde{\mathbf{k}}$ is modified as specified by $|M - \sum_i \cos \tilde{k}_i + i\lambda| < 1$. Since the effective boundary Hamiltonian is Hermitian, boundary spectrum is purely real with $E_b(\tilde{\mathbf{k}}) = \pm \sqrt{\sum_{i \neq j} \sin^2 k_i}$.

3.2 Representative non-Hermitian topological gapped systems

Our theory is based on the generic Dirac models, which are able to describe most topological insulators and superconductors. In principle, it can be readily adopted for various non-Hermitian topological systems. In this section, we focus on two representative models, the 2D topological insulator characterized by \mathbb{Z}_2 type topological invariant and the 4D topological insulator characterized by \mathbb{Z} type second Chern number.

3.2.1 2D quantum spin hall insulator

We start with the Hermitian 2D topological insulator, which can be described by the following Dirac model,

$$\mathcal{H}_{\text{TI},0}(\mathbf{k}) = \sin k_x \Gamma_1 + \sin k_y \Gamma_2 + (M - \cos k_x - \cos k_y) \Gamma_3, \quad (3.48)$$

where the five gamma matrices are $\Gamma_i = \sigma_i \otimes \tau_i$, $\Gamma_4 = \sigma_0 \otimes \tau_3$, $\Gamma_5 = \sigma_0 \otimes \tau_2$ ($i = 1, 2, 3$), with σ_i and τ_i Pauli matrices. This Hamiltonian is time-reversal symmetric, with the time-reversal operator given by $\hat{\mathcal{T}} = \sigma_1 \otimes \tau_2 \hat{\mathcal{K}}$ and $\hat{\mathcal{K}}$ the complex conjugation operator, which satisfies

$$\hat{\mathcal{T}}^{-1} \mathcal{H}_{\text{TI},0}(-\mathbf{k}) \hat{\mathcal{T}} = \mathcal{H}_{\text{TI},0}(\mathbf{k}). \quad (3.49)$$

The energy spectrum is obtained as $E_{\text{TI},0}(\mathbf{k}) = \pm d_{\text{TI}}(\mathbf{k})$, with $d_{\text{TI}}^2(\mathbf{k}) = \sin^2 k_x + \sin^2 k_y + (M - \cos k_x - \cos k_y)^2$, and the corresponding eigenstates are found to be,

$$\begin{aligned} |+, \uparrow\rangle &= \frac{1}{\sqrt{2}d_{\text{TI}}} \begin{pmatrix} \sin k_x - i \sin k_y, & -M(\mathbf{k}), & 0, & d_{\text{TI}} \end{pmatrix}^{\text{T}}, \\ |+, \downarrow\rangle &= \frac{1}{\sqrt{2}d_{\text{TI}}} \begin{pmatrix} M(\mathbf{k}), & \sin k_x + i \sin k_y, & d_{\text{TI}}, & 0 \end{pmatrix}^{\text{T}}, \\ |-, \uparrow\rangle &= \frac{1}{\sqrt{2}d_{\text{TI}}} \begin{pmatrix} -\sin k_x + i \sin k_y, & M(\mathbf{k}), & 0, & d_{\text{TI}} \end{pmatrix}^{\text{T}}, \\ |-, \downarrow\rangle &= \frac{1}{\sqrt{2}d_{\text{TI}}} \begin{pmatrix} -M(\mathbf{k}), & -(\sin k_x + i \sin k_y), & d_{\text{TI}}, & 0 \end{pmatrix}^{\text{T}}, \end{aligned} \quad (3.50)$$

with $M(\mathbf{k}) = M - \cos k_x - \cos k_y$ and T the matrix transposition.

As we have discussed in the introduction chapter, the \mathbb{Z}_2 topological invariant can be obtained from the Pfaffian of the antisymmetric matrix $\omega(\mathbf{k})$ at high symmetry points in the Brillouin zone, defined as

$$\omega(\mathbf{k}) = \langle -\mathbf{k}, \alpha | \hat{\mathcal{T}} | \mathbf{k}, \beta \rangle = \frac{1}{d_{\text{TI}}} \begin{pmatrix} -i \sin k_x + \sin k_y & -iM(\mathbf{k}) \\ iM(\mathbf{k}) & -i \sin k_x - \sin k_y \end{pmatrix}, \quad (3.51)$$

with α and β denoting the band index. The \mathbb{Z}_2 topological invariant can be calculated as

$$(-1)^\nu = \prod_{i=1}^4 \frac{\text{Pf } \omega(\Lambda_i)}{\sqrt{\det \omega(\Lambda_i)}}, \quad (3.52)$$

with Λ_i representing four high symmetry points of $(k_x, k_y) = (0, 0), (0, \pi), (\pi, 0), (\pi, \pi)$. From the expression of $\omega(\mathbf{k})$, we get

$$(-1)^\nu = \text{sgn}(M - 2) \text{sgn}(M + 2), \quad (3.53)$$

which is topologically non-trivial for $M \in (-2, 2)$, with $\nu = 1 \in \mathbb{Z}_2$.

Alternatively, we can use the Wilson loop approach to calculate the topological invariant, which has also been discussed in the introduction chapter and is defined as

$$\mathcal{W}(k_x) = P \exp \left(- \int_{-\pi}^{\pi} dk_y \mathbf{A}(k_x, k_y) \right). \quad (3.54)$$

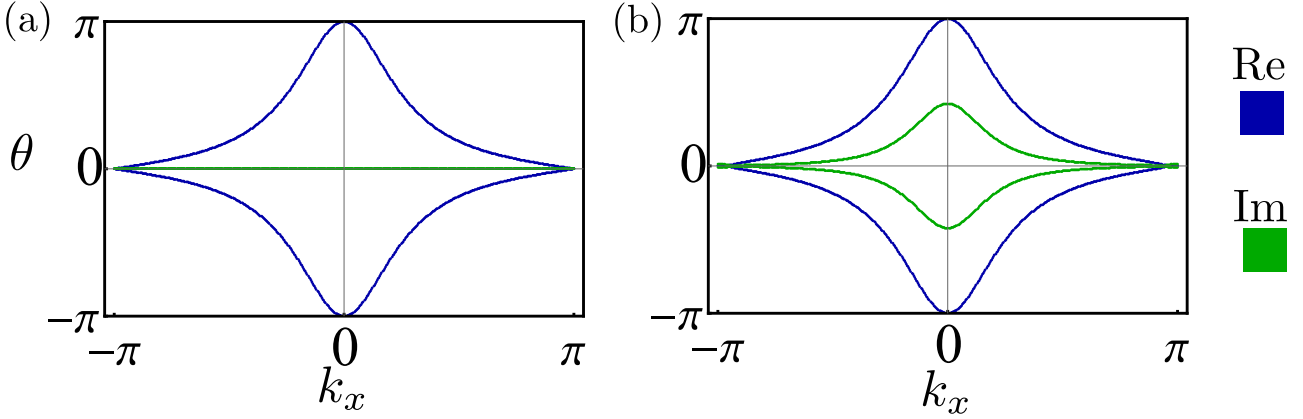


Figure 3.1: 2D topological insulator with non-Hermitian anti-commuting terms. (a) and (b) show the windings of the Wilson loop against k_x for Hermitian topological insulator with $\lambda = 0.0$ and non-Hermitian topological insulator with $\lambda = 0.3$. Here M is set to be 1.0 for both Hermitian and non-Hermitian 2D topological insulator. Blue and green indicates the real and imaginary parts of the Wilson loop, respectively.

with P the path order and $\mathbf{A}(k_x, k_y)$ the non-Abelian Berry connection

$$\mathbf{A}(k_x, k_y) = \begin{pmatrix} \langle\langle -, \uparrow | \partial_{k_y} | -, \uparrow \rangle\rangle & \langle\langle -, \uparrow | \partial_{k_y} | -, \downarrow \rangle\rangle \\ \langle\langle -, \downarrow | \partial_{k_y} | -, \uparrow \rangle\rangle & \langle\langle -, \downarrow | \partial_{k_y} | -, \downarrow \rangle\rangle \end{pmatrix}, \quad (3.55)$$

for the occupied bands. In Fig. 3.1 (a), we show the eigenvalues θ of the Wilson loop $-i \log \mathcal{W}(k_x)$ for the Hermitian 2D topological insulator, where the non-trivial winding indicates the phase is topologically non-trivial according to Sec. 1.2.3.

Next we turn to considering different non-Hermitian perturbations that enter into the 2D topological insulator. The 2D topological insulator with \mathbb{Z}_2 topological invariant is a good candidate to study non-Hermitian effects, as it can host all the three different non-Hermitian perturbations, (i) the non-Hermitian anti-commuting terms, (ii) the non-Hermitian kinetic terms, and (iii) the non-Hermitian mass terms. In the following, we discuss these non-Hermitian perturbations in detail.

Non-Hermitian term of type (i)

We first consider the 2D topological insulator with a non-Hermitian anti-commuting perturbation $i\lambda\Gamma_4$ with PBCs. The non-Hermitian Hamiltonian in momentum space reads

$$\mathcal{H}_{\text{TI}}(\mathbf{k}) = \mathcal{H}_{\text{TI},0}(\mathbf{k}) + i\lambda\Gamma_4, \quad (3.56)$$

with the anti-commutation relation of $\{\Gamma_4, \mathcal{H}_{\text{TI},0}(\mathbf{k})\}$. The energy eigenvalues and eigenstates can be obtained by direct calculations, or alternatively, it can be determined by our theory in Sec. 3.1.1. As the non-Hermitian perturbation scatters eigenstates ψ_0 to $\Gamma_4\psi_0$, the spectrum becomes

$$E_{\text{TI}}(\mathbf{k}) = \pm \sqrt{d_{\text{TI}}^2(\mathbf{k}) - \lambda^2}, \quad (3.57)$$

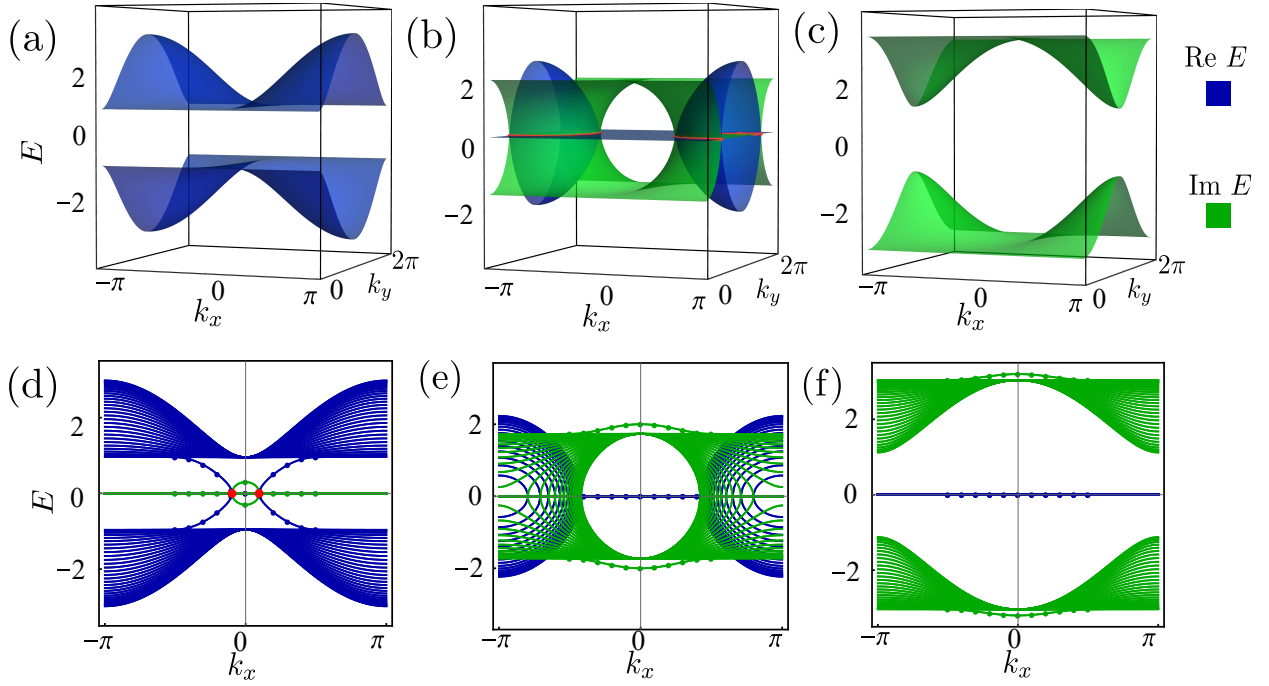


Figure 3.2: Spectra for 2D topological insulator with non-Hermitian anti-commuting terms. (a), (b) and (c) are the bulk spectra for $\lambda^2 < \min d_{\text{TI}}(\mathbf{k})^2$, $\min d_{\text{TI}}(\mathbf{k})^2 < \lambda^2 < \max d_{\text{TI}}(\mathbf{k})^2$ and $d_{\text{TI}}(\mathbf{k})^2 < \lambda^2$. (d), (e) and (f) are the corresponding spectra for the open boundary Hamiltonian. Here M is set to be 1.0, and λ is set to be 0.3, 2.0 and 3.2 for (a), (b) and (c), respectively. Blue and green indicates the real and imaginary parts of the energy spectrum respectively. Red denotes the position of exceptional points.

and the corresponding right eigenstates are modified as

$$\psi_{\pm} = \psi_0 + (iE_{\text{TI},0}/\lambda \pm \sqrt{1 - E_{\text{TI},0}^2/\lambda^2})\Gamma_4\psi_0, \quad (3.58)$$

with ψ_0 given in Eq. (3.50).

For $d_{\text{TI}}^2(\mathbf{k}) > \lambda^2$, the spectrum is purely real in momentum space, thus according to the similarity transformation constructed in Sec. 3.1.1, the Hamiltonian in Eq. (3.56) can be converted to be Hermitian by

$$\mathcal{V}(\mathbf{k})^{-1}\mathcal{H}_{\text{TI}}(\mathbf{k})\mathcal{V}(\mathbf{k}) = \sqrt{1 - \frac{\lambda^2}{d_{\text{TI}}^2(\mathbf{k})}}\mathcal{H}_{\text{TI},0}(\mathbf{k}), \quad (3.59)$$

where $\mathcal{V}(\mathbf{k}) = \exp[-\frac{i}{2}\mathcal{H}_{\text{TI},0}(\mathbf{k})\Gamma_4\eta_{\text{TI}}(\mathbf{k})/d_{\text{TI}}(\mathbf{k})]$, with $e^{\eta_{\text{TI}}(\mathbf{k})} = \sqrt{(d_{\text{TI}}(\mathbf{k}) + \lambda)/(d_{\text{TI}}(\mathbf{k}) - \lambda)}$. The matrix form of $\mathcal{V}(\mathbf{k})$ is,

$$\mathcal{V}(\mathbf{k}) = \cosh \frac{\eta_{\text{TI}}(\mathbf{k})}{2} - i \sinh \frac{\eta_{\text{TI}}(\mathbf{k})}{2} \mathcal{H}_{\text{TI},0}(\mathbf{k})\Gamma_4/d_{\text{TI}}(\mathbf{k}). \quad (3.60)$$

The energy spectrum in momentum space is plotted in Fig. 3.2 (a), which is purely real.

The eigenstates can also be obtained from the similarity transformation in Eq. (3.60). Suppose $|u_n\rangle$

and $E_n(\mathbf{k})$ represent the eigenstates and eigenenergies of the Hermitian Hamiltonian $\mathcal{H}_{\text{TI},0}(\mathbf{k})$ for n th band, then the eigenstates and eigenenergies of the non-Hermitian Hamiltonian $\mathcal{H}_{\text{TI}}(\mathbf{k})$ can be obtained as

$$|u'_n\rangle = \mathcal{V}(\mathbf{k})|u_n\rangle, \quad E'_n = \sqrt{E_n^2(\mathbf{k}) - \lambda^2}. \quad (3.61)$$

We will see the similarity transformation has a significant impact on the topological invariant. As we have discussed, the Wilson loop is obtained by the Berry connection $\mathbf{A}_{m,n} = \langle u_m | \nabla_{\mathbf{k}} | u_n \rangle$. According to eigenstates obtained from the similarity transformation in Eq. (3.61), the Berry connection for the non-Hermitian Hamiltonian $\mathcal{H}_{\text{TI}}(\mathbf{k})$ can be obtained as

$$\langle \langle u'_m | \nabla_{\mathbf{k}} | u'_n \rangle \rangle = \mathbf{A}_{m,n} + \langle u_m | \mathcal{V}(\mathbf{k})^{-1} \nabla_{\mathbf{k}} \mathcal{V}(\mathbf{k}) | u_n \rangle. \quad (3.62)$$

Different with unitary transformations, the second term at RHS above cannot be canceled after a loop integration and hence the topological invariants are not quantized. Thus the topological invariants in non-Hermitian systems are generally not quantized. In Fig. 3.1 (b), then we can see that the eigenvalues θ of the Wilson loop $-i \log \mathcal{W}(k_x)$ for the non-Hermitian 2D topological insulator will acquire an imaginary part, which can be understood as the effect of the non-unitary similarity transformation.

Now we proceed to consider the real space Hamiltonian with OBCs. Taking open boundary conditions in $\hat{\mathbf{y}}$ direction, the real space Hamiltonian reads,

$$H_{\text{TI}}(k_x) = \frac{1}{2i} (\hat{S} - \hat{S}^\dagger) \otimes \Gamma_2 - \frac{1}{2} (\hat{S} + \hat{S}^\dagger) \otimes \Gamma_3 + \mathbb{1}_{N_y} \otimes (\sin k_x \Gamma_1 + (M - \cos k_x) \Gamma_3) + \mathbb{1}_{N_y} \otimes i\lambda \Gamma_4. \quad (3.63)$$

Here \hat{S} and \hat{S}^\dagger are the forward and backward translation operators in \mathbf{y} direction, which let $\hat{S}|i\rangle = |i+1\rangle$ and $\hat{S}^\dagger|i\rangle = |i-1\rangle$, where i labels the i th site in the \mathbf{y} direction.

Following a similar procedure as that in Sec. 3.1.3, the effective boundary Hamiltonian can be obtained as

$$\mathcal{H}_{\text{TI,b}}(k_x) = P \mathcal{H}_{\text{TI}}(\mathbf{k}) P = \sin k_x \gamma^1 + i\lambda \gamma^4, \quad (3.64)$$

with $\gamma^1 = P \Gamma_1 P$ and $\gamma^4 = P \Gamma_4 P$, for k_x in the region of $|\beta| = |M - \cos k_x| < 1$. The boundary spectrum thus can be obtained, $E_{\text{TI,b}}(k_x) = \pm \sqrt{\sin^2 k_x - \lambda^2}$. It is noticed that for $|\lambda| \leq 1$, there are exceptional points of second order on the boundary located at $k_x = \pm \arcsin |\lambda|$, as shown in Fig. 3.2 (d), which have been highlighted in red. The property of exceptional points will be discussed in Sec. 3.4. The boundary states behave exactly as anticipated from our theory in Sec. 3.1.1.

It is also interesting to investigate the cases of larger non-Hermitian potential. From Fig. 3.2 (a) to (c), with increasing λ , the bulk system is gapped with purely real spectrum, gapless with both real and imaginary spectrum, and gapless with purely imaginary spectrum. The corresponding boundary states denoted by dotted lines are shown in Fig. 3.2 (d) to (f), which exist even when the bulk becomes gapless. These boundary states are gapless and have the same localization property as the original Hermitian topological boundary states according to our theory.

Non-Hermitian term of type (ii)

We consider the non-Hermitian perturbation that commutes with the kinetic term $\sin k_y \Gamma_2$ in the model of 2D topological insulator and first consider the case of PBCs. In momentum space the Hamiltonian reads

$$\mathcal{H}_{\text{TI}}(\mathbf{k}) = \sin k_x \Gamma_1 + \sin k_y \Gamma_2 + (M - \cos k_x - \cos k_y) \Gamma_3 + i\lambda \Gamma_2. \quad (3.65)$$

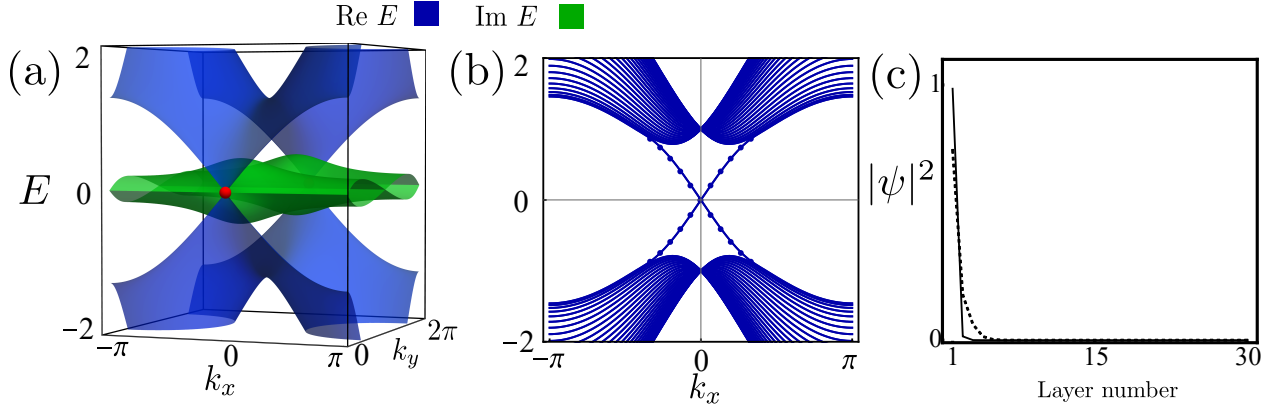


Figure 3.3: Spectra for 2D topological insulator with non-Hermitian kinetic terms. (a) and (b) are the spectra for PBCs and OBCs, respectively. The parameters are set as $\lambda = 0.5$ and $M = 1.5$, so that the open boundary spectrum is purely real and there are exceptional points emerging in the bulk. The blue and green denote real and imaginary parts of the spectrum. The exceptional points are highlighted in red. (c) The wavefunction profile of the right eigenvector for boundary (solid) and bulk (dashed) states.

In momentum space, the energy spectrum can be obtained as $E_{\text{TI}}(\mathbf{k}) = \pm(\sin^2 k_x + \sin^2 k_y + (M - \cos k_x - \cos k_y)^2 - \lambda^2 + 2i\lambda \sin k_y)^{1/2}$, which is complex in general. The band crossing takes place at $\sin k_y = 0$ and $\sin^2 k_x + (M - \cos k_x - \cos k_y)^2 - \lambda^2 = 0$, which forms a zero dimensional exceptional sphere, i.e., exceptional points as shown by the red points in Fig. 3.3 (a).

Next we discuss the case of OBCs. According to our theory in Sec. 3.1.2, the 2D topological insulator with non-Hermitian kinetic term is superficially non-Hermitian in real space with open boundary conditions, namely, the non-Hermitian Hamiltonian can be converted to be Hermitian by non-unitary similarity transformations. From the bulk Hamiltonian in Eq. (3.65), by taking open boundary condition in y direction with N_y layers, the real space Hamiltonian reads,

$$H_{\text{TI}}(k_x) = \frac{1}{2i} (\hat{S} - \hat{S}^\dagger) \otimes \Gamma_2 - \frac{1}{2} (\hat{S} + \hat{S}^\dagger) \otimes \Gamma_3 + \mathbb{1}_{N_y} \otimes (\sin k_x \Gamma_1 + (M - \cos k_x) \Gamma_3) + \mathbb{1}_{N_y} \otimes i\lambda \Gamma_2. \quad (3.66)$$

We can readily adapt the similarity transformation operator developed in Eq. (3.34) for this non-Hermitian Hamiltonian, which is

$$V = \text{diag}(1, \alpha, \alpha^2, \dots, \alpha^{N_y-1}) \otimes [(1 + \alpha) \mathbb{1} + i(1 - \alpha) \Gamma_2 \Gamma_3], \quad (3.67)$$

with $\alpha = \sqrt{(M_k - \lambda)/(M_k + \lambda)}$ and $M_k = M - \cos k_x$. Under this similarity transformation, the Hamiltonian becomes,

$$H'_{\text{TI}}(k_x) = V^{-1} H_{\text{TI}}(k_x) V = \frac{1}{2i} (\hat{S} - \hat{S}^\dagger) \otimes \Gamma_2 - \frac{1}{2} (\hat{S} + \hat{S}^\dagger) \otimes \Gamma_3 + \mathbb{1}_{N_y} \otimes (\sin k_x \Gamma_1 + \sqrt{M_k^2 - \lambda^2} \Gamma_3), \quad (3.68)$$

which is Hermitian for $\lambda^2 < M_k^2$, and the spectrum is purely real in this region. As can be seen in Fig. 3.3 (b), the open boundary spectrum is purely real, where the parameters are chosen as $\lambda = 0.5$ and $M = 1.5$, so that the Hermitian condition of $\lambda^2 < M_k^2$ is satisfied for the similarity transformed Hamiltonian above.

With a closer observation of the spatial part of the similarity transformation operator in Eq. (3.67), one can find that for $\alpha < 1$, i.e., $|(M_k - \lambda)/(M_k + \lambda)| < 1$, the spatial part of this operator decays with increasing layer number. This decay has a significant effect on the wavefunction amplitude. Suppose that the eigenstates of the transformed Hermitian $H'_{\text{TI}}(k_x)$ are denoted as ψ' , which represent both extended bulk and localized boundary states. The right eigenstates of the original non-Hermitian $H_{\text{TI}}(k_x)$ can be obtained as $V\psi'$. The decaying factor in V is imposed on all eigenstates, both bulk and boundary. As a result, both the bulk and boundary states are localized at the boundary, which is dubbed as "non-Hermitian skin effect" [30, 126]. In Fig. 3.3 (c), we show the wavefunction profile for a boundary state and a randomly chosen bulk state, which all localize on the edge.

Next we turn to calculate the surface spectrum. Following a similar procedure as that in Sec. 3.1.3, the effective boundary Hamiltonian can be obtained as

$$\mathcal{H}_b(k_x) = \sin k_x \gamma^1, \quad (3.69)$$

where γ^1 is given by the projection $\gamma^1 = P\Gamma_1P$, with $P = \frac{1}{2}(1 + i\Gamma_3\Gamma_2)$. We find that the boundary modes are localized in the region of $|(M - \cos k_x)^2 - \lambda^2| < 1$, which is obtained by the method of biorthogonal bulk-boundary correspondence from Ref. [127]. The boundary states are denoted by the dotted lines in Fig. 3.3 (b).

Non-Hermitian term of type (iii)

Let us now discuss the 2D topological insulator with a non-Hermitian mass term. The Hamiltonian in momentum space reads,

$$\mathcal{H}_{\text{TI}}(\mathbf{k}) = \sin k_x \Gamma_1 + \sin k_y \Gamma_2 + (M - \cos k_x - \cos k_y) \Gamma_3 + i\lambda \Gamma_3. \quad (3.70)$$

The energy spectrum can be obtained as $E_{\text{TI}}(\mathbf{k}) = \pm(\sin^2 k_x + \sin^2 k_y + (M + \lambda - \cos k_x - \cos k_y)^2)^{1/2}$, which is complex in general. In Fig. 3.4 (a) and (b), we show the real and imaginary parts of the bulk band spectrum. With open boundary condition in \hat{y} direction with N_y layers, the real space Hamiltonian reads,

$$H_{\text{TI}}(k_x) = \frac{1}{2i} (\hat{S} - \hat{S}^\dagger) \otimes \Gamma_2 - \frac{1}{2} (\hat{S} + \hat{S}^\dagger) \otimes \Gamma_3 + \mathbb{1}_{N_y} \otimes (\sin k_x \Gamma_1 + (M - \cos k_x) \Gamma_3) + \mathbb{1}_{N_y} \otimes i\lambda \Gamma_3. \quad (3.71)$$

The real and imaginary parts of the open boundary spectrum, corresponding to the bulk spectrum in (a) and (b), are shown in Fig. 3.4 (c) and (d). Clearly, the band spectrum is complex in general and there is no exceptional points emerging in the band structure. The complex spectra of both bulk and open boundary system is not unexpected, as the non-Hermitian mass term can be viewed as making M complex.

Following a similar procedure as in Sec. 3.1.3, the effective boundary Hamiltonian can be obtained as

$$\mathcal{H}_b(k_x) = \sin k_x \gamma^1, \quad (3.72)$$

where γ^1 is given by the projection $\gamma^1 = P\Gamma_1P$, with $P = \frac{1}{2}(1 + i\Gamma_3\Gamma_2)$. Notice that the non-Hermitian mass term vanishes in obtaining the effective boundary Hamiltonian. Thus the boundary spectrum is purely real. We emphasize that the localization region of the boundary states is changed to $|M - \cos k_x + i\lambda| < 1$. The boundary spectrum is $E_{\text{TI, B}} = \pm \sin k_x$, plotted with dotted lines in Fig. 3.4 (c).

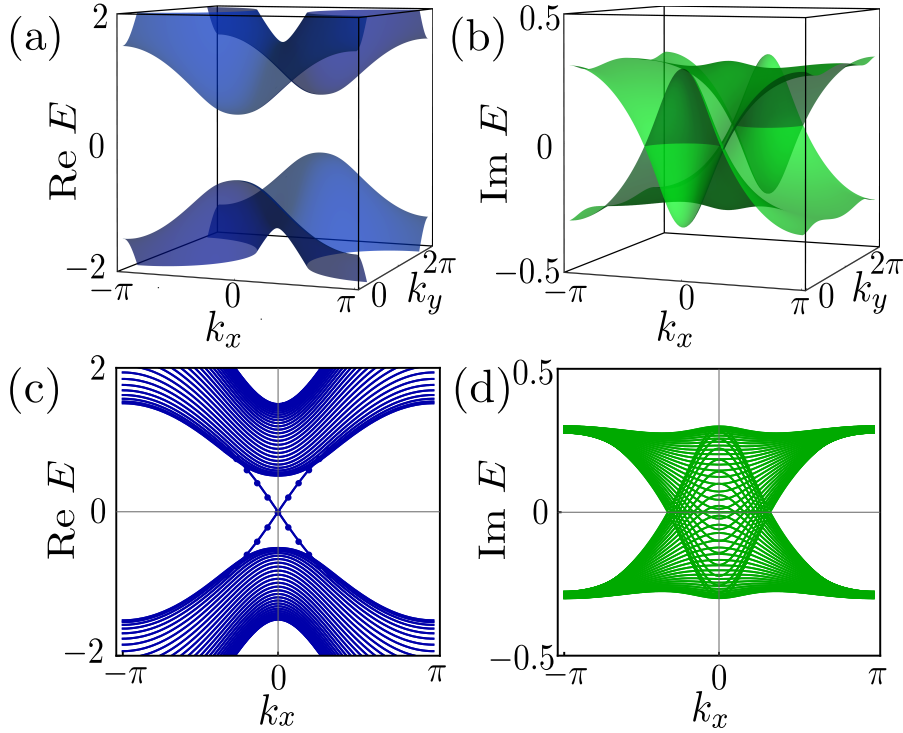


Figure 3.4: (a),(c) Real and (b),(d) imaginary parts of the energy spectra of the two-dimensional topological insulator $H_{\text{TI},0}$ perturbed by the non-Hermitian mass term $i\lambda\Gamma_3$ with periodic and open boundary conditions, respectively. The parameters are chosen as $M = 1.5$ and $\lambda = 0.3$. Solid and dotted lines represent bulk and surface states, respectively.

3.2.2 4D topological insulator characterized by the second Chern number

In this subsection we discuss the 4D topological insulator which is characterized by the second Chern number. Similar to the 2D topological Chern insulator as introduced in the first chapter, a topological term, which is called the second Chern-Simons term, appears in the effective action. Here we briefly review the process of obtaining this term. The path integral for the partition function in $(4+1)$ -dimensional spacetime without the gauge field reads,

$$Z_0 = \int D\psi D\psi^\dagger e^{i\psi^\dagger(p_0 - H(p_i))\psi} \propto \det G_0^{-1}, \quad (3.73)$$

with the Green's function $G_0^{-1}(p) = p_0 - H(p_i)$. Now coupling to a $U(1)$ external gauge field A , the path integral becomes,

$$Z_A \propto \det G_A^{-1}, \quad (3.74)$$

with

$$G_A^{-1}(p, A) = G_0^{-1}(p - eA) \approx G_0^{-1}(p) - eA_\mu \partial_{p_\mu} G_0^{-1}(p), \quad (3.75)$$

where we do the expansion to the first order. The effective action of the gauge field A^μ is obtained from $Z_A = e^{iS_{\text{eff}}}$, which gives $S_{\text{eff}} = \log \det(G_0^{-1}(p) - eA_\mu \partial_{p_\mu} G_0^{-1}(p))$. The effective action is equivalent to

$$S_{\text{eff}} = -\text{tr} \log(G_0) + \text{tr} \log[1 + G_0 \Sigma], \quad (3.76)$$

with $\Sigma = -eA_\mu \partial_{p_\mu} G_0^{-1}(p)$. After the expansion of the second term, the effective action becomes

$$S_{\text{eff}} = -\text{tr} \log(G_0) + \text{tr}(G_0 \Sigma) - \frac{1}{2} \text{tr}(G_0 \Sigma G_0 \Sigma) + \frac{1}{3} \text{tr}(G_0 \Sigma G_0 \Sigma G_0 \Sigma) + \dots \quad (3.77)$$

By calculating these terms in $(4+1)$ -dimensional spacetime, a topological term similar to the $(2+1)$ -dimensional Chern-Simons term arises, which reads [146],

$$S_{\text{CS}} = \frac{C_2}{24\pi^2} \int d^5x \varepsilon^{\mu\nu\rho\sigma\tau} A_\mu \partial_\nu A_\rho \partial_\sigma A_\tau, \quad (3.78)$$

with $\mu, \nu, \rho, \sigma, \tau = 0, 1, 2, 3, 4$. The coefficient reads,

$$C_2 = -\frac{\pi^2}{15} \varepsilon^{\mu\nu\rho\sigma\tau} \int \frac{d^5p}{(2\pi)^5} \text{tr} \left[G_0 \partial_{q_\mu} G_0^{-1} G_0 \partial_{q_\nu} G_0^{-1} G_0 \partial_{q_\rho} G_0^{-1} G_0 \partial_{q_\sigma} G_0^{-1} G_0 \partial_{q_\tau} G_0^{-1} \right], \quad (3.79)$$

which is called the second Chern number.

The lattice Hamiltonian for the 4D Chern insulator with PBCs in momentum spaces

$$\mathcal{H}(\mathbf{k}) = \sin k_x \Gamma_1 + \sin k_y \Gamma_2 + \sin k_z \Gamma_3 + \sin k_w \Gamma_4 + (M - \cos k_x - \cos k_y - \cos k_z - \cos k_w) \Gamma_5, \quad (3.80)$$

with x, y, z, w as spatial dimensions and $\Gamma_\mu, \mu = 1, 2, \dots, 5$ five Dirac matrices satisfying Clifford algebra $\{\Gamma_\mu, \Gamma_\nu\} = 2\delta_{\mu,\nu}$. We denote the vector

$$\mathbf{d} = \{\sin k_x, \sin k_y, \sin k_z, \sin k_w, (M - \cos k_x - \cos k_y - \cos k_z - \cos k_w)\}. \quad (3.81)$$

The topological invariant is given by the second Chern number obtained from Eq. (3.79),

$$C_2 = \frac{3}{8\pi^2} \int d^4k \varepsilon^{abcde} \hat{d}_a \partial_x \hat{d}_b \partial_y \hat{d}_c \partial_z \hat{d}_d \partial_w \hat{d}_e, \quad (3.82)$$

where \hat{d}_a are components of the vector $\hat{\mathbf{d}} = \mathbf{d}/|\mathbf{d}|$. By direct calculations, we find the regions $0 < M < 2$, $2 < M < 4$ and $4 < M$ have different topological phases, as indicated by the topological invariant

$$C_2 = 3, \quad 0 < M < 2; \quad (3.83)$$

$$C_2 = -1, \quad 2 < M < 4; \quad (3.84)$$

$$C_2 = 0, \quad 4 < M. \quad (3.85)$$

non-Hermitian 4D topological insulator

For the 4D topological insulator, there is no anti-commuting non-Hermitian perturbation, since there exists no sixth Dirac matrix. We thus focus on non-Hermitian kinetic terms, which is superficially non-Hermitian in real space. Including non-Hermitian kinetic perturbation $i\lambda\Gamma_2$ and taking the open

boundary condition in y direction, the real space Hamiltonian reads,

$$H_{4\text{DTI}} = \frac{1}{2i}(\widehat{S} - \widehat{S}^\dagger) \otimes \Gamma_2 - \frac{1}{2}(\widehat{S} + \widehat{S}^\dagger) \otimes \Gamma_5 + \mathbb{1} \otimes [\sin k_x \Gamma_1 + \sin k_z \Gamma_3 + \sin k_w \Gamma_4 + (M - \cos k_x - \cos k_z - \cos k_w) \Gamma_5 + i\lambda \Gamma_2]. \quad (3.86)$$

Adopt the standard procedure as discussed in Sec. 3.1.2, we can construct the real space similarity transformation operator as

$$V = \rho_S \otimes \rho_i = \text{diag}(1, \alpha, \alpha^2, \dots, \alpha^{N_y-1}) \otimes [(1 + \alpha)\mathbb{1} + i(1 - \alpha)\Gamma_2\Gamma_5], \quad (3.87)$$

with

$$\alpha = \frac{(M - \cos k_x - \cos k_z - \cos k_w) - \lambda}{(M - \cos k_x - \cos k_z - \cos k_w) + \lambda}. \quad (3.88)$$

The similarity transformed Hamiltonian is

$$V^{-1}H_{4\text{DTI}}V = \frac{1}{2i}(\widehat{S} - \widehat{S}^\dagger) \otimes \Gamma_2 - \frac{1}{2}(\widehat{S} + \widehat{S}^\dagger) \otimes \Gamma_5 + \mathbb{1} \otimes \left[\sin k_x \Gamma_1 + \sin k_z \Gamma_3 + \sin k_w \Gamma_4 + \sqrt{(M - \cos k_x - \cos k_z - \cos k_w)^2 - \lambda^2} \Gamma_5 \right], \quad (3.89)$$

which is Hermitian for $|M - \cos k_x - \cos k_z - \cos k_w| > \lambda$. Suppose that $M - \cos k_x - \cos k_z - \cos k_w$ is larger than zero throughout the surface Brillouin zone, then its minimum value is approached at the high symmetry points of $(k_x, k_z, k_w) = (0, 0, 0)$, which is $M - 3$. For the similarity transformed Hamiltonian to be purely Hermitian, in this case, it is required that $M - 3 > \lambda$.

3.3 Effects of boundary conditions in non-Hermitian lattice systems

In our theory, we show that the boundary conditions of PBCs and OBCs make an important difference in classifying types of non-Hermitian terms. In non-Hermitian systems, the spectra for systems with PBCs and OBCs can be strikingly different [30], while for Hermitian systems, they are basically the same. It is thus necessary to study the boundary conditions in detail. In this section, we discuss the different boundary conditions with a general non-Hermitian tight-binding model [144, 147].

In d dimensional space, in order to investigate the boundary modes, a non-Hermitian tight-binding model with open boundary conditions in one direction should be considered. In the remaining $d - 1$ directions, periodic boundary conditions are assumed so that the crystal momenta in these directions (denoted by \mathbf{k}_\perp) are still good quantum numbers. Taking open boundary conditions with N unit cells in the direction with OBCs, the quasi one-dimensional Hamiltonian can be written as

$$\mathcal{H}(\mathbf{k}_\perp) = \sum_{n=0}^N \left(J_L \mathbf{c}_n^\dagger \mathbf{c}_{n+1} + M \mathbf{c}_n^\dagger \mathbf{c}_n + J_R^\dagger \mathbf{c}_{n+1}^\dagger \mathbf{c}_n \right). \quad (3.90)$$

Here, some simplifications are made. Only hoppings between nearest neighbors are considered, with the left and right hoppings described by J_L and J_R , and M is the onsite potential. Such simplification is justified as large supercells can always be chosen so that there's only nearest hopping between them.

\mathbf{c}_n^\dagger and \mathbf{c}_n are the creation and annihilation operators for the supercells. In non-Hermitian systems, the hopping matrices are assumed to be $J_L = J_R = J$, and can be tuned to satisfy $J^2 = 0$ as in Ref. [144]. The non-Hermiticity of the Hamiltonian is assumed to be carried by M .

A single particle state can be denoted as $|\psi\rangle = \sum_{n=0}^N \Psi_n \mathbf{c}_n^\dagger |0\rangle$, with $|0\rangle$ the vacuum state. From the Schrödinger equation

$$\mathcal{H}(\mathbf{k}_\perp)|\psi\rangle = \varepsilon|\Psi\rangle, \quad (3.91)$$

the following recursive equation can be obtained

$$J\Psi_{n+1} + M\Psi_n + J^\dagger\Psi_{n-1} = \varepsilon\Psi_n, \quad (3.92)$$

where the hopping matrix J can be decomposed by singular value decomposition (SVD), which is,

$$J = V\Xi W^\dagger. \quad (3.93)$$

Here $\Xi = \text{diag}\{\xi_1, \xi_2, \dots, \xi_r\}$, with ξ_i positive real. Notice that r is the rank of J , $r = \text{rank}J$. The expressions for V and W are $V = \{v_1, v_2, \dots, v_r\}$, $W = \{w_1, w_2, \dots, w_r\}$, which satisfy the relations $V^\dagger V = W^\dagger W = 1$, $V^\dagger W = 0$. The first two relations follow from the definition of SVD, while the third relation comes from the nilpotent property of J , i.e., $J^2 = 0$.

Rewriting the relation in Eq. (3.92) in terms of the on-site Green's function $\mathcal{G} = \frac{1}{\varepsilon - M}$ gives $\Psi_n = \mathcal{G}J\Psi_{n+1} + \mathcal{G}J^\dagger\Psi_{n-1}$. Using the expression for J in Eq.(3.93), we obtain

$$\Psi_n = \mathcal{G}V\Xi W^\dagger\Psi_{n+1} + \mathcal{G}W\Xi V^\dagger\Psi_{n-1}. \quad (3.94)$$

To construct the transfer matrix, the substitution of $\alpha_n = V^\dagger\Psi_n$, $\beta_n = W^\dagger\Psi_n$ is used. By multiplying V^\dagger and W^\dagger to Eq. (3.94), the following relation can be obtained

$$\Phi_{n+1} = T\Phi_n, \quad \Phi_n = \begin{pmatrix} \beta_n \\ \alpha_{n-1} \end{pmatrix}, \quad (3.95)$$

with the transfer matrix

$$T = \begin{pmatrix} \Xi^{-1}\mathcal{G}_{vw}^{-1} & -\Xi^{-1}\mathcal{G}_{vw}^{-1}\mathcal{G}_{ww}\Xi \\ \mathcal{G}_{vv}\mathcal{G}_{vw}^{-1} & (\mathcal{G}_{vv} - \mathcal{G}_{vv}\mathcal{G}_{vw}^{-1}\mathcal{G}_{ww})\Xi \end{pmatrix}, \quad (3.96)$$

where $\mathcal{G}_{AB} = B^\dagger\mathcal{G}A$ with $A, B \in \{V, W\}$.

With the transfer matrix T , the following relation can be formulated between Φ_0 and Φ_n ,

$$\Phi_n = T^n\Phi_0, \quad (3.97)$$

with $n \in \mathbb{Z}$.

The difference between PBCs and OBCs spectra can be seen even for case $r = \text{rank}J = 1$. In this case, Ξ is a complex number ξ , and the transfer matrix T is just a two dimensional complex matrix [144, 147],

$$T = \frac{1}{\xi\mathcal{G}_{vw}} \begin{pmatrix} 1 & -\xi\mathcal{G}_{ww} \\ \xi\mathcal{G}_{vv} & \xi^2(\mathcal{G}_{vv}\mathcal{G}_{vw} - \mathcal{G}_{vv}\mathcal{G}_{ww}) \end{pmatrix}. \quad (3.98)$$

The eigenvalues of T are denoted as ρ_{\pm} , which satisfy the relation,

$$\text{tr } T = \rho_+ + \rho_-, \quad \det T = \rho_+ \rho_-. \quad (3.99)$$

In the following the condition for bulk states in PBCs and OBCs are discussed based on the transfer matrix.

- Under PBCs, for a system with N supercells, the following relation should be satisfied,

$$\Phi_n = \Phi_{n+N} \rightarrow \Phi_n = T^N \Phi_n. \quad (3.100)$$

Thus $1 \in \text{Spec}[T^N]$, here Spec means the spectrum. Accordingly, the eigenvalues of T have the form $e^{i\phi}$, where $\phi = 2\pi l/N$ with l integer. Denote $\rho_+ = e^{i\phi}$, from Eq. (3.99), the following relation can be derived for PBCs,

$$\text{tr } T = e^{i\phi} + \det T e^{-i\phi}. \quad (3.101)$$

- Under OBCs, for a system with N supercells, at the boundary the wavefunction vanishes ($\Psi_0 = \Psi_{N+1} = 0$). From the transfer matrix, the following relation can be found

$$\begin{pmatrix} 0 \\ \alpha_N \end{pmatrix} = T^N \begin{pmatrix} \beta_1 \\ 0 \end{pmatrix} \quad (3.102)$$

For $r = 1$, this can be solved analytically. Here we adopt the results obtained in Ref. [144], with the relation for OBCs as

$$\text{tr } T = 2\sqrt{\det T} \cos \phi. \quad (3.103)$$

The condition for the PBCs and OBCs bulk spectrum to be identical is that $\det T$ is unimodular, i.e.,

$$|\det T| = 1. \quad (3.104)$$

This can be seen by expressing $\det T = e^{-2i\chi}$, then the conditions for PBCs (Eq. (3.101)) and OBCs (Eq. (3.103)) becomes identical, i.e., $\text{tr } T = 2e^{-i\chi} \cos \phi$. In the following, we will give two examples where $|\det T|$ is and is not unimodular.

Su-Schrieffer–Heeger model with kinetic non-Hermitian terms

We take the Su-Schrieffer–Heeger (SSH) model as an example to illustrate the above concepts. In momentum space, with the non-Hermitian kinetic term, the Hamiltonian reads,

$$\mathcal{H}_{\text{SSH}}(\mathbf{k}) = (t_1 + t_2 \cos k)\sigma_1 + t_2 \sin k \sigma_2 + i\lambda \sigma_2. \quad (3.105)$$

For $\lambda = 0$, the system is topological for $|t_1| < |t_2|$. Taking open boundary conditions with N unit cells, we can get the corresponding Hamiltonian as

$$\mathcal{H}_{\text{SSH}} = \sum_{n=0}^N \left(J \mathbf{c}_n^\dagger \mathbf{c}_{n+1} + M \mathbf{c}_n^\dagger \mathbf{c}_n + J^\dagger \mathbf{c}_{n+1}^\dagger \mathbf{c}_n \right), \quad (3.106)$$

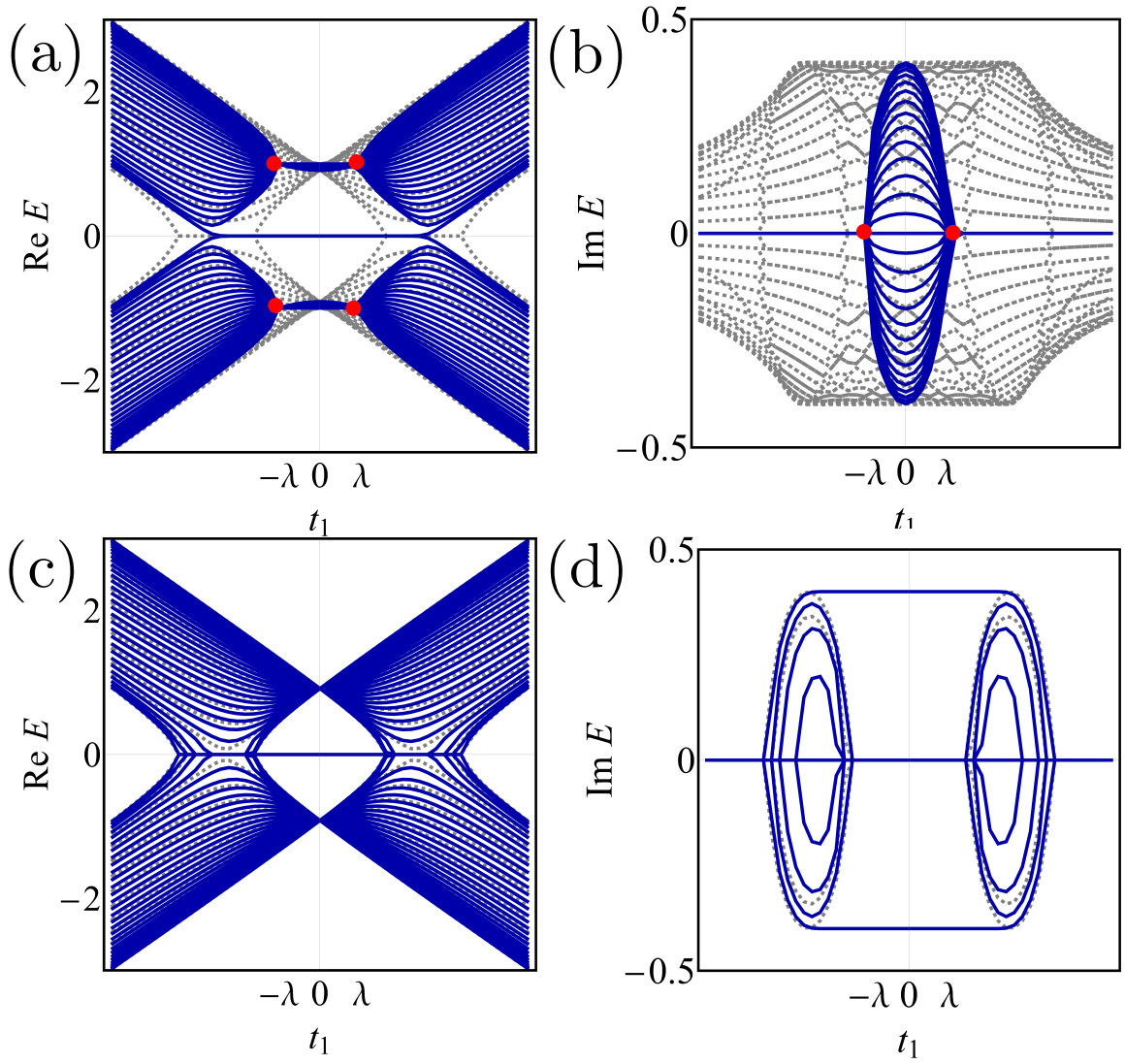


Figure 3.5: (a) real and (b) imaginary parts of the spectrum of the SSH model with non-Hermitian kinetic term $i\lambda\sigma_2$. (c) real and (d) imaginary parts of the spectrum of the SSH model with non-Hermitian anti-commuting term $i\lambda\sigma_3$. Solid blue represents the spectrum with OBCs, while dashed gray represent spectrum with PBCs. The red dots denote the exceptional points.

with

$$J = \frac{t_2}{2}\sigma_1 + \frac{t_2}{2i}\sigma_2 = \begin{pmatrix} 0 & 0 \\ t_2 & 0 \end{pmatrix}, \quad M = t_1\sigma_1 + i\lambda\sigma_2 = \begin{pmatrix} 0 & t_1 + \lambda \\ t_1 - \lambda & 0 \end{pmatrix}. \quad (3.107)$$

The on-site Green's function is obtained as

$$\frac{1}{E - M} = \frac{1}{E - t_1^2 + \lambda^2} \begin{pmatrix} E^2 & t_1 + \lambda \\ t_1 - \lambda & E \end{pmatrix}. \quad (3.108)$$

The SVD of $J = V \Xi W^\dagger$ yields

$$V = \begin{pmatrix} 0 & 1 \\ 1 & 0 \end{pmatrix}, \quad \Xi = \begin{pmatrix} t_2 & 0 \\ 0 & 0 \end{pmatrix}, \quad W = \begin{pmatrix} 1 & 0 \\ 0 & 1 \end{pmatrix}. \quad (3.109)$$

Clearly, $\text{rank} J = 1$, which is suitable for using the conclusion obtained from the transfer matrix in Eq. (3.98). Note that we need to use the reduced form of SVD, $J = v \xi w^\dagger$ with $v = (0, 1)^\text{T}$, $\xi = t_2$ and $w = (1, 0)^\text{T}$. The transfer matrix for the SSH model is obtained as

$$T = \frac{1}{\mathcal{G}_{vw}} \begin{pmatrix} 1/\xi & -\mathcal{G}_{ww} \\ \mathcal{G}_{vv} & \xi(\mathcal{G}_{vw}\mathcal{G}_{wv} - \mathcal{G}_{vv}\mathcal{G}_{ww}) \end{pmatrix} = \frac{1}{t_1 + \lambda} \begin{pmatrix} (E^2 - t_1^2 + \lambda^2)/t_2 & -E \\ E & -t_2 \end{pmatrix}, \quad (3.110)$$

with the determinant

$$\det T = \frac{t_1 - \lambda}{t_1 + \lambda}. \quad (3.111)$$

Generally, for $|\lambda| \neq 0$, which corresponds to the non-Hermitian case, the determinant is not unimodular. Thus the spectra for PBCs and the OBCs are not identical. A special case is when $\lambda = t_1$, which corresponds to $\det T = 0$, the real space spectrum exhibits exceptional point, as can be seen from the spectrum in Fig. 3.5.

This can also be seen from our theory of classifying different non-Hermitian terms. In real space, alternative to the transfer matrix method, the Hamiltonian with OBCs can be expressed as

$$H_{\text{SSH}} = \mathbb{1} \otimes (t_1 \sigma_1 + i \lambda \sigma_2) + (S + S^\dagger) \otimes \frac{t_2}{2} \sigma_1 + (S - S^\dagger) \otimes \frac{t_2}{2i} \sigma_2. \quad (3.112)$$

This Hamiltonian is superficially non-Hermitian in real space and can be transformed to be Hermitian. According to our theory, the similarity transform is found to be

$$V = \text{diag}\{1, \beta, \beta^2, \dots, \beta^{N-1}\} \otimes \rho_{\text{SSH},s} = \text{diag}\{1, \beta, \beta^2, \dots, \beta^{N-1}\} \otimes \text{diag}\{\sqrt{t_1 + \lambda}, \sqrt{t_1 - \lambda}\}, \quad (3.113)$$

with $\beta = \sqrt{t_1 - \lambda}/\sqrt{t_1 + \lambda}$. Thus the similarity transform is obtained as,

$$H'_{\text{SSH}} = V^{-1} H_{\text{SSH}} V = \sqrt{t_1^2 - \lambda^2} \sigma_1 \otimes \mathbb{1} + \frac{t_2}{2} \sigma_1 \otimes (S + S^\dagger) + \frac{t_2}{2i} \sigma_2 \otimes (S - S^\dagger). \quad (3.114)$$

Though the similarity transformation operator violates the translational symmetry, the transformed real space Hamiltonian is still translational symmetric, which corresponds to the following momentum space Hamiltonian of

$$\mathcal{H}_{\text{SSH}}(\mathbf{k}) = (\sqrt{t_1^2 - \lambda^2} + t_2 \cos k) \sigma_1 + t_2 \sin k \sigma_2 + i \lambda \sigma_2. \quad (3.115)$$

The spectrum of this momentum space Hamiltonian is identical to that of the non-Hermitian real space Hamiltonian of Eq. (3.112), which differs drastically from the non-Hermitian Hamiltonian in

Eq. (3.105).

Su-Schrieffer–Heeger model with anti-commuting terms

With the non-Hermitian anti-commuting term, the Hamiltonian with PBCs in momentum space reads,

$$\mathcal{H}_{\text{SSH}}(\mathbf{k}) = (t_1 + t_2 \cos k)\sigma_1 + t_2 \sin k\sigma_2 + i\lambda\sigma_3. \quad (3.116)$$

The energy spectrum is obtained as $E_{\text{SSH}}(\mathbf{k}) = \pm((t_1 + t_2 \cos k)^2 + t_2^2 - \lambda^2)^{1/2}$. The Hamiltonian is superficially non-Hermitian with PBCs and can be turned Hermitian by similarity transformation.

Taking open boundary conditions with finite unit cells of N , we can get the corresponding Hamiltonian as

$$\mathcal{H}_{\text{SSH}} = \sum_{n=0}^N \left(J\mathbf{c}_n^\dagger \mathbf{c}_{n+1} + M\mathbf{c}_n^\dagger \mathbf{c}_n + J^\dagger \mathbf{c}_{n+1}^\dagger \mathbf{c}_n \right), \quad (3.117)$$

with

$$J = \frac{t_2}{2}\sigma_1 + \frac{t_2}{2i}\sigma_2 = \begin{pmatrix} 0 & 0 \\ t_2 & 0 \end{pmatrix}, \quad M = t_1\sigma_1 + i\lambda\sigma_3 = \begin{pmatrix} i\lambda & t_1 \\ t_1 & -i\lambda \end{pmatrix}. \quad (3.118)$$

We can see that comparing to the kinetic case in Eq. (3.107), J is the same, while the expression of M is changed. Correspondingly the on-site Green's function is different as well,

$$\frac{1}{E - M} = \frac{1}{E^2 - t_1^2 + \lambda^2} \begin{pmatrix} E + i\lambda & t_1 \\ t_1 & E - i\lambda \end{pmatrix}. \quad (3.119)$$

Following a similar procedure as that in Eq. (3.110), the transfer matrix can be obtained as

$$T = \frac{1}{t_2} \begin{pmatrix} (E^2 - t_1^2 + \lambda^2)/t_2 & -(E + i\lambda) \\ E - i\lambda & -t_2 \end{pmatrix}. \quad (3.120)$$

The determinant of the transfer matrix can be obtained as,

$$\det T = 1. \quad (3.121)$$

Thus, as shown in Figs. 3.5 (c) and (d), the spectrum is identical for system with OBCs and PBCs.

3.4 Exceptional points

While Hermitian operators are always diagonalizable by unitary transformations, it is not the case for non-Hermitian operators. Non-diagonalizable operators in non-Hermitian physics can be brought to Jordan normal form, which has non-zero superdiagonal entries (immediately above the main diagonal) equal to one, where the corresponding diagonal entries are identical. These identical diagonal entries are still eigenvalues, but there exists only one corresponding eigenvector. Mathematically, the multiplicity of an eigenvalue for an operator is called the algebraic multiplicity, and the number of linearly independent eigenvectors of this eigenvalue is its geometric multiplicity. An operator that has an eigenvalue whose

algebraic multiplicity is larger than its geometric multiplicity is non-diagonalizable (or defective).

For non-Hermitian Hamiltonians, the special points in parameter space where the Hamiltonian is not diagonalizable are called the exceptional points, which can be treated as a characteristic feature of non-Hermitian systems. At this special point, two or more eigenstates coalesce (become linearly dependent), and the spectrum exhibits singularities. There are many interesting phenomena associated with these exceptional points, e.g., enhanced sensitivity of microcavity sensors [148, 149], single-mode lasing of photonic devices [117, 118, 136, 137], and stopping of light in coupled optical waveguides [138]. More interestingly, these exceptional points also appear in non-Hermitian topological systems [129, 130, 132–135].

In this section, we focus on the property of exceptional points. For simplicity but without loss of generality, we suppose that at one particular exceptional point, the Hamiltonian H_0 is non-diagonalizable with energy E_0 , which can be brought to be a Jordan block of order m ,

$$J(E_0) = S^{-1}H_0S = \begin{pmatrix} E_0 & 1 & 0 & \cdots & 0 \\ 0 & E_0 & 1 & \cdots & 0 \\ \vdots & \vdots & \vdots & \ddots & \vdots \\ 0 & 0 & 0 & E_0 & 1 \\ 0 & 0 & 0 & 0 & E_0 \end{pmatrix}_{m \times m}, \quad (3.122)$$

with S an invertible matrix. There is only one eigenvector of H_0 as the eigenspace is one dimensional, but we can find a set of associate right vectors which satisfy,

$$\begin{aligned} H_0|u_1\rangle &= E_0|u_1\rangle, \\ H_0|u_2\rangle &= E_0|u_2\rangle + |u_1\rangle, \\ &\vdots \\ H_0|u_m\rangle &= E_0|u_m\rangle + |u_{m-1}\rangle. \end{aligned} \quad (3.123)$$

The set of $\{|u_1\rangle, |u_2\rangle, \dots, |u_m\rangle\}$ is called the right Jordan chain. Correspondingly, there is also a set of left vectors which satisfy

$$\begin{aligned} \langle\langle v_1|H_0 &= \langle\langle v_1|E_0, \\ \langle\langle v_2|H_0 &= \langle\langle v_2|E_0 + \langle\langle v_1|, \\ &\vdots \\ \langle\langle v_m|H_0 &= \langle\langle v_m|E_0 + \langle\langle v_{m-1}|. \end{aligned} \quad (3.124)$$

which form left Jordan chain $\{\langle\langle v_1|, \langle\langle v_2|, \dots, \langle\langle v_m|\}$. The left and right eigenvector satisfy the self-orthogonality condition

$$\langle\langle v_1|u_1\rangle = 0. \quad (3.125)$$

For the rest elements of the left and right Jordan chain, we can impose the normalization condition,

$$\langle\langle v_1|u_m\rangle = 1, \quad \langle\langle v_2|u_m\rangle = \langle\langle v_3|u_m\rangle = \dots = \langle\langle v_m|u_m\rangle = 0, \quad (3.126)$$

and vice versa for $|u_k\rangle$ with $k \leq m$.

3.4.1 Physics around exceptional points

Here we want to derive the eigenstates and energies in the vicinity of an exceptional point. Suppose in the neighborhood of the exceptional point, the Hamiltonian is altered by εV , which reads [150],

$$H(\varepsilon) = H_0 + \varepsilon V. \quad (3.127)$$

The eigenvalues can be determined by the determinant,

$$P(\varepsilon, E) = \det(E\mathbb{1} - H_0 - \varepsilon V). \quad (3.128)$$

Before going on, it is worthwhile to point out the difference from the Hermitian case, for which the Hamiltonian H_0 is diagonalizable. The determinant stays unchanged if we perform the similarity transformation of $S^{-1}(E\mathbb{1} - H_0 + \varepsilon V)S$, after which the determinant becomes, see Eq. (3.122),

$$P(\varepsilon, E) = \det((E - E_0)\mathbb{1} - J(0) - \varepsilon \tilde{V}), \quad (3.129)$$

with $\tilde{V} = S^{-1}VS$. A remarkable feature of non-Hermitian systems is that $J(0)$ could be nilpotent for non-diagonal matrices, and this will lead to peculiar behaviors around the exceptional points.

We can view ε as the function of the eigenvalue E , which in the neighborhood of E_0 , it will approach zero, and at E_0 , it vanishes as $\varepsilon(E_0) = 0$. With this property, ε must be in the form of

$$\varepsilon(E) = \varepsilon_m(E - E_0)^m + \mathcal{O}((E - E_0)^{m+1}), \quad (3.130)$$

with \mathcal{O} indicating higher order terms.

Since the algebraic multiplicity of H_0 is m , the determinant satisfies the following relation (derivative against E),

$$\frac{\partial P(\varepsilon, E)}{\partial E} \Big|_{(0, E_0)} = \frac{\partial^2 P(\varepsilon, E)}{\partial E^2} \Big|_{(0, E_0)} = \dots = \frac{\partial^{m-1} P(\varepsilon, E)}{\partial E^{m-1}} \Big|_{(0, E_0)} = 0, \quad \frac{\partial^m P(\varepsilon, E)}{\partial E^m} \Big|_{(0, E_0)} \neq 0. \quad (3.131)$$

In addition, if the following assumption is imposed (derivative against ε),

$$\frac{\partial P(\varepsilon, E)}{\partial \varepsilon} \Big|_{(0, E_0)} \neq 0, \quad (3.132)$$

according to Eqs. (3.131) and (3.132), we can write down the expression for the determinant,

$$P(\varepsilon, E) = a_{10}\varepsilon + a_{0m}(E - E_0)^m + \mathcal{O}((E - E_0)^{m+1}), \quad (3.133)$$

with

$$a_{10} = \frac{\partial P(\varepsilon, E)}{\partial \varepsilon} \Big|_{(0, E_0)}, \quad \text{and} \quad a_{0m} = \frac{\partial^m P(\varepsilon, E)}{m! \partial E^m} \Big|_{(0, E_0)}. \quad (3.134)$$

Plugging Eq. (3.130) into Eq. (3.133), and using the condition that the determinant $P(\varepsilon, E) = 0$ for the eigenvalue E_0 , we have

$$\varepsilon(\lambda) = \varepsilon_m(E - E_0)^m + \mathcal{O}((E - E_0)^{m+1}). \quad (3.135)$$

with

$$\varepsilon_m = -\frac{a_{0m}}{a_{10}} = -\frac{\frac{\partial^m P(\varepsilon, E)}{m! \partial E^m} \Big|_{(0, E_0)}}{\frac{\partial P(\varepsilon, E)}{\partial \varepsilon} \Big|_{(0, E_0)}}. \quad (3.136)$$

Conversely, from Eq. (3.135), we can get the Puiseux series for E ,

$$E = E_0 + \alpha_1 \varepsilon^{\frac{1}{m}} + o(\varepsilon^{\frac{2}{m}}), \quad (3.137)$$

with

$$\alpha_1 = \varepsilon_m^{-\frac{1}{m}}. \quad (3.138)$$

A problem is that the expression of α_1 obtained ε_m from Eq. (3.136) is not directly calculable in practice. In the following, we determine the expression for α_1 in an alternative way. We first return to the Schrödinger equation,

$$(H(\varepsilon) - E\mathbb{1})|u(E)\rangle = 0. \quad (3.139)$$

Since $\varepsilon = \varepsilon_m(E - E_0)^m + \mathcal{O}((E - E_0)^{m+1})$, we can do Taylor expansion around E_0 at the left side of the above Schrödinger equation,

$$\begin{aligned} & (H(\varepsilon_m(E - E_0)^m + \mathcal{O}((E - E_0)^{m+1})) - E_0\mathbb{1} - (E - E_0)\mathbb{1})|u(E)\rangle \\ &= \left((H_0 - E_0\mathbb{1}) - (E - E_0)\mathbb{1} + H'(0)\varepsilon_m(E - E_0)^m \right) \\ & \quad \left(|u(E_0)\rangle + \frac{\partial |u(E_0)\rangle}{\partial E} (E - E_0) + \dots + \frac{\partial^m |u(E_0)\rangle}{m! \partial E^m} (E - E_0)^m + \mathcal{O}((E - E_0)^{m+1}) \right) \\ &= (H_0 - E_0\mathbb{1})|u(E_0)\rangle \\ & \quad + \left((H_0 - E_0\mathbb{1}) \frac{\partial |u(E_0)\rangle}{\partial E} - |u(E_0)\rangle \right) (E - E_0) \\ & \quad \dots \\ & \quad + \left((H_0 - E_0\mathbb{1}) \frac{\partial^k |u(E_0)\rangle}{k! \partial E^k} - \frac{\partial^{k-1} |u(E_0)\rangle}{(k-1)! \partial E^{k-1}} \right) (E - E_0)^k \\ & \quad \dots \\ & \quad + \left((H_0 - E_0\mathbb{1}) \frac{\partial^m |u(E_0)\rangle}{m! \partial E^m} - \frac{\partial^{m-1} |u(E_0)\rangle}{(m-1)! \partial E^{m-1}} + \varepsilon_m H'(0) |u(E_0)\rangle \right) (E - E_0)^m + \mathcal{O}((E - E_0)^{m+1}). \end{aligned} \quad (3.140)$$

Notice, we have expanded both the Hamiltonian and the eigenvector with respect to $E - E_0$. From the Schrödinger equation, each prefactor of $(E - E_0)^k$ for $0 \leq k \leq m - 1$ is zero, thus we get the relations,

$$(H_0 - E_0\mathbb{1}) \frac{\partial^k |u(E_0)\rangle}{k! \partial E^k} - \frac{\partial^{k-1} |u(E_0)\rangle}{(k-1)! \partial E^{k-1}} = 0, \quad (3.141)$$

which means $\partial^k |u(E_0)\rangle / (k! \partial E^k)$ forms the right Jordan chain $\{|u_1\rangle, |u_2\rangle, \dots, |u_m\rangle\}$ for H_0 according

to Eq. (3.123). And the prefactor of $(E - E_0)^m$ in Eq. (3.140) should also be zero, which reads

$$(H_0 - E_0 \mathbb{1}) \frac{\partial^m |u(E_0)\rangle}{m! \partial E^m} - \frac{\partial^{m-1} |u(E_0)\rangle}{(m-1)! \partial E^{m-1}} + \varepsilon_m H'(0) |u(E_0)\rangle = 0. \quad (3.142)$$

By applying the left eigenvector $\langle\langle v_1 |$ onto above equation, and impose the normalization condition $\langle\langle v_1 | u_m \rangle = 1$, with $|u_m\rangle = \partial^{m-1} |u(E_0)\rangle / [(m-1)! \partial E^{m-1}]$, we arrive at the relation,

$$\langle\langle v_1 | \varepsilon_m H'(0) | u_1 \rangle = 1, \quad (3.143)$$

which means

$$\alpha_1^m = \varepsilon_m^{-1} = \langle\langle v_1 | H'(0) | u_1 \rangle. \quad (3.144)$$

Thus we have obtained the expression for α_1^m .

In the above derivation, we can see that the eigenstate $|u(E)\rangle$ can also be expanded around E_0 ,

$$|u(E)\rangle = |u(E_0)\rangle + \frac{\partial |u(E_0)\rangle}{\partial E} (E - E_0) + \dots + \frac{\partial^m |u(E_0)\rangle}{m! \partial E^m} (E - E_0)^m + o((E - E_0)^{m+1}) \quad (3.145)$$

and $\partial^k |u(E_0)\rangle / (k! \partial E^k)$ forms the right Jordan chain $\{|u_1\rangle, |u_2\rangle, \dots, |u_m\rangle\}$. To the first order, the eigenvector is

$$|u(E)\rangle = |u_1\rangle + (E - E_0) |u_2\rangle + \mathcal{O}((E - E_0)^2) \quad (3.146)$$

Since the Puiseux series for the eigenvalue E is

$$E = E_0 + \alpha_1 \varepsilon^{\frac{1}{m}} + \mathcal{O}(\varepsilon^{\frac{2}{m}}), \quad (3.147)$$

the right eigenvector to the leading order is

$$|u(E)\rangle = |u_1\rangle + \alpha_1 \varepsilon^{\frac{1}{m}} |u_2\rangle + \mathcal{O}(\varepsilon^{\frac{2}{m}}), \quad (3.148)$$

with $\alpha_1^m = \langle\langle v_1 | H'(0) | u_1 \rangle$ and $H'(0) = \partial H(\varepsilon) / \partial \varepsilon |_{\varepsilon=0}$.

3.4.2 \mathbb{Z}/N classification of non-Hermitian Hamiltonian with exceptional point

Suppose that a non-Hermitian Hamiltonian is parameterized by \mathbf{k} , which can be written as $H(\mathbf{k})$, and an order N exceptional point exists at \mathbf{k}_0 with energy eigenvalue E_0 . Notice here \mathbf{k} can represent a set of parameters $\mathbf{k} = (k_1, k_2, k_3, \dots)$. In the neighborhood of this exceptional point, which can be denoted by $\mathbf{k} = \mathbf{k}_0 + \delta \mathbf{k}$, to the leading order, according to Eq. (3.147), the energy eigenvalue can be expressed as

$$E(\mathbf{k}) = E_0 + \lambda(\mathbf{k}) \varepsilon^{1/N} + \mathcal{O}(\varepsilon^{1/N}), \quad (3.149)$$

with $\varepsilon = |\delta \mathbf{k}|$. The coefficient λ is determined by

$$\lambda^N = \sum_i \langle\langle v_0 | \partial_{k_i} H(\mathbf{k}) | u_0 \rangle \partial_{\varepsilon} k_i, \quad (3.150)$$

with $\langle\langle v_0 |$ and $|u_0\rangle$ the left and right eigenvectors at the exceptional point satisfying

$$\langle\langle v_0 | H(\mathbf{k}_0) = E_0 \langle\langle v_0 | \quad \text{and} \quad H(\mathbf{k}_0) | u_0 \rangle = E_0 | u_0 \rangle. \quad (3.151)$$

The right side of Eq. (3.150) is complex which can be expressed in the form of $|\lambda^N|e^{i\theta(\mathbf{k})}$. Thus the eigenvalue to the leading order becomes,

$$E(\mathbf{k}) = E_0 + |\lambda|e^{i\theta(\mathbf{k})/N}. \quad (3.152)$$

By encircling the exceptional points in \mathbf{k} space with a circle S^1 , a topological invariant can be defined as

$$v = \oint_{S^1} \frac{d\mathbf{k}}{2\pi i} \partial_{\mathbf{k}} \arg \lambda(\mathbf{k}), \quad (3.153)$$

which belongs to the group \mathbb{Z}/N . In the following, we provide two physical examples.

Second order exceptional points (EP2) in a spinless Dirac semimetal

In a two-dimensional spinless Dirac system with non-Hermitian terms, the Hamiltonian is [129]

$$H(k_x, k_y) = (k_x + i\lambda)\sigma_1 + k_y\sigma_2, \quad (3.154)$$

which for example can be realized in photonic or electronic systems. The energy eigenvalues are $E_{\pm} = \pm\sqrt{k_x^2 + k_y^2 - \lambda^2 + 2ik_x\lambda}$. There are two exceptional points located at $(0, \pm\lambda)$ with eigenvalues of 0. We choose a small circle parameterized by $(k_x, k_y) = (\rho \cos \theta, \rho \sin \theta - \lambda)$ with $\rho \ll \lambda$ to encircle the exceptional point $(0, -\lambda)$. At the exceptional point, the Hamiltonian and the Jordan canonical form is

$$H(0, -\lambda) = \begin{pmatrix} 0 & 2i\lambda \\ 0 & 0 \end{pmatrix} \text{ and } J_2(0, -\lambda) = \begin{pmatrix} 0 & 1 \\ 0 & 0 \end{pmatrix}. \quad (3.155)$$

The eigenvectors are

$$\langle\langle \mathbf{v}_0 | = \begin{pmatrix} 0 & 1 \end{pmatrix}, \quad | \mathbf{u}_0 \rangle = \begin{pmatrix} 2i\lambda \\ 0 \end{pmatrix}. \quad (3.156)$$

Using Eq. (3.150), we obtain the eigenvalue on the circle,

$$E(\theta) = \sqrt{2i\rho\lambda}e^{i\theta/2}. \quad (3.157)$$

The winding number of the energy eigenvalue is obtained

$$v = \oint \frac{d\theta}{2\pi i} \partial_{\theta} \arg E(\theta) = \frac{1}{2}, \quad (3.158)$$

which belongs to the group of $\mathbb{Z}/2$.

Third order exceptional points (EP3) in a three waveguide system

Here we adopt the non-Hermitian Hamiltonian for a three wave guide system from Ref. [151],

$$H(k_x, k_y) = \begin{pmatrix} k_x + ik_y - 2i\gamma & \sqrt{2}v & 0 \\ \sqrt{2}v & 0 & \sqrt{2}v \\ 0 & \sqrt{2}v & k_x + ik_y + 2i\gamma \end{pmatrix}. \quad (3.159)$$

Here k_x and k_y are just some general real parameters. A third order exceptional point occurs at $(0,0)$ for $\gamma = v = 1$. The Jordan canonical form at the exceptional point is

$$H(0,0) = \begin{pmatrix} -2i\gamma & \sqrt{2}v & \\ \sqrt{2}v & 0 & \sqrt{2}v \\ 0 & \sqrt{2}v & 2i\gamma \end{pmatrix} \text{ and } J_3(0,0) = \begin{pmatrix} 0 & 1 & \\ & 0 & 1 \\ & & 0 \end{pmatrix}. \quad (3.160)$$

The eigenvector at the exceptional point is

$$\langle\langle \mathbf{v}_0 | = (2 \quad 2\sqrt{2}i \quad -2), \quad | \mathbf{u}_0 \rangle = \begin{pmatrix} -1 \\ -\sqrt{2}i \\ 1 \end{pmatrix}. \quad (3.161)$$

By choosing the circle of $(k_x, k_y) = (\rho \cos \theta, \rho \sin \theta)$ and using Eq. (3.150), we obtain the eigenvalue on the circle,

$$E = \sqrt[3]{-4\rho} e^{i\theta/3}. \quad (3.162)$$

The winding number of the energy eigenvalue is

$$v = \oint \frac{d\theta}{2\pi i} \partial_\theta \arg E = \frac{1}{3}, \quad (3.163)$$

which belongs to the group of $\mathbb{Z}/3$.

3.4.3 Green's function at exceptional points

Here, we want to study the form of the single-particle Green's function at exceptional points. We will see that the singular spectrum at exceptional points leads to higher-order poles in the Green's function. Suppose a non-Hermitian Hamiltonian \hat{H} exhibits an exceptional point of order n , which is also supposed to be the dimension of the Hamiltonian. At the exceptional point, the Jordan normal form can be written as

$$\hat{S}^{-1} \hat{H} \hat{S} = \begin{pmatrix} E_{\text{EP}} & & & \\ & E_{\text{EP}} & & \\ & & \ddots & \\ & & & E_{\text{EP}} \end{pmatrix} + \begin{pmatrix} 0 & 1 & & \\ & 0 & \ddots & \\ & & \ddots & 1 \\ & & & 0 \end{pmatrix} = E_{\text{EP}} \mathbb{1} + \hat{N}, \quad (3.164)$$

with \hat{N} a nilpotent matrix, which vanishes to the n^{th} power as $\hat{N}^n = 0$.

The Green's function is given by

$$\begin{aligned} \hat{G}(E) &= \frac{1}{E - \hat{H}} = \frac{1}{\hat{S}(E - E_{\text{EP}} - \hat{N})\hat{S}^{-1}} \\ &= \hat{S} \frac{\lambda}{(1 - \lambda \hat{N})} \hat{S}^{-1}. \end{aligned} \quad (3.165)$$

with $\lambda = \frac{1}{E - E_{\text{EP}}}$. The inverse of $1 - \lambda\hat{N}$ is given by

$$\frac{1}{(1 - \lambda\hat{N})} = \sum_{i=0}^{n-1} (\lambda\hat{N})^i, \quad (3.166)$$

which can be verified as

$$(1 - \lambda\hat{N}) \frac{1}{(1 - \lambda\hat{N})} = (1 - \lambda\hat{N}) \sum_{i=0}^{n-1} (\lambda\hat{N})^i = 1, \quad (3.167)$$

where we use the fact $(\lambda\hat{N})^n = 0$. Then the Green's function is

$$\begin{aligned} \hat{G}(E) &= \hat{S} \frac{\lambda}{(1 - \lambda\hat{N})} \hat{S}^{-1} \\ &= \hat{S} \left(\lambda + \lambda^2\hat{N} + \lambda^3\hat{N}^2 + \dots + \lambda^n\hat{N}^{n-1} \right) \hat{S}^{-1} \\ &= \frac{1}{E - E_{\text{EP}}} + \frac{1}{(E - E_{\text{EP}})^2} \left(\hat{H} - E_{\text{EP}} \right) + \frac{1}{(E - E_{\text{EP}})^3} \left(\hat{H} - E_{\text{EP}} \right)^2 + \dots + \frac{1}{(E - E_{\text{EP}})^n} \left(\hat{H} - E_{\text{EP}} \right)^{n-1}. \end{aligned} \quad (3.168)$$

Thus at an n th order exceptional point, there will be an n th order pole of the Green's function.

Such a high-order pole leads to many interesting physical phenomena. For instance, in non-Hermitian photonic systems, it is shown that a system near an EP can exhibit a non-Lorentzian frequency response and the peak intensity of the frequency response is enhanced significantly due to the high-order pole [152, 153]. The role of Green's functions at the exceptional point is still awaiting to be explored in the context of topological phases of matter. We expect it will bring exotic and interesting phenomena, for instance, to local density of states, and transport properties.

3.5 Conclusions

We have systematically studied non-Hermitian topological gapped systems by classifying non-Hermitian Dirac Hamiltonians with generic non-Hermitian terms. We find that non-Hermitian terms can be classified into three types, according to the Clifford algebra, (i) non-Hermitian anti-commuting terms, which anti-commute with the Dirac Hamiltonian, (ii) non-Hermitian kinetic terms, and (iii) non-Hermitian mass terms. We have revealed a two-fold duality for the d dimensional Dirac models with non-Hermitian terms of the first two types, depending on whether the non-Hermiticity can be removed by non-unitary similarity transformations with either periodic or open boundary conditions. The Dirac model with type (iii) non-Hermitian terms is intrinsically non-Hermitian as it cannot be transformed to be Hermitian regardless of boundary conditions. Our theory has been applied to understanding the band topology and topological boundary states of two representative systems of two dimensional and four dimensional topological insulator systems.

We find that the boundary condition plays a key role in classifying different non-Hermitian terms. Different to Hermitian systems, the boundary conditions not only influence the boundary states but also the bulk states in non-Hermitian systems, i.e., the band spectrum can differ drastically with different

boundary conditions. To study their effect, the transfer matrix method is adopted for a generic tight-binding model, from which the role of boundary conditions is clarified.

As exceptional points are characteristic features of non-Hermitian systems, their mathematical origin and physical consequences are discussed comprehensively. For the Dirac models with type (i) and (ii) non-Hermitian terms, we find there are exceptional spheres of dimension $(d - 2)$ in the surface and bulk band structures, respectively. Our findings can be used as guiding principles for the design of applications in, e.g., photonic devices. For example, our analysis shows that single mode lasing [117, 118, 136], which utilizes bulk exceptional points, is only possible in Dirac models perturbed by the second type of non-Hermitian terms. Sensors, on the other hand, which make use of surface exceptional points, can be designed using Dirac models with the first type of non-Hermitian terms. We emphasize, that the exceptional points are extremely sensitive to the boundary conditions, as they are bare (i.e., not dense) in parameter space. That is, infinitesimally small perturbations can change them into regular points, a fact that can be exploited for sensor applications. This important fact deserves further investigations, both from a fundamental and technical point of view.

4

Chapter 4

Non-Hermitian topological Weyl and Dirac semimetals

4.1 Introduction

Besides in topological gapped systems, non-trivial band topology can arise also in gapless systems, such as topological semimetals and nodal superconductors. Therefore, it is natural to extend our discussion of non-Hermitian topological band theory to gapless systems. In topological semimetals, the topological invariants are usually defined with respect to gapless points, usually in terms of an integral along a surface enclosing these points [13]. The non-trivial topological invariants in the bulk will lead to exotic topological surface states at the boundary. The low-energy effective theory that describes the physics around the gapless point usually exhibits a quantum anomaly, which results from the breakdown of classical symmetry at the quantum level. The quantum anomaly is closely related with anomalous transport properties in topological semimetals. In this chapter, instead of developing a general theory for non-Hermitian topological gapless systems, we focus on two important cases, namely, the non-Hermitian Weyl and Dirac semimetals.

We start with the Lagrangian of $\mathcal{L} = \bar{\psi} \left(i\gamma^\mu \partial_\mu - m \right) \psi$ for the Dirac fields denoted by ψ in d spatial dimensions. Here $\bar{\psi} = \psi^\dagger \gamma_0$, and $\mu = 0, 1, \dots, d$ labels the time and space dimensions. The $d+1$ gamma matrices satisfy the Clifford algebra of $\{\gamma^\mu, \gamma^\nu\} = 2g^{\mu\nu}$ with $g = \text{diag}(+1, -1, \dots)$. The Dirac equation, which was originally proposed by P.A.M. Dirac in 1928, can be obtained as $\left(i\gamma^\mu \partial_\mu - m \right) \psi = 0$ from the Lagrangian by the Euler–Lagrange equation. This Dirac Lagrangian is adopted in high-energy physics as it is Lorentz-invariant in that under Lorentz transformations of $\Lambda = \exp(i\theta_{\mu\nu} S^{\mu\nu})$ with $S^{\mu\nu} = \frac{i}{4}[\gamma^\mu, \gamma^\nu]$, the Lagrangian remain the same. In 1929, Weyl noticed that in odd spatial dimensions, the Dirac equation can be further reduced by constructing an Hermitian matrix $\gamma^5 = i^k \gamma^0 \gamma^1 \dots \gamma^d$ with $k = (d-1)/2$. γ^5 is guaranteed to commute with the kinetic terms of $\gamma^0 \gamma^\mu$, which means that in the massless case ($m = 0$), they can be diagonalized simultaneously. Thus the chiral components of $\gamma^5 \psi_\pm = \pm \psi_\pm$ can be identified, and the Dirac Lagrangian can be further reduced. In three spatial dimensions, by choosing the chiral representation of $\gamma^0 = \mathbb{I} \otimes \tau_x$ and $\gamma^i = \sigma^i \otimes i\tau_y$, the Lagrangian can be decomposed as $\mathcal{L} = L_+ + L_- = \psi_+^\dagger \bar{\sigma}^\mu i\partial_\mu \psi_+ + \psi_-^\dagger \sigma^\mu i\partial_\mu \psi_-$ with $\sigma^\mu = (1, \sigma^i)$ and $\bar{\sigma}^\mu = (1, -\sigma^i)$. The Dirac equation can be decomposed to $i\partial_t \psi_\pm = H_\pm \psi_\pm$, with the Weyl Hamiltonian $H_\pm(\mathbf{p}) = \mp \mathbf{p} \cdot \boldsymbol{\sigma}$

[154]. However, the Weyl fermions are hard to spot in high-energy physics, as the Lorentz invariance cannot be kept for the individual Weyl Lagrangians.

In condensed matter physics, it is possible to realize the Weyl fermions due to less restrictive symmetry requirements and relatively low energy scale compared with high-energy physics. The Weyl fermion was first experimentally observed in Weyl semimetals [17]. In Weyl semimetals, the valance bands touch conductance bands and they form linear dispersing cones around the touching points. Excitations around these points can be described by Weyl Hamiltonians. This kind of Weyl fermions behaves like a monopole of Berry curvature in reciprocal space, and has a monopole charge of ± 1 , corresponding to the chirality of Weyl fermions. The non-trivial topology of the bulk manifests itself at the surface as exotic Fermi arc states. The Weyl semimetals also serve as fertile ground to discover new physics. Indeed, research on Weyl semimetals has lead to various fascinating phenomena, such as chiral magnetic effect and anomalous Hall effects [60, 63, 64, 72, 155–158]. In this chapter, we introduce different non-Hermitian potentials into Weyl semimetals. We pay special attention to the boundary conditions, as they play a significant role in non-Hermitian systems. We find there are two kinds of non-Hermitian potentials, the non-Hermitian kinetic terms and mass terms. For each kind of the non-Hermitian terms, we focus on their topological properties and topological surface states subject to different slab geometries.

We will further discuss the non-Hermitian topological Dirac semimetals in three dimensions. In Hermitian Dirac materials, around band degeneracy points (Dirac points), low energy quasiparticle excitations that can be described by Dirac equation in relativistic quantum mechanics have been spotted [159–162]. Beyond fundamental interest and practical value in itself, Dirac points play a key role as the bridge between different topological phases in the topological band theory [10, 13, 163]. The investigation of non-Hermitian Dirac semimetals therefore will pave the way for research on different non-Hermitian topological phases. We will especially focus on \mathcal{PT} symmetric-non-Hermitian Dirac semimetals. This is of fundamental interest, as a recent revolutionary development in quantum mechanics is using the \mathcal{PT} symmetry, which guarantees real spectra in the \mathcal{PT} -unbroken case, as an alternative to Hermiticity [32, 33, 164, 165]. Though experimentally challenging at first, it is later discovered that photonics offers an ideal platform for \mathcal{PT} -symmetric quantum theory, where non-Hermitian components are naturally introduced by optical radiation and loss/gain [95, 96, 98, 99, 143]. For \mathcal{PT} -symmetric Dirac semimetals, we find there are three kinds of \mathcal{PT} -symmetric non-Hermitian potentials. For each of them, we will discuss their spectra under different boundary conditions, the bulk topology, and the bulk boundary correspondence.

4.2 Weyl semimetals

To search for Weyl semimetals in condensed matter physics, a natural consideration is to look for three-dimensional materials with touching points between conduction and valence bands in the Brillouin zone, around which energy dispersion is linear in all directions. As the Weyl node is two-fold degenerate, the physics around it can be effectively captured by a 2×2 Hamiltonian. The most general form of the Hamiltonian can be expressed as [154]

$$H(\mathbf{k}) = f_1(\mathbf{k})\sigma_1 + f_2(\mathbf{k})\sigma_2 + f_3(\mathbf{k})\sigma_3, \quad (4.1)$$

where $f_i(\mathbf{k})$ are general real functions and σ_i with $i = 1, 2, 3$ denote the Pauli matrices. The energy

spectrum is obtained as $E(\mathbf{k}) = \pm\sqrt{f_1(\mathbf{k})^2 + f_2(\mathbf{k})^2 + f_3(\mathbf{k})^2}$. The band touching points occur with the condition that $f_1(\mathbf{k}) = f_2(\mathbf{k}) = f_3(\mathbf{k}) = 0$, which can be tuned by the parameters of spatial dimensions in three-dimensional Brillouin zone. Actually, the \mathbf{k} points that fulfill the requirement of each $f_i(\mathbf{k}) = 0$ form a two-dimensional plane. The simultaneous fulfillment of all three requirements occurs at the intersection of the three independent planes, which will typically be a point. Remarkably, the existence of this point is stable against small perturbations. This can be easily understood as the inclusion of small perturbation into $f_i(\mathbf{k})$ just shifts the position of the two-dimensional plane, which relocates the position of the intersection point but does not affect its existence. Around the band touching point $\mathbf{k} = \mathbf{k}_0 + \delta\mathbf{k}$, we can do the Taylor expansion of $H(\mathbf{k})$, which yields

$$H(\mathbf{k}) = \sum_{i=1}^3 \mathbf{v}_i \cdot \delta\mathbf{k}\sigma_i, \quad (4.2)$$

up to a constant term. Here $\mathbf{v}_i = \nabla_{\mathbf{k}}f_i(\mathbf{k})|_{\mathbf{k}_0}$ denotes the effective velocities. It is emphasized that this is in the form of the Weyl Hamiltonian. For experimental convenience, it is usually required that the Weyl node is located near the Fermi level.

An intriguing fact is that in three-dimensional lattices, Weyl points always come in opposite chirality pairs. This can be understood intuitively by the Berry flux. As we have discussed in the introduction chapter, the Berry connection can be defined in the band theory as $\mathbf{A}_n(\mathbf{k}) = -i\langle u_n(\mathbf{k})|\nabla_{\mathbf{k}}|u_n(\mathbf{k})\rangle$ for the n th band. The corresponding Berry flux can be obtained from $\Omega_n^{ij}(\mathbf{k}) = \partial_{k_i}A_n^j - \partial_{k_j}A_n^i$. The Berry flux piercing any surface enclosing the Weyl point is $2\pi C$ with C the chirality. In three-dimensional Brillouin zone, due to periodicity, the Berry flux piercing opposite surfaces of the Brillouin zone are the same in both magnitude and direction. Therefore the total flux penetrating the whole Brillouin zone is zero. As the total flux equals to the summation of the contribution of the Weyl points inside the Brillouin zone as $2\pi \sum_i C_i$, the vanishing of which indicates that the Weyl points in lattice must come in opposite chirality pairs. This also suggests that removing Weyl nodes can only be achieved by the annihilation between Weyl points of opposite chirality. This is known as the Nielsen-Ninomiya no-go theorem [166, 167].

4.2.1 Fermi arc surface states and topological invariants

From the above discussion, the simplest lattice model for Weyl semimetals must contain at least two Weyl nodes with opposite chirality. We find the lattice Dirac Hamiltonian is able to achieve this goal. With periodic boundary conditions, the model Hamiltonian in momentum space reads,

$$\mathcal{H}(\mathbf{k}) = \sin k_x\sigma_1 + \sin k_y\sigma_2 + (M - \cos k_x - \cos k_y - \cos k_z)\sigma_3, \quad (4.3)$$

for $1 < M < 3$. The energy spectrum is $E = \pm(\sin^2 k_x + \sin^2 k_y + (M - \cos k_x - \cos k_y - \cos k_z)^2)^{1/2}$, which is shown in Fig. 4.1 (a). The two Weyl points are located at $(0, 0, \pm k_c)$, with $k_c = \arccos(M - 2)$. We can do a Taylor expansion around the two Weyl points to get the effective Hamiltonian as $H_{\text{Weyl}} = \delta k_x\sigma_1 + \delta k_y\sigma_2 + \pm\sqrt{1 - \cos^2 k_c}(\delta k_z \mp k_c)$. Clearly, the two Weyl points exhibit opposite chirality and are separated by $2k_c$ on the k_z axis. Actually, we can visualize the Weyl points by treating $\mathbf{d} = (\sin k_x, \sin k_y, M - \cos k_x - \cos k_y - \cos k_z)$ as the vector field that is plotted out in Fig. 4.1 (b), where the monopole structure is highlighted in red.

We now turn to the low-energy effective model that corresponds to the lattice model in Eq. (4.3),

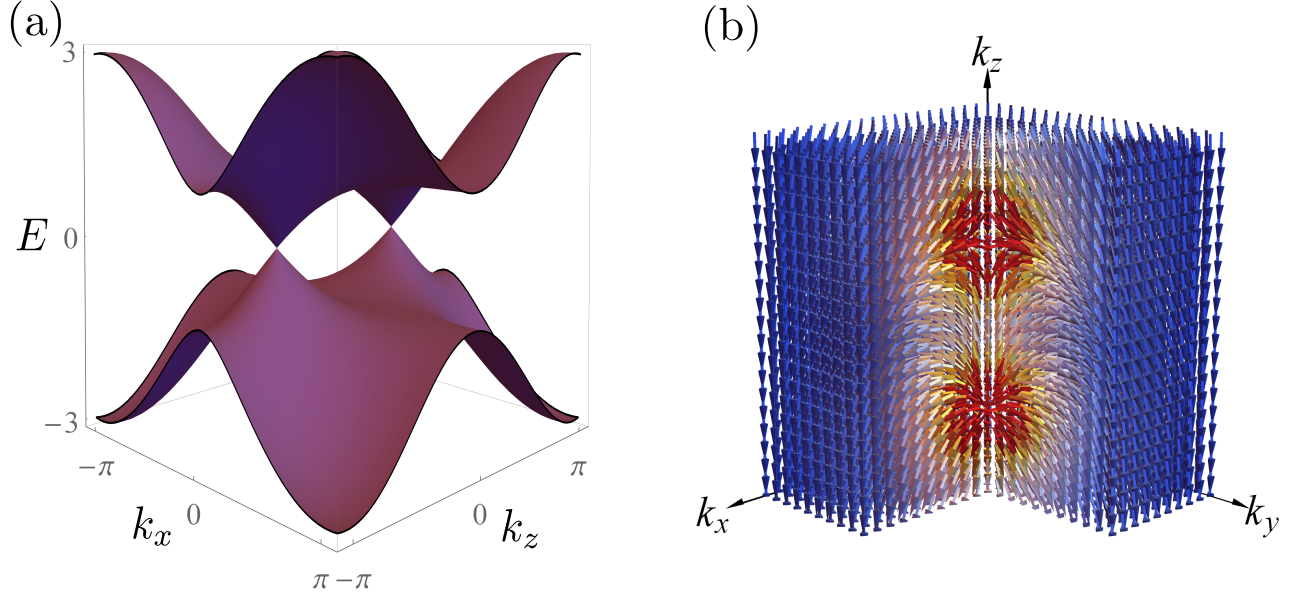


Figure 4.1: (a) Energy spectrum of the Hermitian lattice model of the Weyl semimetal in Eq. (4.3) with $k_y = 0$. The parameter is chosen as $M = 2$ so that the two Weyl points are located at $(0, 0, -\pi/2)$. (b) The vector field of $\mathbf{d} = (\sin k_x, \sin k_y, M - \cos k_x - \cos k_y - \cos k_z)$ for the Weyl semimetal, with the monopole region highlighted in red.

which enables us to analytically investigate the system. The effective Hamiltonian reads,

$$\mathcal{H}_{\text{eff}}(\mathbf{k}) = A(k_x\sigma_1 + k_y\sigma_2) + (M_0 - M_1(k_x^2 + k_y^2 + k_z^2))\sigma_3. \quad (4.4)$$

Here we have added the parameters A , M_0 and M_1 to make the model more realistic. By setting $A = 1$, $M_1 = 1/2$ and $M_0 = M - 3$, Eq. (4.4) corresponds to the lattice model of Eq. (4.3) after the substitution of $\sin k_i \rightarrow k_i$ and $\cos k_i \rightarrow 1 - k_i^2/2$.

To investigate the topological boundary states, we adopt the same method used in the chapter of the Dirac nodal-line semimetals. Taking a semi-infinite system in the half plane of $y \leq 0$ with open boundary conditions, k_x and k_z are still good quantum numbers. Hence, the real space Hamiltonian with open boundary conditions can be denoted as $\mathcal{H}_{\text{eff}}(k_x, -i\partial_y, k_z)$, with the replacement of $k_y \rightarrow -i\partial_y$. We adopt the ansatz for the boundary eigenstates as $|\psi_\lambda\rangle = e^{i(k_x x + k_z z)} e^{\lambda y} (\psi_1 \ \psi_2)^T$, with T the matrix transposition.

Solving the Schrödinger equation of $\mathcal{H}_{\text{eff}}(k_x, -i\partial_y, k_z)\psi_\lambda = E\psi_\lambda$ with open boundary conditions at $y = 0$ and $y = -\infty$, the surface spectrum is found to be [168]

$$E_{\text{arc}} = \pm A k_x. \quad (4.5)$$

The surface states are localized in the region of $k_x^2 + k_z^2 < k_c^2$, with $k_c = \arccos(M_0/M_1)$. At $k_x = 0$, the surface spectrum is $E_{\text{arc}} = 0$ in the region of $-k_c < k_z < k_c$. This is the Fermi arc surface states, that attach to two Weyl points in the bulk.

The Fermi arc surface states can be understood from the bulk-boundary correspondence. In the

three-dimensional bulk Brillouin zone, we can treat the two dimensional planes at each k_z value as two dimensional subsystems. The Chern number can be defined for each subsystem. Since each Weyl point carries Chern number of ± 1 , by crossing the Weyl points, the Chern number must change. In this way, the Chern number for the subsystems inside the region of $-k_c < k_z < k_c$ is different with those outside, which leads to the Fermi arc surface states.

4.2.2 Landau bands and magnetoconductivity

We consider a magnetic field applied along the z direction, $\mathbf{B} = (0, 0, B)$. Under the choice of the Landau gauge, the vector potential is $\mathbf{A} = (-yB, 0, 0)$. Such a gauge field does not break the translational symmetry in x and z direction, thus k_x and k_z are still good quantum numbers. Through minimum coupling, the wave vector in the Hamiltonian is replaced as [169],

$$\mathbf{k} = (k_x - \frac{eB}{\hbar}y, -i\partial_y, k_z). \quad (4.6)$$

We introduce the ladder operator a with the following relations

$$k_x - \frac{eB}{\hbar}y = \frac{1}{\sqrt{2}l_B}(a^\dagger + a), \quad (4.7)$$

$$-i\partial_y = \frac{1}{\sqrt{2}l_B i}(a^\dagger - a). \quad (4.8)$$

Here $l_B = \sqrt{\frac{\hbar}{eB}}$. With the introduction of the ladder operator, we find the components in the Hamiltonian $\mathcal{H}_{\text{eff}}(\mathbf{k})$ are substituted as

$$k_x^2 + k_y^2 \rightarrow \omega(a^\dagger a + \frac{1}{2}), \quad k_+ \rightarrow \frac{\sqrt{2}}{l_B}a^\dagger, \quad \text{and} \quad k_- \rightarrow \frac{\sqrt{2}}{l_B}a, \quad (4.9)$$

with $k_+ = k_x + ik_y$ and $k_- = k_x - ik_y$. The resultant Hamiltonian is

$$\mathcal{H}_{\text{eff}}(a, k_z) = A \left(\frac{\sqrt{2}}{l_B}a\sigma_+ + \frac{\sqrt{2}}{l_B}a^\dagger\sigma_- \right) + M(a^\dagger a, k_z)\sigma_3, \quad (4.10)$$

where $M(a^\dagger a, k_z) = [M_0 - \omega(a^\dagger a + \frac{1}{2}) - M_1 k_z^2]$, with $\omega = \frac{2M_1}{l_B^2}$. Here $\sigma_+ = \frac{1}{2}(\sigma_1 + i\sigma_2)$ and $\sigma_- = \frac{1}{2}(\sigma_1 - i\sigma_2)$. From Eqs. (4.7) and (4.8), the expressions for a and a^\dagger are found to be

$$a = -\frac{1}{\sqrt{2}}[(y - l_B^2 k_x)/l_B + l_B \partial_y], \quad (4.11)$$

$$a^\dagger = -\frac{1}{\sqrt{2}}[(y - l_B^2 k_x)/l_B - l_B \partial_y], \quad (4.12)$$

It is clear that the Hamiltonian is in the direct sum form,

$$\mathcal{H}'_{\text{eff}}(k_z) = -M(0, k_z) \oplus \begin{pmatrix} M(0, k_z) & \eta\sqrt{1} \\ \eta\sqrt{1} & -M(1, k_z) \end{pmatrix} \oplus \dots \oplus \begin{pmatrix} M(n-1, k_z) & \eta\sqrt{n} \\ \eta\sqrt{n} & -M(n, k_z) \end{pmatrix} \oplus \dots \quad (4.17)$$

Thus, the energy eigenvalue for the zeroth Landau level is

$$E_0 = -M(0, k_z) = \omega/2 - M_0 + M_1 k_z^2, \quad |\psi_0\rangle = (1, 0)^T. \quad (4.18)$$

Notice that there is only one chiral state at the zeroth Landau level. For the n th level, the eigenvalues are

$$E_n^\pm = \frac{\omega}{2} \pm \sqrt{M_n^2 + n\eta^2}, \quad (4.19)$$

with \pm denotes the pseudo-spin degree of freedom, $M_n = (M_0 - \omega n - M_1 k_z^2)$, $\omega = 2M_1/l_B^2$, and $\eta = \frac{\sqrt{2}A}{l_B}$. The corresponding eigenstates are

$$|\psi_{n,+}\rangle = \left(\cos \frac{\theta_n}{2}, \sin \frac{\theta_n}{2} \right)^T, \quad (4.20)$$

$$|\psi_{n,-}\rangle = \left(\sin \frac{\theta_n}{2}, -\cos \frac{\theta_n}{2} \right)^T, \quad (4.21)$$

with $\cos \theta_n = \frac{M_n}{\sqrt{M_n^2 + 2n/l_B^2}}$. The spectrum for Landau levels is plotted in Fig. 4.2 (a). It should be emphasized that for the zeroth Landau level, there is only one chiral state.

Suppose that the Fermi level lies at zero energy, applying the electric field in the direction of the magnetic field, the electrons will be transported from one Weyl node to the other, as shown by the red dots in Fig. 4.2 (a). This will cause an imbalance of electrons between two Weyl nodes (chiral electron imbalance), which has its origin in the chiral anomaly, as shown schematically in Fig. 4.2 (b).

We now discuss the conductance under the magnetic field in z direction. The zeroth Landau band is half filled with the Fermi surface located at zero energy. Thus the transport properties of the system are dominantly determined by the zeroth Landau band. As the zeroth Landau level can be treated as a dimensional chain, according to the transport theory, by ignoring the scattering between Landau bands, the conductance can be obtained as [169]

$$\sigma_{zz} = N_L \frac{e^2}{h} = \frac{e^3}{h^2} B, \quad (4.22)$$

with N_L the degeneracy of the zeroth Landau band. The conductance is linear with respect to magnetic field B . This conductance has its origin in the chiral anomaly as we show next.

4.2.3 Chiral Anomaly

A quantum anomaly arises when a classical symmetry is broken at the quantum level. In this subsection we will first review the chiral anomaly for massless Dirac fields, and then investigate the chiral anomaly and the associated chiral magnetic effect in Weyl semimetals.

We first briefly discuss Noether's theory of conservation laws for a continuous symmetry of a classical theory. Suppose that the Lagrangian $\mathcal{L}[\phi, \partial_\mu \phi]$ is only a function of fields ϕ and their first derivatives

$\partial_\mu\phi$. Under the variation of $\phi \rightarrow \phi + \delta\phi$, the change in the action can be obtained as

$$\delta\mathcal{L} = \frac{\partial L}{\partial\phi}\delta\phi + \frac{\partial L}{\partial(\partial_\mu\phi)}\delta(\partial_\mu\phi) = \left(\frac{\partial L}{\partial\phi} - \partial_\mu\frac{\partial L}{\partial(\partial_\mu\phi)}\right)\delta\phi + \partial_\mu\left(\frac{\partial L}{\partial(\partial_\mu\phi)}\delta\phi\right). \quad (4.23)$$

The first part at the RHS vanishes when the equation of motion is satisfied. We consider the system is invariant under some continuous symmetry, which depends on the parameter α that can be taken infinitesimally small. The symmetry invariance leads to the following relation,

$$\frac{\delta\mathcal{L}}{\delta\alpha} = \partial_\mu\left(\frac{\partial L}{\partial(\partial_\mu\phi)}\frac{\delta\phi}{\delta\alpha}\right) = 0. \quad (4.24)$$

Thus, we arrive at the Noether's theorem,

$$\partial_\mu J_\mu = 0, \quad (4.25)$$

with

$$J_\mu = \frac{\partial L}{\partial(\partial_\mu\phi)}\frac{\delta\phi}{\delta\alpha}. \quad (4.26)$$

Here J_μ is known as the Noether current, a conserved quantity that corresponds to the continuous symmetry of the classical theory.

Chiral anomaly in massless Dirac fields

We first review the chiral anomaly in the massless Dirac fields. The Lagrangian for the Dirac fields reads,

$$\mathcal{L} = \bar{\psi}\gamma^\mu(i\partial_\mu - eA_\mu)\psi, \quad (4.27)$$

with $\mu = 0, 1, 2, 3$. The Lagrangian is invariant under the action of the normal (vector) and chiral (axial) phase rotations of fermions,

$$\psi \rightarrow e^{i\alpha}\psi, \quad \psi \rightarrow e^{i\alpha\gamma^5}\psi, \quad (4.28)$$

with $\alpha \in \mathbb{R}$. Correspondingly, $\bar{\psi} \rightarrow \bar{\psi}e^{-i\alpha}$ and $\bar{\psi} \rightarrow \bar{\psi}e^{i\alpha\gamma^5}$. Taking α to be infinitesimal, the normal and chiral phase transformations lead to the change of $\delta\psi = i\alpha\psi$ and $\delta\psi = i\alpha\gamma^5\psi$, respectively. From Eq. (4.26), the two kinds of symmetries lead to the following conserved quantities,

$$j^\mu = \bar{\psi}\gamma^\mu\psi, \quad j_A^\mu = \bar{\psi}\gamma^\mu\gamma^5\psi, \quad (4.29)$$

which are called the normal (vector) and chiral (axial) current. These two currents are conserved according to Noether's theorem in the classical theory,

$$\partial_\mu j_\mu = 0, \quad \partial_\mu j_A^\mu = 0. \quad (4.30)$$

But as we will show, after the regularization at the quantum level, the chiral current is not conserved, which equals to

$$\partial_\mu j_A^\mu = -\frac{e^2}{16\pi^2}\varepsilon^{\mu\nu\rho\sigma}F_{\mu\nu}F_{\rho\sigma}. \quad (4.31)$$

Here F denote the electromagnetic tensor. This means the classical axial symmetry fails to be preserved at the quantum level after the regularization. This is a kind of quantum anomaly, and it is called the chiral anomaly here.

In the following, we derive the chiral anomaly following the Fujikawa method [170], which approaches the anomaly from the measure. For the Dirac fields, the path integral can be expressed as

$$\mathcal{Z} = \int \mathcal{D}\psi \mathcal{D}\bar{\psi} e^{i \int d^4x \mathcal{L}_{\text{qed}}}, \quad (4.32)$$

where we include the electromagnetic field background into the Lagrangian,

$$\mathcal{L}_{\text{qed}} = \bar{\psi} \gamma^\mu (i\partial_\mu - eA_\mu) \psi - \frac{1}{4} F_{\mu\nu}^2. \quad (4.33)$$

Recalling the rules for Gaussian integrals of $\int \eta_i = 0$ and $\int d\eta_i \eta_j = \delta_{ij}$ with $\{\eta_i, \eta_j\} = \delta_{ij}$, the integral identity $\int d\eta_N \cdots d\eta_1 \eta_1 \cdots \eta_N = 1$ can be established. Under a linear transformation $\eta_i = \sum_j a_{ij} \eta'_j$, the product changes as $\eta_1 \cdots \eta_N = \det[a] \eta'_1 \cdots \eta'_N$. By the integral identity, it can be inferred that the corresponding measure changes as $d\eta_N \cdots d\eta_1 = \frac{1}{\det[a]} d\eta'_N \cdots d\eta'_1$. Considering a general linear transformation on the fermions in Eq (4.32), $\psi \rightarrow \Delta\psi$, $\bar{\psi} \rightarrow \bar{\psi} \Delta_c$, the change in the measure reads,

$$\mathcal{D}\psi \mathcal{D}\bar{\psi} \rightarrow \frac{1}{\mathcal{J} \mathcal{J}_c} \mathcal{D}\psi \mathcal{D}\bar{\psi}, \quad (4.34)$$

with the Jacobians $\mathcal{J} = \det \Delta$ and $\mathcal{J}_c = \det \Delta_c$. We will use the familiar relation of $\det \Delta = \exp \text{tr} \ln \Delta$ in the following.

We first consider a local phase rotation by $\psi'(x) = e^{i\alpha(x)} \psi(x)$, thus $\Delta(x) = e^{i\alpha(x)}$ and $\Delta_c(x) = e^{-i\alpha(x)}$. We first express the term $\text{tr} \ln \Delta(x) = \int d^4x \langle x | \text{Tr} \ln \Delta(x) | x \rangle$ by introducing the one-particle Hilbert space $\{|x\rangle\}$. Notice here Tr represents the trace for the internal degree of freedom, while tr represent the trace of both internal degree and spatial degree of freedom. Under such treatments, we can write the Jacobian as

$$\mathcal{J} = \mathcal{J}_c^\dagger = \exp \left(4i \int d^4x \alpha(x) \delta^4(0) \right), \quad (4.35)$$

where we have used $\langle x | x \rangle = \delta^4(0)$. In this case $\mathcal{J} \mathcal{J}_c = 1$, even with the factor $\delta^4(0)$ to be infinite, thus the measure is invariant and there is no anomaly.

However, for the chiral phase rotation of $\psi' = e^{i\alpha\gamma^5} \psi$, the linear transformations are found to be $\Delta(x) = \Delta_c(x) = e^{i\alpha\gamma^5}$, thus we have

$$\mathcal{J} = \mathcal{J}_c = \exp \left(i \int d^4x \alpha(x) \delta^4(0) \text{Tr}[\gamma^5] \right). \quad (4.36)$$

The measure will change by \mathcal{J}^2 . In this case, as $\delta^4(0)$ tends to infinite while $\text{Tr}[\gamma^5]$ is zero which means their product is undefined, the change in the measure is undefined. Regularization of this term will lead to the chiral anomaly.

We now rewrite the Jacobian in Eq. (4.36) in the the one-particle Hilbert space as

$$\mathcal{J} = \exp \left(i \int d^4x \operatorname{Tr}[\langle x | \alpha(x) \gamma^5 | x \rangle] \right). \quad (4.37)$$

The divergence in the change of the measure can be regularized by the standard method of the heat kernel regularization. We introduce the gauge invariant exponential regulator of the form $\exp(\mathbb{M}^2/\Lambda^2)$, with the Dirac operator $\mathbb{M} = \gamma^\mu \Pi_\mu = \gamma^\mu [p_\mu + ieA_\mu]$. We can do the simplification for the Dirac operator as

$$\mathbb{M}^2 = \gamma^\mu \gamma^\nu \Pi_\mu \Pi_\nu = \frac{1}{2} \{\gamma^\mu, \gamma^\nu\} \Pi_\mu \Pi_\nu + \frac{1}{2} [\gamma^\mu, \gamma^\nu] \Pi_\mu \Pi_\nu = \Pi_\mu \Pi_\mu - \frac{ie}{2} \gamma^\mu \gamma^\nu F_{\mu\nu}. \quad (4.38)$$

We focus on the exponent in Eq. (4.37),

$$\lim_{\Lambda \rightarrow \infty} \int d^4x \operatorname{Tr} \left[\langle x | \alpha(x) \gamma^5 e^{\mathbb{M}^2/\Lambda^2} | x \rangle \right] = \lim_{\Lambda \rightarrow \infty} \int d^4x \alpha(x) \operatorname{Tr} \left[\langle x | \gamma^5 \exp \left(\frac{(p - eA)^2 - \frac{ie}{2} \gamma^\mu \gamma^\nu F_{\mu\nu}}{\Lambda^2} \right) | x \rangle \right]. \quad (4.39)$$

We do the Taylor expansion to the exponential in Eq. (4.39), and drop out the term that does not survive in the limit of $\Lambda \rightarrow \infty$. After the trace operation, Eq. (4.39) becomes

$$\begin{aligned} \lim_{\Lambda \rightarrow \infty} \int d^4x \operatorname{Tr} \left[\langle x | \gamma^5 e^{\mathbb{M}^2/\Lambda^2} | x \rangle \right] \\ = - \int d^4x \alpha(x) \frac{e^2}{8} \operatorname{Tr} \left[\gamma^5 \gamma^\mu \gamma^\nu \gamma^\rho \gamma^\sigma \right] F_{\mu\nu} F_{\rho\sigma} \lim_{\Lambda \rightarrow \infty} \left[\frac{1}{\Lambda^4} \langle x | e^{(p-eA)^2/\Lambda^2} | x \rangle \right]. \end{aligned} \quad (4.40)$$

Here $\operatorname{Tr} \left[\gamma^5 \gamma^\mu \gamma^\nu \gamma^\rho \gamma^\sigma \right] = 4\epsilon^{\mu\nu\rho\sigma}$. We can perform a Fourier transformation to convert $|x\rangle$ to $|k\rangle$ with $p|k\rangle = k|k\rangle$, and do the shift of $k \rightarrow k + eA$. Then the last factor in the RHS of the above equation becomes,

$$\frac{1}{\Lambda^4} \langle x | e^{(p-eA)^2/\Lambda^2} | x \rangle = \frac{1}{\Lambda^4} \int \frac{d^4k}{(2\pi)^4} e^{k^2/\Lambda^2} = \frac{i}{\Lambda^4} \int \frac{d^4k_E}{(2\pi)^4} e^{-k_E^2/\Lambda^2} = \frac{i}{16\pi^2}, \quad (4.41)$$

where we have used the Wick rotation $k_0 \rightarrow ik_0$. Thus the change in the measure can be obtained as

$$\mathcal{J} = \exp \left(-i \int d^4x \alpha(x) \frac{e^2}{32\pi^2} \epsilon^{\mu\nu\rho\sigma} F_{\mu\nu} F_{\rho\sigma} \right). \quad (4.42)$$

As we have shown, under the chiral phase rotation, the change in the action $\mathcal{L}_{\text{qed}} \rightarrow \mathcal{L}_{\text{qed}} + \alpha(x) \partial_\mu j_A^\mu$ leads to the change of

$$\exp \left(i \int d^4x \alpha(x) \partial_\mu j_A^\mu \right) \quad (4.43)$$

in the path integral. The change in the measure is \mathcal{J}^{-2} , which reads

$$\exp \left(i \int d^4x \alpha(x) \frac{e^2}{16\pi^2} \epsilon^{\mu\nu\rho\sigma} F_{\mu\nu} F_{\rho\sigma} \right). \quad (4.44)$$

Taking into account both terms, we arrive at the equation

$$\partial_\mu j_A^\mu = -\frac{e^2}{16\pi^2} \varepsilon^{\mu\nu\rho\sigma} F_{\mu\nu} F_{\rho\sigma}, \quad (4.45)$$

which violates the the chiral gauge symmetry, and therefore is called the chiral anomaly.

Chiral Anomaly in Weyl semimetals

As we have discussed, the minimum lattice model for Weyl semimetals must contain at least two Weyl nodes with opposite chirality. Recall that a Dirac node is also composed of two Weyl points with opposite chirality. This kind of similarity enables us to treat the pair of Weyl nodes in the Weyl semimetal as the node degree of freedom, denoted by τ_z . The low-energy effective Hamiltonian for the Weyl semimetal reads [60],

$$H = \tau^z \boldsymbol{\sigma} \cdot \mathbf{k} + \tau^z b_0 + \boldsymbol{\sigma} \cdot \mathbf{b}, \quad (4.46)$$

with $\boldsymbol{\sigma}$ describing the conduction-valence band degree of freedom. The two Weyl nodes are located at $+\mathbf{b}$ and $-\mathbf{b}$ in the three-dimensional Brillouin zone with an energy difference of $2b_0$.

The corresponding action that takes into account the coupling with an external electromagnetic field reads,

$$S = \int d\tau d^3x \psi^\dagger \left[\partial_\tau + ieA_0 + \tau^z \boldsymbol{\sigma} \cdot (-i\nabla + e\mathbf{A}) + b_0\tau^z + \tau^z \boldsymbol{\sigma} \cdot \mathbf{b}\tau^z \right] \psi, \quad (4.47)$$

with $\psi = (\psi_L, \psi_R)$ composed of Weyl fermions with opposite chirality. We can write $\bar{\psi} = \psi^\dagger \gamma^0$. For the gamma matrices, we choose $\gamma^0 = \tau^x \otimes \sigma^0$, $\gamma^i = i\tau^y \otimes \sigma^i$, $\gamma^5 = \tau^z \otimes \sigma^0$, with $i = 1, 2, 3$. Note that the five gamma matrices anticommute with each other. After these treatments, the action can be rewritten as

$$S = \int d^4x \bar{\psi} i\gamma^\mu \left(\partial_\mu + ieA_\mu + ib_\mu \gamma^5 \right) \psi, \quad (4.48)$$

with $\mu = 1, 2, 3, 4$. Here b_i with $i = 1, 2, 3$ are components of \mathbf{b} and $b_4 = -ib_0$. The corresponding path integral can be written as

$$\mathcal{Z} = \int \mathcal{D}\psi \mathcal{D}\bar{\psi} e^{-S}. \quad (4.49)$$

Comparing with the standard action of Dirac fields from the Lagrangian in Eq. (4.27), we find that if the extra b_μ term is reduced to zero, the above action is exactly the same as the action for the Dirac fields.

Actually the extra b_μ term can be eliminated by an infinite sequence of infinitesimal chiral gauge transformations of

$$\psi \rightarrow e^{-ids\theta(x)\gamma^5/2} \psi, \quad \bar{\psi} \rightarrow \bar{\psi} e^{-ids\theta(x)\gamma^5/2}, \quad (4.50)$$

with $\theta(x) = 2b_\mu x_\mu$. The differential ds of the variable $s \in [0, 1]$ parametrizes the infinite sequence of the chiral gauge transformation. This elimination process inevitably induces the change in the measure, which reads

$$\mathcal{D}\psi \mathcal{D}\bar{\psi} \rightarrow \frac{1}{J^2} \mathcal{D}\psi \mathcal{D}\bar{\psi}, \quad (4.51)$$

with $J = \det e^{-ids\theta(x)\gamma^5/2}$. Comparing with the change in the measure for the Dirac fields in Eq. (4.35),

everything is the same if we do the substitution of

$$\alpha(x) \rightarrow -ds \frac{\theta(x)}{2}. \quad (4.52)$$

Similar to Eq. (4.44), the extra b_μ term induces a change in the path integral as

$$\mathcal{J}^{-2} = \exp \left(-ids \int d^4x \theta(x) \frac{e^2}{32\pi^2} \varepsilon^{\mu\nu\rho\sigma} F_{\mu\nu} F_{\rho\sigma} \right), \quad (4.53)$$

with the extra terms from the chiral transformation eliminated in the regularization process. After fully eliminating the $b_\mu \gamma^5$ term in Eq. (4.48), the total change in the action in the measure can be obtained by integration over the variable s ,

$$S_\theta = i \int_0^1 ds \int d^4x \theta(x) I(x) = \frac{ie^2}{32\pi^2} \int d^4x \theta(x) \varepsilon^{\mu\nu\rho\sigma} F_{\mu\nu} F_{\rho\sigma}. \quad (4.54)$$

This result is in accordance with that in Ref. [60] with a similar approach.

Notice that $\varepsilon^{\mu\nu\rho\sigma} F_{\mu\nu} F_{\rho\sigma} = 4\varepsilon^{\mu\nu\rho\sigma} \partial_\mu A_\nu \partial_\rho A_\sigma$. We can do the integration by parts on S_θ , which yields,

$$S_\theta = \frac{e^2}{8\pi^2} \int dt d^3x \partial_\mu \theta(x) \varepsilon^{\mu\nu\rho\sigma} A_\nu \partial_\rho A_\sigma = \frac{e^2}{4\pi^2} \int dt d^3x b_\mu \varepsilon^{\mu\nu\rho\sigma} A_\nu \partial_\rho A_\sigma, \quad (4.55)$$

with $\theta(x) = 2b_\mu x_\mu$.

As in the field theory context, the vector potential always couples to some currents, thus the effective action can be written as $S_\theta = \int d^4x j_\mu A_\mu$. Varying the effective action with respect to the electromagnetic gauge A_μ will yield the current. We focus on the chiral magnetic effect, which comes from the b_0 term

$$j_\nu = \frac{e^2}{2\pi^2} b_0 \varepsilon^{0\nu\rho\sigma} \partial_\rho A_\sigma. \quad (4.56)$$

It can be further written as

$$\mathbf{j} = \frac{e^2}{2\pi^2} b_0 \mathbf{B}, \quad (4.57)$$

with $\mathbf{B} = \nabla \times \mathbf{A}$ the magnetic field. We can see that the current is proportional to the magnetic field, which is the chiral magnetic effect. Now we try to understand the b_0 term, which is the energy difference between the two Weyl points. Suppose that the chemical potentials for the left and the right Weyl node are μ_L and μ_R , respectively, then $b_0 = \mu_R - \mu_L$ denotes the chemical potential difference between the two nodes. The energy cost per unit time by moving the electron from left to right is $b_0 d(N_R - N_L)/dt$, which equals to the power delivered by the current $\mathbf{j} \cdot \mathbf{E}$. From this equivalence, we can obtain the relation

$$\frac{d(N_R - N_L)}{dt} = \frac{e^2}{2\pi^2} \mathbf{E} \cdot \mathbf{B}. \quad (4.58)$$

When the electric field is applied in the direction of the magnetic field, electrons from one Weyl node will be transported to the other with opposite chirality, causing an imbalance between two Weyl nodes, as shown in Fig. 4.2.

4.3 Non-Hermitian Weyl semimetals

In this section, we focus on the non-Hermitian Weyl semimetals. We will consider adding different kinds of non-Hermitian potentials to the lattice Weyl Hamiltonian described in Eq. (4.3). The non-Hermitian Weyl Hamiltonian can be written in a general form as

$$H(\mathbf{k}) = \sin k_x \sigma_1 + \sin k_y \sigma_2 + (m - \cos k_x - \cos k_y - \cos k_z) \sigma_3 + i\lambda \sigma_\mu, \quad (4.59)$$

where $i\lambda \sigma_\mu$ is the non-Hermitian potential. As we have discussed, in the absence of a non-Hermitian potential, the above Hamiltonian exhibits Weyl nodes that are located at

$$\mathbf{k}_c = (0, 0, \pm \arccos(m - 2)). \quad (4.60)$$

Near these Weyl nodes, as we have shown, the physics can be effectively described by the low energy effective Hamiltonian $H_W(\mathbf{k}) = \sum_{i=1}^3 \mathbf{v}_i \cdot \delta \mathbf{k} \sigma_i$. For simplicity and without loss of generality, we focus on the case of $H_W(\mathbf{k}) = \mathbf{k} \cdot \boldsymbol{\sigma}$. With the inclusion of the non-Hermitian potential, the Hamiltonian becomes,

$$H'_W(\mathbf{k}) = \mathbf{k} \cdot \boldsymbol{\sigma} + i\lambda \sigma_\mu. \quad (4.61)$$

We focus on the representative example of $i\lambda \sigma_3$. The energy spectrum is $E_W = \pm(k_x^2 + k_y^2 + k_z^2 - \lambda^2 + 2i\lambda k_z)^{1/2}$. Instead of a point, the band crossing points now form a ring with radius of λ located at the center of $k_z = 0$ plane. This ring is called the Weyl exceptional ring, as the composing points are all exceptional points.

We find the Chern number of the Weyl point is inherited by the Weyl exceptional ring. We can choose a sphere S^2 with radius k_ρ centered at the origin and calculate the Berry curvature and Chern number on it. This sphere can be parametrized by $\mathbf{k} = (k_\rho \sin \theta \cos \phi, k_\rho \sin \theta \sin \phi, k_\rho \cos \theta)$, then the Hamiltonian on the sphere is

$$H_W(\mathbf{k})' = k_\rho \begin{pmatrix} i\lambda' + \cos \theta & \sin \theta e^{-i\phi} \\ \sin \theta e^{i\phi} & -(i\lambda' + \cos \theta) \end{pmatrix}, \quad (4.62)$$

with $\lambda' = \lambda/k_\rho$. The eigenvalue for the valance band is

$$E_- = -d = -\sqrt{1 - \lambda'^2 + 2i\lambda' \cos \theta}, \quad (4.63)$$

and the corresponding right ($H|\psi\rangle = E\psi$) and left eigenstates ($\langle\langle\psi|H = \langle\langle\psi|E$) are,

$$\begin{aligned} |\psi_-\rangle &= \frac{1}{\sqrt{2d(d + i\lambda' + \cos \theta)}} \begin{pmatrix} \sin \theta e^{-i\phi} \\ -d - (\cos \theta + i\lambda') \end{pmatrix}, \\ \langle\langle\psi_-| &= \frac{1}{\sqrt{2d(d + i\lambda' + \cos \theta)}} \begin{pmatrix} \sin \theta e^{i\phi} & -d - (\cos \theta + i\lambda') \end{pmatrix}, \end{aligned} \quad (4.64)$$

with the normalization condition of $\langle\langle\psi_-|\psi_-\rangle = 1$. The Berry curvature is calculated with the formula

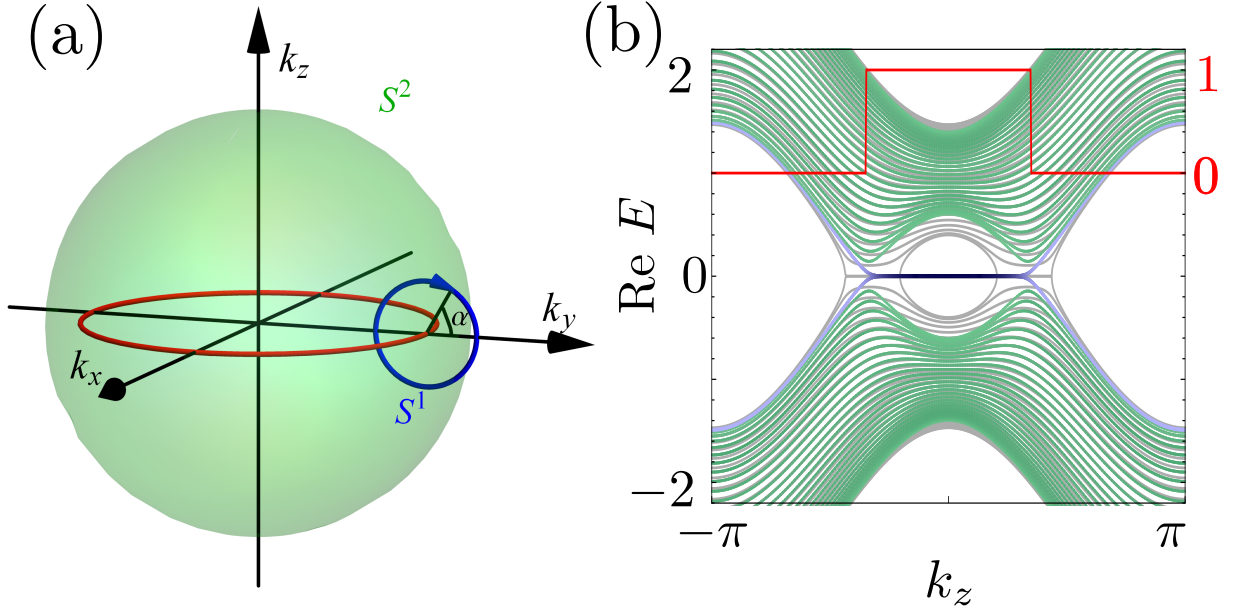


Figure 4.3: *Non-Hermitian Weyl semimetal.* (a) The red ring denotes the Weyl exceptional ring, which can be enclosed by the one-dimensional sphere S^1 (blue) and two-dimensional sphere S^2 (green). (b) Real part of the energy spectra for the Weyl Hamiltonian with the non-Hermitian term $i\lambda\sigma_2$. The green curves are for the case of open boundary conditions and the gray curves for that of periodic boundary conditions. The surface states is highlighted in blue and black. The topological invariant C_{k_z} is given in red and shows that we find topological surface states when $C_{k_z} = +1$ and no surface states when $C_{k_z} = 0$. The parameters are chosen as $\lambda = 0.3$ and $m = 2.5$.

$\Omega_{\theta\phi} = i \left(\langle \partial_{\theta}\psi_- | \partial_{\phi}\psi_- \rangle - \langle \partial_{\phi}\psi_- | \partial_{\theta}\psi_- \rangle \right)$, which yields

$$\Omega_{\theta\phi} = \frac{(1 + i\lambda' \cos \theta) \sin \theta}{2(1 - \lambda'^2 + 2i\lambda' \cos \theta)^{\frac{3}{2}}}. \quad (4.65)$$

Then the Chern number on the sphere S^2 can be calculated as

$$C_2 = \frac{1}{2\pi} \int_0^{2\pi} d\phi \int_0^{\pi} d\theta \Omega_{\theta\phi} = \int_0^{\pi} \frac{(1 + i\lambda' \cos \theta) \sin \theta}{2(1 - \lambda'^2 + 2i\lambda' \cos \theta)^{\frac{3}{2}}} d\theta = \int_{-1}^1 \frac{1 + i\lambda' x}{2(1 - \lambda'^2 + 2i\lambda' x)^{\frac{3}{2}}} dx. \quad (4.66)$$

Making a substitution of $x = 2t - 1$, the integral above becomes

$$\int_0^1 \frac{1 - i\lambda' + 2i\lambda't}{(1 - 2i\lambda' - \lambda'^2 + 4i\lambda't)^{\frac{3}{2}}} dt = \frac{1}{(1 - i\lambda')^2} \int_0^1 \frac{1}{(1 - zt)^{\frac{3}{2}}} dt + \frac{2i\lambda'}{(1 - i\lambda')^3} \int_0^1 \frac{t}{(1 - zt)^{\frac{3}{2}}} dt \quad (4.67)$$

with $z = (-4i\lambda')/(1 - i\lambda')^2$. The first and second term in the last step above are actually integral

representations of the hypergeometric function. Thus

$$C_2 = \frac{1}{(1-i\lambda')^2} \Gamma(1)\Gamma(1)\mathbf{F}\left(\frac{3}{2}, 1, 2; z\right) + \frac{2i\lambda'}{(1-i\lambda')^3} \Gamma(1)\Gamma(2)\mathbf{F}\left(\frac{3}{2}, 2, 3; z\right) = \frac{1+i\lambda'}{2(1-i\lambda')\sqrt{\frac{(1+i\lambda')^2}{(1-i\lambda')^2}}} + \frac{1}{2}, \quad (4.68)$$

with $\mathbf{F}(a, b, c; z) = \sum_{s=0}^{+\infty} \frac{(a)_s (b)_s}{\Gamma(c+s)} \frac{z^s}{s!}$ and $\Gamma(x)$ the Gamma function [171]. The integral is accompanied with the condition that $|\arg(1-z)| \leq \pi$, which yields $|\arg[(1+i\lambda')/(1-i\lambda')]| \leq \pi/2$ and $\lambda' = \lambda/k_\rho < 1$. Since $|\arg[(1+i\lambda')/(1-i\lambda')]| \leq \pi/2$, the square root in Eq. (4.68) equals to $(1+i\lambda')/(1-i\lambda')$ without an extra phase. Thus for $k_\rho > \lambda$, the Chern number is

$$C_2 = \chi = +1. \quad (4.69)$$

Besides the Chern number, there is another topological invariant for the Weyl exceptional ring that is unique in non-Hermitian systems, which belongs to the $N/2$ group as we introduced in the previous chapter. Here we show a detailed derivation for this topological invariant. At the exceptional point $\mathbf{k}_{\text{EP}} = (0, \lambda, 0)$ on the Weyl exceptional ring, the Hamiltonian becomes $H_{\text{EP}} = H_{\text{WR}}(\mathbf{k}_{\text{EP}})$ and there is only one eigenstate $|\psi_0^{\text{EP}}\rangle$. Together with the associated vector $|\psi_1^{\text{EP}}\rangle$, they satisfy

$$H_{\text{EP}}|\psi_0^{\text{EP}}\rangle = E_{\text{EP}}|\psi_0^{\text{EP}}\rangle, \quad H_{\text{EP}}|\psi_1^{\text{EP}}\rangle = E_{\text{EP}}|\psi_1^{\text{EP}}\rangle + |\psi_0^{\text{EP}}\rangle. \quad (4.70)$$

The corresponding left vectors satisfy $\langle\langle\psi_0^{\text{EP}}|H_{\text{EP}} = \langle\langle\psi_0^{\text{EP}}|E_{\text{EP}}$ and $\langle\langle\psi_1^{\text{EP}}|H_{\text{EP}} = \langle\langle\psi_1^{\text{EP}}|E_{\text{EP}} + \langle\langle\psi_0^{\text{EP}}|$. The left and right eigenstates are self-orthogonal $\langle\langle\psi_0^{\text{EP}}|\psi_0^{\text{EP}}\rangle\rangle = 0$. The set of eigenstates and the associated vectors at the exceptional point is called Jordan chain in the mathematical literature, and by imposing the normalization conditions for the Jordan chain of $\langle\langle\psi_1^{\text{EP}}|\psi_0^{\text{EP}}\rangle\rangle = 1$ and $\langle\langle\psi_1^{\text{EP}}|\psi_1^{\text{EP}}\rangle\rangle = 0$, we can get the eigenstate as $|\psi_0^{\text{EP}}\rangle = 1/\sqrt{2} \begin{pmatrix} \chi & 1 \end{pmatrix}^T$, $|\psi_1^{\text{EP}}\rangle = 1/(i\lambda\sqrt{2}) \begin{pmatrix} \chi & 0 \end{pmatrix}^T$ and $\langle\langle\psi_0^{\text{EP}}| = i\lambda\sqrt{2} \begin{pmatrix} \chi & -1 \end{pmatrix}$, $\langle\langle\psi_1^{\text{EP}}| = \sqrt{2} \begin{pmatrix} 0 & 1 \end{pmatrix}$ after restoring χ in the derivation.

We can encircle the Weyl exceptional ring at \mathbf{k}_{EP} by the blue circle S^1 in Fig. 4.3 (a), which can be parametrized as $(0, \lambda + \rho \cos \alpha, \rho \sin \alpha)$. Suppose S^1 is in the close neighborhood of the exceptional point ($\rho \ll \lambda$), we can obtain eigenvalues and eigenstates to the leading order as

$$E_{(S^1, \pm)} = E_{\text{EP}} \pm \sqrt{\mu(\alpha)}, \quad (4.71)$$

$$|\psi_{S^1, \pm}\rangle = |\psi_0^{\text{EP}}\rangle \pm \sqrt{\mu(\alpha)}|\psi_1^{\text{EP}}\rangle,$$

with

$$\mu(\alpha) = \sum_{i=x,y,z} \langle\langle\psi_0^{\text{EP}}|\partial H_{\text{WR}}(\mathbf{k})/\partial k_i|\psi_0^{\text{EP}}\rangle\rangle (k_i - \mathbf{k}_{\text{EP},i}), \quad (4.72)$$

which equals to $2\lambda\rho e^{i\chi\alpha}$. The left eigenstates can be obtained similarly by $\langle\langle\psi_{S^1, \pm}| = \langle\langle\psi_0^{\text{EP}}| \pm \sqrt{\mu(\alpha)}\langle\langle\psi_1^{\text{EP}}|$. With the eigenstates, we can compute the Berry phase γ_+ for the conductance band along S^1 ,

$$\gamma_+ = \oint_{2S^1} d\alpha \frac{i\langle\langle\psi_{S^1, +}|\partial_\alpha|\psi_{S^1, +}\rangle\rangle}{\langle\langle\psi_{S^1, +}|\psi_{S^1, +}\rangle\rangle} = \frac{1}{2} \oint_{2S^1} d\alpha i\partial_\alpha \ln \sqrt{\mu(\alpha)}. \quad (4.73)$$

Since $i\partial_\alpha \ln \sqrt{\mu(\alpha)} = \partial_\alpha \arg \sqrt{\mu(\alpha)}$ for $\mu(\alpha)$ in Eq. (4.72), we can see that the Berry phase is essentially

the same as the winding number of eigenvalue,

$$\gamma_+ = \frac{1}{2} \oint_{2S^1} d\alpha \partial_\alpha \arg \sqrt{\mu(\alpha)} = \frac{1}{2} \oint_{2S^1} d\alpha \partial_\alpha \arg E_{(S^1,+)}. \quad (4.74)$$

With the expression for $\mu(\alpha)$, the topological invariant of C_1 is

$$C_1 = \frac{1}{2\pi} \oint_{S^1} \partial_\alpha \arg \left(\sqrt{2\lambda\rho} e^{i\chi\alpha/2} \right) = \frac{\chi}{2} = \frac{1}{2}, \quad (4.75)$$

which is topologically non-trivial. Thus, besides the Chern number, there is another topological invariant from the winding number of the complex eigenvalues.

From the Hamiltonian of Eq. (4.59), there are two kinds of non-Hermitian potentials according to our classification scheme in the precious chapter, (i) the non-Hermitian kinetic terms, $i\lambda\sigma_1$ and $i\lambda\sigma_2$; (ii) the non-Hermitian mass terms, $i\lambda\sigma_3$. We should emphasize that the two non-Hermitian kinetic terms are equivalent to each other, as in the original Hermitian Weyl Hamiltonian, k_x and k_y are equivalent. Therefore, in the following discussions, we will focus on the non-Hermitian terms of $i\lambda\sigma_2$ and $i\lambda\sigma_3$.

4.3.1 Non-Hermitian potential $i\lambda\sigma_2$

We first consider the non-Hermitian potential $i\lambda\sigma_2$, which is equivalent to the non-Hermitian potential $i\lambda\sigma_1$. The spectrum of the Hamiltonian with the non-Hermitian potential $i\lambda\sigma_2$ is given by

$$E = \pm \sqrt{(\sin k_x)^2 + (\sin k_y)^2 + M_{\mathbf{k}}^2 - \lambda^2 + 2i\lambda \sin k_y}, \quad (4.76)$$

where $M_{\mathbf{k}} = m - \cos k_x - \cos k_y - \cos k_z$. We note that the spectrum is purely real for $k_y = 0$ and $\lambda^2 < \min_{\mathbf{k}} [M_{\mathbf{k}}^2 + (\sin k_x)^2]$. The spectrum is purely imaginary for $k_y = 0$ and $\lambda^2 > \max_{\mathbf{k}} [M_{\mathbf{k}}^2 + (\sin k_x)^2]$. In the following, we will discuss the spectra and topology for two kinds of boundary conditions. As boundary conditions play an important role in determining both the spectra and topology, we will pay special attention to boundary conditions in our discussions.

Spectra and topology for the (010) slab

In real space with open boundary conditions in the y direction (i.e., for the (010) slab), the Hamiltonian with the non-Hermitian potential $i\lambda\sigma_2$ reads

$$H_R(y, k_x, k_z) = \frac{1}{2i} \sigma_2 \otimes (S - S^\dagger) - \frac{1}{2} \sigma_3 \otimes (S + S^\dagger) + \sin k_x \sigma_1 \otimes \mathbb{1} + [(m - \cos k_x - \cos k_z) \sigma_3 + i\lambda\sigma_2] \otimes \mathbb{1}, \quad (4.77)$$

where S and S^\dagger are the forward and backward translation operators (shift operators), which let $x \rightarrow x+1$ and $x \rightarrow x-1$, respectively. For open boundary conditions, the S matrix reads

$$S = \begin{pmatrix} 0 & 0 & 0 & \cdots & 0 \\ 1 & 0 & 0 & \cdots & 0 \\ 0 & 1 & 0 & \cdots & 0 \\ \vdots & \vdots & \ddots & \ddots & \vdots \\ 0 & 0 & \cdots & 1 & 0 \end{pmatrix}, \quad S_{i,j} = \delta_{i,j+1} \quad \text{for } i = 1 \dots N-1. \quad (4.78)$$

For the (010) slab, the spectrum with open and periodic boundary conditions look very different. This is because $i\lambda\sigma_2$ commutes with the kinetic term $\sin k_y\sigma_2$, which allows us to transform the system with open boundary conditions to an Hermitian Hamiltonian, essentially by absorbing the non-Hermitian term in the shift operator as we have discussed in the previous chapter. This, however, is not possible for periodic boundary conditions.

In order to study how the spectrum of the Hamiltonian changes as we go from periodic to open boundary conditions, we introduce the operator \hat{S}_β with the Hamiltonian

$$\begin{aligned} \hat{H}_\beta(y, k_x, k_z) &= \frac{1}{2i}\sigma_2 \otimes (\hat{S}_\beta - \hat{S}_\beta^\dagger) - \frac{1}{2}\sigma_3 \otimes (\hat{S}_\beta + \hat{S}_\beta^\dagger) + \sin k_x\sigma_1 \otimes \mathbb{1} \\ &\quad + [(m - \cos k_x - \cos k_z)\sigma_3 + i\lambda\sigma_2] \otimes \mathbb{1}, \end{aligned} \quad (4.79)$$

where

$$\hat{S}_\beta = \begin{pmatrix} 0 & 0 & 0 & \dots & \beta \\ 1 & 0 & 0 & \dots & 0 \\ 0 & 1 & 0 & \dots & 0 \\ \vdots & \vdots & \ddots & \ddots & \vdots \\ 0 & 0 & \dots & 1 & 0 \end{pmatrix}. \quad (4.80)$$

As we slowly interpolate from periodic to open boundary conditions by changing the parameter β from 1 to 0, we go through an exceptional point in the spectrum, where the matrix is no longer diagonalizable. The geometric multiplicity is given by the dimension of the kernel of the $H_R - E\mathbb{1}$. For a matrix to be diagonalizable the geometric and algebraic multiplicities of the eigenvalues must be equal. We find that this is no longer the case in a finite lattice system at some critical β_c .

Relation between PBCs and OBCs As we have shown in the previous chapter, the spectra and topology between systems of periodic and open boundary conditions might differ drastically. This difference can be effectively explained through the transfer matrix method, which has been introduced in the previous chapter. We first separate out the k_y components from the Hamiltonian (4.59). This gives

$$H(\mathbf{k}) = \begin{pmatrix} -\frac{1}{2}(e^{+ik_y} + e^{-ik_y}) & -\frac{1}{2}(e^{+ik_y} - e^{-ik_y}) \\ +\frac{1}{2}(e^{+ik_y} - e^{-ik_y}) & +\frac{1}{2}(e^{+ik_y} + e^{-ik_y}) \end{pmatrix} + \sin k_x\sigma_1 + M_{\mathbf{k}}\sigma_3 + i\lambda\sigma_2, \quad (4.81)$$

where $M_{\mathbf{k}} = m - \cos k_x - \cos k_z$. Then we identify the hopping matrix J and the on-site matrix M in the Bloch Hamiltonian as

$$J = \begin{pmatrix} -\frac{1}{2} & -\frac{1}{2} \\ +\frac{1}{2} & +\frac{1}{2} \end{pmatrix}, \quad M = \sin k_x\sigma_1 + M_{\mathbf{k}}\sigma_3 + i\lambda\sigma_2. \quad (4.82)$$

We note that J is nilpotent with index 2, since $J^2 = 0$, and that J has rank $r = 1$, since the two rows/columns are linearly dependent. Next, we need to construct the on-site Greens function \mathcal{G} and

find the singular value decomposition of J . We obtain

$$\mathcal{G} = (E\mathbb{1} - M)^{-1} = \frac{E\sigma_0 + \sin k_x \sigma_1 + i\lambda \sigma_2 + M_{\mathbf{k}} \sigma_3}{E^2 + \lambda^2 - M_{\mathbf{k}}^2 - \sin^2 k_x}. \quad (4.83)$$

The singular value decomposition of J gives

$$J = V \Xi W^\dagger, \quad V = \frac{1}{\sqrt{2}} \begin{pmatrix} -1 & 1 \\ 1 & 1 \end{pmatrix}, \quad \Xi = \begin{pmatrix} 1 & 0 \\ 0 & 0 \end{pmatrix}, \quad W = \frac{1}{\sqrt{2}} \begin{pmatrix} 1 & -1 \\ 1 & 1 \end{pmatrix}. \quad (4.84)$$

We observe that J has only one singular value $\xi = 1$. Hence, we can find the reduced singular value decomposition

$$J = v \xi w^\dagger, \quad v = \begin{pmatrix} -\frac{1}{\sqrt{2}} \\ \frac{1}{\sqrt{2}} \end{pmatrix}, \quad w = \begin{pmatrix} \frac{1}{\sqrt{2}} \\ \frac{1}{\sqrt{2}} \end{pmatrix}. \quad (4.85)$$

With this, we are ready to compute the transfer matrix T , which is defined in the previous chapter as

$$T = \frac{1}{\xi \mathcal{G}_{vw}} \begin{pmatrix} 1 & -\xi \mathcal{G}_{ww} \\ \xi \mathcal{G}_{vv} & \xi^2 (\mathcal{G}_{vw} \mathcal{G}_{ww} - \mathcal{G}_{vv} \mathcal{G}_{ww}) \end{pmatrix} = \frac{1}{\mathcal{G}_{vw}} \begin{pmatrix} 1 & -\mathcal{G}_{ww} \\ \mathcal{G}_{vv} & \mathcal{G}_{vw} \mathcal{G}_{ww} - \mathcal{G}_{vv} \mathcal{G}_{ww} \end{pmatrix}, \quad (4.86)$$

where $\mathcal{G}_{ab} = b^\dagger \mathcal{G} a$ with $a, b \in \{v, w\}$. Inserting Eq. (4.83), we obtain

$$T = \frac{1}{M_{\mathbf{k}} - \lambda} \begin{pmatrix} \sin^2 k_x + M_{\mathbf{k}}^2 - \lambda^2 - E^2 & \sin k_x + E \\ \sin k_x - E & 1 \end{pmatrix}. \quad (4.87)$$

The determinant and the trace of the transfer matrix T are given by

$$\begin{aligned} \det T &= \frac{M_{\mathbf{k}} + \lambda}{M_{\mathbf{k}} - \lambda}, \\ \text{Tr } T &= \frac{1 + \sin^2 k_x + M_{\mathbf{k}}^2 - \lambda^2 - E^2}{M_{\mathbf{k}} - \lambda}. \end{aligned} \quad (4.88)$$

It is clear that for $\lambda \neq 0$, the determinant of the transfer matrix satisfies

$$|\det T| \neq 1, \quad (4.89)$$

which means that the spectra of open and periodic boundary conditions are different [144]. We numerically calculate the open and periodic systems' spectra as shown in Fig. 4.3 (b), which indeed differ from each other. Also note that when $\det T = 0$ or ∞ , i.e., for $M_{\mathbf{k}} = \pm\lambda$, the real-space Hamiltonian exhibits exceptional points of an order that scales with system size. This implies unidirectionality in the hopping, i.e., the states can propagate only in one direction.

From the transfer matrix we can also find expressions for bulk spectra with open and periodic boundary conditions. The condition for the existence of bulk Bloch states with PBCs is

$$\text{Tr } T = e^{i\phi} + \det T e^{-i\phi}, \quad (4.90)$$

where $\phi = 2\pi l/N$, $l \in \{0, \dots, N-1\}$. In the limit $N \rightarrow \infty$ we set $\phi \in [0, 2\pi)$. From Eq. (4.88), we obtain

$$E_{\text{PBC}} = \pm \sqrt{1 + \sin^2 k_x - \lambda^2 + M_{\mathbf{k}}^2 - 2M_{\mathbf{k}} \cos \phi + 2i\lambda \sin \phi}. \quad (4.91)$$

The condition for the existence of bulk bands with open boundary conditions is given by

$$\text{Tr } T = 2\sqrt{\det T} \cos \phi, \quad (4.92)$$

with $\phi \in [0, \pi]$. Inserting the expression for T , Eq. (4.88), gives

$$E_{\text{OBC}} = \pm \sqrt{1 + \sin^2 k_x - \lambda^2 + M_{\mathbf{k}}^2 - 2\sqrt{M_{\mathbf{k}}^2 - \lambda^2} \cos \phi}. \quad (4.93)$$

Similarity transformation For the (010) slab we can turn the Hamiltonian with OBCs to be Hermitian through similarity transformations. This is because $i\lambda\sigma_2$ commutes with the kinetic term $\sin k_y\sigma_2$, which indicates that the Hamiltonian is superficially non-Hermitian according to our theory in the previous chapter.

As now the the lattice Hamiltonian of the non-Hermitian Weyl semimetal, shown in Eq. (4.77), is still of the Dirac Hamiltonian form, we can construct the similarity transformation developed in the previous chapter. The similarity transformation for the internal degree parts is constructed as

$$\rho' = \frac{1}{2\sqrt{\alpha}} [(\alpha + 1)\sigma_0 + (\alpha - 1)\sigma_1], \quad (4.94)$$

with $\alpha = \sqrt{(M_{\mathbf{k}} - \lambda)/(M_{\mathbf{k}} + \lambda)}$. Together with the spatial part, the total similarity transformation operator is constructed as

$$\rho = \rho' \otimes \text{diag}(1, \alpha, \alpha^2, \dots, \alpha^{N_y-1}), \quad (4.95)$$

where N_y is the number of unit cells in the y direction. Indeed, performing the similarity transform of ρ on Eq. (4.77) gives

$$\begin{aligned} \tilde{H}_R(y, k_x, k_z) &= \rho^{-1} \hat{H}_R(y, k_x, k_z) \rho \\ &= \sqrt{M_{\mathbf{k}}^2 - \lambda^2} \sigma_3 \otimes \mathbb{1} + \sin k_x \sigma_1 \otimes \mathbb{1} + \frac{1}{2i} \sigma_2 \otimes (S - S^\dagger) - \frac{1}{2} \sigma_3 \otimes (S + S^\dagger). \end{aligned} \quad (4.96)$$

Transforming this back to momentum space gives

$$\tilde{H}(\mathbf{k}) = \sin k_x \sigma_1 + \sin k_y \sigma_2 + \left[\sqrt{M_{\mathbf{k}}^2 - \lambda^2} - \cos k_y \right] \sigma_3. \quad (4.97)$$

The above equation has the form of a Hermitian Weyl semi-metal around the Weyl node. This Weyl Hamiltonian exhibits Weyl nodes which are located at

$$\mathbf{k}_0 = (0, 0, \pm \arccos[m - 1 \pm \sqrt{1 + \lambda^2}]). \quad (4.98)$$

It is well known that for fixed k_z , Eq. (4.97) is topological for

$$\sqrt{M_{\mathbf{k}}^2 - \lambda^2} < 1 \quad \Leftrightarrow \quad \sqrt{(m - \cos k_x - \cos k_z)^2 - \lambda^2} < 1. \quad (4.99)$$

The corresponding topological invariant is the Chern number, which is given by

$$C_{k_z} = \frac{1}{4\pi} \oint_{\mathcal{C}_{k_z}} dk_x dk_y \hat{\mathbf{d}}_{\mathbf{k}} \cdot \left[\partial_{k_x} \hat{\mathbf{d}}_{\mathbf{k}} \times \partial_{k_y} \hat{\mathbf{d}}_{\mathbf{k}} \right], \quad \text{with } \hat{\mathbf{d}}_{\mathbf{k}} = \frac{\mathbf{d}_{\mathbf{k}}}{|\mathbf{d}_{\mathbf{k}}|}, \quad (4.100)$$

and $d_x(\mathbf{k}) = \sin k_x$, $d_y(\mathbf{k}) = \sin k_y$, and $d_z(\mathbf{k}) = \sqrt{M_{\mathbf{k}}^2 - \lambda^2} - \cos k_y$. This Chern number evaluates to

$$C_{k_z} = \begin{cases} 0 & |k_z| > \arccos[m - 1 \pm \sqrt{1 + \lambda^2}] \\ +1 & |k_z| < \arccos[m - 1 \pm \sqrt{1 + \lambda^2}] \end{cases}. \quad (4.101)$$

Whenever $C_{k_z} \neq 0$ the non-Hermitian Weyl Hamiltonian exhibits a topological surface state, leading to an arc state connecting the Weyl points (4.98). In Fig. 4.3(b), the Chern number obtained in this way corresponds well with the topological boundary states obtained numerically. We will directly compute the topological surface states in the following.

Computation of surface states Via the bulk-boundary correspondence, we expect that there are surface states for $\sqrt{M_{\mathbf{k}}^2 - \lambda^2} < 1$, i.e., when $C_{k_z} \neq 0$. To confirm this, we now explicitly compute the surface states. From the Hamiltonian in Eq. (4.77), we know that except for the \mathbf{y} direction, the translational symmetry in the other directions is preserved. Thus we adopt the ansatz for the right eigenstates

$$|\psi_{\tilde{\mathbf{k}}}\rangle = \sum_{i=1}^{N_y} \beta^i |i\rangle \otimes |\xi_{\tilde{\mathbf{k}}}\rangle, \quad (4.102)$$

with $\tilde{\mathbf{k}}$ representing (k_x, k_z) . For the non-Hermitian Hamiltonian, the conjugation of the right eigenstates does not give the left eigenstates generally. Thus for the left eigenstates we adopt a similar ansatz,

$$\langle\langle \psi_{\tilde{\mathbf{k}}} | = \sum_{i=1}^{N_y} \langle i | \otimes \langle\langle \xi_{\tilde{\mathbf{k}}} | \beta'^i. \quad (4.103)$$

To study the localization of modes, we consider the biorthogonal expectation value of the projection operator $\Pi_i = |i\rangle\langle i|$, which is

$$\langle\langle \psi_{\tilde{\mathbf{k}}} | \Pi_i | \psi_{\tilde{\mathbf{k}}} \rangle = |\beta\beta'|^i. \quad (4.104)$$

For $|\beta\beta'| < 1$, the mode is exponentially localized to the $i = 1$ unit cell, while for $|\beta\beta'| > 1$, it is localized at the $i = N_y$ unit cell.

For the right eigenvector, in solving the Schrödinger equation of

$$\hat{H}_R(y, k_x, k_z) |\psi_{\tilde{\mathbf{k}}}\rangle = \hat{E}_{k_x} |\psi_{\tilde{\mathbf{k}}}\rangle, \quad (4.105)$$

we find it gives two constraints,

$$\left[\sin k_x \sigma_1 + \frac{1}{2i}(\beta - \beta^{-1})\sigma_2 + (M - \cos k_x - \cos k_z - \frac{1}{2}(\beta + \beta^{-1}))\sigma_3 + i\lambda\sigma_2 \right] |\xi_{k_x}\rangle = \hat{E}_{k_x} |\xi_{k_x}\rangle \quad (4.106)$$

and

$$\left[\sin k_x \sigma_1 + \frac{1}{2i}\beta\sigma_2 + (M - \cos k_x - \cos k_z - \frac{1}{2}\beta)\sigma_3 + i\lambda\sigma_2 \right] |\xi_{k_x}\rangle = \hat{E}_{k_x} |\xi_{k_x}\rangle. \quad (4.107)$$

The difference between the above two equations yields a simpler relation,

$$i\sigma_3\sigma_2|\xi_{k_x}\rangle = |\xi_{k_x}\rangle. \quad (4.108)$$

This means the boundary states are the positive eigenvalue of $i\sigma_3\sigma_2$, from which we can construct the projector for the boundary states

$$P = \frac{1}{2}(1 + i\sigma_3\sigma_2). \quad (4.109)$$

With the relation of Eq. (4.108), Eq. (4.107) becomes,

$$\left[\sin k_x \sigma_x + (M - \cos k_x + \lambda - \beta)\sigma_3 \right] |\xi_{k_x}\rangle = \hat{E}_{k_x} |\xi_{k_x}\rangle, \quad (4.110)$$

and under the projection P , Eq. (4.107) also becomes,

$$\sin k_x \sigma_x |\xi_{k_x}\rangle = \hat{E}_{k_x} |\xi_{k_x}\rangle. \quad (4.111)$$

The difference between Eqs. (4.110) and (4.111) gives $\beta = M - \cos k_x + \lambda$. Thus we have

$$\beta = M - \cos k_x + \lambda, \quad E_b(k_x) = \sin k_x \quad (4.112)$$

The above procedure can be performed for the left eigenstates with the ansatz $\langle\langle \psi_{\tilde{\mathbf{k}}} | = \sum_{i=1}^{N_y} \langle i | \otimes \langle\langle \tilde{\xi}_{\tilde{\mathbf{k}}} | \beta^i$, which yields

$$\beta' = M - \cos k_x - \lambda, \quad E_b(k_x) = \sin k_x. \quad (4.113)$$

To study the localization of mode, we adopt the criterion in Eq. (4.104). We find that there are surface states localized at the $i = 1$ layer, with

$$E_b(k_x) = \sin k_x, \quad \sqrt{(m - \cos k_x - \cos k_y)^2 - \lambda^2} < 1. \quad (4.114)$$

The surface states at the $i = N_y$ layer can be obtained similarly as

$$E_b(k_x) = -\sin k_x, \quad \sqrt{(m - \cos k_x - \cos k_y)^2 - \lambda^2} < 1. \quad (4.115)$$

The obtained boundary modes agree well with the topological criterion (4.99), which also agrees with the numerical results, as shown in Fig. 4.3 (b).

Non-Hermitian skin effect From Eq. (4.96) it follows that if $|\phi\rangle$ is an eigenstate of the Hermitian Hamiltonian $\tilde{H}(y, k_x, k_z)$, then $\rho|\phi\rangle$ is a right eigenstate of the non-Hermitian Hamiltonian $H(y, k_x, k_z)$. Similarly, $\langle\phi|\rho^{-1}$ is a left eigenstate of the non-Hermitian Hamiltonian. From Eq. (4.104) it follows

that the amplitude of these states is given by

$$\begin{aligned}\langle \phi | \rho^\dagger \Pi_y \rho | \phi \rangle &= \frac{1}{2} \langle \phi_y | \begin{pmatrix} \alpha^2 + 1 & \alpha^2 - 1 \\ \alpha^2 - 1 & \alpha^2 + 1 \end{pmatrix} | \phi_y \rangle |\alpha|^{2y-3}, \\ \langle \phi | \rho^{-1} \Pi_y (\rho^{-1})^\dagger | \phi \rangle &= \frac{1}{2} \langle \phi_y | \begin{pmatrix} 1 + \alpha^2 & 1 - \alpha^2 \\ 1 - \alpha^2 & 1 + \alpha^2 \end{pmatrix} | \phi_y \rangle |\alpha|^{1-2y}.\end{aligned}\quad (4.116)$$

Hence, we see that the amplitude of the right eigenstates have weight mostly at the $i = 1$ boundary, whereas the amplitude of the left eigenstates is localized at the $i = N_y$ boundary. This phenomenon has been referred to in the literature as the “non-Hermitian skin effect” [30].

However, if we compute the localization within the bi-orthogonal basis, i.e., in terms of the bi-orthogonal left and right eigenstates, we find

$$\langle \phi | \rho^{-1} \Pi_y \rho | \phi \rangle = \langle \phi | \Pi_y | \phi \rangle, \quad (4.117)$$

which indicates that the states should be spread out throughout the bulk, in terms of the bi-orthogonal basis.

Spectra and topology for the (100) slab

For the (100) surface, we need to Fourier transform the Hamiltonian (4.59) along the x direction. This gives

$$\begin{aligned}H(x, k_y, k_z) &= \frac{1}{2i} \sigma_1 \otimes (S - S^\dagger) - \frac{1}{2} \sigma_3 \otimes (S + S^\dagger) + \sin k_y \sigma_2 \otimes \mathbb{1} \\ &\quad + [(m - \cos k_y - \cos k_z) \sigma_3 + i\lambda \sigma_2] \otimes \mathbb{1}.\end{aligned}\quad (4.118)$$

We observe that for $k_y = 0$ the spectrum is purely real and the non-Hermitian potential $i\lambda \sigma_2$ anti-commutes with the Hamiltonian. In this case, we can map the non-Hermitian Hamiltonian to an Hermitian one, whose spectrum is rescaled by a prefactor. It turns out that we can even keep k_y finite, and still do a useful similarity transformation. That is, for $k_y \neq 0$ we can map the Hamiltonian to a Hermitian one with a complex prefactor. However, the role of such similarity transformations needs further investigation.

Relation between PBCs and OBCs To derive the transfer matrix for the (100) slab we first separate out the k_x components from Hamiltonian (4.59)

$$H(\mathbf{k}) = \begin{pmatrix} -\frac{1}{2}(e^{+ik_x} + e^{-ik_x}) & +\frac{1}{2i}(e^{+ik_x} - e^{-ik_x}) \\ +\frac{1}{2i}(e^{+ik_x} - e^{-ik_x}) & +\frac{1}{2}(e^{+ik_x} + e^{-ik_x}) \end{pmatrix} + \sin k_y \sigma_2 + M_{\mathbf{k}} \sigma_3 + i\lambda \sigma_2, \quad (4.119)$$

where $M_{\mathbf{k}} = m - \cos k_y - \cos k_z$. From this we can identify the hopping matrix J and the on-site matrix M

$$J = \begin{pmatrix} -\frac{1}{2} & +\frac{1}{2i} \\ +\frac{1}{2i} & +\frac{1}{2} \end{pmatrix}, \quad M = \sin k_y \sigma_2 + M_{\mathbf{k}} \sigma_3 + i\lambda \sigma_2. \quad (4.120)$$

As before, J is nilpotent with index 2 and has rank $r = 1$. The reduced singular value decomposition of J is

$$J = v\xi w^\dagger, \quad v = \begin{pmatrix} -\frac{i}{\sqrt{2}} \\ \frac{1}{\sqrt{2}} \end{pmatrix}, \quad w = \begin{pmatrix} \frac{i}{\sqrt{2}} \\ \frac{1}{\sqrt{2}} \end{pmatrix}, \quad (4.121)$$

with the singular value $\xi = 1$. The on-site Greens function \mathcal{G} is given by

$$\mathcal{G} = (E\mathbb{1} - M)^{-1} = \frac{E\sigma_0 + \sin k_y\sigma_2 + M_{\mathbf{k}}\sigma_3 + i\lambda\sigma_2}{E^2 - M_{\mathbf{k}}^2 - (\sin k_y + i\lambda)^2}. \quad (4.122)$$

Now, we can insert this in the formula for the transfer matrix

$$\begin{aligned} T &= \frac{1}{\mathcal{G}_{vw}} \begin{pmatrix} 1 & -\mathcal{G}_{ww} \\ \mathcal{G}_{vv} & \mathcal{G}_{vw}\mathcal{G}_{ww} - \mathcal{G}_{vv}\mathcal{G}_{ww} \end{pmatrix} \\ &= \frac{1}{M_{\mathbf{k}}} \begin{pmatrix} (\sin k_y + i\lambda)^2 + M_{\mathbf{k}}^2 - E^2 & E - \sin k_y - i\lambda \\ -E - \sin k_y - i\lambda & 1 \end{pmatrix}. \end{aligned} \quad (4.123)$$

Thus the determinant of the transfer matrix is obtained as

$$\det T = \det \left| \frac{1}{M_{\mathbf{k}}} \begin{pmatrix} (\sin k_y + i\lambda)^2 + M_{\mathbf{k}}^2 - E^2 & E - \sin k_y - i\lambda \\ -E - \sin k_y - i\lambda & 1 \end{pmatrix} \right| = 1. \quad (4.124)$$

From this it follows that the spectrum with open and periodic boundary conditions is the same, and there is also no non-Hermitian skin effect [144]. The trace of the transfer matrix is

$$\text{Tr } T = \frac{1}{M_{\mathbf{k}}} \left[1 + (\sin k_y + i\lambda)^2 + M_{\mathbf{k}}^2 - E^2 \right]. \quad (4.125)$$

The bulk spectra can be obtained from the transfer matrix method. From the condition for the existence of bulk Bloch states with PBCs and OBCs we obtain

$$E_{\text{PBC}} = E_{\text{OBC}} = \pm \sqrt{1 + M_{\mathbf{k}}^2 + (\sin k_y + i\lambda)^2 - 2M_{\mathbf{k}} \cos \phi}. \quad (4.126)$$

Similarity transformation Though in this case, the spectrum is generally complex with PBCs and OBCs, we can still perform a similarity transformation in momentum space. To derive this transformation matrix ρ we first need to find the bi-orthonormal left and right eigenvectors of $H(\mathbf{k})$, Eq. (4.59). For the right eigenvectors we obtain

$$|+\rangle = \frac{1}{\sqrt{2\eta(\eta + M_{\mathbf{k}})}} \begin{pmatrix} M_{\mathbf{k}} + \eta \\ \sin k_x + i \sin k_y - \lambda \end{pmatrix}, \quad |-\rangle = \frac{1}{\sqrt{2\eta(\eta - M_{\mathbf{k}})}} \begin{pmatrix} M_{\mathbf{k}} - \eta \\ \sin k_x + i \sin k_y - \lambda \end{pmatrix}, \quad (4.127)$$

and for the left eigenvectors we have

$$\langle\langle +| = \frac{1}{\sqrt{2\eta(\eta + M_{\mathbf{k}})}} \begin{pmatrix} M_{\mathbf{k}} + \eta \\ \sin k_x - i \sin k_y + \lambda \end{pmatrix}, \quad \langle\langle -| = \frac{1}{\sqrt{2\eta(\eta - M_{\mathbf{k}})}} \begin{pmatrix} M_{\mathbf{k}} - \eta \\ \sin k_x - i \sin k_y + \lambda \end{pmatrix}. \quad (4.128)$$

Hence, $H(\mathbf{k})$ is diagonalized by the matrix

$$V(\lambda) = (|+\rangle, |-\rangle), \quad V^{-1}(\lambda) = (\langle\langle +|, \langle\langle -|)^T. \quad (4.129)$$

With this, the similarity transform ρ that maps $H(\mathbf{k})$ onto a Hermitian Hamiltonian is given by

$$\rho = V(\lambda)V^{-1}(0), \quad (4.130)$$

and we obtain

$$\rho^{-1}H(\mathbf{k})\rho = \sqrt{1 + \frac{2i\lambda \sin k_y - \lambda^2}{(\sin k_x)^2 + (\sin k_y)^2 + M_{\mathbf{k}}^2}} \tilde{H}(\mathbf{k}), \quad (4.131)$$

where $\tilde{H}(\mathbf{k})$ is the Hermitian Hamiltonian with $\lambda = 0$. However, the role of such kind of similarity transformation remains to be explored. Note that due to the square root prefactor in the above equation, the Fourier transform of the Hamiltonian \tilde{H} is non-local in real space.

Computation of surface states In computing the surface states of the (100) slab, we adopt again the ansatz

$$|\psi_{\tilde{\mathbf{k}}}\rangle = \sum_{i=1}^{N_y} \beta^i |i\rangle \otimes |\xi_{\tilde{\mathbf{k}}}\rangle, \quad \langle\langle \psi_{\tilde{\mathbf{k}}}| = \sum_{i=1}^{N_y} \langle i| \otimes \langle\langle \xi_{\tilde{\mathbf{k}}}|\beta^i, \quad (4.132)$$

for the right and left eigenstates, respectively. Here $\tilde{\mathbf{k}} = (k_y, k_z)$. The procedure is very similar to that for solving the surface states in (010) slab. Thus here we briefly describe the computation process with an emphasis on the difference.

In solving the Schödinger equation of

$$\hat{H}_R(x, k_y, k_z)|\psi_{\tilde{\mathbf{k}}}\rangle = \hat{E}_{k_x}|\psi_{\tilde{\mathbf{k}}}\rangle, \quad (4.133)$$

we find it gives two constraints,

$$\left[\frac{1}{2i}(\beta - \beta^{-1})\sigma_1 + \sin k_y \sigma_2 + (M - \cos k_y - \cos k_z - \frac{1}{2}(\beta + \beta^{-1}))\sigma_3 + i\lambda \sigma_2 \right] |\xi_{k_x}\rangle = \hat{E}_{k_x} |\xi_{k_x}\rangle, \quad (4.134)$$

and

$$\left[\frac{1}{2i}\beta \sigma_2 + \sin k_y \sigma_2 + (M - \cos k_y - \cos k_z - \frac{1}{2}\beta)\sigma_3 + i\lambda \sigma_2 \right] |\xi_{k_x}\rangle = \hat{E}_{k_x} |\xi_{k_x}\rangle. \quad (4.135)$$

Adopting a similar procedure as that from Eq. (4.108) to Eq. (4.111), we can obtain from the right eigenstates

$$\beta = m - \cos k_y - \cos k_z, \quad E_b(k_y) = -\sin k_y - i\lambda, \quad (4.136)$$

and for the left eigenstates we find the a similar solution of $\beta' = m - \cos k_y - \cos k_z$, $E_b(k_y) = -\sin k_y - i\lambda$. From the criterion $|\beta\beta'| < 1$, we find that there are surface states at the $i = 1$ unit cell with

$$E_b(k_y) = -\sin k_y - i\lambda, \quad |m - \cos k_y - \cos k_z| < 1. \quad (4.137)$$

By a similar procedure, the surface states at the $i = N_y$ unit cell can be obtained as

$$E_b(k_y) = \sin k_y + i\lambda, \quad |m - \cos k_y - \cos k_z| < 1. \quad (4.138)$$

4.3.2 Non-Hermitian potential $i\lambda\sigma_3$

Here, we consider the non-Hermitian potential $i\lambda\sigma_3$. With PBCs, the Hamiltonian in momentum space reads

$$H(\mathbf{k}) = \sin k_x \sigma_1 + \sin k_y \sigma_2 + (M_{\mathbf{k}} + i\lambda) \sigma_3. \quad (4.139)$$

The spectrum is given by

$$E = \pm\eta = \pm\sqrt{(\sin k_x)^2 + (\sin k_y)^2 + M_{\mathbf{k}}^2 + 2i\lambda M_{\mathbf{k}} - \lambda^2}. \quad (4.140)$$

We see that the spectrum is in general complex. From the momentum space Hamiltonian in Eq. (4.139), it can be inferred that k_x is equivalent to k_y . Thus it suffices to study the spectra and topology for the (010) slab.

In real space with OBCs in the y direction, the Hamiltonian with the non-Hermitian potential $i\lambda\sigma_3$ reads

$$\begin{aligned} H(y, k_x, k_z) &= \frac{1}{2i} \sigma_2 \otimes (S - S^\dagger) - \frac{1}{2} \sigma_3 \otimes (S + S^\dagger) + \sin k_x \sigma_1 \otimes \mathbb{1} \\ &\quad + [(m - \cos k_x - \cos k_z) \sigma_3 + i\lambda \sigma_3] \otimes \mathbb{1}, \end{aligned} \quad (4.141)$$

where S and S^\dagger are the forward and backward translation operators, respectively. We see from Eq. (4.139) and Eq. (4.141) that the role of the non-Hermitian mass term $i\lambda\sigma_3$ is to make M complex. Thus the spectrum is generally complex in both real and momentum space, which indicates that the system is intrinsically Hermitian in real and momentum space.

As usual, we make the following ansatz for the left and right eigenvectors of the surface states

$$|\psi_{\tilde{\mathbf{k}}}\rangle = \sum_{i=1}^{N_y} \beta^i |i\rangle \otimes |\xi_{\tilde{\mathbf{k}}}\rangle, \quad \langle\langle \psi_{\tilde{\mathbf{k}}} | = \sum_{i=1}^{N_y} \langle i | \otimes \langle\langle \xi_{\tilde{\mathbf{k}}} | \beta'^i. \quad (4.142)$$

with $\tilde{\mathbf{k}}$ representing (k_x, k_z) .

Following a similar procedure in solving the Schödinger equation of

$$\hat{H}_R(y, k_x, k_z) |\psi_{\tilde{\mathbf{k}}}\rangle = \hat{E}_{k_x} |\psi_{\tilde{\mathbf{k}}}\rangle, \quad (4.143)$$

we find that the surface spectrum is

$$E_b(k_x) = \pm \sin k_x, \quad \sqrt{(m - \cos k_x - \cos k_z)^2 + \lambda^2} < 1. \quad (4.144)$$

Relation between PBCs and OBCs We perform a similar transformation as in Sec. 4.3.1 and find for the singular value decomposition of the hopping matrix J

$$J = v\xi w^\dagger, \quad v = \begin{pmatrix} -\frac{1}{\sqrt{2}} \\ \frac{1}{\sqrt{2}} \end{pmatrix}, \quad w = \begin{pmatrix} \frac{1}{\sqrt{2}} \\ \frac{1}{\sqrt{2}} \end{pmatrix}, \quad (4.145)$$

with the singular value $\xi = 1$ and for the on-site Greens function, it is

$$\mathcal{G} = (E\mathbb{1} - M)^{-1} = \frac{E\sigma_0 + \sin k_x \sigma_1 + M_{\mathbf{k}} \sigma_3 + i\lambda \sigma_3}{E^2 - (M_{\mathbf{k}} + i\lambda)^2 - \sin^2 k_x}. \quad (4.146)$$

Form this, we obtain for the transfer matrix T

$$T = \frac{1}{M_{\mathbf{k}} + i\lambda} \begin{pmatrix} \sin^2 k_x + (M_{\mathbf{k}} + i\lambda)^2 - E^2 & \sin k_x + E \\ \sin k_x - E & 1 \end{pmatrix}. \quad (4.147)$$

Hence, $\det T = 1$, which suggests that the bulk spectrum for open and periodic boundary conditions should be the same [144]. Also, there is no non-Hermitian skin effect.

The trace of the transfer matrix is given by

$$\text{Tr } T = \frac{1 + \sin^2 k_x + (M_{\mathbf{k}} + i\lambda)^2 - E^2}{M_{\mathbf{k}} + i\lambda}. \quad (4.148)$$

The bulk spectrum can be computed by the conditions for the bulk spectra with PBCs and OBCs, which is

$$E_{\text{PBC}} = E_{\text{OBC}} = \pm \sqrt{1 + \sin^2 k_x + (M_{\mathbf{k}} + i\lambda)^2 - 2(M_{\mathbf{k}} + i\lambda) \cos \phi}. \quad (4.149)$$

4.4 \mathcal{PT} -symmetric non-Hermitian Dirac semimetals

In the introduction section, we have briefly discussed the basic concepts of Dirac fermions in Hermitian systems. In this section, we will focus on \mathcal{PT} -symmetric non-Hermitian Dirac semimetals. The Dirac semimetal is a topological material with fourfold degenerate band crossing points and linear dispersion in its vicinity. For the continuum model in momentum space, the general form of Hamiltonian for an Hermitian Dirac point is

$$H_{\text{Dirac}}(\mathbf{k}) = k_x \Gamma_1 + k_y \Gamma_2 + k_z \Gamma_3, \quad (4.150)$$

with Γ_μ the gamma matrices satisfying the Clifford algebra $\{\Gamma_\mu, \Gamma_\nu\} = 2\eta_{\mu\nu}$. The energy eigenvalues are $E_{\text{Dirac}} = \pm \sqrt{k_x^2 + k_y^2 + k_z^2}$. The two doubly degenerate bands touch at the Dirac point, which is of fourfold degeneracy. This Hamiltonian is invariant under the combined symmetry of time-reversal symmetry \mathcal{T} and the space inversion symmetry \mathcal{P} ,

$$(\mathcal{PT}) H_{\text{Dirac}}(\mathbf{k}) (\mathcal{PT})^{-1} = H_{\text{Dirac}}(\mathbf{k}) \quad (4.151)$$

with \mathcal{PT} the antiunitary symmetry operator. Since we are interested in non-Hermitian systems, which is

commonly realized in photonic systems, we focus on the case of $(\mathcal{PT})^2 = +1$, and for simplicity we take $\mathcal{PT} = \hat{\mathcal{K}}$, with $\hat{\mathcal{K}}$ the complex conjugate operator. Under this \mathcal{PT} symmetry, the five anti-commuting gamma matrices can be chosen as

$$\begin{aligned}\Gamma_1 &= \sigma_1 \otimes \tau_0, & \Gamma_2 &= \sigma_2 \otimes \tau_2, & \Gamma_3 &= \sigma_3 \otimes \tau_0, \\ \Gamma_4 &= \sigma_2 \otimes \tau_1, & \Gamma_5 &= \sigma_2 \otimes \tau_3.\end{aligned}\tag{4.152}$$

Among these five gamma matrices, Γ_1, Γ_2 and Γ_3 are even, while Γ_4 and Γ_5 are odd under \mathcal{PT} symmetry. With this choice of gamma matrices, the \mathcal{PT} symmetry requirement in Eq. (4.151) is satisfied. Notice that under a unitary transformation of $U = \exp(i\sigma_0 \otimes \tau_1 \pi/4)$, $H_{\text{Dirac}}(\mathbf{k})$ can be brought into the block-diagonal form

$$U^{-1}H_{\text{Dirac}}(\mathbf{k})U = \begin{pmatrix} H_{\text{Weyl}} & \\ & H_{\text{Weyl}}^* \end{pmatrix}.\tag{4.153}$$

Here $H_{\text{Weyl}} = k_x\sigma_1 + k_y\sigma_2 + k_z\sigma_3$ describes the Weyl node of chirality $\chi = +1$ and $H_{\text{Weyl}}^* = k_x\sigma_1 - k_y\sigma_2 + k_z\sigma_3$ the Weyl node of chirality $\chi = -1$. Thus, it is clear that the Dirac point is composed of two Weyl points with opposite chirality.

Topological invariants

The Dirac point is associated with a Z_2 monopole charge. We consider a sphere S^2 surrounding the Dirac point, which can be divided into two patches, the northern and southern hemispheres. One can find real and smooth gauge for eigenvectors on each hemisphere satisfying the reality condition. However, one cannot find such a gauge for the entire sphere. Thus, we need to analyze eigenvectors on the north and south hemisphere separated by an equator with stereographic coordinates. The eigenvectors on each hemisphere are real and smooth. On the equator parameterized by the azimuthal angle ϕ , for the valance band, the eigenvectors from the north hemisphere are

$$|-, 1\rangle^N = (\cos \phi, -1, \sin \phi, 0)^T, \quad |-, 2\rangle^N = (-\sin \phi, 0, \cos \phi, -1)^T,\tag{4.154}$$

and for the south hemisphere, the eigenvectors are

$$|-, 1\rangle^S = (1, -\cos \phi, 0, \sin \phi)^T, \quad |-, 2\rangle^S = (0, -\sin \phi, 1, -\cos \phi)^T,\tag{4.155}$$

The real transition function $g_{SN}^{\mathbb{R}} \in O(2)$ on the equator is defined by

$$|-, \alpha\rangle^S = [g_{SN}^{\mathbb{R}}]_{\alpha\beta} |-, \beta\rangle^N,\tag{4.156}$$

which can be obtained as

$$g_{SN}^{\mathbb{R}}(\phi) = \begin{pmatrix} \cos \phi & -\sin \phi \\ \sin \phi & \cos \phi \end{pmatrix}.\tag{4.157}$$

The winding number of this path is $+1$, corresponding to the nontrivial element of $\pi_1[O(2)] = \mathbb{Z}_2$. As discussed, this kind of real Dirac point has been proposed in experimentally realizable materials.

Alternatively, the topological invariant of the real monopole is given by [172]

$$\nu_{\text{R}} = -\frac{1}{4\pi} \int_{S^2} \text{Tr}(I\mathcal{F}_{\text{R}}),\tag{4.158}$$

with \mathcal{F}_R the curvature for the real Berry bundle and $I = -i\sigma_2$ the generator of the $SO(2)$ group. The real Berry curvature \mathcal{F}_R is derived from the real connection $\mathcal{A}_{\alpha\beta}^R = \langle \alpha, k | d | \beta, k \rangle$ with the eigenstates $|\alpha, k\rangle$ satisfying the reality condition,

$$|\alpha, k\rangle = \mathcal{PT}|\alpha, k\rangle. \quad (4.159)$$

In the following non-Hermitian cases, when the PT symmetry is spontaneously broken, i.e. $|\alpha, k\rangle \neq \mathcal{PT}|\alpha, k\rangle$, we will use the alternative definition of Berry connection,

$$\mathcal{A}_{\alpha\beta}^R = \langle \langle \alpha, k | d | \beta, k \rangle, \quad (4.160)$$

where the left and right eigenstates are defined as

$$H|\alpha, k\rangle = E|\alpha, k\rangle, \quad H^\dagger|\alpha, k\rangle = E^*|\alpha, k\rangle. \quad (4.161)$$

Now we turn to the real Dirac Fermion H_{Dirac} . We choose the sphere S^2 encircling the Dirac point parametrized by $(k_x, k_y, k_z) = \rho(\sin\theta \cos\phi, \sin\theta \sin\phi, \cos\theta)$, and the eigenstates for the two conduction bands are

$$|\psi_{+,\uparrow}\rangle = \begin{pmatrix} -\cos\frac{\theta}{2}\sin\phi & \cos\frac{\theta}{2}\cos\phi & 0 & \sin\frac{\theta}{2} \end{pmatrix}^T, \quad |\psi_{+,\downarrow}\rangle = \begin{pmatrix} \cos\frac{\theta}{2}\cos\phi & \cos\frac{\theta}{2}\sin\phi & \sin\frac{\theta}{2} & 0 \end{pmatrix}^T. \quad (4.162)$$

In this case the left and right eigenvectors are conjugate transpose to each other. From the eigenstates, we can calculate the Berry connection as

$$\begin{aligned} A_\theta &= \begin{pmatrix} \langle \psi_{+,\uparrow} | \partial_\theta | \psi_{+,\uparrow} \rangle & \langle \psi_{+,\uparrow} | \partial_\theta | \psi_{+,\downarrow} \rangle \\ \langle \psi_{+,\downarrow} | \partial_\theta | \psi_{+,\uparrow} \rangle & \langle \psi_{+,\downarrow} | \partial_\theta | \psi_{+,\downarrow} \rangle \end{pmatrix}, \\ A_\phi &= \begin{pmatrix} \langle \psi_{+,\uparrow} | \partial_\phi | \psi_{+,\uparrow} \rangle & \langle \psi_{+,\uparrow} | \partial_\phi | \psi_{+,\downarrow} \rangle \\ \langle \psi_{+,\downarrow} | \partial_\phi | \psi_{+,\uparrow} \rangle & \langle \psi_{+,\downarrow} | \partial_\phi | \psi_{+,\downarrow} \rangle \end{pmatrix}. \end{aligned} \quad (4.163)$$

The real Berry connection is obtained as

$$\mathcal{F}_{\theta\phi} = \partial_\theta A_\phi - \partial_\phi A_\theta = \begin{pmatrix} 0 & -\frac{\sin\theta}{2} \\ \frac{\sin\theta}{2} & 0 \end{pmatrix}. \quad (4.164)$$

Thus the \mathbb{Z}_2 monopole charge is obtained as

$$\nu = -\frac{1}{4\pi} \int_0^{2\pi} d\phi \int_0^\pi d\theta \text{Tr}(I\mathcal{F}_{\theta\phi}) = \frac{1}{2} \int_0^\pi \sin\theta d\theta = +1, \quad (4.165)$$

which is topologically non-trivial.

Chiral anomaly in Dirac semimetals

We have shown the chiral anomaly for the massless Dirac fields in the subsection 4.2.3. In this section, we will discuss the chiral anomaly in Dirac semimetals. As we are interested in the \mathcal{PT} -symmetric Dirac semimetals, we can construct the low-energy effective Hamiltonian according to the Hamiltonian

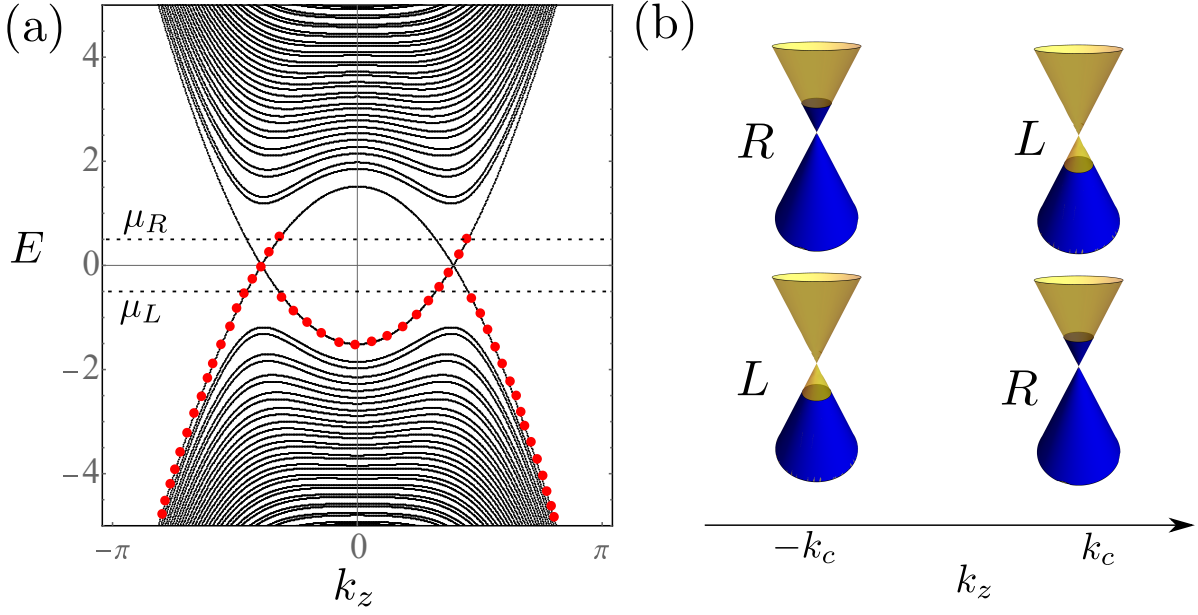


Figure 4.4: (a) The energy spectrum against wavevector k_z of the Landau levels for the low-energy effective model of Eq. (4.166) in a magnetic field B applied along the z direction. (b) The schematic picture showing the change of electrons at two Dirac points under the parallel electric and magnetic fields. L and R denotes the Weyl nodes with opposite chirality inside the Dirac point.

in the form of Eq. (4.153), which reads

$$H_D = \begin{pmatrix} H_W(\mathbf{k}) & \\ & H_W(\mathbf{k})^* \end{pmatrix}, \quad (4.166)$$

with $H_W(\mathbf{k}) = A(k_x\sigma_1 + k_y\sigma_2) + (M_0 - M_1(k_x^2 + k_y^2 + k_z^2))\sigma_3$ the low-energy effective model for Weyl semimetals with two nodes given in Eq. (4.4).

To discuss the Landau bands, we follow a similar procedure as that in the subsection 4.2.2. We consider a magnetic field applied along the z direction, $\mathbf{B} = (0, 0, B)$. Under the choice of the Landau gauge, the vector potential is $\mathbf{A} = (-yB, 0, 0)$. Such a gauge field does not break the translation symmetry in x and z directions, thus k_x and k_z are still good quantum numbers. The wave vector in the Hamiltonian is replaced by the operator $\mathbf{k} = (k_x - \frac{eB}{\hbar}y, -i\partial_y, k_z)$. We introduce the ladder operator a by the relations

$$k_x - \frac{eB}{\hbar}y = \frac{1}{\sqrt{2}l_B}(a^\dagger + a), \quad -i\partial_y = \frac{1}{\sqrt{2}l_B i}(a^\dagger - a), \quad (4.167)$$

with $l_B = \sqrt{\frac{\hbar}{eB}}$. With the introduction of the ladder operators, we find the components in the Hamiltonian $\mathcal{H}_{\text{eff}}(\mathbf{k})$ are substituted as

$$k_x^2 + k_y^2 \rightarrow \omega(a^\dagger a + \frac{1}{2}), \quad k_+ \rightarrow \frac{\sqrt{2}}{l_B}a^\dagger, \quad \text{and} \quad k_- \rightarrow \frac{\sqrt{2}}{l_B}a, \quad (4.168)$$

with $k_+ = k_x + ik_y$ and $k_- = k_x - ik_y$. After a unitary transformation by $\sigma_1 \otimes \tau_0$, the resultant Hamiltonian is

$$\mathcal{H}_D(a, k_z) = \begin{pmatrix} \eta a \sigma_- + \eta a^\dagger \sigma_+ - M(a^\dagger a, k_z) \sigma_3 & \\ & \eta a \sigma_+ + \eta a^\dagger \sigma_- - M(a^\dagger a, k_z) \sigma_3 \end{pmatrix}, \quad (4.169)$$

where the operators a and a^\dagger satisfy the commutation relation $[a, a^\dagger] = 1$. Similar to the Weyl semimetal case, we can define the excitation number states $|n\rangle = \frac{(a^\dagger)^n}{\sqrt{n!}}|0\rangle$, which fulfill

$$\hat{n} = a^\dagger a, \quad \hat{n}|n\rangle = n|n\rangle, \quad (4.170)$$

$$a|n\rangle = \sqrt{n}|n-1\rangle, \quad \text{and} \quad a^\dagger|n\rangle = \sqrt{n+1}|n+1\rangle. \quad (4.171)$$

In the excitation number representation of $|n\rangle$, we can obtain the energy spectrum as

$$E_{0,W} = +M(0, k_z) = +(\omega/2 - M_0 + M_1 k_z^2), \quad (4.172)$$

$$E_{0,W^*} = -M(0, k_z) = -(\omega/2 - M_0 + M_1 k_z^2). \quad (4.173)$$

Here W and W^* represent the contributions from Weyl components of opposite chirality. For the n th level the energies are given by

$$E_{n,W}^\pm = \frac{\omega}{2} \pm \sqrt{M_n^2 + n\eta^2}, \quad E_{n,W^*}^\pm = -\frac{\omega}{2} \pm \sqrt{M_n^2 + n\eta^2} \quad (4.174)$$

with $M_n = (M_0 - \omega n - M_1 k_z^2)$, $\omega = 2M_1/l_B^2$ and $\eta = \frac{\sqrt{2}A}{l_B}$. The Landau spectrum is plotted in Fig. 4.4 (a).

Suppose that the Fermi energy lies at zero energy, we can apply an electric field in the direction of the magnetic field. We use L and R to label the Weyl nodes with opposite chirality inside a Dirac point. In an electric field, electrons will be transported from the L Weyl node at $-k_c$ to the R node at $+k_c$, and correspondingly, electrons from the L Weyl node at $+k_c$ will be transported to the R node at $-k_c$. This transport process is shown by the red dots in Fig. 4.4 (a). This process is due to the chiral anomaly in Dirac semimetals discussed in Sec. 4.2.3, and will cause an imbalance of electrons between two Weyl nodes inside a Dirac point, as shown schematically in Fig. 4.4 (b).

4.4.1 Classification of \mathcal{PT} -symmetric non-Hermitian Dirac semimetals

We are interested in non-Hermitian terms that preserve \mathcal{PT} symmetry. Notice that by multiplying an imaginary unit, $i\Gamma_4$ ($i\Gamma_5$) becomes even under \mathcal{PT} symmetry and its Hermiticity is broken, realizing \mathcal{PT} -symmetric non-Hermitian terms. Apart from this, as Γ_1 , Γ_2 and Γ_3 are \mathcal{PT} -symmetric, their products are still \mathcal{PT} -symmetric. Among them, we find $\gamma_1 = \Gamma_2\Gamma_3$, $\gamma_2 = \Gamma_3\Gamma_1$, $\gamma_3 = \Gamma_1\Gamma_2$, and $\gamma_0 = \Gamma_1\Gamma_2\Gamma_3$ are both \mathcal{PT} -symmetric and non-Hermitian. According to their physical consequence in momentum space, the \mathcal{PT} -symmetric non-Hermitian terms can be grouped into three cases,

$$\gamma_0 = \Gamma_1\Gamma_2\Gamma_3, \quad (I)$$

$$\gamma_1 = \Gamma_2\Gamma_3 = i\sigma_1 \otimes \tau_2, \quad \gamma_2 = \Gamma_3\Gamma_1 = i\sigma_2 \otimes \tau_0, \quad \gamma_3 = \Gamma_1\Gamma_2 = i\sigma_3 \otimes \tau_2, \quad (II)$$

$$\gamma_4 = i\Gamma_4, \quad \gamma_5 = i\Gamma_5. \quad (III)$$

An intriguing fact is that the \mathcal{PT} symmetry itself is not enough to guarantee the reality condition. One can show that there are two cases for the reality of the eigenvalues: they must be real, or they form complex conjugate pairs. For the first case, the spectra reality condition is preserved, and it is called \mathcal{PT} -symmetric phase; For the latter case, the reality condition is broken, and thus it is called the phase with spontaneous \mathcal{PT} symmetry breaking. The transition between these two phases is associated with exceptional points [145, 165]. In the following we will discuss each of the three cases listed above.

- (I) Two Weyl exceptional points separated by their imaginary energies. The Hamiltonian is $H_{\text{Weyl-point}} = H_D + \lambda\gamma_0 = k_x\Gamma_1 + k_y\Gamma_2 + k_z\Gamma_3 + \lambda\gamma_0$ with γ_0 commuting with H_D . Under a unitary transformation of $U = \exp(i\sigma_0 \otimes \tau_1\pi/4)$, the Hamiltonian becomes

$$U^{-1}H_{\text{Weyl-point}}U = \begin{pmatrix} H_{\text{Weyl}} + i\lambda\sigma_0 & \\ & (H_{\text{Weyl}} + i\lambda\sigma_0)^* \end{pmatrix}, \quad (4.175)$$

with $H_{\text{Weyl}} = k_x\sigma_1 + k_y\sigma_2 + k_z\sigma_3$ and $*$ representing the complex conjugation. The energy eigenvalues for one part are $E_{\text{Weyl-point}} = \pm\sqrt{k_x^2 + k_y^2 + k_z^2} + i\lambda$ and for the other they are $E_{\text{Weyl-point}}^* = \pm\sqrt{k_x^2 + k_y^2 + k_z^2} - i\lambda$. The band crossings are doubly degenerate points with linear dispersion in the vicinity, which means they are Weyl points with a constant imaginary part. The non-Hermitian potential $\lambda\gamma_0$ breaks the double degeneracy of the original bands, and turn the Dirac point into two Weyl points. The two Weyl points are separated by their imaginary energies.

- (II) Two separated Weyl exceptional rings. The Hamiltonian is $H_{\text{Weyl-Ring}} = H_D + \lambda\gamma_i$, with $i = 1, 2, 3$. The expressions for γ_i are,

$$\gamma_1 = \Gamma_2\Gamma_3 = i\sigma_1 \otimes \tau_2, \quad \gamma_2 = \Gamma_3\Gamma_1 = i\sigma_2 \otimes \tau_0, \quad \gamma_3 = \Gamma_1\Gamma_2 = i\sigma_3 \otimes \tau_2. \quad (4.176)$$

After a unitary transform of U , the Hamiltonian becomes,

$$U^{-1}H_{\text{Weyl-Ring}}U = \begin{pmatrix} H_{\text{Weyl}} + i\lambda\sigma_i & \\ & (H_{\text{Weyl}} + i\lambda\sigma_i)^* \end{pmatrix}. \quad (4.177)$$

Under the non-Hermitian potential of $\lambda\gamma_2$, the Dirac point separates into two parts, one is $H_{\text{Weyl}} + i\lambda\sigma_2$ with eigenvalues of $E_{\text{Weyl-Ring}} = \pm\sqrt{k_x^2 + (k_y + i\lambda)^2 + k_z^2}$, and the other is $H_{\text{Weyl}}^* - i\lambda\sigma_2$ with eigenvalues of $E_{\text{Weyl-Ring}}^* = \pm\sqrt{k_x^2 + (k_y - i\lambda)^2 + k_z^2}$. For these two cases, the complex band crossing happens at

$$k_x^2 + k_y^2 + k_z^2 - \lambda^2 = 0 \text{ and } k_y = 0, \quad (4.178)$$

which forms a ring on $k_x = 0$ plane with $k_y^2 + k_z^2 = \lambda^2$. Notice that the non-Hermitian potential $\lambda\gamma_2$ breaks the double degeneracy of the original Dirac bands, and thus the resultant two rings are called the Weyl exceptional rings, which are separated by their imaginary energies.

- (III) Dirac exceptional sphere. $H_{\text{Sphere}} = H_{\text{Dirac}}(\mathbf{k}) + i\lambda\Gamma_{4(5)}$. We take Γ_4 as an example. After a unitary transformation, the Hamiltonian is

$$U^{-1}H_{\text{Sphere}}U = \begin{pmatrix} H_{\text{Weyl}} & i\lambda\sigma_2 \\ i\lambda\sigma_2 & H_{\text{Weyl}}^* \end{pmatrix}. \quad (4.179)$$

The energy eigenvalues are $E_{\text{Sphere}} = \pm \sqrt{k_x^2 + k_y^2 + k_z^2 - \lambda^2}$, which preserves the double degeneracy of the Dirac bands, and the band crossing happens at

$$k_x^2 + k_y^2 + k_z^2 = \lambda^2, \quad (4.180)$$

which forms a sphere with radius λ . We call it the Dirac exceptional sphere.

For the three cases, we will use the non-Hermitian lattice model to reveal the topological property of these \mathcal{PT} -symmetric non-Hermitian Dirac semimetals. We start from the model Hamiltonian of the Hermitian Dirac semimetal in momentum space,

$$H_D = \sin k_x \Gamma_1 + \sin k_y \Gamma_2 + (m - \cos k_x - \cos k_y - \cos k_z) \Gamma_3, \quad (4.181)$$

for $1 < m < 3$, with two Dirac points located at $(0, 0, \pm k_c) = (0, 0, \pm \arccos(m - 2))$. Around the two Dirac points, the effective Hamiltonian can be obtained approximately as,

$$H_{\text{eff}} = \delta k_x \Gamma_1 + \delta k_y \Gamma_2 \pm \delta k_z \Gamma_3, \quad (4.182)$$

which describe a Dirac node similar to the continuum model in Eq. (4.150).

4.4.2 Case (II): Double Weyl exceptional rings

In this section, we discuss the term γ_i with $i = 1, 2, 3$. Here we take the non-Hermitian potential $i\lambda\gamma_2$ as an example, the non-Hermitian lattice model reads,

$$H_{\text{WR}} = \sin k_x \Gamma_1 + \sin k_y \Gamma_2 + (m - \cos k_x - \cos k_y - \cos k_z) \Gamma_3 + \lambda\gamma_2. \quad (4.183)$$

The energy spectrum in momentum space is shown in Fig. 4.5(a) against k_x and k_y with $k_z = 0$. We can see that the band crossing points form two ring, and their position in the Brillouin zone is plotted in Fig. 4.5(b). These two separate rings are called Weyl exceptional rings, which form around the original Dirac point at $(0, 0, \pm \arccos(m - 2))$. The name ‘‘exceptional’’ comes from the fact that the eigenvalues and the corresponding eigenvalues coalesce at exceptional points, and for the model in Eq. (4.183), these points form an exceptional ring.

Exceptional ring

We discuss the exceptional ring at $(0, 0, k_c)$ with the effective Hamiltonian

$$H_{\text{eff-ring}} = \delta k_x \Gamma_1 + \delta k_y \Gamma_2 + \delta k_z \Gamma_3 + \lambda\gamma_2. \quad (4.184)$$

The ring can be parametrized as $(k_x, k_y, k_z) = \lambda(\cos \theta, 0, \sin \theta)$. Then the Hamiltonian on the exceptional ring is

$$H_{\text{exp-ring}} = \lambda \begin{pmatrix} \sin \theta & 1 + \cos \theta & 0 & 0 \\ -1 + \cos \theta & -\sin \theta & 0 & 0 \\ 0 & 0 & \sin \theta & 1 + \cos \theta \\ 0 & 0 & -1 + \cos \theta & -\sin \theta \end{pmatrix}. \quad (4.185)$$

Since on the ring the eigenvalues are 0, the determinant is given by $(H_{\text{exp-ring}} - 0\mathbb{1})^2 = 0$. Thus the minimal polynomial is of the form $m(\lambda) = (\lambda - 0)^2$, and the largest Jordan block is of the dimension

2×2 . The eigenvectors on the exceptional ring are obtained as

$$\begin{aligned} |\psi_1\rangle &= \begin{pmatrix} 0 & 0 & -\cos \frac{\theta}{2} & \sin \frac{\theta}{2} \end{pmatrix}^T, \\ |\psi_2\rangle &= \begin{pmatrix} -\cos \frac{\theta}{2} & \sin \frac{\theta}{2} & 0 & 0 \end{pmatrix}^T, \end{aligned} \quad (4.186)$$

which span a two dimensional eigenspace. As the largest Jordan block is of 2×2 dimensions and there are only two independent eigenvectors, the Jordan canonical form of the Hamiltonian on the exceptional ring is

$$J_{\text{ring}} = \begin{pmatrix} 0 & 1 & 0 & 0 \\ 0 & 0 & 0 & 0 \\ 0 & 0 & 0 & 1 \\ 0 & 0 & 0 & 0 \end{pmatrix}. \quad (4.187)$$

From the Jordan canonical form we have the relation $H_{\text{exp-ring}}|\psi'_1\rangle = |\psi_1\rangle$ and $H_{\text{exp-ring}}|\psi'_2\rangle = |\psi_2\rangle$ for the other independent vectors. They form a matrix P ,

$$P = \begin{pmatrix} 0 & 0 & -\cos \frac{\theta}{2} & 0 \\ 0 & 0 & \sin \frac{\theta}{2} & -\frac{1}{2} \sec \frac{\theta}{2} \\ -\cos \frac{\theta}{2} & 0 & 0 & 0 \\ \sin \frac{\theta}{2} & -\frac{1}{2} \sec \frac{\theta}{2} & 0 & 0 \end{pmatrix}. \quad (4.188)$$

which makes $P^{-1}H_{\text{exp-ring}}P = J_{\text{ring}}$.

As the energy spectra become complex, it is possible that they possess a topological structure. For the exceptional points in the spectrum, a topological invariant for a single band can be defined as

$$\nu_m(S^1) = \frac{1}{2\pi} \oint_{S^1} \nabla_{\mathbf{k}} \arg E_m(\mathbf{k}), \quad (4.189)$$

with S^1 a closed loop in k -space. This topological invariant reflects the winding of the energy eigenvalue on the complex plane.

For the pair of mutually complex conjugate Weyl exceptional rings, the energy eigenvalues for two conductance bands are,

$$E_{\text{WR-eff}} = \pm \sqrt{\delta k_x^2 + \delta k_y^2 + \delta k_z^2 - \lambda^2 \pm 2i\lambda\delta k_y}, \quad (4.190)$$

with two Weyl exceptional rings at the same position, on $\delta k_y = 0$ plane with $\delta k_x^2 + \delta k_z^2 = \lambda^2$. We can still find a small circle S^1 encircling the red exceptional ring in Fig. 4.5 (b). The small circle S^1 can be parametrized as $(\delta k_x, \delta k_y, \delta k_z) = (0, \rho \sin \gamma, \lambda - \rho \cos \gamma)$, then the eigenvalues on this path are

$$E_{S^1, \pm} = \sqrt{\rho^2 - 2\lambda\rho \cos \gamma \pm 2i\lambda\rho \sin \gamma}. \quad (4.191)$$

With $\rho \ll \lambda$, eigenvalues can be approximated as $E_{S^1, \pm} = i\sqrt{2\lambda\rho}e^{\mp i\gamma/2}$. The topological charge then is

$$\nu(S^1) = -\frac{1}{2\pi} \oint_{S^1} \nabla_{\mathbf{k}} \arg E_{S^1, +}(\mathbf{k}) = -\frac{1}{2\pi} \int_0^{2\pi} d\gamma \partial_\gamma (-\gamma/2) = +\frac{1}{2}. \quad (4.192)$$

This quantized nonzero topological charge protects the pair of mutually complex conjugate Weyl ex-

exceptional rings in momentum space.

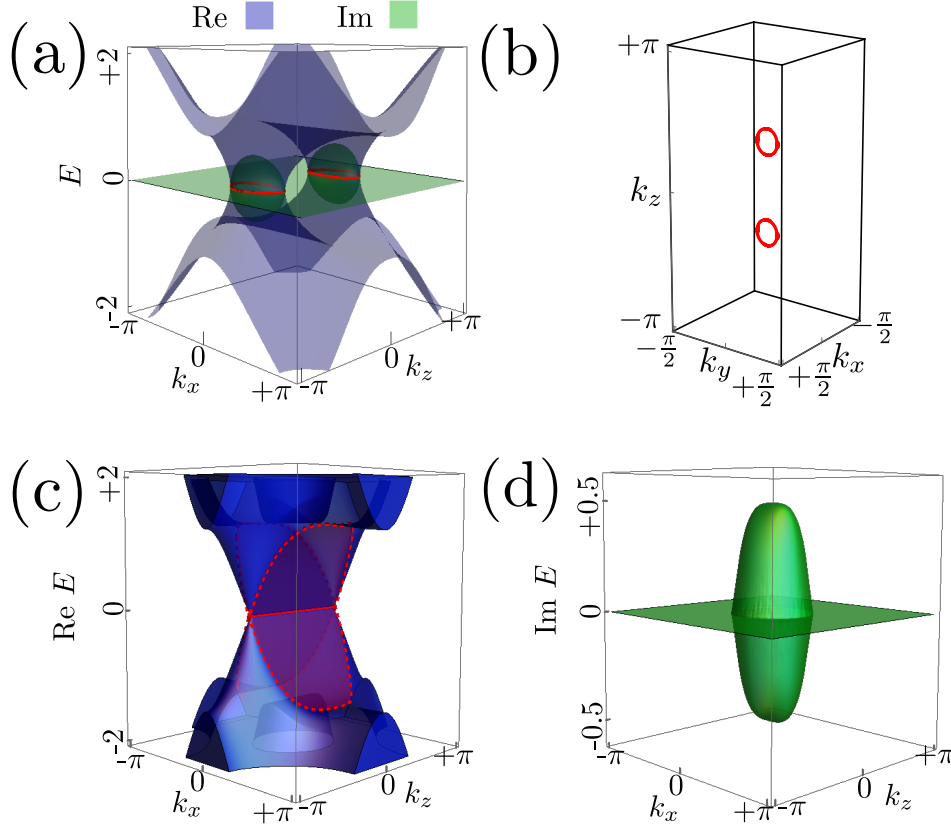


Figure 4.5: (a) Energy spectrum in momentum space at $k_y = 0$. The two double Weyl exceptional rings are located at $(0, 0, \pm k_c)$ and are plotted in red in (b); The real part (c) and the imaginary part (d) of the open boundary Hamiltonian is plotted. In (c) the Fermi arc is highlighted by red line. Red shadow bounded by dotted lines is the surface spectrum calculated analytically.

Relation between PBCs and OBCs

As we have shown in the previous chapter, the spectra and topology between systems of periodic and open boundary conditions might differ drastically. This difference can be effectively explained through the transfer matrix method, which has been introduced in the previous chapter. With OBCs in y direction, we first separate out the k_y components from the Hamiltonian (4.183). Then we can identify the hopping matrix J and the on-site matrix M in the Bloch Hamiltonian as

$$J = \begin{pmatrix} -\frac{1}{2} & & & \frac{i}{2} \\ & \frac{1}{2} & -\frac{i}{2} & \\ & -\frac{i}{2} & -\frac{1}{2} & \\ \frac{i}{2} & & & \frac{1}{2} \end{pmatrix}, \quad M = \sin k_x \Gamma_1 + M_{\mathbf{k}} \Gamma_3 + \lambda \gamma_2, \quad (4.193)$$

where $M_{\mathbf{k}} = m - \cos k_x - \cos k_z$. We note that J is nilpotent with index 2, since $J^2 = 0$, and that J has rank $r = 1$, since the two rows/columns are linearly dependent. Next, we need to construct the on-site Greens function \mathcal{G} and find the singular value decomposition of J . We obtain

$$\mathcal{G} = (E\mathbb{1} - M)^{-1} = \frac{E\Gamma_0 + \sin k_x \Gamma_1 + \lambda \gamma_2 + M_{\mathbf{k}} \Gamma_3}{E^2 + \lambda^2 - M_{\mathbf{k}}^2 - \sin^2 k_x}, \quad (4.194)$$

with Γ_0 the identity matrix. The singular value decomposition of J gives

$$J = V \Xi W^\dagger, V = \frac{1}{\sqrt{2}} \begin{pmatrix} i & 0 & -i & 0 \\ 0 & -i & 0 & -i \\ 0 & -1 & 0 & 1 \\ 1 & 0 & 1 & 0 \end{pmatrix}, \Xi = \begin{pmatrix} 1 & 0 & 0 & 0 \\ 0 & 1 & 0 & 0 \\ 0 & 0 & 0 & 0 \\ 0 & 0 & 0 & 0 \end{pmatrix}, W = \frac{1}{\sqrt{2}} \begin{pmatrix} -i & 0 & i & 0 \\ 0 & -i & 0 & i \\ 0 & 1 & 0 & 1 \\ 1 & 0 & 1 & 0 \end{pmatrix}. \quad (4.195)$$

We observe that J has only one singular value $\xi = \text{diag}(1, 1)$. Hence, we can find the reduced singular value decomposition

$$J = v \xi w^\dagger, \quad v = \frac{1}{\sqrt{2}} \begin{pmatrix} i & 0 \\ 0 & -i \\ 0 & -1 \\ 1 & 0 \end{pmatrix}, \quad w = \frac{1}{\sqrt{2}} \begin{pmatrix} -i & 0 \\ 0 & i \\ 0 & 1 \\ 1 & 0 \end{pmatrix}. \quad (4.196)$$

With this, we are ready to compute the transfer matrix T , which is defined in the previous chapter as

$$T = \begin{pmatrix} \Xi^{-1} \mathcal{G}_{vw}^{-1} & -\Xi^{-1} \mathcal{G}_{vw}^{-1} \mathcal{G}_{ww} \Xi \\ \mathcal{G}_{vv} \mathcal{G}_{vw}^{-1} & (\mathcal{G}_{ww} - \mathcal{G}_{vv} \mathcal{G}_{vw}^{-1} \mathcal{G}_{ww}) \Xi \end{pmatrix}, \quad (4.197)$$

where $\mathcal{G}_{ab} = b^\dagger \mathcal{G} a$ with $a, b \in \{v, w\}$. Inserting Eq. (4.194), we obtain

$$T = \begin{pmatrix} T_+ & \\ & T_- \end{pmatrix} \quad (4.198)$$

where the components are

$$T_+ = \frac{1}{M_{\mathbf{k}} - \lambda} \begin{pmatrix} \sin^2 k_x + M_{\mathbf{k}}^2 - \lambda^2 - E^2 & E + \sin k_x \\ -E + \sin k_x & 1 \end{pmatrix}, \quad (4.199)$$

and

$$T_- = \frac{1}{M_{\mathbf{k}} + \lambda} \begin{pmatrix} \sin^2 k_x + M_{\mathbf{k}}^2 - \lambda^2 - E^2 & E - \sin k_x \\ -E - \sin k_x & 1 \end{pmatrix}. \quad (4.200)$$

With the expression of the transfer matrix, we find the total determinant is 1. However,

$$\text{Det } T_+ = \left(\frac{M_{\mathbf{k}} + \lambda}{M_{\mathbf{k}} - \lambda} \right), \text{Det } T_- = \left(\frac{M_{\mathbf{k}} - \lambda}{M_{\mathbf{k}} + \lambda} \right) \quad (4.201)$$

For $\lambda \neq 0$, these determinants are not 1, which means the spectra of PBCs and OBCs differ from

each other. It is highly possible that the bulk-boundary correspondence might fail in this case. In the following, we discuss the topological property and the topological surface states.

Topological property and bulk-boundary correspondence

The non-Hermitian potential $\lambda\gamma_2$ commutes with $\sin k_y\Gamma_2$, and anti-commutes with the remaining terms,

$$\{\gamma_2, \Gamma_1\} = 0, \quad [\gamma_2, \Gamma_2] = 0, \quad \{\gamma_2, \Gamma_3\} = 0. \quad (4.202)$$

According to our theory in the previous chapter, this is called the non-Hermitian kinetic term. The spectrum for the open boundary system in real space is mostly real, and a similarity transform can be found to turn the Hamiltonian Hermitian in most regions.

Taking OBCs in \mathbf{y} direction with N_y layers, the real space Hamiltonian reads

$$H_{\text{WR}}(k_x, k_z, y) = \sin k_x \Gamma_1 \otimes + \frac{1}{2i} \Gamma_2 \otimes (S - S^\dagger) - \frac{1}{2} \Gamma_3 \otimes (S + S^\dagger) + ((m - \cos k_x - \cos k_z) \Gamma_3 + \lambda \gamma_2) \otimes \mathbb{1}, \quad (4.203)$$

with $\mathbb{1}$ the identity operator with dimension N_y , and S the translation operator. The similarity transform in real space gives,

$$\begin{aligned} \tilde{H}_{\text{WR}}(k_x, k_z, y) &= \rho_{\text{WR}}^{-1} H_{\text{WR}}(k_x, y) \rho_{\text{WR}} \\ &= \sin k_x \Gamma_1 \otimes \mathbb{1} + \frac{1}{2i} \Gamma_2 \otimes (S - S^\dagger) - \frac{1}{2} \Gamma_3 \otimes (S + S^\dagger) + \left(\sqrt{(m - \cos k_x - \cos k_z)^2 - \lambda^2} \right) \Gamma_3 \otimes \mathbb{1} \end{aligned} \quad (4.204)$$

where the similarity transformation operator is $\rho_{\text{WR}} = \text{diag}(\beta^1, \beta^2, \dots, \beta^y, \dots, \beta^{N_y})$, with $1 < y < N_y$ the site index. Here β^y can be brought into block diagonal form by the unitary transformation

$$U^{-1} \beta^y U = \begin{pmatrix} \alpha^{-y} \rho & \\ & \alpha^y \rho \end{pmatrix}, \quad (4.205)$$

where $\rho = (\alpha + 1)\sigma_0 + (\alpha - 1)\sigma_1$ and $\alpha = [(M_{\mathbf{k}} - \lambda)/(M_{\mathbf{k}} + \lambda)]^{1/2}$.

The similarity transformed open boundary Hamiltonian in real space corresponds to the Bloch Hamiltonian of

$$\tilde{H}_{\text{WR}}(k_x, k_y, k_z) = \sin k_x \Gamma_1 + \sin k_y \Gamma_2 + (\sqrt{(M - \cos k_x - \cos k_z)^2 - \lambda^2} - \cos k_y) \Gamma_3. \quad (4.206)$$

It is important to notice that this similarity transformed Hamiltonian still describes a Dirac semimetal, but the Dirac points are now located at $(0, 0, \pm \arccos(M - 1 - \sqrt{\lambda^2 + 1}))$.

From the similarity transformed Hamiltonian, for this kind of Dirac semimetals, we expect that Fermi arcs are attached to the bulk Dirac points. Thus, the Fermi arc surface states are attached to the Dirac points located at $(0, 0, \pm \arccos(M - 1 - \sqrt{\lambda^2 + 1}))$.

Fermi Arc surface states The bulk boundary-correspondence of the non-Hermitian Hamiltonian in Eq. (4.183) can be derived from the similarity transformed Hamiltonian in Eq. (4.206). To verify this, we start from the open boundary Hamiltonian of Eq. (4.203).

The following ansatz for right and left boundary states for the open boundary Hamiltonian is used,

$$|\psi_{\tilde{\mathbf{k}}}\rangle = \sum_{y=1}^{N_y} (\alpha_{k_x, k_z, \text{R}})^y |y\rangle \otimes |\xi_{\tilde{\mathbf{k}}}\rangle, \quad \langle\langle \psi_{\tilde{\mathbf{k}}} | = \sum_{y=1}^{N_y} \langle y | \otimes \langle\langle \xi_{\tilde{\mathbf{k}}} | (\alpha_{k_x, k_z, \text{L}})^y. \quad (4.207)$$

with ξ_{k_x, k_z} a spinor and $\alpha_{k_x, k_z, \text{R/L}}$ a scalar. Here $\tilde{\mathbf{k}} = (k_x, k_z)$. In non-Hermitian systems, the left and right eigenvectors are combined to get the localization of modes, $\langle\langle \psi_{\tilde{\mathbf{k}}} | \Pi_y | \psi_{\tilde{\mathbf{k}}}\rangle = \left(\alpha_{k_x, k_z, \text{R}} \alpha_{k_x, k_z, \text{L}} \right)^y$ with $\Pi_y = |y\rangle\langle y|$ the projection on to the y th unit cell. The criteria for the localization at $y = 1$ boundary is given by,

$$|\alpha_{k_x, k_z, \text{R}} \alpha_{k_x, k_z, \text{L}}| < 1. \quad (4.208)$$

In solving the Schrödinger equation,

$$H_{\text{WR}}(k_x, k_z, y) |\psi_{\tilde{\mathbf{k}}}\rangle = E(k_x, k_z) |\psi_{\tilde{\mathbf{k}}}\rangle, \quad (4.209)$$

we find the following two relations for the boundary states. The Schrödinger equation for the bulk layers is

$$\left[\sin k_x \Gamma_1 + \frac{\alpha_{k_x, k_z, \text{R}} - \alpha_{k_x, k_z, \text{R}}^{-1}}{2i} \Gamma_2 + \left(m - \cos k_x - \cos k_z - \frac{\alpha_{k_x, k_z, \text{R}} + \alpha_{k_x, k_z, \text{R}}^{-1}}{2} \right) \Gamma_3 + \lambda \gamma_2 \right] |\xi_{\tilde{\mathbf{k}}}\rangle = E(k_x, k_z) |\xi_{\tilde{\mathbf{k}}}\rangle \quad (4.210)$$

and for the first layer it is

$$\left[\sin k_x \Gamma_1 + \frac{\alpha_{k_x, k_z, \text{R}}}{2i} \Gamma_2 + \left(m - \cos k_x - \cos k_z - \frac{\alpha_{k_x, k_z, \text{R}}}{2} \right) \Gamma_3 + \lambda \gamma_2 \right] |\xi_{\tilde{\mathbf{k}}}\rangle = E(k_x, k_z) |\xi_{\tilde{\mathbf{k}}}\rangle. \quad (4.211)$$

Taking the difference between the above two equations, we get

$$(-i\Gamma_2 + \Gamma_3) |\xi_{k_x, k_z}\rangle = 0. \quad (4.212)$$

Plugging this equation into the previous equation, and modifying it by multiplying Γ_3 on both sides, we get the following two relations,

$$\left[\sin k_x \Gamma_1 + \left(m - \cos k_x - \cos k_z - \alpha_{k_x, k_z, \text{R}} \right) \Gamma_3 + \lambda \gamma_2 \right] |\xi_{k_x, k_z}\rangle = E(k_x, k_z) |\xi_{k_x, k_z}\rangle, \quad (4.213)$$

$$i\Gamma_3 \Gamma_2 |\xi_{k_x, k_z}\rangle = \xi_{k_x, k_z}\rangle. \quad (4.214)$$

As commuting operators share common eigenvectors, which requires

$$\alpha_{k_x, k_z, \text{R}} \Gamma_3 = \left(m - \cos k_x - \cos k_z \right) \Gamma_3 + \lambda \gamma_2. \quad (4.215)$$

From a similar process for the left eigenvector, we can obtain

$$\alpha_{k_x, k_z, \text{L}} \Gamma_3 = \left(m - \cos k_x - \cos k_z \right) \Gamma_3 - \lambda \gamma_2. \quad (4.216)$$

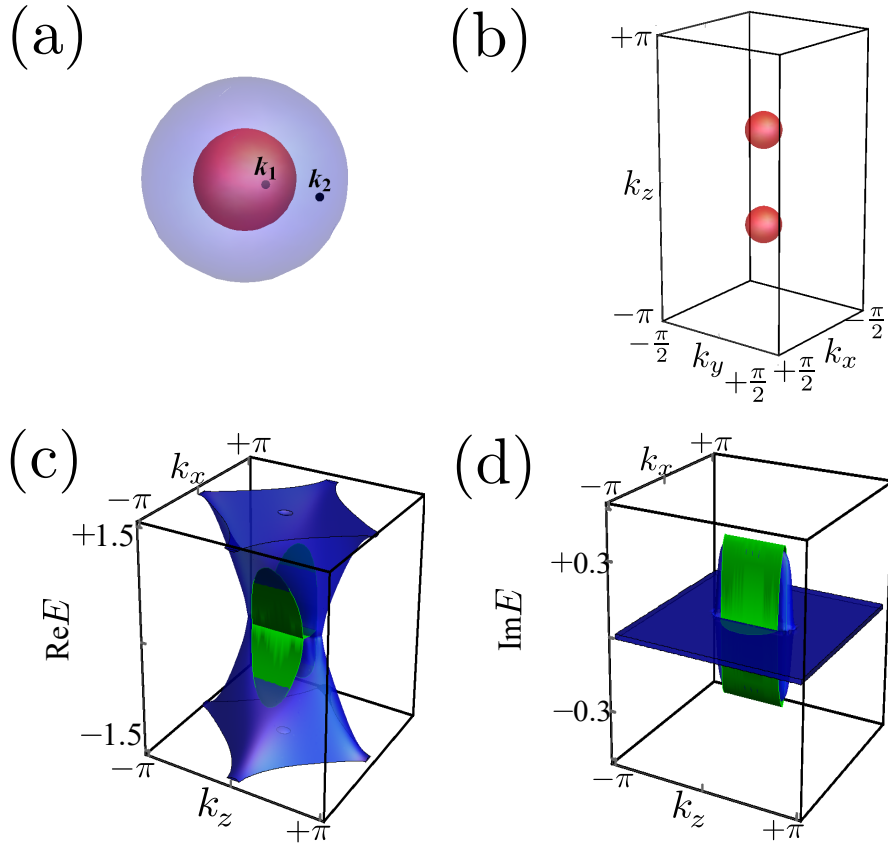


Figure 4.6: (a) The inner red sphere denotes the Dirac exceptional sphere. \mathbf{k}_1 and \mathbf{k}_2 together form S^0 that is used to calculate the topological charge $\nu(S^0)$. The outer blue sphere S^2 is chosen to enclose the Dirac exceptional sphere, and is used to calculate the \mathbb{Z}_2 topological charge. (b) The location of the two Dirac exceptional spheres. (c) The real part of the surface spectrum from the tight-binding model. (d) The imaginary part of the surface spectrum. The green curve is the surface spectrum calculated analytically.

Thus we have,

$$|\alpha_{k_x, k_z, R} \alpha_{k_x, k_z, L}| = |(m - \cos k_x - \cos k_z)^2 - \lambda^2| < 1. \quad (4.217)$$

From Eq. (4.213), the surface states satisfy $\sin k_x \Gamma_1 |\xi_{k_x, k_z}\rangle = E(k_x, k_z) |\xi_{k_x, k_z}\rangle$, which gives,

$$E(k_x, k_z) = \pm \sin k_x, \quad \text{with } |(m - \cos k_x - \cos k_z)^2 - \lambda^2| < 1. \quad (4.218)$$

The localization region for the surface states at $k_x = 0$ can be obtained as $-\arccos(M - 1 - \sqrt{\lambda^2 + 1}) < k_z < \arccos(M - 1 - \sqrt{\lambda^2 + 1})$, which is the same as that from the bulk-boundary correspondence of the similarity transformed Hamiltonian in Eq. (4.206). In Fig. 4.5 (c) and (d), the real and imaginary parts of the open boundary Hamiltonian are shown. The topological boundary states obtained above agree well with the numerical results.

4.4.3 Case III: Dirac exceptional sphere

In this section, we discuss the Dirac exceptional sphere case. Here we take the non-Hermitian potential $\lambda\gamma_4$ as an example. With PBCs, the non-Hermitian lattice model in momentum space reads,

$$H_{\text{SP}} = \sin k_x \Gamma_1 + \sin k_y \Gamma_2 + (m - \cos k_x - \cos k_y - \cos k_z) \Gamma_3 + \lambda \gamma_4. \quad (4.219)$$

Around the original Dirac point at $(0, 0, \pm \arccos(m - 2))$, two exceptional spheres form, as shown by the red spheres in Fig. 4.6(b). These two spheres are composed of exceptional points where the eigenvalues and the corresponding eigenvectors coalesce.

Dirac exceptional sphere

We discuss the exceptional sphere at $(0, 0, k_c)$ with the effective Hamiltonian of

$$H_{\text{eff-sphere}} = \delta k_x \Gamma_1 + \delta k_y \Gamma_2 + \delta k_z \Gamma_3 + \lambda \gamma_4 \quad (4.220)$$

The exceptional surface with zero eigenvalues can be parametrized as $(\delta k_x, \delta k_y, \delta k_z) = \lambda(\sin \theta \cos \phi, \sin \theta \sin \phi, \cos \theta)$, and the Hamiltonian on the sphere is

$$H_{\text{exp-sphere}} = \lambda \begin{pmatrix} \cos \theta & \sin \theta e^{-i\phi} & 0 & 1 \\ \sin \theta e^{i\phi} & -\cos \theta & -1 & 0 \\ 0 & 1 & \cos \theta & \sin \theta e^{i\phi} \\ -1 & 0 & \sin \theta e^{-i\phi} & -\cos \theta \end{pmatrix}. \quad (4.221)$$

Since $(H_{\text{surf}} - 0\mathbb{1})^2 = 0$ with eigenvalue 0, the minimal polynomial is of the form $m(\lambda) = (\lambda - 0)^2$, and the largest Jordan block is of the dimension 2×2 . The eigenvectors on the exceptional surface are

$$|\psi_1\rangle = (\cos \theta \quad e^{i\phi} \sin \theta \quad 0 \quad -1)^T, \quad |\psi_2\rangle = (e^{-i\phi} \sin \theta \quad -\cos \theta \quad 1 \quad 0)^T, \quad (4.222)$$

which span a two-dimensional eigenspace. From the dimension of the Jordan block and the dimension of the eigenspace, the Jordan canonical form of the Hamiltonian on the exceptional surface is

$$J = \begin{pmatrix} 0 & 1 & 0 & 0 \\ 0 & 0 & 0 & 0 \\ 0 & 0 & 0 & 1 \\ 0 & 0 & 0 & 0 \end{pmatrix}. \quad (4.223)$$

From this Jordan canonical form, we can find other linearly independent vectors from the following relations

$$H'_{\text{surf}} |\psi'_1\rangle = |\psi_1\rangle, \quad H'_{\text{surf}} |\psi'_2\rangle = |\psi_2\rangle. \quad (4.224)$$

The transformation matrix then is composed of $\{|\psi_1\rangle, |\psi'_1\rangle, |\psi_2\rangle, |\psi'_2\rangle\}$,

$$P = \begin{pmatrix} \cos \theta & 1 & e^{-i\phi} \sin \theta & 0 \\ e^{i\phi} \sin \theta & 0 & -\cos \theta & 1 \\ 0 & 0 & 1 & 0 \\ -1 & 0 & 0 & 0 \end{pmatrix}. \quad (4.225)$$

With this the condition $J = P^{-1}H_{\text{exp-sphere}}P$ can be verified.

The spatial co-dimension of the Dirac exceptional sphere in three dimension is zero, so that a zero dimensional sphere S^0 , which consists of two points of \mathbf{k}_1 inside and \mathbf{k}_2 outside the sphere, can be selected to enclose Dirac exceptional sphere. S^0 is shown by two black dots in FIG 4.6(a). Similar to the vorticity of energy eigenvalues in Eq. (4.189), the topological charge by S^0 can be defined as

$$\nu(S^0) = \frac{1}{2\pi}(\arg E_{n,\mathbf{k}_1} - \arg E_{n,\mathbf{k}_2}), \quad (4.226)$$

with n denoting the band index. The energy eigenvalues of the Dirac exceptional sphere in Eq. (4.179) are $E_{\pm} = \pm\sqrt{k_x^2 + k_y^2 + k_z^2 - \lambda^2}$, which is purely real outside and purely imaginary inside the sphere.

Then the eigenvalues for the conduction bands for \mathbf{k}_1 are $E_1 = \sqrt{k_1^2 - \lambda^2}$ and for \mathbf{k}_2 , they are $E_2 = \sqrt{k_2^2 - \lambda^2}$. The magnitudes of \mathbf{k}_1 and \mathbf{k}_2 satisfy $k_1 < \lambda$ and $k_2 > \lambda$. By the definition of our topological invariant in Eq. (4.226), the topological charge can be computed as

$$\nu(S^0) = \frac{1}{2\pi}(\arg E_1 - \arg E_2) = \frac{1}{2}, \quad (4.227)$$

which indicates the exceptional sphere is topologically non-trivial.

Relation between PBCs and OBCs

As we have shown in the previous chapter, the spectra and topology between systems of periodic and open boundary conditions might differ drastically. This difference can be effectively explained through the transfer matrix method, which has been introduced in the previous chapter. We first separate out the k_y components from the Hamiltonian (4.219). Then we identify the hopping matrix J and the on-site matrix M in the Bloch Hamiltonian as

$$J = \begin{pmatrix} -\frac{1}{2} & & & \frac{i}{2} \\ & -\frac{1}{2} & -\frac{i}{2} & \\ & -\frac{i}{2} & \frac{1}{2} & \\ \frac{i}{2} & & & \frac{1}{2} \end{pmatrix}, \quad M = \sin k_x \Gamma_1 + M_{\mathbf{k}} \Gamma_3 + i\lambda \Gamma_4, \quad (4.228)$$

where $M_{\mathbf{k}} = m - \cos k_x - \cos k_z$. We note that J is nilpotent with index 2, since $J^2 = 0$, and that J has rank $r = 1$, since the four rows/columns are linearly dependent. Next, we need to construct the on-site Greens function \mathcal{G} and find the singular value decomposition of J . We obtain

$$\mathcal{G} = (E\mathbb{1} - M)^{-1} = \frac{E\Gamma_0 + \sin k_x \Gamma_1 + M_{\mathbf{k}} \Gamma_3 + i\lambda \Gamma_4}{E^2 + \lambda^2 - M_{\mathbf{k}}^2 - \sin^2 k_x}, \quad (4.229)$$

with Γ_0 the identity matrix. The singular value decomposition of J gives the same results as the non-Hermitian kinetic case. We thus are ready to compute the transfer matrix T , which is

$$T = \frac{1}{M_{\mathbf{k}}} \begin{pmatrix} \sin^2 k_x + M_{\mathbf{k}}^2 - E^2 & 0 & E + i\lambda & i \sin k_x \\ 0 & \sin^2 k_x + M_{\mathbf{k}}^2 - E^2 & -i \sin k_x & E - i\lambda \\ -E + i\lambda & i \sin k_x & 1 & 0 \\ -i \sin k_x & -E - i\lambda & 0 & 1 \end{pmatrix}. \quad (4.230)$$

With the expression of the transfer matrix, we find its determinant is

$$\text{Det } T = 1, \quad (4.231)$$

which is independent of λ . Thus the spectra with PBCs and OBCs are basically the same. Thus, the bulk-boundary correspondence might still work for this case.

Topological invariants and bulk-boundary correspondence

The non-Hermitian $\lambda\gamma_4$ potential anti-commutes with the Hermitian Dirac Hamiltonian

$$\{H_D, \gamma_4\} = 0. \quad (4.232)$$

The energy spectrum is $E_{\text{SP}} = \pm\eta(\mathbf{k}) = \pm\sqrt{d^2(\mathbf{k}) - \lambda^2} = \pm(\sin^2 k_x + \sin^2 k_y + (m - \cos k_x - \cos k_y - \cos k_z)^2 - \lambda^2)^{1/2}$. For the region of $\sin^2 k_x + \sin^2 k_y + (m - \cos k_x - \cos k_y - \cos k_z)^2 > \lambda^2$ in the Brillouin zone, the energy eigenvalues are real. From the anti-commutation relation, it can be inferred that a similarity transformation can be found to convert the Hamiltonian to be Hermitian in the region where the spectrum is real. In the following we adopt the standard procedure to calculate the similarity transform operator as discussed in the previous chapter.

Notice that the flattened Hamiltonian $\tilde{\mathcal{H}}_D(\mathbf{k}) = \mathcal{H}_D(\mathbf{k})/d(\mathbf{k})$ and γ_4 form the Clifford algebra, and therefore $i[\tilde{\mathcal{H}}_D(\mathbf{k}), \gamma_4]/4$ generates rotations of the plane spanned by $\tilde{\mathcal{H}}_D(\mathbf{k})$ and γ_4 . In the following, we shall construct this rotation operator. By using $(\mathcal{H}_D(\mathbf{k})\Gamma)^2 = -1$, we can obtain the following relation,

$$\mathcal{V}(\mathbf{k}) = e^{-i\frac{\eta(\mathbf{k})}{2}\tilde{\mathcal{H}}_D(\mathbf{k})\Gamma} = \cosh \frac{\eta(\mathbf{k})}{2} - i \sinh \frac{\eta(\mathbf{k})}{2} \tilde{\mathcal{H}}_D(\mathbf{k})\Gamma. \quad (4.233)$$

Thus we can obtain the similarity transformed Hamiltonian as

$$\mathcal{V}(\mathbf{k})^{-1}(H_D + \lambda\gamma_4)\mathcal{V}(\mathbf{k}) = \frac{\sqrt{d^2(\mathbf{k}) - \lambda^2}}{d(\mathbf{k})} H_D, \quad (4.234)$$

with $d^2(\mathbf{k}) = \sin^2 k_x + \sin^2 k_y + (m - \cos k_x - \cos k_y - \cos k_z)^2$. Next we are going to discuss the topological property of the Dirac exceptional sphere.

We have shown that the topological charge of \mathbb{Z}_2 type Dirac monopole can be calculated by the real transition function $g_{SN}^{\mathbb{R}}$ in Eq. (4.157). Outside the Dirac exceptional sphere, as the reality condition for the wavefunction is preserved, the real transition function $g_{SN}^{\mathbb{R}}$ can still be well defined.

Here we choose a sphere S^2 that encloses the entire Dirac exceptional sphere, as shown by the blue sphere in Fig 4.6 (a). The radius of this sphere is chosen to be k , with $k > \lambda$. For simplicity, we scale the Hamiltonian with $1/k$, so that

$$H_{\text{sphere}}/k = H_{\text{Dirac}}/k + i\lambda_k\Gamma_4, \quad (4.235)$$

with $\lambda_k = \lambda/k < 1$. Correspondingly, the radius of S^2 sphere is scaled to be one. By choosing stereographic coordinates for the north and south hemispheres, we can obtain the eigenvectors. On the

equator, for the valence band, the eigenvectors from the north hemisphere are

$$|-, 1\rangle^N = (\cos \phi, -\sqrt{1 - \lambda_k^2}, \lambda_k + \sin \phi, 0)^T, \quad (4.236)$$

$$|-, 2\rangle^N = (\lambda_k - \sin \phi, 0, \cos \phi, -\sqrt{1 - \lambda_k^2})^T, \quad (4.237)$$

and for the south hemisphere, they are

$$|-, 1\rangle^S = (\sqrt{1 - \lambda_k^2}, -\cos \phi, 0, \lambda_k + \sin \phi)^T, \quad (4.238)$$

$$|-, 2\rangle^S = (0, \lambda_k - \sin \phi, \sqrt{1 - \lambda_k^2}, -\cos \phi)^T. \quad (4.239)$$

By setting $\lambda_k = 0$, the eigenvectors return to those of an Hermitian Dirac point as shown in Sec. 4.4. The real transition function $g_{SN}^{\mathbb{R}}$ on the equator defined by $|-, \alpha\rangle^S = [g_{SN}^{\mathbb{R}}]_{\alpha\beta} |-, \beta\rangle^N$ can be obtained as

$$g_{SN}^{\mathbb{R}}(\phi) = \begin{pmatrix} \cos \phi & -\sin \phi \\ \sin \phi & \cos \phi \end{pmatrix}, \quad (4.240)$$

which is the same as that in Eq. (4.157) for a Dirac point without the non-Hermitian term. Thus this Dirac exceptional sphere has the same \mathbb{Z}_2 type monopole charge as that of the Dirac point. Since the monopole charge is preserved and the PBCs and OBCs spectra don't differ from each other, we expect the Fermi arc surface states are also preserved.

Fermi arc surface states To study the surface states, we take OBCs in \mathbf{y} direction with N_y layers, the Hamiltonian in real space reads,

$$H_{\text{SP}}(k_x, k_z, y) = \mathbb{1} \otimes (\sin k_x \Gamma_1 + \lambda \gamma_4) + \frac{1}{2i} \Gamma_2 \otimes (S - S^\dagger) - \frac{1}{2} \Gamma_3 \otimes (S + S^\dagger) + \mathbb{1} \otimes (m - \cos k_x - \cos k_z) \Gamma_3. \quad (4.241)$$

The following ansatz for the right and left boundary states for the open boundary Hamiltonian is used,

$$|\psi_{\tilde{\mathbf{k}}}\rangle = \sum_{y=1}^{N_y} (\alpha_{k_x, k_z, \text{R}})^y |y\rangle \otimes |\xi_{\tilde{\mathbf{k}}}\rangle, \quad \langle\langle \psi_{\tilde{\mathbf{k}}} | = \sum_{y=1}^{N_y} \langle y | \otimes \langle\langle \xi_{\tilde{\mathbf{k}}} | (\alpha_{k_x, k_z, \text{L}})^y. \quad (4.242)$$

with ξ_{k_x, k_z} a spinor and $\alpha_{k_x, k_z, \text{R/L}}$ a scalar. Here $\tilde{\mathbf{k}} = (k_x, k_z)$. We will still use the criterion of Eq. (4.208) to determine the localization of modes. By solving the Schrödinger equation,

$$H_{\text{WR}}(k_x, k_z, y) |\psi_{\tilde{\mathbf{k}}}\rangle = E(k_x, k_z) |\psi_{\tilde{\mathbf{k}}}\rangle, \quad (4.243)$$

and use the boundary conditions, we can obtain the expression for $\alpha_{k_x, k_z, \text{R/L}}$ as

$$\alpha_{k_x, k_z, \text{R}} = M - \cos k_x - \cos k_z, \quad \alpha_{k_x, k_z, \text{L}} = M - \cos k_x - \cos k_z. \quad (4.244)$$

The localized surface states region then is given by $|\alpha_{k_x, k_z, \text{L}} \alpha_{k_x, k_z, \text{L}}| < 1$, which is

$$|M - \cos k_x - \cos k_z| < 1. \quad (4.245)$$

The surface spectrum is obtained as

$$E = \pm \sqrt{\sin^2 k_x - \lambda^2}, \text{ with } |M - \cos k_x - \cos k_z| < 1. \quad (4.246)$$

The energy spectrum is shown in Fig. 4.6. The above obtained boundary modes agree well with numerical results. Notice in this case, Fermi arc surface states are attached to the center of the Dirac exceptional sphere in the bulk. This can be understood from the fact that the boundary conditions in this case does not alter the PBCs and OBCs spectra, thus the bulk topology might still well predict the boundary modes.

4.5 Conclusions

We have discussed topological Weyl semimetals with all possible non-Hermitian potentials. We have identified two kinds of non-Hermitian potentials, the non-Hermitian kinetic terms and the non-Hermitian mass terms. For each of them, we have discussed the bulk topology, the relation between periodic and open boundary conditions using the transfer matrix method, and the topological boundary states in different slab geometries. For the Weyl Hamiltonian with non-Hermitian kinetic terms, we have found that the spectra between periodic and open boundary conditions differ drastically from each other. The open boundary Hamiltonian can be converted to be Hermitian in most regions. The topological boundary states from the Bloch Hamiltonian that corresponds to the similarity transformed open boundary Hamiltonian agree well with the topological boundary states by direct calculation from the non-Hermitian Hamiltonian. For the Weyl Hamiltonian with non-Hermitian mass terms, the Hamiltonian cannot be converted to be Hermitian in both real and momentum space. The spectra between periodic and open boundary conditions agree with each other, and except for an imaginary part, the topological surface modes of the non-Hermitian Hamiltonian are basically the same with the Hermitian case.

We have further discussed the \mathcal{PT} symmetric non-Hermitian Dirac semimetals. We find that the inclusion of \mathcal{PT} symmetric non-Hermitian potentials can turn a Dirac point into (I) two separate Weyl points, (II) a pair of mutually complex conjugate Weyl exceptional rings, and (III) a Dirac exceptional sphere. We find that in case (II) the pair of mutually complex conjugate Weyl exceptional rings are protected by the vorticity defined on the ring that interlinks with the Weyl exceptional ring. Interestingly, with open boundary conditions, the non-Hermitian Hamiltonian in real space can be turned Hermitian for most regions in the Brillouin zone. The similarity transformed Hamiltonian exhibits correct bulk boundary correspondence, which is verified by directly calculating the topological boundary states. In case (III), while the Dirac exceptional sphere inherits the \mathbb{Z}_2 monopole charge from the original Dirac point, it can be further characterized by an $1/2$ topological invariant unique to non-Hermitian systems. For this kind of non-Hermitian terms, the spectra for both systems with periodic and open boundary conditions are basically the same. The topological boundary states obtained analytically agree well with the numerics. Our work can be extended to general non-Hermitian perturbations that even do not respect \mathcal{PT} symmetry, with a similar approach. In this case, we expect new topological phases and topological phase transitions to be discovered. Since the Dirac point serves as the bridge between different gapped topological phases, non-Hermitian perturbations help build more bridges in the from of exceptional points/rings/spheres, thus largely enriching the concept of topological band theory.

5 Chapter 5

Conclusion and outlook

In this thesis, we have extended the study of topological phases of matter from the Hermitian to the non-Hermitian regime. Chapter 1 serves as an introduction for non-experts in this field and provides a summary of concepts that lays a theoretical footing for this thesis. Topological materials and their characterization by topological invariants are discussed. Through the discussion of symmetry and topology, the classification table of non-interacting topological phases is established. It is found that topological phases at each entry of the classification table can be described by Dirac Hamiltonians, which will be extensively used also for non-Hermitian topological phases. A brief introduction to non-Hermitian systems is made with a focus on the non-Hermitian features of topological band theory.

In chapter 2, we have investigated the \mathcal{PT} -symmetric Hermitian Dirac nodal-line semimetals, and extended our discussion to the \mathcal{PT} -symmetric non-Hermitian semimetals. In the Hermitian nodal-line semimetals, the topological phase is protected by the \mathcal{PT} symmetry and can be characterized by a quantized $\pm\pi$ Berry phase. The correspondence between exotic drumhead surface states and the bulk non-trivial topological invariants are discussed through both numerical and analytical calculations. From the low-energy effective model of the nodal-line semimetals, we have identified a $(3 + 1)$ -dimensional parity anomaly which is not possible in high-energy physics. The parity anomaly leads to an anomalous transverse current in the bulk. To generate and detect such a current, we have proposed a dumbbell filtering device to generate a net topological current, based on the property of the topologically protected surface states of the dumbbell device. The robustness of our device is discussed with respect to small spin-orbit coupling, finite dispersion of the nodal ring, as well as moderately strong disorder. We anticipate our proposal can be experimentally realized in materials, such as, CaAgAs and CaAgP. In the non-Hermitian nodal-line semimetals, for which the \mathcal{PT} symmetry is still preserved, the Berry phase that characterizes the Dirac nodal ring can still be computed in the bulk, though in a different form. However, the correspondence between the topological surface states and the bulk non-trivial topological invariants cannot be established, because the non-Hermitian Berry phase cannot be well defined throughout the Brillouin zone. A theory for non-Hermitian topological phases is therefore required.

We have presented a general formalism to study non-Hermitian topological gapped systems in chapter 3. Similar to the Hermitian cases, most non-Hermitian topological gapped systems can be described by massive Dirac Hamiltonians with the inclusion of non-Hermitian terms. We present a systematic investigation on the non-Hermitian terms that do not induce band crossings in the bulk. It is found that for d -dimensional massive Dirac Hamiltonians, there are three different types of non-Hermitian terms: (i) non-Hermitian terms that anti-commute with the Dirac Hamiltonian, (ii) non-Hermitian kinetic terms, and (iii) non-Hermitian mass terms. Subject to different boundary conditions, these

three types of non-Hermitian Hamiltonians are studied in terms of non-unitary similarity transformations. If the Hamiltonian can be converted to be Hermitian by a similarity transformation, it is called superficially non-Hermitian, otherwise it is intrinsically non-Hermitian. With open boundary conditions, terms of type (i) give rise to intrinsic non-Hermiticity, while terms of type (ii) lead to superficial non-Hermiticity. In contrast, with periodic boundary conditions, type (i) perturbations induce superficial non-Hermiticity, while type-(ii) perturbations generate intrinsic non-Hermiticity. Thus a two-fold duality is revealed for these two types of non-Hermitian perturbations. In this duality relation, we find that exceptional points, a characteristic feature of non-Hermitian systems, form exceptional spheres of dimension $(d - 2)$ in the surface and bulk band structures for type (i) and (ii) cases, respectively. On the other hand, terms of type (iii) result in intrinsic non-Hermiticity and there are no exceptional points, regardless of boundary conditions.

Finally, in chapter 4, we have investigated non-Hermitian topological gapless systems. Instead of trying to establish a general theory, we have focused on two important systems, namely topological non-Hermitian Weyl semimetals and the \mathcal{PT} symmetric non-Hermitian Dirac semimetals. For the non-Hermitian Weyl semimetals, which can be represented by a Dirac Hamiltonian, we adopt a similar approach as that in chapter 3 and find that there are only two types of non-Hermitian terms, non-Hermitian kinetic terms and mass terms. These two types of non-Hermitian terms are studied in different slab geometries, where the band topology and topological boundary states are revealed. For the \mathcal{PT} symmetric non-Hermitian Dirac semimetals, it is found that besides Weyl points, the inclusion of \mathcal{PT} symmetric non-Hermitian potentials can turn a Dirac point into a pair of mutually complex conjugate Weyl exceptional rings and a Dirac exceptional sphere with periodic boundary conditions. However, the correspondence between bulk and boundary could fail in non-Hermitian systems. It is found that for the Weyl exceptional rings, the periodic and open boundary spectra differ drastically from each other, and Fermi arc surface states correspond to Dirac points instead of Weyl exceptional rings. On the other hand, for the Dirac exceptional sphere case, the periodic and open boundary spectra are basically the same, a non-Hermitian version of the Fermi arc surface states is found to correspond to the Dirac exceptional spheres in the bulk.

Our findings can be used as guiding principles for the design of applications in, e.g., photonic cavity arrays. For example, our analysis shows that topological Dirac systems perturbed by non-Hermitian mass terms exhibit robust surface states with purely real spectrum. In photonic cavity arrays, these surface states provide robust channels for light propagation, which are protected against perturbations and disorder. Importantly, this property can be exploited for the design of efficient laser systems that are immune to disorder. That is, optically pumping the boundary of the cavity array induces single-mode lasing in the surface states, with high slope efficiency. It follows from our analysis that these phenomena should occur in a broader class of photonic band structures, namely in any topological Dirac system perturbed by non-Hermitian mass terms. Besides non-Hermitian Weyl and Dirac Hamiltonians, our approach can be generalized in a straightforward manner to generic gapless Dirac Hamiltonians, i.e., to non-Hermitian periodic lattices with semimetallic band structures. Furthermore it would be interesting to study the role of symmetries, specifically, how the symmetries constrain the form of the non-Hermitian terms. It is possible that a general and exhaustive classification of gapless systems with exceptional points could be established based on symmetry and topology. This is of fundamental interest to theory and of particular importance in view of the numerous applications of exceptional points in photonic devices.

Bibliography

- [1] Y. Okamoto, T. Inohara, A. Yamakage, Y. Yamakawa, and K. Takenaka, *Journal of the Physical Society of Japan* **85**, 123701 (2016).
- [2] E. Emmanouilidou, B. Shen, X. Deng, T.-R. Chang, A. Shi, G. Kotliar, S.-Y. Xu, and N. Ni, *Phys. Rev. B* **95**, 245113 (2017).
- [3] K. v. Klitzing, G. Dorda, and M. Pepper, *Phys. Rev. Lett.* **45**, 494 (1980).
- [4] D. J. Thouless, M. Kohmoto, M. P. Nightingale, and M. den Nijs, *Phys. Rev. Lett.* **49**, 405 (1982).
- [5] F. D. M. Haldane, *Phys. Rev. Lett.* **61**, 2015 (1988).
- [6] B. A. Bernevig, T. L. Hughes, and S.-C. Zhang, *Science* **314**, 1757 (2006).
- [7] C. L. Kane and E. J. Mele, *Phys. Rev. Lett.* **95**, 226801 (2005).
- [8] X.-L. Qi, Y.-S. Wu, and S.-C. Zhang, *Phys. Rev. B* **74**, 085308 (2006).
- [9] M. Koenig, S. Wiedmann, C. Bruene, A. Roth, H. Buhmann, L. W. Molenkamp, X.-L. Qi, and S.-C. Zhang, *Science* **318**, 766 (2007).
- [10] S. Ryu, A. P. Schnyder, A. Furusaki, and A. W. W. Ludwig, *New J. Phys.* **12**, 065010 (2010).
- [11] X.-L. Qi and S.-C. Zhang, *Rev. Mod. Phys.* **83**, 1057 (2011).
- [12] Y. Ando, *J. Phys. Soc. Jpn.* **82**, 102001 (2013).
- [13] C.-K. Chiu, J. C. Y. Teo, A. P. Schnyder, and S. Ryu, *Rev. Mod. Phys.* **88**, 035005 (2016).
- [14] C.-X. Liu, S.-C. Zhang, and X.-L. Qi, *Annu. Rev. Condens. Matter Phys.* **7**, 301 (2016).
- [15] T. Zhang, Y. Jiang, Z. Song, H. Huang, Y. He, Z. Fang, H. Weng, and C. Fang, *Nature* **566**, 475 (2019).
- [16] F. Tang, H. C. Po, A. Vishwanath, and X. Wan, *Nature* **566**, 486 (2019).
- [17] S.-Y. Xu, I. Belopolski, N. Alidoust, M. Neupane, G. Bian, C. Zhang, R. Sankar, G. Chang, Z. Yuan, C.-C. Lee, et al., *Science* **349**, 613 (2015).
- [18] Z. Wang, A. Alexandradinata, R. J. Cava, and B. A. Bernevig, *Nature* **532**, 189 (2016).
- [19] B. Bradlyn, J. Cano, Z. Wang, M. G. Vergniory, C. Felser, R. J. Cava, and B. A. Bernevig, *Science* **353**, aaf5037 (2016).
- [20] H. Shen, B. Zhen, and L. Fu, *Phys. Rev. Lett.* **120**, 146402 (2018).

- [21] Z. Gong, Y. Ashida, K. Kawabata, K. Takasan, S. Higashikawa, and M. Ueda, *Phys. Rev. X* **8**, 031079 (2018).
- [22] B. A. Bernevig and T. L. Hughes, *Topological Insulators and Topological Superconductors* (Princeton University Press, 2013).
- [23] D. Tong, *Lectures on the Quantum Hall Effect* (arXiv:1606.06687, 2016).
- [24] C.-Z. Chang, J. Zhang, X. Feng, J. Shen, Z. Zhang, M. Guo, K. Li, Y. Ou, P. Wei, L.-L. Wang, et al., *Science* **340**, 167 (2013).
- [25] L. Fu and C. L. Kane, *Phys. Rev. B* **74**, 195312 (2006).
- [26] A. Alexandradinata, Z. Wang, and B. A. Bernevig, *Phys. Rev. X* **6**, 021008 (2016).
- [27] A. Alexandradinata, X. Dai, and B. A. Bernevig, *Phys. Rev. B* **89**, 155114 (2014).
- [28] T. Morimoto and A. Furusaki, *Phys. Rev. B* **88**, 125129 (2013).
- [29] A. Kitaev, *AIP Conference Proceedings* **1134**, 22 (2009).
- [30] S. Yao and Z. Wang, *Phys. Rev. Lett.* **121**, 086803 (2018).
- [31] C. M. Bender and S. Boettcher, *Phys. Rev. Lett.* **80**, 5243 (1998).
- [32] C. M. Bender, S. Boettcher, and P. N. Meisinger, *Journal of Mathematical Physics* **40**, 2201 (1999).
- [33] C. M. Bender, D. C. Brody, and H. F. Jones, *Phys. Rev. Lett.* **89**, 270401 (2002).
- [34] C. M. Bender, *Rep. Prog. Phys.* **70**, 947 (2007).
- [35] P. Hosur and X. Qi, *Comptes Rendus Physique* **14**, 857 (2013).
- [36] A. Zee, *Quantum Field Theory in a Nutshell* (Princeton University Press (Princeton), 2010).
- [37] S. Ryu, J. E. Moore, and A. W. W. Ludwig, *Phys. Rev. B* **85**, 045104 (2012).
- [38] A. A. Burkov, *Journal of Physics: Condensed Matter* **27**, 113201 (2015).
- [39] S. A. Parameswaran, T. Grover, D. A. Abanin, D. A. Pesin, and A. Vishwanath, *Phys. Rev. X* **4**, 031035 (2014).
- [40] G. E. Volovik, *Universe in a helium droplet* (Oxford University Press, Oxford UK, 2003).
- [41] G. E. Volovik, *Topology of quantum vacuum*, vol. 870 of *Lecture Notes in Physics* (Springer Berlin, 2013).
- [42] P. Hořava, *Phys. Rev. Lett.* **95**, 016405 (2005).
- [43] Y. X. Zhao and Z. D. Wang, *Phys. Rev. Lett.* **110**, 240404 (2013).
- [44] A. A. Burkov, M. D. Hook, and L. Balents, *Phys. Rev. B* **84**, 235126 (2011).

-
- [45] S. Matsuura, P.-Y. Chang, A. P. Schnyder, and S. Ryu, *New Journal of Physics* **15**, 065001 (2013).
- [46] C.-K. Chiu and A. P. Schnyder, *Phys. Rev. B* **90**, 205136 (2014).
- [47] Y. X. Zhao, A. P. Schnyder, and Z. D. Wang, *Phys. Rev. Lett.* **116**, 156402 (2016).
- [48] Y. X. Zhao and A. P. Schnyder, *Phys. Rev. B* **94**, 195109 (2016).
- [49] Y. Kim, B. J. Wieder, C. L. Kane, and A. M. Rappe, *Phys. Rev. Lett.* **115**, 036806 (2015).
- [50] Y.-H. Chan, C.-K. Chiu, M. Y. Chou, and A. P. Schnyder, *Phys. Rev. B* **93**, 205132 (2016).
- [51] A. Yamakage, Y. Yamakawa, Y. Tanaka, and Y. Okamoto, *Journal of the Physical Society of Japan* **85**, 013708 (2016).
- [52] L. S. Xie, L. M. Schoop, E. M. Seibel, Q. D. Gibson, W. Xie, and R. J. Cava, *APL Mater.* **3**, 083602 (2015).
- [53] T. T. Heikkilä and G. E. Volovik, *New Journal of Physics* **17**, 093019 (2015).
- [54] D.-W. Zhang, Y. X. Zhao, R.-B. Liu, Z.-Y. Xue, S.-L. Zhu, and Z. D. Wang, *Phys. Rev. A* **93**, 043617 (2016).
- [55] Y. Wu, L.-L. Wang, E. Mun, D. D. Johnson, D. Mou, L. Huang, Y. Lee, S. L. Budko, P. C. Canfield, and A. Kaminski, *Nat Phys* **12**, 667 (2016).
- [56] R. Yu, H. Weng, Z. Fang, X. Dai, and X. Hu, *Phys. Rev. Lett.* **115**, 036807 (2015).
- [57] Q. Xu, R. Yu, Z. Fang, X. Dai, and H. Weng, *Phys. Rev. B* **95**, 045136 (2017).
- [58] G. P. Mikitik and Y. V. Sharlai, *Phys. Rev. Lett.* **93**, 106403 (2004).
- [59] M. Hirayama, R. Okugawa, T. Miyake, and S. Murakami, *Nature Communications* **8**, 14022 (2017).
- [60] A. A. Zyuzin and A. A. Burkov, *Phys. Rev. B* **86**, 115133 (2012).
- [61] D. Xiao, W. Yao, and Q. Niu, *Phys. Rev. Lett.* **99**, 236809 (2007).
- [62] D. Xiao, M.-C. Chang, and Q. Niu, *Rev. Mod. Phys.* **82**, 1959 (2010).
- [63] X. Huang, L. Zhao, Y. Long, P. Wang, D. Chen, Z. Yang, H. Liang, M. Xue, H. Weng, Z. Fang, et al., *Phys. Rev. X* **5**, 031023 (2015).
- [64] C.-L. Zhang, S.-Y. Xu, I. Belopolski, Z. Yuan, Z. Lin, B. Tong, G. Bian, N. Alidoust, C.-C. Lee, S.-M. Huang, et al., *Nature Communications* **7**, 10735 (2016).
- [65] J. Xiong, S. K. Kushwaha, T. Liang, J. W. Krizan, M. Hirschberger, W. Wang, R. J. Cava, and N. P. Ong, *Science* **350**, 413 (2015).
- [66] S. L. Adler, *Phys. Rev.* **177**, 2426 (1969).
- [67] J. S. Bell and R. Jackiw, *Il Nuovo Cimento A (1965-1970)* **60**, 47 (1969).
-

- [68] H. Nielsen and M. Ninomiya, *Physics Letters B* **130**, 389 (1983).
- [69] V. Aji, *Phys. Rev. B* **85**, 241101 (2012).
- [70] D. T. Son and B. Z. Spivak, *Phys. Rev. B* **88**, 104412 (2013).
- [71] K.-Y. Yang, Y.-M. Lu, and Y. Ran, *Phys. Rev. B* **84**, 075129 (2011).
- [72] C.-X. Liu, P. Ye, and X.-L. Qi, *Phys. Rev. B* **87**, 235306 (2013).
- [73] A. J. Niemi and G. W. Semenoff, *Phys. Rev. Lett.* **51**, 2077 (1983).
- [74] A. N. Redlich, *Phys. Rev. D* **29**, 2366 (1984).
- [75] G. V. Dunne, in *Topological Aspects of Low Dimensional Systems*, edited by A. Comtet, T. Jolicœur, S. Ouvry, and F. David (Springer Berlin, 1999), p. 177.
- [76] R. V. Gorbachev, J. C. W. Song, G. L. Yu, A. V. Kretinin, F. Withers, Y. Cao, A. Mishchenko, I. V. Grigorieva, K. S. Novoselov, L. S. Levitov, et al., *Science* **346**, 448 (2014).
- [77] Y. Shimazaki, M. Yamamoto, I. V. Borzenets, K. Watanabe, T. Taniguchi, and S. Tarucha, *Nature Physics* **11**, 1032 (2015).
- [78] M. Sui, G. Chen, L. Ma, W.-Y. Shan, D. Tian, K. Watanabe, T. Taniguchi, X. Jin, W. Yao, D. Xiao, et al., *Nature Physics* **11**, 1027 (2015).
- [79] K. F. Mak, K. L. McGill, J. Park, and P. L. McEuen, *Science* **344**, 1489 (2014).
- [80] H. Zeng, J. Dai, W. Yao, D. Xiao, and X. Cui, *Nature Nanotechnology* **7**, 490 (2012).
- [81] K. F. Mak, K. He, J. Shan, and T. F. Heinz, *Nature Nanotechnology* **7**, 494 (2012).
- [82] J. Zak, *Phys. Rev. Lett.* **62**, 2747 (1989).
- [83] D. Vanderbilt and R. D. King-Smith, *Phys. Rev. B* **48**, 4442 (1993).
- [84] G. Sundaram and Q. Niu, *Phys. Rev. B* **59**, 14915 (1999).
- [85] R. Landauer, *IBM Journal of Research and Development* **1**, 223 (1957).
- [86] M. Büttiker, Y. Imry, R. Landauer, and S. Pinhas, *Phys. Rev. B* **31**, 6207 (1985).
- [87] C. W. Groth, M. Wimmer, A. R. Akhmerov, and X. Waintal, *New Journal of Physics* **16**, 063065 (2014).
- [88] P. J. W. Moll, N. L. Nair, T. Helm, A. C. Potter, I. Kimchi, A. Vishwanath, and J. G. Analytis, *Nature* **535**, 266 (2016).
- [89] M. Schaffer, B. Schaffer, and Q. Ramasse, *Ultramicroscopy* **114**, 62 (2012).
- [90] Y. Wang and R. M. Nandkishore, arXiv:1705.10809 (2017).
- [91] C. M. Bender and S. Boettcher, *Phys. Rev. Lett.* **80**, 5243 (1998).

-
- [92] X.-B. Wang, X.-M. Ma, E. Emmanouilidou, B. Shen, C.-H. Hsu, C.-S. Zhou, Y. Zuo, R.-R. Song, S.-Y. Xu, G. Wang, et al., *Phys. Rev. B* **96**, 161112 (2017).
- [93] J. Nayak, N. Kumar, S.-C. Wu, C. Shekhar, J. Fink, E. E. D. Rienks, G. H. Fecher, Y. Sun, and C. Felser, arXiv:1708.07814 (2017).
- [94] D. Takane, K. Nakayama, S. Souma, T. Wada, Y. Okamoto, K. Takenaka, Y. Yamakawa, A. Yamakage, T. Mitsuhashi, K. Horiba, et al., arXiv:1708.06874 (2017).
- [95] K. G. Makris, R. El-Ganainy, D. N. Christodoulides, and Z. H. Musslimani, *Phys. Rev. Lett.* **100**, 103904 (2008).
- [96] R. El-Ganainy, K. G. Makris, M. Khajavikhan, Z. H. Musslimani, S. Rotter, and D. N. Christodoulides, *Nature Physics* **14**, 11 (2018).
- [97] Z. H. Musslimani, K. G. Makris, R. El-Ganainy, and D. N. Christodoulides, *Phys. Rev. Lett.* **100**, 030402 (2008).
- [98] A. Guo, G. J. Salamo, D. Duchesne, R. Morandotti, M. Volatier-Ravat, V. Aimez, G. A. Siviloglou, and D. N. Christodoulides, *Phys. Rev. Lett.* **103**, 093902 (2009).
- [99] C. E. Ruter, K. G. Makris, R. El-Ganainy, D. N. Christodoulides, M. Segev, and D. Kip, *Nature Physics* **6**, 192 (2010).
- [100] B. Peng, S. K. Ozdemir, F. Lei, F. Monifi, M. Gianfreda, G. L. Long, S. Fan, F. Nori, C. M. Bender, and L. Yang, *Nature Physics* **10**, 394 (2014).
- [101] A. Regensburger, C. Bersch, M.-A. Miri, G. Onishchukov, D. N. Christodoulides, and U. Peschel, *Nature* **488**, 167 (2012).
- [102] T. Gao, E. Estrecho, K. Y. Bliokh, T. C. H. Liew, M. D. Fraser, S. Brodbeck, M. Kamp, C. Schneider, S. Hofling, Y. Yamamoto, et al., *Nature* **526**, 554 (2015).
- [103] H. Cao and J. Wiersig, *Rev. Mod. Phys.* **87**, 61 (2015).
- [104] S. Klaiman, U. Ganther, and N. Moiseyev, *Phys. Rev. Lett.* **101**, 080402 (2008).
- [105] L. Chang, X. Jiang, S. Hua, C. Yang, J. Wen, L. Jiang, G. Li, G. Wang, and M. Xiao, *Nature Photonics* **8**, 524 (2014).
- [106] H. Xu, D. Mason, L. Jiang, and J. G. E. Harris, *Nature* **537**, 80 (2016).
- [107] B. Peng, S. K. Ozdemir, S. Rotter, H. Yilmaz, M. Liertzer, F. Monifi, C. M. Bender, F. Nori, and L. Yang, *Science* **346**, 328 (2014).
- [108] A. A. Zyuzin and A. Y. Zyuzin, *Phys. Rev. B* **97**, 041203 (2018).
- [109] N. Harrison, *Phys. Rev. Lett.* **121**, 026602 (2018).
- [110] K. Kawabata, Y. Ashida, H. Katsura, and M. Ueda, *Phys. Rev. B* **98**, 085116 (2018).
- [111] H. Shen and L. Fu, *Phys. Rev. Lett.* **121**, 026403 (2018).
-

- [112] T. Yoshida, R. Peters, and N. Kawakami, *Phys. Rev. B* **98**, 035141 (2018).
- [113] V. Kozii and L. Fu, arXiv:1708.05841 (2017).
- [114] J. A. S. Lourenco, R. L. Eneias, and R. G. Pereira, *Phys. Rev. B* **98**, 085126 (2018).
- [115] M. Nakagawa, N. Kawakami, and M. Ueda, *Phys. Rev. Lett.* **121**, 203001 (2018).
- [116] J. Avila, F. Peñaranda, E. Prada, P. San-Jose, and R. Aguado, arXiv:1807.04677 (2018).
- [117] M. A. Bandres, S. Wittek, G. Harari, M. Parto, J. Ren, M. Segev, D. N. Christodoulides, and M. Khajavikhan, *Science* p. eaar4005 (2018).
- [118] G. Harari, M. A. Bandres, Y. Lumer, M. C. Rechtsman, Y. D. Chong, M. Khajavikhan, D. N. Christodoulides, and M. Segev, *Science* p. eaar4003 (2018).
- [119] S. Weimann, M. Kremer, Y. Plotnik, Y. Lumer, S. Nolte, K. G. Makris, M. Segev, M. C. Rechtsman, and A. Szameit, *Nature Materials* **16**, 433 (2017).
- [120] A. Cerjan, S. Huang, K. P. Chen, Y. Chong, and M. C. Rechtsman, arXiv:1808.09541 (2018).
- [121] D. Leykam, K. Y. Bliokh, C. Huang, Y. D. Chong, and F. Nori, *Phys. Rev. Lett.* **118**, 040401 (2017).
- [122] M. Pan, H. Zhao, P. Miao, S. Longhi, and L. Feng, *Nature Communications* **9**, 1308 (2018).
- [123] T. E. Lee, *Phys. Rev. Lett.* **116**, 133903 (2016).
- [124] V. M. Martinez Alvarez, J. E. Barrios Vargas, and L. E. F. Foa Torres, *Phys. Rev. B* **97**, 121401 (2018).
- [125] C. H. Lee and R. Thomale, arXiv:1809.02125 (2018).
- [126] S. Yao, F. Song, and Z. Wang, *Phys. Rev. Lett.* **121**, 136802 (2018).
- [127] F. K. Kunst, E. Edvardsson, J. C. Budich, and E. J. Bergholtz, *Phys. Rev. Lett.* **121**, 026808 (2018).
- [128] K. Kawabata, K. Shiozaki, and M. Ueda, *Phys. Rev. B* **98**, 165148 (2018).
- [129] H. Zhou, C. Peng, Y. Yoon, C. W. Hsu, K. A. Nelson, L. Fu, J. D. Joannopoulos, M. Soljacic, and B. Zhen, *Science* p. eaap9859 (2018).
- [130] Y. Xu, S.-T. Wang, and L.-M. Duan, *Phys. Rev. Lett.* **118**, 045701 (2017).
- [131] K. Kawabata, K. Shiozaki, M. Ueda, and M. Sato, arXiv:1812.09133 (2018).
- [132] M. Papaj, H. Isobe, and L. Fu, arXiv:1802.00443 (2018).
- [133] J. Carlstrom and E. J. Bergholtz, *Phys. Rev. A* **98**, 042114 (2018).
- [134] Z. Yang and J. Hu, arXiv:1807.05661 (2018).
- [135] A. Cerjan, M. Xiao, L. Yuan, and S. Fan, *Phys. Rev. B* **97**, 075128 (2018).

-
- [136] L. Feng, Z. J. Wong, R.-M. Ma, Y. Wang, and X. Zhang, *Science* **346**, 972 (2014).
- [137] H. Hodaei, M.-A. Miri, M. Heinrich, D. N. Christodoulides, and M. Khajavikhan, *Science* **346**, 975 (2014).
- [138] T. Goldzak, A. A. Mailybaev, and N. Moiseyev, *Phys. Rev. Lett.* **120**, 013901 (2018).
- [139] M. Parto, S. Wittek, H. Hodaei, G. Harari, M. A. Bandres, J. Ren, M. C. Rechtsman, M. Segev, D. N. Christodoulides, and M. Khajavikhan, *Phys. Rev. Lett.* **120**, 113901 (2018).
- [140] R. Yao, H. Li, B. Zheng, S. An, J. Ding, C.-S. Lee, H. Zhang, and W. Guo, arXiv:1804.01587 (2018).
- [141] H. Zhao, P. Miao, M. H. Teimourpour, S. Malzard, R. El-Ganainy, H. Schomerus, and L. Feng, *Nature Communications* **9**, 981 (2018).
- [142] P. St-Jean, V. Goblot, E. Galopin, A. Lemaître, T. Ozawa, L. L. Gratiet, I. Sagnes, J. Bloch, and A. Amo, *Nature Photonics* **11**, 651 (2017).
- [143] L. Feng, R. El-Ganainy, and L. Ge, *Nature Photonics* **11**, 752 (2017).
- [144] F. K. Kunst and V. Dwivedi, arXiv:1812.02186 (2018).
- [145] W. D. Heiss, *J. Phys. A: Math. Theor.* **45**, 444016 (2012).
- [146] X.-L. Qi, T. L. Hughes, and S.-C. Zhang, *Phys. Rev. B* **78**, 195424 (2008).
- [147] V. Dwivedi and V. Chua, *Phys. Rev. B* **93**, 134304 (2016).
- [148] J. Wiersig, *Phys. Rev. Lett.* **112**, 203901 (2014).
- [149] W. Chen, S. Kaya Ozdemir, G. Zhao, J. Wiersig, and L. Yang, *Nature* **548**, 192 (2017).
- [150] T. Kato, *Perturbation Theory for Linear Operators*, Classics in Mathematics (Springer-Verlag, Berlin Heidelberg, 1995), 2nd ed.
- [151] G. Demange and E.-M. Graefe, *J. Phys. A: Math. Theor.* **45**, 025303 (2011).
- [152] S. Sunada, *Phys. Rev. A* **97**, 043804 (2018).
- [153] A. Pick, B. Zhen, O. D. Miller, C. W. Hsu, F. Hernandez, A. W. Rodriguez, M. Soljačić, and S. G. Johnson, *Opt. Express* **25**, 12325 (2017).
- [154] N. P. Armitage, E. J. Mele, and A. Vishwanath, *Rev. Mod. Phys.* **90**, 015001 (2018).
- [155] M. M. Vazifeh and M. Franz, *Phys. Rev. Lett.* **111**, 027201 (2013).
- [156] C. Shekhar, A. K. Nayak, Y. Sun, M. Schmidt, M. Nicklas, I. Leermakers, U. Zeitler, Y. Skourski, J. Wosnitza, Z. Liu, et al., *Nat Phys* **advance online publication** (2015).
- [157] Z. Wang and S.-C. Zhang, *Phys. Rev. B* **87**, 161107 (2013).
- [158] P. E. C. Ashby and J. P. Carbotte, *Phys. Rev. B* **87**, 245131 (2013).

- [159] K. S. Novoselov, A. K. Geim, S. V. Morozov, D. Jiang, M. I. Katsnelson, I. V. Grigorieva, S. V. Dubonos, and A. A. Firsov, *Nature* **438**, 197 (2005).
- [160] Z. K. Liu, B. Zhou, Y. Zhang, Z. J. Wang, H. M. Weng, D. Prabhakaran, S.-K. Mo, Z. X. Shen, Z. Fang, X. Dai, et al., *Science* **343**, 864 (2014).
- [161] M. Neupane, S.-Y. Xu, R. Sankar, N. Alidoust, G. Bian, C. Liu, I. Belopolski, T.-R. Chang, H.-T. Jeng, H. Lin, et al., *Nature Communications* **5**, 3786 (2014).
- [162] S. Borisenko, Q. Gibson, D. Evtushinsky, V. Zabolotnyy, B. Buechner, and R. J. Cava, *Phys. Rev. Lett.* **113**, 027603 (2014).
- [163] L. Fu, C. L. Kane, and E. J. Mele, *Phys. Rev. Lett.* **98**, 106803 (2007).
- [164] N. Hatano and D. R. Nelson, *Phys. Rev. Lett.* **77**, 570 (1996).
- [165] V. V. Konotop, J. Yang, and D. A. Zezyulin, *Rev. Mod. Phys.* **88**, 035002 (2016).
- [166] H. B. Nielsen and M. Ninomiya, *Nuclear Physics B* **185**, 20 (1981).
- [167] H. B. Nielsen and M. Ninomiya, *Nuclear Physics B* **193**, 173 (1981).
- [168] S.-B. Zhang, H.-Z. Lu, and S.-Q. Shen, *New J. Phys.* **18**, 053039 (2016).
- [169] H.-Z. Lu, S.-B. Zhang, and S.-Q. Shen, *Phys. Rev. B* **92**, 045203 (2015).
- [170] K. Fujikawa and H. Suzuki, *Path Integrals and Quantum Anomalies* (Oxford University Press, 2004).
- [171] DLMF, *NIST Digital Library of Mathematical Functions*, <http://dlmf.nist.gov/15.2>, Release 1.0.18 of 2018-03-27, f. W. J. Olver, A. B. Olde Daalhuis, D. W. Lozier, B. I. Schneider, R. F. Boisvert, C. W. Clark, B. R. Miller and B. V. Saunders, eds.
- [172] Y. X. Zhao and Y. Lu, *Phys. Rev. Lett.* **118**, 056401 (2017).